The mobility and fate of chromium in soils and sediments: implications for chromium cycling in natural and contaminated environments

Yao Zhao

Submitted in accordance with the requirement for the degree of Doctor of Philosophy

The University of Leeds
School of Earth and Environment

March 2022

The candidate confirms that the work submitted is his own, except where work, which has formed part of jointly authored publications has been included. The contributions of the candidate and the other authors to this work have been indicated overleaf. The candidate confirms that appropriate credit has been given where reference has been made to the work of others.

Declaration

Chapter 4 is a reproduction of a manuscript currently under "minor revision" decision, submitted to the journal *Geochimica et Cosmochimica Acta* as:

Zhao Y., Moore O. W., Xiao K. Q., Curti L., Frariña A.O., Banwart S. A., Peacock C. L. (2021) The role and fate of organic carbon during aging of ferrihydrite.

All experimental work has been conducted by the candidate, where Oliver W. Moore and Ke-Qing Xiao have given useful suggestions to solving problems in experiments. The X-ray absorption spectroscopy (XAS) measurement were conducted by Lisa Curti, and Alba Otero Frariña and Oliver Moore helped analyse the XAS data. The interpretation of experimental data and modelling work have been undertaken by the candidate with the help and guidance of his supervisors: Caroline L. Peacock and Steven A. Banwart. The preparation and revision of the manuscript have been undertaken by the candidate with the help of Caroline L. Peacock.

Chapter 5 is a reproduction of a manuscript currently in the final stages of preparation for submission to the journal *Geochimica et Cosmochimica Acta* as:

Zhao Y., Moore O. W., Xiao K. Q., Banwart S. A., Peacock C. L. (2021) The mobility and fate of Cr(VI) during aging of ferrihydrite and ferrihydrite organominerals.

All experimental work has been conducted by the candidate, where Oliver W. Moore and Ke-Qing Xiao have given useful suggestions to solving problems in experiments. The interpretation of experimental data, modelling work and preparation of the manuscript has been undertaken by the candidate with the help and guidance of his supervisors: Caroline L. Peacock and Steven A. Banwart.

Chapter 6 is a reproduction of a manuscript currently in preparation for submission to the journal *Geochimic et Cosmochimica Acta* as:

Zhao Y., Moore O. W., Xiao K. Q., Frariña A.O., Banwart S. A., Peacock C. L. (2021)

Behaviours and fate of chromium and carbon during Fe(II)-induced transformation of ferrihydrite organominerals.

All experimental work has been conducted by the candidate, where Ke-Qing Xiao has given supportive help in experimental options. The interpretation of experimental data, and preparation of the manuscript has been undertaken by the candidate with the help and guidance of his supervisors: Caroline L. Peacock and Steven A. Banwart. The preparation of the manuscript has been undertaken by the candidate with the help from Ke-Qing Xiao, Alba Otero Fariña, Oliver W. Moore, Steven A. Banwart and Caroline L. Peacock.

Acknowledgements

I have a lot of feelings when I look back on my Ph.D study. During this period, I changed from a beginner in this field to a qualified researcher, which is totally attributed to my supervisors. I deeply appreciate the invaluable support from Caroline Peacock and Steve Banwart. They gave me excellent guidance and training throughout the project, which was a perfect start for my research. They also helped me build confidence, release upset emotions and find inner peace to enjoy research and life, which means a lot to me. I also appreciate the help from Oliver W. Moore, Ke-Qing Xiao, Alba Otero-Farina, Lisa Curti and Peyman Babakhani. I thank everyone from the Cohen Geochemistry group, especially Yi-Jun Xiong, Tian-chen He, Andy Connelly, Fiona Keay, Stephen Reid and Andrew Hobson for laboratory support. I also would like to thank my friends for their support to help me go through the panic caused by Covid-19. Finally, I would like to thank for my wife, who keep company with me over 12 years. She is the brightest star in my sky. She gives me the inspiration, courage and direction. I really appreciate her understanding and support especially when I live in different countries. I really thank the funding for my Ph.D project provided by University of Leeds and China Scholarship Council.

Abstract

Chromium is one of the most common metal contaminants or one of most important nutrients depending on its valences and concentrations, whose mobility is controlled by soil minerals especially iron (oxyhydr)oxide. However, how mineralogical transformation of iron (oxyhydr)oxide in the presence of organic carbon (OC) controls the fixation and migration of chromium in many environments is largely unknown.

This thesis is to investigate influences of OC with different carboxyl-richness on the mobility and fate of chromium during the transformation of iron (oxyhydr)oxide under different redox conditions. I track changes in reactivity of iron (oxyhydr)oxide, the distribution of OC and/or chromium during the transformation of iron (oxyhydr)oxide in oxic or anoxic environments via employing wet chemical methods and techniques like LECO SC-144DR Dual Range Sulphur and Carbon Analyzer, Fourier-transform infrared spectroscopy and inductively coupled plasma mass spectrometry.

In Fh-OC coprecipitates, the binding strength of OC increases with the carboxyl-richness of the sequestered OC moieties. During the aging experiment under oxic conditions, my results indicate that OC with higher binding strength coprecipitated with Fh becomes proportionally more stable with the solid phase and thus less mobile during mineralogical transformation and aging in natural environments. Additionally, the strongly-bound carboxyl-rich OC significantly suppresses Cr(VI) adsorption and slows down and decreases the capture of Cr(VI) inside neo-formed minerals during the aging process, while the weakly-bound carboxyl-poor OC has no discernable influence on Cr(VI) adsorption but accelerates and increases the capture of Cr(VI) inside neo-formed minerals.

During Fe(II)-induced transformation of Fh organominerals under anoxic conditions, the presence of OC decreases the capture of Cr (mainly Cr(III)) inside neo-formed minerals, where the suppression on the Cr capture is enhanced with increasing carboxyl-richness of the sequestered OC. The presence of Cr(III) also aids the stabilisation of OC with the solid phase and increases the amount of non-desorbable C, where the elevation of OC stabilised and OC captured by Cr(III) is enhanced with increasing carboxyl-richness of the OC moieties. Overall, the mobility and fate of Cr(VI) in different environments is strongly controlled by the carboxyl-richness of the sequestered OC moieties in Fh organominerals. These findings are important for deepening our understanding about the role of Fe minerals-OC composites in global trace metal cycling.

Contents

Declaration……………………………………………………………..……………..………II

Acknowledgements…..…………………………..………………………..………………………IV

Abstract……………………………………………………………...…………………………V

Contents………………………………………………………………………………………VII

List of Figures……………………………………………………………………..………..XII

List of Tables…………………………………………………………………..……….XVII

Chapter 1 Introduction 1

1.1 Background information 1

1.2 Research aims and objectives 3

1.3 Thesis outline 4

Chapter 2 Literature review 5

2.1 Natural and Anthropogenic Sources of Cr to the Soil Environment 6

  2.1.1 Chemistry of Cr 6

  2.1.2 Sources and concentrations of Cr in the soil environment.. 7

2.2 Cycling of Cr in Soils 8

  2.2.1 Interactions between Cr and soil components.. 8

  2.2.2 Cycling of Cr in the soil environment.. 10

2.3 Sorption of Cr to Iron (oxyhydr)oxide...12

  2.3.1 Ferrihydrite.. 12

  2.3.2 Ferrihydrite Organo-minerals 13

  2.3.3 Cr(VI) sorption by iron (oxyhydr)oxides... 16

  2.3.4 Cr(III) sorption onto iron (oxyhydr)oxides 21

2.4 Mineralogical transformation of Fh 23

  2.4.1 Mineralogical transformation of Fh in oxic environment 23

  2.4.2 Fe(II)-induced transformation of Fh 25

2.5 Redistribution of OC during mineralogical transformation of Fh organominerals .26

2.6 Mobility and fate of Cr(VI) during mineralogical transformation of iron (oxyhydr)oxide under oxic and anoxic conditions..27

  2.6.1 Redistribution of Cr(VI) during aging process under oxic conditions........................... 27

  2.6.2 Fate of Cr(VI) during mineralogical transformation of iron (oxyhydr)oxide under anoxic condition.. 28

Chapter 3 Methods 29

3.1 Laboratory based methods 30
  3.1.1 Synthesis of pure Fh and Fh organominerals 30
  3.1.2 OC adsorption onto pure Fh 32
  3.1.3 Cr(VI) adsorption onto pure Fh and Fh organominerals 32
  3.1.4 Mineralogical transformation of pure Fh and Fh organominerals 33
  3.1.5 Fe(II)-induced mineralogical transformation of pure Fh and Fh organominerals 34
  3.1.6 Synthesis reference goethite, lepidocrocite and magnetite 35
3.2 Analytical and spectroscopic tools 36
  3.2.1 Inductively Coupled Plasma-Mass Spectrometry (ICP-MS) 36
  3.2.2 Atomoc Absorption Spectrophotometer (AAS) 36
  3.2.3 LECO SC-144DR Dual Range Sulphur and Carbon Analyzer 36
  3.2.4 Attenuated Total Reflectance Fourier transform infra-red spectroscopy (FTIR) 37
  3.2.5 Brunauer-Emmett-Teller surface area analysis (BET) 38
  3.2.6 Ultraviolet–visible (UV–Vis) spectroscopy 38
  3.2.7 X-ray diffraction 39
  3.2.8 Scanning transmission X-ray microscopy near-edge X-ray absorption fine structure spectroscopy (STXM NEXAFS) 40
3.3 OC and Cr(VI) surface complexation modelling 40

Chapter 4 The role and fate of organic carbon during aging of ferrihydrite 42

4.1 Introduction 42
4.2 Materials and methods 47
  4.2.1 Preparation of Fh organomineral coprecipitates 47
  4.2.2 Characterisation of Fh organomineral coprecipitates 48
  4.2.3 Aging of Fh organomineral coprecipitates 51
  4.2.4 Measured physiochemical characteristics of Fh organomineral coprecipitates during aging 52
4.3 Results 54
  4.3.1 Characterisation of Fh organomineral coprecipitates prior to aging 54
  4.3.2 Adsorption of carboxylic acids to ferrihydrite 55
  4.3.3 Aging of ferrihydrite coprecipitates 56
  4.3.4 Carbon distribution during aging of ferrihydrite coprecipitates 59
4.4 Discussion 65

4.4.1 Sequestration of carboxyl-rich OC with ferrihydrite prior to aging 65
4.4.2 Influence of carboxyl-rich OC on the aging of ferrihydrite 77
4.4.3 Distribution of carboxyl-rich OC during aging of ferrihydrite 81
4.5 Conclusions 89

Chapter 5 The mobility and fate of Cr(VI) during aging of ferrihydrite and ferrihydrite organominerals 91

5.1 Introduction 92
5.2 Materials and methods 97
5.2.1 Preparation of Fh and Fh organomineral coprecipitates 97
5.2.2 Cr(VI) adsorption on Fh and Fh organomineral coprecipitates and surface complexation modelling 99
5.2.3 Mineralogical transformation of Cr(VI)-adsorbed Fh and Fh organomineral coprecipitates 101
5.3 Results 103
5.3.1 Cr(VI) adsorption on pure ferrihydrite and ferrihydrite organominerals 103
5.3.2 Transformation rates of pure ferrihydrite and ferrihydrite organominerals under the influence of Cr(VI) 111
5.3.3 Distribution of OC during the mineralogical transformation 114
5.3.4 Distribution of Cr(VI) during the mineralogical transformation 117
5.4 Discussion 120
5.4.1 Influence of carboxyl-rich OC with different binding strengths on Cr(VI) adsorption to ferrihydrite organominerals 120
5.4.2 Influence of Cr(VI) adsorption on the kinetics of ferrihydrite and ferrihydrite organomineral transformation 125
5.4.3 Distribution of Cr(VI) during the mineralogical transformation 126
5.5 Conclusion 134

Chapter 6 Behaviours and fate of chromium and carbon during Fe(II)-induced transformation of ferrihydrite organominerals 136

6.1 Introduction 137
6.2 Experimental methods 140
6.2.1 Preparations for mineralogical transformation experiment 140

6.2.2 FTIR characterization 143
6.3 Results 145
6.3.1 Mineralogical transformation of iron minerals 145
6.3.2 Distribution of Cr species during Fe(II)-induced transformation of pure Fh and Fh organominerals 147
6.3.3 Influence of Cr on properties of secondary iron minerals 150
6.3.4 Carbon distribution during Fe(II)-catalysed transformation 153
6.4 Discussion 155
6.4.1 Fe(II)-induced ferrihydrite and Fh organominerals transformation in the presence of Cr and OC. 155
6.4.2 Cr speciation and distribution during Fe(II)-catalysed Fh transformation 157
6.4.3 Influences of Cr on properties of secondary iron minerals 161
6.4.4 Carbon distribution during Fe(II)-induced ferrihydrite transformation 162
6.5 Conclusion 166

Chapter 7 Summary and suggestions for future research…… 168

7.1 The role and fate of organic carbon during aging of ferrihydrite 175
7.2 The mobility and fate of Cr during aging of ferrihydrite and ferrihydrite organominerals 175
7.3 Behaviours and fate of chromium and carbon during Fe(II)-induced transformation of ferrihydrite organominerals 175
7.4 Suggestions for future research 175

Appendix 176

Reference 191

List of Figures

Figure 2.1 Eh-pH diagram for the system Cr-O_2-H_2O, assuming that the concentration of Cr = 10^{-6} M at solid/liquid boundaries (modified from Dhal et al., 2013)……………………….7

Figure 2.2. Chromium cycle in soil environment (modified from (Dhal et al., 2013b))…....11

Figure 4.1. Carbon 1s NEXAFS spectra for Fh_Pen1/5_1.2wt%C and both Fh_Hex2/6 and Fh_But3/7 coprecipitates at the lower and upper end of wt%C sequestered (solid and dashed-dotted lines), together with Pen1/5, Hex2/6 and But3/7 unreacted acid standards (dotted lines). Black, blue and red colours represent Pen1/5, Hex2/6 and But3/7 data, respectively. Carboxyl C peak position for the unreacted Pen1/5, Hex2/6 and But3/7 standards are shown with vertical dashed black, blue and red lines, respectively. Spectra are stacked with an arbitrary offset for clarity. Pen1/5, Hex2/6 and But3/7 represent simple carboxyl-rich OC with one, two and three carboxyl groups, respectively..……………………………………………………………….55

Figure 4.2. OC adsorption on pure Fh as a function of pH (3.5-10). Experiments were performed with about 4 $\times 10^{-4}$ M OC (Pen1/5: 4.16 $\times 10^{-4}$ M; Hex2/6: 4.29×10^{-4} M and But3/7: 4.17×10^{-4} M) in 0.01 M $NaNO_3$ background electrolyte and a solid-solution ratio of 2 g dry sorbent L^{-1}. Black, blue and red symbols represent Pen1/5, Hex2/6 and But3/7 data, respectively. Pen1/5, Hex2/6 and But3/7 represent simple carboxyl-rich OC with one, two and three carboxyl groups, respectively. Error bars represent standard deviations of duplicate samples. ……………………………………………………………………………...56

Figure 4.3. Fraction of Fh remaining after acid extraction for Fh coprecipitates and pure Fh at pH 5 (a) and 6.5 (b). Experiments were performed with Fh coprecipitates in 0.01 M $NaNO_3$ background electrolyte and a solid-solution ratio of 2 g dry sorbent L^{-1} at 75 ℃. Black, blue and red symbols represent Pen1/5, Hex2/6 and But3/7 data, respectively. Pen1/5, Hex2/6 and But3/7 represent simple carboxyl-rich OC with one, two and three carboxyl groups, respectively. Error bars represent standard deviations of at least duplicate samples………. 58

Figure 4.4. Temporal changes in the total amount of C in the Fh coprecipitate solid phase during 19 days aging at a) pH 5.0 and b) pH 6.5. Experiments were performed with Fh coprecipitates in 0.01 M $NaNO_3$ background electrolyte and a solid-solution ratio of 2 g dry sorbent L^{-1} at 75 ℃. Black, blue and red symbols represent Pen1/5, Hex2/6 and But3/7 data, respectively. Pen1/5, Hex2/6 and But3/7 represent simple carboxyl-rich OC with one, two and

three carboxyl groups, respectively. Error bars represent standard deviations of at least duplicate samples……………………………………………………………………………..61

Figure 4.5. Temporal changes in the total amount of non-desorbable C in the Fh coprecipitates solid phase during 19 days aging at a) pH 5.0 and b) pH 6.5. Experiments were performed with Fh coprecipitates in 0.01 M $NaNO_3$ background electrolyte and a solid-solution ratio of 2 g dry sorbent L^{-1} at 75 ℃. Black, blue and red symbols represent Pen1/5, Hex2/6 and But3/7 data, respectively. The solid minerals were treated with 0.1 M NaOH for 24 h to extract OC. Pen1/5, Hex2/6 and But3/7 represent simple carboxyl-rich OC with one, two and three carboxyl groups, respectively. Error bars represent standard deviations of at least duplicate samples…………63

Figure 4.6. Possible adsorption configurations of carboxylic acids adsorbed to Fe (oxyhydr)oxides from spectroscopic evidence: a) One-carboxyl adsorption in which mono-carboxylic acids adsorb via their one carboxyl group in either a single-bonded or twice-bonded configuration, and di-carboxylic acids adsorb via one carboxyl group which binds to one FeOH site in a monodentate mononuclear configuration; b) Two-carboxyl adsorption in which di- and tri-carboxylic acids adsorb using two carboxyl groups which bind to either one FeOH site in a bidentate mononuclear configuration or two FeOH sites in a bidentate binuclear configuration; and c) Three-carboxyl adsorption in which tri-carboxylic acids adsorb using three carboxyl groups in a tridentate trinuclear configuration. ………………………………………………72

Figure 4.7. Surface species for: a) Pen1/5, b) Hex2/6 and c) But3/7 as function of pH based on complexation model fits (lines) to adsorption data (symbols). Black, blue and red symbols represent Pen1/5, Hex2/6 and But3/7 data, respectively. Monodentate (red lines), bidentate (blue lines) and tridentate (purple lines) represent one, two and three carboxyl binding, respectively, via corner sharing complexation (solid red, blue, purple lines) and edge-sharing complexation (dashed red, blue, purple lines). The black solid lines are the sum of the modelled species, representing the total amount of OC adsorbed. Pen1/5, Hex2/6 and But3/7 represent simple carboxyl-rich OC with one, two and three carboxyl groups, respectively. Error bars represent standard deviations of at least duplicate samples. ……………………………………75

Figure 4.8. Percentage of C that is non-desorbable with aging. The percentage of non-desorbable C is calculated by $[C_{\text{non-desorbable}}]/[C_{\text{total}}]$. Black, blue and red symbols represent Pen1/5, Hex2/6 and But3/7 data, respectively. Pen1/5, Hex2/6 and But3/7 represent simple carboxyl-rich OC with one, two and three carboxyl groups, respectively. Error bars represent standard deviations of at least duplicate samples. ……………………………………………89

Figure 5.1. Calculation of chromium speciation at 1.92 $\times10^{-6}$, 1.92 $\times10^{-5}$, 1.92 $\times10^{-4}$ M $[Cr(VI)]_{total}$ in 0.1 M $NaNO_3$ background electrolyte……………………………………104

Figure 5.2. Cr(VI) adsorption on pure Fh and Fh organominerals as a function of pH (3.5-10). Experiment conditions are 1.92 $\times10^{-6}$, 1.92 $\times10^{-5}$, 1.92 $\times10^{-4}$ M $[Cr(VI)_{total}]$ for Fh (0.01 wt%, 0.1 wt% and 1.0 wt% Cr at 100% adsorption, respectively) and 1.92 $\times10^{-5}$ M $[Cr(VI)_{total}]$ for Fh organominerals (0.1 wt% Cr at 100% adsorption), in 1 g sorbent L^{-1} in 0.1 M $NaNO_3$ background electrolyte. Pen1/5, Hex2/6 and But3/7 represent simple carboxyl-rich OC with one-, two- and three-carboxyl groups, respectively. The average error bar for duplicate experiments is smaller than the data points……………………………………………105

Figure 5.3. Model fits for Cr(VI) adsorption on pure Fh and Fh organominerals. (a)-(c) for pure Fh with Cr(VI) concentrations at 0.01 wt%Cr, 0.1 wt%Cr and 1.0 wt%Cr at 100% adsorption. (d)-(l) for Fh organominerals with Cr(VI) concentration at 0.1 wt%Cr at 100% adsorption. Black solid squares are the Cr(VI) adsorption experimental data; black lines are the predicted total Cr(VI) adsorption; blue lines are the predicted bidentate Cr(VI) complexes ($\equiv(FeO)_2CrOO^-$); red lines are the predicted monodentate Cr(VI) complexes ($\equiv(FeO)CrO_3^{-1.5}$). Pen1/5, Hex2/6 and But3/7 represent simple carboxyl-rich OC with one-, two- and three-carboxyl groups, respectively. The average error bar for duplicate experiments is smaller than the data points……………………………………………………………111

Figure 5.4. Transformation rate of pure Fh with different Cr(VI) adsorbed at (a) pH 5 with 0.1 wt%Cr (Cr/Fe=0.002), 1.1 wt%Cr (Cr/Fe=0.02) and 5.4 wt%Cr (Cr/Fe=0.10) at 100% adsorption; (b) pH 6.5 with 0.1 wt%Cr (Cr/Fe=0.002) and 1.1 wt%Cr (Cr/Fe=0.02) at 100% adsorption; and (c) at different pH conditions (pH 5, pH 6.5 and pH 8) with 1.1 wt%Cr (Cr/Fe=0.02) at 100% adsorption……………………………………………………..113

Figure 5.5. Transformation rate of Fh organominerals in the absence and presence of Cr(VI). a) and b) transformation rate of Fh organominerals without Cr(VI) (open symbols) and with Cr(VI) (solid symbols) at 0.1 wt%Cr (Cr/Fe=0.002) at 100% adsorption at pH 5 and pH 6.5, respectively. c) and d) enhanced retardation caused by Cr(VI) at 0.1 wt%Cr (Cr/Fe=0.002) at 100% adsorption at pH 5 and pH 6.5, respectively, derived from transformation rates with Cr(VI) adsorbed minus those without Cr(VI) adsorbed. Pen1/5, Hex2/6 and But3/7 represent simple carboxyl-rich OC with one-, two- and three-carboxyl groups, respectively…………114

Figure 5.6. Temporal changes of total C% with solid phase in the absence (open symbols) and presence (solid symbols) of Cr(VI) at 0.1 wt%Cr (Cr/Fe=0.002) at 100% adsorption during 19-days transformation at a) pH 5.0 and b) pH 6.5. Experiments were performed with Fh

organominerals in 0.01 M $NaNO_3$ background electrolyte and a solid-solution ratio of 2 g dry sorbent L^{-1} at 75℃. Pen1/5, Hex2/6 and But3/7 represent simple carboxyl-rich OC with one- two- and three- carboxyl groups, respectively……………………………………………116

Figure 5.7. Distribution of Cr(VI) with different Cr(VI) adsorbed (0.1 wt%Cr (Cr/Fe=0.002), 1.1 wt%Cr (Cr/Fe=0.02) and 5.4 wt%Cr (Cr/Fe=0.10) at 100% adsorption) during the transformation of pure Fh at pH 5, pH 6.5 and pH 8……………………………………..118

Figure 5.8. Distribution of Cr(VI) with 0.1 wt%Cr (Cr/Fe = 0.002) at 100% adsorption during the transformation of Fh organominerals at a) pH 5 and b) 6.5…………………………..119

Figure 5.9. Diagram illustrating the influences of OC with different binding strengths on the total amount of Cr(VI) that is non-desorbable with 0.1 M NaOH and the rate constant for the capture of non-desorbable Cr(VI) into structural defects and surface pores during the mineralogical transformation of iron (oxyhydr)oxide organominerals……………………..134

Figure 6.1. Time-dependent changes in total amount of aqueous and desorbable Fe(II) during the transformation of pure Fh and Fh-organo minerals with and without Cr(VI) adsorbed…145

Figure 6.2. Relative proportions of Gt (red solid circles) and Lp (black open squares), respectively, during the Fe(II)-catalyzed transformation of pure Fh and Fh-organominerals (Fh_Pen1/5_8.7wt%C, Fh_Hex2/6_8.4wt%C and Fh_But3/7_10.1wt%C) with or without Cr(VI) at pH 5.75 and 7.00………………………………………………………………147

Figure 6.3. Temporal changes of Cr species during the Fe(II)-catalyzed transformation of pure Fh and Fh organominerals at a) pH 5.75 and b) pH 7.00. Experiments were performed with Fh-OC composites in 0.01 M $NaNO_3$ background electrolyte and a solid-solution ration of 2 g dry sorbent L^{-1} in the presence of 40.5 ppm Fe(II) by batch experiment. Pen1/5, Hex2/6 and But3/7 represent simple carboxyl rich OC with one, two and three carboxyl groups, respectively…149

Figure 6.4. Gaussian deconvolution analyses of the OH-stretching region in ATR-FTIR spectra for pure a) ferrihydrite, b) goethite and c) lepidocrocite. From higher to lower frequencies are non-stoichiometric hydroxyls and stoichiometric (or bulk) OH groups with a shoulder……………………………………………………………………………..151

Figure 6.5. ATR-FTIR spectra at pH 5.75 as a function of time for pure Fh a) without Cr and b) with Cr and the corresponding Gaussian deconvolution analyses after reacting for 18 days c) without Cr and d) with Cr. The solid lines in a) and b) are the sum of different OH groups in each sample, where solid lines with different colors indicate the total band migration over the 18 days and the dashed line indicates changes in non-stoichiometric OH stretching bands. From

higher to lower frequencies in c) and d) are non-stoichiometric hydroxyls and stoichiometric (or bulk) OH groups with a shoulder……………………………………………………………152

Figure 6.6. ATR-FTIR spectra at pH 7.00 as a function of time for pure Fh a) without and with Cr and Gaussian deconvolution analyses after reacting for 1day b) without Cr and c) with Cr. The dashed line in a) indicates changes in non-stoichiometric OH stretching bands. From higher to lower frequencies in b) and c) are non-stoichiometric hydroxyls and stoichiometric (or bulk) OH groups with a shoulder……………………………………………………………153

Figure 6.7. Temporal changes in the total amount of C in the Fh-OC solid phase during Fe(II)-catalyzed transformation at a) pH 5.75 and b) pH 7.00 in the presence of Cr (red solid circles) and in the absence of Cr (black open squares). Experiments were performed with Fh-OC composites in 0.01 M $NaNO_3$ background electrolyte and a solid-solution ration of 2 g dry sorbent L^{-1} in the presence of 40.5 ppm Fe(II). Pen1/5, Hex2/6 and But3/7 represent simple carboxyl rich OC with one, two and three carboxyl groups, respectively. Note differing scale on y-axis for Fh_Pen1/5……………………………………………………………………154

Figure 6.8. Temporal changes in the total amount of non-desorbable C in the Fh-organominerals solid phase during Fe(II)-induced transformation at a) pH 5.75 and b) pH 7.00 in the presence of Cr (red solid circles) and in the absence of Cr (black open squares). The red and black dotted lines are with and without Cr, respectively, indicating influence of Cr(III) on the amount of non-desorbable C. Pen1/5, Hex2/6 and But3/7 represent simple carboxyl rich OC with one, two and three carboxyl groups, respectively. Error bars represent standard deviations of at least duplicate samples………………………………………………………...155

Figure 6.9 The capture of Cr(III) during Fe(II)-induced transformation of Fh and Fh organominerals. a) two phases of capture of Cr(III) based on the transformation processes and b) influences of OC on the capture of Cr(III). ………………………………………………159

Figure 6.10 Influences of Cr(III) on the stabilization of OC including a) the total solid C and b) the non-desorbable C during Fe(II)-induced transformation. ……………………………164

List of Tables

Table 2.1 Complexes of Cr(VI) and Cr(III) with iron (oxyhydr)oxide and carboxylic OC…..9

Table 3.1 Information of Fh organominerals synthesized……………………………...…31

Table 4.1. SSA and TPV for pure Fh, Fh_Pen1/5_1.2wt%C, Fh_Hex2/6_7.0wt%C and Fh_But3/7_7.3wt%C after 19 days aging at pH 6.5…………………………………...…….59

Table 4.2a. Total amount of C in the Fh coprecipitates before and after 19 days aging……64

Table 4.2b. Total amount of non-desorbable C in the Fh coprecipitates before and after 19 days aging………………………...……………………………………...……..……….64

Table 4.3. Surface coverage of Fh coprecipitates by adsorbed C……………………………68

Table 4.4. Input parameters for the surface complexation model for adsorption of carboxylic acids on pure Fh……………………………..…………………………………………74

Table 4.5a. Surface coverage of Fe minerals for Fh_Pen1/5_1.2wt%C, Fh_Hex2/6_7.0wt%C and Fh_But3/7_7.3wt%C after 19 days aging at pH 6.5……………………………………...…84

Table 4.5b. Adsorption capacity of Fe minerals for Fh_Pen1/5_1.2wt%C, Fh_Hex2/6_7.0wt%C and Fh_But3/7_7.3wt%C after 19 days aging …...…………………...…84

Table 5.1. Information of Fh organominerals synthesized…...………………...……………98

Table 5.2. Parameters for the surface complexation model for adsorption of Cr(VI) and carboxylic acids on pure Fh and Fh organominerals………………………………………109

Table 5.3. Rates of capture of non-desorbable Cr(VI) during transformation of pure Fh and Fh organominerals……………………………………………………………………….120

Table 5.4. Surface coverage of surface sites on Fh end-member by organic acids and Cr(VI)…………………………………………………………………………………….124

Table 6.1. Rate of exchange from Cr(III)$_{\text{desorbable}}$ to Cr$_{\text{non-desorbable}}$ during Fe(II)-induced transformation of pure Fh and Fh organominerals………………………………………150

Table 6.2 The highest influences of Cr on C$_{\text{total-solid}}$ during the Fe(II)-induced transformation of Fh-organominerals……………………………………………………….......…165

Chapter 1 Introduction

1.1 Background information

Chromium is the 7th most abundant element in both the Earth’s crust and mantle (Katz and Salem, 1994). Depending on its two most common valences Cr(VI) or Cr(III), it can be one of the most common metal contaminants in soil, groundwater and surface water bodies (Dhal et al., 2013b) or be one of the essential nutrients to fauna, respectively (Jeejeebhoy et al., 1977; Scawarz and Mertz, 1959). Hexavalent chromium Cr(VI) is highly toxic and also more soluble and bioavailable than trivalent chromium Cr(III), and thus presents a mobile biohazard in aquatic and soil ecosystems (Chandra and Kulshreshtha, 2004; Costa, 1997; Shanker et al., 2005). The potential environmental harm posed by Cr(VI) means that it is important to understand how this species interacts with soil constituents in order to predict Cr mobility and fate, and to develop soil remediation methods.

Compared to other soil minerals, iron (oxyhydr)oxides, especially ferrihydrite (Fh), have widespread occurrence, high specific surface area and various binding sites for adsorption of solution species (Hiemstra, 2013; Larsen and Postma, 2001; Michel et al., 2007b). As such they act as efficient adsorbents of organic compounds (Cornell and Schwertmann, 2003) and heavy metal (aluminium, transmission metals, lanthanide and actinide elements) contaminants including Cr(VI) in soils (Gu et al., 2017; Mikutta et al., 2014). Authigenic Fh is metastable under oxic conditions, however, and undergoes thermodynamically spontaneous geochemical and mineralogical transformation to other more stable secondary iron (oxyhydr)oxides, like goethite (Gt) and hematite (Hm) (Das et al., 2011b). Because the transformation involves many types of geochemical reactions and physical processes like dissolution, precipitation, aggregation, adsorption and desorption (Sakakibara et al., 2019) and the secondary iron minerals also have physical and chemical properties that are different from Fh (Cornell and Schwertmann, 2003), the mineralogical transformation can influence the mobility of adsorbed organics and heavy metals (Francisco et al., 2018; Hu et al., 2020; Hu et al., 2018; Sakakibara et al., 2019). In addition Fh formed in natural environments is typically associated with dissolved or particulate organic carbon (OC) to form organominerals. Recent studies show that up to 40% of total OC in various soils is bound to reactive iron phases, likely during coprecipitation (Wagai and Mayer, 2007; Zhao et al., 2016). The presence of OC can significantly influence Fh transformation in terms of transformation rate, pathway and the chemical and physical properties of secondary iron minerals (Amstaetter et al., 2012; Fredrickson et al., 1998; Hansel et al., 2003; Hu et al., 2020; Lovley et al., 1996). The presence of OC also influence the properties of iron (oxyhydr)oxide: OC can influence adsorption site availability via blocking surface or provide additional adsorption sites (Chen et al., 2014; Shimizu et al., 2013); OC can increase crystallographic defects (Eusterhues et al., 2014) or surface pores (Mikutta et al., 2014) of iron (oxyhydr)oxide by inhibiting crystal growth during forming process. On the other hand, iron (oxyhydr)oxides make great contributions to the stabilization of OC, which can adsorb / coprecipitate with OC and thus stabilise OC against microbial degradation under both oxic and anoxic conditions (Hemingway et al., 2019; Kaiser and Guggenberger, 2007; Li et al., 2020; Mikutta et al., 2006; Newcomb et al., 2017; Torn et al., 1997; Zhao et al., 2016). The re-distribution of OC associated with Fh is thus induced when the transformation of Fh occurs in natural environment. As such, the transformation of Fh and Fh organominerals plays an important role in controlling the stabilization of OC and the adsorption and capture of Cr in soils.

Resent studies show that OC may be sequestered in the structure defects or surface pores of newly formed minerals during transformation (Hu et al., 2020; Lu et al., 2019b), or partially released from iron (oxyhydr)oxides because the amount of OC associated with initial solid minerals exceed the adsorption capacity of secondary iron minerals and/or the dissolution of iron (oxyhydr)oxide occurs during transformation (Adhikari et al., 2017; Jelavić et al., 2020). Whether OC is retained or released during transformation depends on several factors, including C/Fe ratio (Adhikari et al., 2017; Chen et al., 2015), whether OC is adsorbed or coprecipitated (Han et al., 2019), the structure and electron-shuttling properties of the OC (Amstaetter et al., 2012), the crystalline structures of secondary mineral products (Hu et al., 2020; Lu et al., 2019b), and the presence of heavy metals like Pb(II) (Lu et al., 2019b). Despite these studies however, the effects of different types and binding strengths of OC and the presence of Cr on the mineralogical transformation and the mobility and fate of OC are still unknown.

There are a limited number of studies focusing on the mobility of Cr(VI) during the mineralogical transformation of iron (oxyhy)oxides under oxic conditions. The transformation of Fh generally increases the proportion of non-desorbable Cr(VI) because some Cr(VI) are incorporated into structure defects or surface pores of secondary iron minerals (Yu et al., 2020; Yu et al., 2021; Zhu et al., 2019), which decreases the mobility of Cr(VI). Whilst the transformation of Fh also increases aqueous Cr(VI) because of the lower specific surface area of secondary iron minerals (Zhu et al., 2019), which increase the migration of Cr(VI). However, the influence of OC on the distribution of Cr during the mineralogical transformation of iron (oxyhydr)oxide organomienrals has not been studied in any substantial detail. Studies are also rare to reveal the microscopic mechanistic interactions between iron (oxyhydr)oxide organominerals and Cr(VI), in which the focus is not on the chemical reduction of Cr(VI). Therefore, the influence of OC on Cr(VI) adsorption behaviour to iron (oxyhydr)oxide organominerals, and the mobility and fate of Cr(VI) during the transformation of these organominerals is still largely unknown.

Similarly rare are studies that focus on the behaviour of Cr(VI) during the mineralogical transformation under anoxic condition, where the mobile Cr(VI) is readily reduced to relatively less soluble and therefore lower-mobility Cr(III) (Buerge and Hug, 1997). As a trivalent cation Cr^{3+} has strong affinity to iron (oxyhydr)oxides and OC (Gustafsson et al., 2014; Yang et al., 2020; Zhang et al., 2017; Zhang et al., 2018), whilst Cr^{3+} readily incorporates into iron (oxyhydr)oxide by isomorphous substitution (Charlet and Manceau, 1992; Choppala and Burton, 2018; Dai et al., 2016; Hua et al., 2018; Manceau et al., 2000; Maslar et al., 2001; Tang et al., 2010; Trolard et al., 1995). To the authors' knowledge, however, only one study investigates the influence of OC on the distribution of Cr during the mineralogical transformation of iron (oxyhydr)oxide organominerals in reducing environments, where it is observed that the transformation of Fh-humic acid composites increases non-desorbable Cr after aging, probably via a redox reaction which reduces more soluble Cr(VI) to less soluble Cr(III) forms (Yu et al., 2020). There is little information that reveals detailed information about how OC influences the transformation of iron (oxygydr)oxide as well as the mobility and fate of Cr (mainly Cr(III)) in reducing environment.

1.2 Research aims and objectives

The overarching aim of the current study is to deepen our understanding of the role of Fh organominerals in the stabilization of OC and in the migration and fixation of chromium in soils and sediments. As such, the specific research objectives of this thesis address three aspects:

(1) Investigate how OC binding strength controls the aging process of Fh and subsequent retention or release of the associated OC during aging under oxic conditions;

(2) investigate how OC binding strength influences Cr(VI) adsorption to Fh organominerals and the capture of Cr(VI) inside minerals during aging of Fh under oxic conditions;

(3) investigate how OC carboxyl-richness influences the mineralogical transformation of iron (oxyhydr)oxide under anoxic conditions and the subsequent re-distribution of Cr as transformation proceeds, and investigate how Cr(III) influences the stabilization of OC during the transformation process.

1.3 Thesis outline

This thesis consists of seven chapters. This introductory chapter (Chapter 1) is followed by a detailed literature review relevant to this project (Chapter 2). Chapter 3 contains a detailed description of experimental and analytical methods used throughout this work, followed by three individual results chapters. Chapter 4 investigates influences of OC binding strength on the aging of iron (oxyhydr)oxide, and the mobility and fate of the OC during the aging process under oxic conditions. Chapter 5 provides new insight into influences of OC binding strength on Cr(VI) adsorption to Fh organominerals and the capture of Cr(VI) in minerals as the aging proceeds under oxic conditions. Chapter 6 investigate influences of OC carboxyl-richness on Fe(II)-induced transformation and the subsequent re-distribution of Cr as transformation proceeds, and provides new information about the influences of Cr(III) on the stabilization of OC during the transformation process. The final chapter (Chapter 7) is to summarize the broader significance of results from chapters 4-6 and discuss possible future work resulting from this PhD thesis.

Chapter 2 Literature review

The following chapter gives a detailed literature review relevant to this work. This chapter is described as:

2.1 Natural and Anthropogenic Sources of Cr to the Soil Environment 6
  2.1.1 Chemistry of Cr 6
  2.1.2 Sources and concentrations of Cr in the soil environment 7
2.2 Cycling of Cr in Soils 8
  2.2.1 Interactions between Cr and soil components 8
  2.2.2 Cycling of Cr in the soil environment 10
2.3 Sorption of Cr to Iron (oxyhydr)oxide 12
  2.3.1 Ferrihydrite 12
  2.3.2 Ferrihydrite Organo-minerals 13
  2.3.3 Cr(VI) sorption by iron (oxyhydr)oxides 16
  2.3.4 Cr(III) sorption onto iron (oxyhydr)oxides 21
2.4 Mineralogical transformation of Fh 23
  2.4.1 Mineralogical transformation of Fh in oxic environment 23
  2.4.2 Fe(II)-induced transformation of Fh 25
2.5 Redistribution of OC during mineralogical transformation of Fh organominerals .26
2.6 Mobility and fate of Cr(VI) during mineralogical transformation of iron (oxyhydr)oxide under oxic and anoxic conditions 27
  2.6.1 Redistribution of Cr(VI) during aging process under oxic conditions 27
  2.6.2 Fate of Cr(VI) during mineralogical transformation of iron (oxyhydr)oxide under anoxic condition 28

2.1 Natural and Anthropogenic Sources of Cr to the Soil Environment

2.1.1 Chemistry of Cr

Chromium is the 21th most abundant element in Earth's crust (Shahid et al., 2017) and also one of most common metal contaminants (Dhal et al., 2013b). Among nine valence states of chromium (-2 to +6), Cr(VI) and Cr(III) are two common and stable oxidation states in natural waters, which correspond to different chemical properties and behaviours.

Cr(VI) is the most oxidized, mobile, reactive and toxic form of chromium in the natural environment. Depending on different pH and concentration conditions, Cr(VI) exists as several aqueous species, namely, $HCrO_4^-$, CrO_4^{2-}, $Cr_2O_7^{2-}$ and H_2CrO_4, where $HCrO_4^-$ normally predominates at pH 1-6 and CrO_4^{2-} dominates at pH > 7 (Figure 2.1) (Barrera-Díaz et al., 2012; Dhal et al., 2013a). Many redox couples composed of the aqueous species of Cr(VI) and Cr(III) (e.g. CrO_4^{2-}/Cr^{3+}) are relatively strong and highly reactive. The oxidised species is generally thermodynamically stable, relative to the $O_{2(aq)}/H_2O$ redox couple, under oxic conditions. Hexavalent (Cr(VI)) species can easily diffuse across biological membranes (Alexander and Aaseth, 1995; Dreyfuss, 1964; Wiegand et al., 1985), causing oxidative damage to biological molecules with DNA alteration and other toxic effects during the reduction reaction in cells. Cr(VI) contamination can reduce microbial growth and activities like inhibiting respiration and photosynthesis (Fasulo et al., 1983), altering soil microbial communities (Turpeinen et al., 2004; Zhou et al., 2002). The presence of Cr(VI) also significantly influence the growth of plants like deleting protein contents and nitrate reductase activity, micronuclei formation and chromosome aberrations, leading to chlorosis and necrosis (Cervantes et al., 2001). Biological exposure to Cr(VI) can also cause severe effects on fauna like causing diarrhea, ulcers, eye and skin irritation, kidney dysfunction, lung carcinoma, mutagenesis and birth defects and decrease in reproductive health (Jobby et al., 2018). The potential environmental harm posed by hexavalent chromium means that it is important to understand how Cr(VI) interacts with soil constituents in order to predict Cr mobility and fate, and develop soil remediation methods.

Cr(III) predominates under reducing conditions and mainly exists as oxyhydroxide mineral phases such as ($Cr(OH)_{3(s)}$) that are sparingly soluble. The dissolved Cr(III) exists as Cr^{3+}, $Cr(OH)^{2+}$ and $Cr(OH)_3^0$ and $Cr(OH)_4^-$ in aqueous solution (Figure 2.1) (Rai et al., 1986; Rai and Zachara, 1986). Whereas, these aqueous Cr(III) species show a strong adsorption onto soil components such as Fe (oxyhydr)oxide, clay minerals and silica phases as well as organic particulate surfaces that act as ligands resulting in the formation of complexes, all of which, together with the relatively insoluble Cr(III) precipitates, limits Cr(III) mobility (Palmer and Wittbrodt, 1991; Richard and Bourg, 1991a). Cr(III) at lower concentration is less toxic and is an essential mineral nutrient to fauna during bio-processes, like carbohydrate, lipid and protein metabolism and amino- and nucleic acid synthesis (Jeejeebhoy et al., 1977; Scawarz and Mertz, 1959). Therefore, interaction mechanisms of Cr(III) with soil components is key to understanding and predicting the stabilization, migration and bio-availability of Cr(III) in soils and sediments.

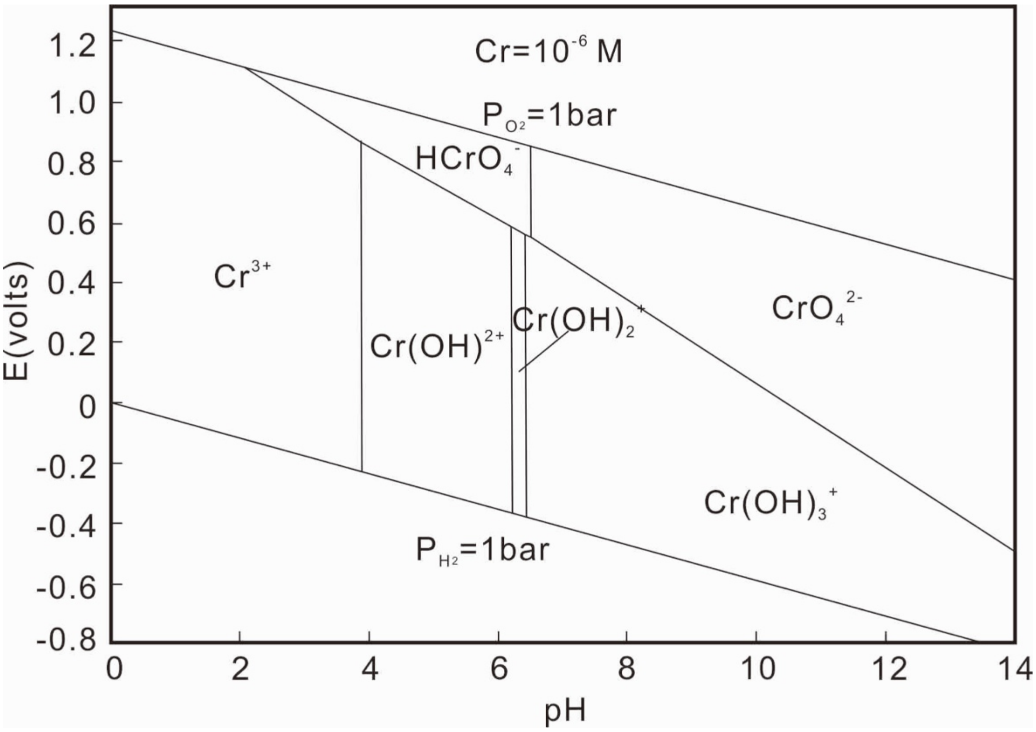

Figure 2.1 Eh-pH diagram for the system Cr-O_2-H_2O, assuming that the concentration of Cr = 10^{-6} M at solid/liquid boundaries (modified from Dhal et al., 2013).

2.1.2 Sources and concentrations of Cr in the soil environment

In the natural environment, chromium occurs in rocks, soils, water, and volcanic dust and gases (Shanker et al., 2005). Chromium exists in primary rocks like chromite ($FeCr_2O_4$) in serpentine or ultramafic rocks (Avudainayagam et al., 2003; Babula et al., 2009), or occurs in original and secondary minerals by co-precipitating with manganese (Mn), Aluminum (Al), and/or iron (Fe) oxides and hydroxides (Stumm and Morgan, 1996). The concentration of Cr in the parent rocks vary greatly from 5-120 ppm in sedimentary and igneous rocks to 1600-3400 ppm in ultramafic rocks (Kabata-Pendias, 2000). Natural levels of Cr in the Earth's crust vary in the range of 0.1-0.3 ppm, while Cr concentrations in major soils, fresh water and seawater are 15-100 ppm, 0.1-117 ppm and 0.2-50 ppm, respectively (Shahid et al., 2017).

Actually, another significant source of chromium, especially Cr(VI), is derived from human activities, such as chromite ore processing residue, leather tanning, metallurgy, alloying, electroplating, ceramic glazes, metal alloy corrosion by water, wood preservation, pressure treated lumber, refractory bricks, textile dyes and mordants, production of paints and pigments, and pulp and paper production (Butera et al., 2015; Chen et al., 2016; Kimbrough et al., 1999; Quantin et al., 2008; Sneddon, 2012). If waste from these industries (e.g. sludge, fly ash and slag) is disposed of on land and in water bodies, and without proper treatment, it becomes a major source of Cr(VI) in the environment. For example, soil and sediments from the former industrial complex of Porto-Romano, Albania contain Cr(total) and Cr(VI) concentrations up to 1130-24409 ppm and 12200 ppm, respectively (Shtiza et al., 2008), which are extraordinarily higher than the maximum allowable levels of total Cr (64-200 ppm) in agricultural soils (Ding et al., 2014) and Cr(VI) (50 ppb) in drinking water (Lilli et al., 2015).

2.2 Cycling of Cr in Soils

2.2.1 Interactions between Cr and soil components

2.2.1.1 Soil components

Inorganic components including primary and secondary minerals are an important component of soils with dominant proportions on a weight basis. Soil minerals generally include clay phases (kaolin, montmorillonite, illite and calcite), silicate minerals as well as Al, Fe and Mn (oxyhydr)oxides, which are involved in various soil functions (Sparks, 2003). Among various soil minerals, iron (oxyhydr)oxide has a relatively larger adsorption capacity and greater binding intensity to adsorb inorganic and organic species (Cornell and Schwertmann, 2003), often contributing a dominant role in controlling the cycling of trace elements nutrients or heavy metal contaminants.

The importance of organic components in soils also has attracted huge attention around the world. Organic components consist of organic residues, living soil biomass, humic substances (humin, humic acid and fulvic acid) and non-humic substances (e.g. amino acids, carbohydrates). Although soil organic matter (SOM) has usually lower than 5% of soil dry mass, it has extremely high reactivity and pronouncely influence on soil chemical reactions. For instance, SOM can improves soil structure, aeration, aggregation, water-holding capacity and adsorption capacity as well as influence the redox environment. Together with iron (oxyhydr)oxides, organic components act as crucial controllers of various nutrients and contaminants (Dai et al., 2004; Zeng et al., 2011; Zhou et al., 2018a).

2.2.1.2 Interactions between Cr and soil components

The two main forms of chromium (Cr(III) and Cr(VI)) can react with soil components via various processes like sorption/desorption, precipitation/dissolution behaviours and redox reactions (Ertani et al., 2017). (1) adsorption/desorption: both Cr(III) and Cr(VI) are strongly adsorbed by Al, Fe and Mn (oxyhydr)oxides and clay minerals in soils, decreasing the mobility of Cr(III/VI). Additionally, Cr(III) has high affinity for organic substances (Adriano, 1984) (Gustafsson et al., 2014; Xia et al., 2020), forming low-solubility stable complexation with macro-molecular structures (like humic acids and fulvic acids) or forming high-solubility complexation with dissolved organic ligands (such as citric acid). (2) oxidation/reduction: Cr(VI) species are strong oxidizing agents and can be easily reduced to Cr(III) in the presence of electron donors like S^{2-}, Fe^{2-} and organic matter, while Cr(III) species can also be oxidized to Cr(VI) in the presence of oxygen and manganese oxides. (3) precipitation/dissolution: Cr(III) has lower solubility and easily co-precipitates with Al(III), Mn(II) and Fe(III) hydroxide (Stumm and Morgan, 1996), while Cr(VI) species tends to have higher solubility (Adriano, 1986).

Table 2.1 Complexes of Cr(VI) and Cr(III) with iron (oxyhydr)oxide and carboxylic OC

	Structure	references
Cr(VI) adsorption onto iron (oxyhydr)oxide	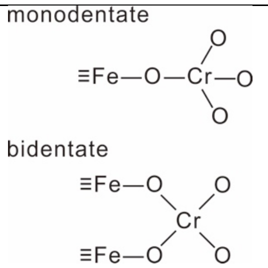	(Johnston and Chrysochoou, 2014)

Cr(VI) chelation with oxalate	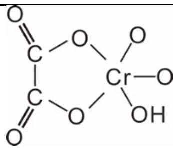	(Jiang et al., 2018)
Cr(III) adsorption onto iron (oxyhydr)oxide	edge sharing 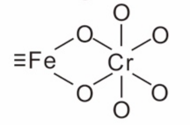 double corner sharing 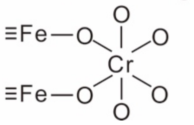	(Charlet and Manceau, 1992)
Cr(III) adsorption onto carboxylic OC	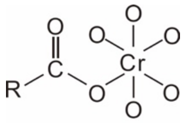 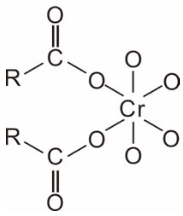	(Gustafsson et al., 2014; Yang et al., 2020)
Cr(III) precipitation	$Cr^{3+} + 3\ OH^- = Cr(OH)_{3(s)}$	

2.2.2 Cycling of Cr in the soil environment

The cycle of Cr(VI) in the soil environment is shown in Figure 2.2. The Cr(VI) released into the environment can be fixed through adsorption by minerals, humic substances, plants and bacteria. A part of the released Cr(VI) can also be converted to Cr(III) through redox reactions by plants, microorganisms in upper soils as well as humus, anaerobic bacteria, Fe(II) and S^{2-} in deeper soil, where Cr(III) that is reduced from Cr(VI) can easily form polymers or co-precipitates with organic/inorganic ligands to be fixed with solid phase. Whereas, some of the fixed Cr(III) can subsequently re-mobilize by chelating with dissolved organic matter like citrate, and subsequently can be oxidized into Cr(VI) spontaneously by reaction with manganese oxides ($MnO_{2(s)}$) in soils and sediments.

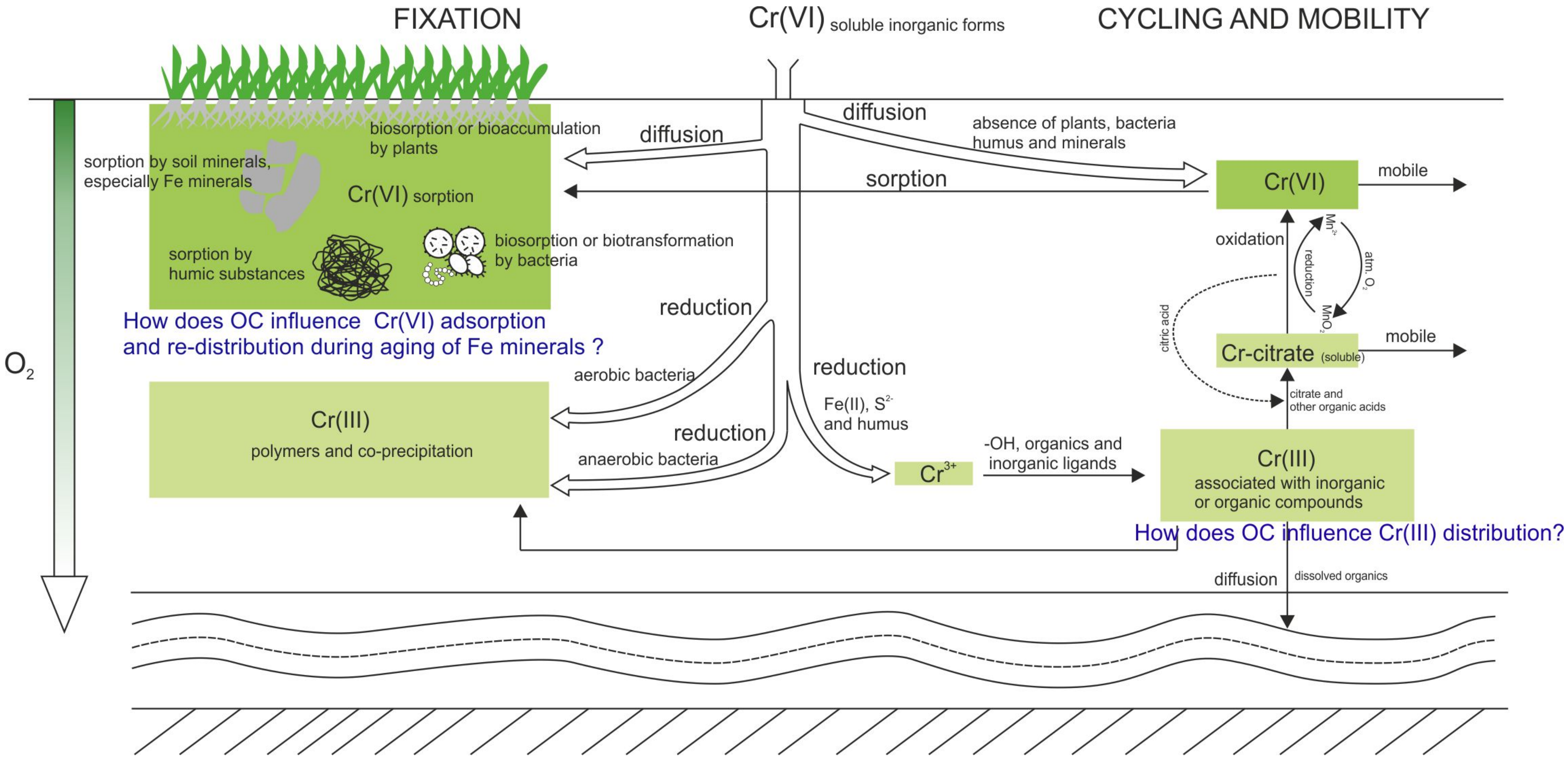

Figure 2.2. Chromium cycle in soil environment (modified from (Dhal et al., 2013b))

2.3 Sorption of Cr to Iron (oxyhydr)oxide

2.3.1 Ferrihydrite

2.3.1.1 Occurrence

As mentioned above, iron (hydr)oxides, especially ferrihydrite, are prevalent soil minerals (Cornell and Schwertmann, 2003). During iron cycling, mobile Fe(II) species are oxidized to Fe(III) species at redox interfaces, e.g. between oxic and anoxic zones. Subsequently, Fe(III) species undergo hydrolysis and even at low aqueous concentrations, under certain pH conditions ($pH > \sim 3$) readily form ferrihydrite minerals. Ferrihydrite is amorphous and metastable with respect to more thermodynamically stable minerals, and is the precursor of goethite, hematite and other crystalline iron oxide minerals (Cornell and Schwertmann, 2003).

2.3.1.2 Structure

Ferrihydrite has poor structural ordering and exhibits broad peaks characterized by XRD. Based on different XRD patterns, Fh forms are commonly designated as 2-line ferrihydrite (two broad peaks) and 6-line ferrihydrite (six broad peaks), which are derived from the different size of their coherent scattering domains (Kukkadapu et al., 2003). The sequence of transformation is that 2-line ferrihydrite may transform to 6-line ferrihydrite and then convert to more crystallize minerals like hematite (Cudennec and Lecerf, 2006).

The structure of the 6-line ferrihydrite has been determined and described as a superposition of a defect-free phase and defect phases (Jansen et al., 2002). The structure of 2-line ferrihydrite however, is still a intense debate (Whitaker et al., 2021). Two distinct structural models are used to describe the structure of 2-line Fh. The first

("Dritz model") is composed of 100% octahedral Fe(III) and contains three phases, a defective Fh phase, a defect free Fh phase, and small proportions of ultra-dispersed hematite phase (Drits et al., 1993). The second ("Michel model") is composed of one central tetrahedral Fe(III) unit and twelve peripheral octahedral Fe(III) units, and is a single phase model (Michel et al., 2010; Michel et al., 2007a). The "Michel model" is supported by the observation of tetrahedral Fe(III) in synthetic 2-line Fh through X-ray adsorption spectroscopy (Maillot et al., 2011; Mikutta, 2011; Peak and Regier, 2012; Whitaker et al., 2021) and scattering studies (Harrington et al., 2011).

2.3.1.3 Properties

The specific surface area (SSA, m^2/g) is an important mineral property, which determines the adsorption capacity (mole /gram) of minerals. As mentioned above, ferrihydrite is poorly crystalized with shorter physical scale of coherent scattering domains, which leads to greater specific surface area and higher density of adsorption sites for adsorbates. Generally, SSA of ferrihydrite ranges from 200-400 m^2/g, much higher than that for hematite (10-90 m^2/g), goethite (15-88 m^2/g) and lepidocrocite (15-260 m^2/g) (Cornell and Schwertmann, 2003).

2.3.2 Ferrihydrite Organo-minerals

2.3.2.1 Occurrence

Pure ferrihydrite is never found in natural soils, but is always associated with organic soil components, especially in the form of humic substances and/or microbial cells (Fortin and Langley, 2005). Because of its high SSA and abundant binding sites, ferrihydrite has the capacity to readily form complexes with organic matter in various environments (Chorover and Amistadi, 2001; Schwertmann and Cornell, 2008; Torn et al., 1997). The association of OC with minerals typically occurs through a variety of sequestration processes that remove OC from solution to the solid mineral particles

(Sposito, 2008). Sequestration processes can include the surface sorption, or adsorption, of OC to preformed mineral particles and also the coprecipitation of OC with neoformed mineral phases, where OC is removed from solution as a consequence of mineral precipitation (Eusterhues et al., 2011). About 21.5% of the organic carbon in sediments is bound to Fe via coprecipitation and direct chelation (Lalonde et al., 2012), whilst up to 40% of total SOM in various soils is reportedly bound with reactive iron minerals, most likely during coprecipitation (Wagai and Mayer, 2007; Zhao et al., 2016). Therefore, the Fh organominerals are prevalent in various environment and are crucial in controlling the mobility of various nutrients and pollutants that chemically bind with OC and Fh.

2.3.2.2 Structure

The presence of organic matter even in small amounts can significantly influence the growth of Fh. Ferrihydrite formed under the influence of OC tends to have smaller particle size and/or lower crystallinity, larger lattice spacings and more distorted $Fe(O,OH)_6$ octahedra (Cismasu et al., 2011; Eusterhues et al., 2008; Mikutta, 2011). Recent X-ray adsorption spectroscopy results document that synthetic 2-line Fh consists of minor amounts of tetrahedral Fe(III), while biogenic Fh is dominated by octahedral Fe(III) because of the small domain size and incorporation of OC (Whitaker et al., 2021).

The formation of ferrihydrite in the presence of organic matter involves processes such as adsorption, coprecipitation, flocculation/coagulation, and inhibition of crystal growth (Schwertmann, 1966). The presence of organic matter inhibits crystal growth of ferrihydrite, leading to smaller coprecipitated-ferrihydrite crystal size and greater structural disorder like increased lattice spacing and more distorted $Fe(O,OH)_6$ octahedra (Cismasu et al., 2011; Eusterhues et al., 2008; Mikutta, 2011). As small amounts of organic matter can significantly change particle size and the structural order of Fh, it will have different crystallinity and reactivity when formed in natural environments, in comparison with synthetic Fh formed in the absence of organic matter (Eusterhues et al., 2008).

2.3.2.3 Properties

Ferrihydrite formed in the presence of OC tends to have smaller particle size and more porous structure corresponding to larger surface specific area, whilst OC can block the surface sites and surface pores leading to lower specific surface area and total pore volume measured/estimated with the BET method (Mikutta et al., 2014). On the other hand, the OC end member that contributes to formation of Fh organominerals can provide additional adsorption sites for adsorbates like Cr(III) (Xia et al., 2020; Yang et al., 2020). The smaller size and poorer crystallinity of Fh organominerals also leads to higher reactivity as an adsorbent surface, compared to pure Fh (Eusterhues et al., 2014). Actually, OC can influence the aggregation and increase the colloidal stability of newly formed Fh polymeric flocs. Adsorption of negatively charged OC onto positively charged iron minerals creates negatively charged OC-coated particles that repel one another and hinder aggregation (Illés and Tombácz, 2006). Organic carbon, especially large molecular humic substances, can also bridge between different mineral particles to hinder aggregation and increase the colloidal stability of the aqueous suspension (Cornell and Schwertmann, 1979b). Meanwhile, OC can also increase the chemical stability of Fh against the transformation to other more crystalline iron minerals (Chen et al., 2015; Schwertmann, 1966). Therefore Fh organominerals are generally more environmentally stable than pure Fh (Whitaker et al., 2021).

2.3.3 Cr(VI) sorption by iron (oxyhydr)oxides

2.3.3.1 Cr(VI) adsorption onto pure Fh

Macroscopic Cr(VI) sorption behaviour to the iron (oxyhydr)oxides, ferrihydrite and goethite, has been well documented (Ding et al., 2018; Grossl et al., 1997; Hajji et al., 2019; Johnston and Chrysochoou, 2012, 2016; van Beinum et al., 2006; Villalobos et al., 2001; Weerasooriya and Tobschall, 2000; Xie et al., 2015; Zhao et al., 2011), with the adsorption exhibiting a typical anion adsorption edge. Namely the adsorption decreases with increasing pH because the mineral surface charge gets negative when more –FeOH groups are deprotonated with increasing pH (Grossl et al., 1997; Veselská et al., 2016; Weerasooriya and Tobschall, 2000; Xie et al., 2015). In particular, Cr(VI) adsorption edges onto ferrihydrite show no significant difference with changes in Cr(VI) concentration and sorbate/sorbent ration (Cr(VI) concentions of 10^{-6}, 10^{-5}, 10^{-4} M) or ionic strength (0.001, 0.01, 0.1 M KNO_3) (Veselská et al., 2016).

At the microscopic leve, Cr(VI) tends to form inner-sphere bidentate complexes at high surface coverages and monodentate complexes at lower coverages on both goethite and ferrihydrite, confirmed by spectroscopic information (Fendorf et al., 1997; Johnston and Chrysochoou, 2012, 2014) and surface complexation modeling (Veselská et al., 2016; Xie et al., 2015). Futhermore, Grossl et al. (1997) proposed a two-step mechanism to explain how chromate is adsorbed on geothite and forms an inner-sphere bidentate surface complex. In the first step, an inner-sphere monodentate surface complex is formed, and the subsequent step involves a second ligand exchange reaction, resulting in the formation of a bidentate surface complex (Grossl et al., 1997). With respect to formation of the bidentate Cr(VI) complex, formation of the pre-cursor monodentate Cr(VI) complex is particularly susceptible to ionic strength (Johnston and Chrysochoou, 2012, 2014; Xie et al., 2015).

2.3.3.2 Competitive adsorption between Cr(VI) species and other ions

Cr(VI) adsorption onto iron (oxyhydr)oxide is slightly influenced by cations like Ca^{2+} and Mg^{2+} but can be influenced by anions like sulphate and phosphate (Richard et al., 1991). The competing adsorption between anions and Cr(VI) depends on their concentrations, relative affinities to mineral surface and surface site concentration (Rai, 1986). Because of the different relative affinities to a mineral surface, different concentrations of different anions are required to suppress Cr(VI) adsorption on iron (oxyhydr)oxide. For example, higher concentrations of sulphate with lower affinity are required to inhibit Cr(VI) adsorption, compared to phosphate with higher affinity that can significantly repress the adsorption of Cr(VI) (Xie et al., 2015). Generally, the higher-affinity competitive anions can easily influence the sorption of Cr(VI) on iron (oxyhydr)oxide.

However, few studies have been done to study competitive adsorption between organic matter and Cr(VI). The adsorption of OC to iron (hydr)oxide can be influenced by many factors like the number and type of OC functional groups, structures and molar weight, which add the complexity of studying the Cr(VI) sorption onto Fh organominerals. Early work reveals competitive adsorption between oxalate and Cr(VI), and emphasises the importance of the relative adsorption affinity of Cr(VI) and OC to iron (oxyhydr)oxides (Measuere and Fish, 1992). Therefore, the relative affinity to iron (oxyhydr)oxide between Cr(VI) and OC is also an important factor influencing Cr(VI) adsorption.

2.3.3.3 Cr(VI) sorption by Fh organominerals

The concepts of additive adsorption and non-additive adsorption are both reported to describe the binding of metal species to organominerals. For additive adsorption, the sum of the metal species adsorption on the end-member mineral and on the OC fractions equals that of the organomineral composites (Zachara et al., 1994); for non-additive adsorption the sum of the metals species adsorption on the end-member mineral and OC fractions does not equal that of organomineral (Vermeer et al., 1999). The additive adsorption capacity can be derived from the additional binding sites associated with OC and/or new high-affinity sites formed during OC reacting with minerals (Alcacio et al., 2001; Ali and Dzombak, 1996). The additive adsorption of trace metals onto Fh organominerals has been reported in previous studies, like Cu adsorption onto Fh-bacteria composites with Fh dominating (Moon and Peacock, 2013), Cu adsorption onto Fh-HA composites (Fariña et al., 2018) and Cd adsorption onto Fh-HA composites (Du et al., 2018).

Non-additive adsorption behaviour is attributed to a surface charge effect, where the negative charge of OC is influenced by the positive charge of the mineral surface and then net influences the metal species adsorption. Non-additive adsorption is observed in studies like Cu adsorption onto Fh-bacteria composites with OC dominating (Moon and Peacock, 2013), Cu adsorption onto Gt-HA composites (Fariña et al., 2018), Cd adsorption onto Fh-bacteria composites (Song et al., 2009) and Pb adsorption onto Fh-bacteria composites (Kulczycki et al., 2005). Therefore, the complexity of physiochemical interactions between Fh and organic matter, and lack of conditional parameter values for reactions between naturally-occurring Fh and OC, make it difficult to predict metal species sorption onto Fh-OC composites in natural and contaminated environments (Moon and Peacock, 2013).

The interactions between Cr(VI) and Fh organominerals are more complex as both adsorption and reduction are involved (Chen et al., 2019). Aqueous Cr(VI) species can be reduced by various functional groups in OC like phenol, quinone-hydroquinone pairs and α-hydroxy carboxylic acids (Brose and James, 2013; Scott et al., 1998). Actually, Cr(VI) species can also chelate with OC to form a 5-membered chelate ring, which involves specific functional groups and structure. Organic matter with two carboxyl groups (oxalic), with one carboxyl and one α-hydroxy group (such as tartaric, citric and malic acids), with a carboxyl and an amino group on the same carbon atom (such as 2-picolinic, EDTA and nitrilotriacetic acids), can form stable 5-membered chelate rings with Cr(VI) (Jiang et al., 2019). This coordination between OC and Cr(VI) is often coupled with redox reactions. The complexation makes the structure of Cr(VI) more distorted and improves the reactivity of Cr(VI) toward the reduction reaction (Jiang et al., 2019).

For these Fh organominerals made with OC without reducibility, OC can significantly affect the properties of Fh to influence Cr(VI) sorption. For example, the formation with OC can decrease Fh particle size, increase SSA and TPV (total volume of pores) and block surface binding sites and surface pores. Organic carbon can also compete for the adsorption sites with Cr(VI), possibly suppressing Cr(VI) adsorption. Mikutta et al. (2014) report As(V) adsorption onto Fh organominerals, where adsorption of As(V) was facilitated by desorption of weakly bonded organic matter and disaggregation that resulted in greater surface binding capacity for As(V) species. Furthermore, small mesopores (2-10 nm) promoted the fast As uptake particularly to Fh-OC coprecipitates and could also impair As desorption because As easier accesses the intraparticle sorption sites via diffusion in mesopores (Mikutta et al., 2014). This indicates the OC in Fh organominerals may also have similar influences on Cr(VI) adsorption via the same mechanisms, but no study focuses on this question.

2.3.3.4 Adsorption models of Cr(VI) by iron (oxyhydr)oxides

Surface complexation models (SCMs) are regarded as valuable tools that include important thermodynamic reaction details compared with traditional distribution factors (Kd) to describe adsorption processes and estimate the partitioning of ions at the solid-solution interface (Goldberg et al., 2007). Many models have been successfully utilized to simulate Cr(VI) adsorption onto single soil components. These models include those such as the diffuse layer model (DLM) and the triple layer model (TLM) utilized in the competitive adsorption experiments of oxalate and Cr(VI) on goethite (Mesuere and Fish, 1992b), the DLM and TLM utilized in Cr(VI) adsorption onto various soil mineral components (like illite, kaolinite, birnessite and ferrihydrite) (Veselská et al., 2016), and the charge distribution multisite surface complexation model (CD-MUSIC) utilized in the competitive adsorption experiment of phosphate and Cr(VI) (Xie et al., 2015).

Their development and application to describe adsorption reactions in soils is still challenging due to the heterogeneity of composition and complexity of interactions in soil systems. Few studies have been done in more complex systems like iron oxides (ferrihydrite and goethite) (Bompoti et al., 2019), soil component mixtures (Veselská et al., 2019) or even natural soils (Gu et al., 2017; Pérez et al., 2014; Veselská et al., 2019). All of these studies highlight iron (oxyhydr)oxides as contributing the most important reactive surfaces for Cr(VI) retention in soils (Gu et al., 2017; Pérez et al., 2014; Veselská et al., 2019).

For Cr(VI) adsorption onto Fh organominerals, OC can be adsorbed onto end-member Fh by ligand exchange to form inner-sphere complex. In this case, OC can be a competitor for adsorption of Cr(VI) species. How to simulate OC and Cr(VI) sorption onto iron (oxyhydr)oxide at the same time is key to describing Cr(VI) sorption. Previous researchers reported several successful applications of the DLM and TLM to simulate the adsorption of simple organic acids on Fh or Gt (Evanko and Dzombak, 1999; Mesuere and Fish, 1992a, b), which means DLM and TLM can offer practical ways to estimate Cr(VI) adsorption onto Fh organominerals formed with simple organic acids.

2.3.4 Cr(III) sorption onto iron (oxyhydr)oxides

2.3.4.1 Solubility and precipitation of Cr(III)

Cr(III) usually forms sparingly soluble oxides and (oxy)hydroxides (Tang et al., 2010), and Cr(III) hydroxide has a minimum solubility between pH 7 and 10 (Rai et al., 1987). Based on different solubility of $Cr(OH)_3(s)$ as a function of pH, different aqueous species, namely $Cr(OH)^{2+}$, $Cr(OH)_3^0$ and $Cr(OH)_4^-$ dominated over < pH 7, pH 7~10 and > pH 10, respectively. The freshly precipitated $Cr(OH)_{3(am)}$ was amorphous as observed by XRD. Pure $Cr(OH)_{3(am)}$ exhibits a higher stability to remain non-crystalline with respect to pure $Fe(OH)_{3(am)}$ (Amonette and Rai, 1990). It also shows a strong affinity for carbonate ions (Amonette and Rai, 1990), indicating that $Cr(OH)_{3(am)}$ may be a strong adsorbent for other ligands with similar binding mechanisms, including those of low molecular weight organic carbon compounds.

2.3.4.2 Cr(III) sorption by iron (oxyhydr)oxides

Cr(III) species can be retained by iron (oxyhydr)oxides by adsorption and co-precipitation (Charlet and Manceau, 1992). The adsorption of Cr(III) species onto iron (oxyhydr)oxide occurs via inner-sphere surface complexation. The mineral surface can catalyze the hydrolysis and polymerization of Cr(III) ions and facilitate the precipitation of a surface hydrous Cr(III) (hydr)oxide even under undersaturated conditions with respect to the bulk solution composition. The surface precipitate and the pure $Cr(OH)_{3(am)}$ are observed to have the same local structure (γ-CrOOH) (Charlet and Manceau, 1992).

Cr(III) can also co-precipitate with Fe(III) in any ratio, behaving thermodynamically as a “solid solution” (Sass and Rai, 1987), because they have very similar ionic radii and comparable hydrolysis properties (Manceau et al., 2000). The Cr(III) and Fe(III) coprecipitates show a different characters with respect to physical mixtures of $Fe(OH)_{3(a)}$ and $Cr(OH)_{3(a)}$, observed by infrared spectroscopy (Amonette and Rai, 1990). For co-precipitates of Cr(III) and Fe(III) with various Cr/Fe ratios, the structure changes progressively from that of γ- CrOOH in pure $Cr(OH)_{3(s)}$ (single corner bridging with metal shells ~4.0 Å) to α- MeOOH in pure $Fe(OH)_{3(s)}$ (with metal shells at ~3.0 and 3.4 Å), based on X-ray absorption fine-structure (EXAFS) and X-ray absorption near-edge structure (XANES) spectroscopic data (Charlet and Manceau, 1992; Tang et al., 2010). A recent study shows that the Cr(III) sorption mechanism progressively changes from structural substitution to a surface enrichment by adsorption or surface precipitation with molecular ratio of Cr/Fe increasing during precipitation of $(Fe, Cr)(OH)_{3(am)}$ (Dai et al., 2016). For high Cr/Fe ratios at 2.5, a "core-shell" structure of $(Fe, Cr)(OH)_{3(am)}$ particles is hypothesized, where $(Fe, Cr)(OH)_3$ in shells are more rich in Cr than that in cores (Dai et al., 2016).

The Cr(III) can be substituted in various iron minerals like ferrihydrite, goethite, hematite and magnetite, but Cr(III) is not found in lepidocrocite (Cornell and Schwertmann, 2003). The chemical selective dissolution results show that Cr as a substitute for Fe in goethite, hematite and magnetite has the same proportions (Trolard et al., 1995). Therefore, most iron (oxyhydr)oxides except lepidocrocite can be a good host for Cr(III) and play an important role in immobilization of Cr(III) in soils.

2.3.4.3 Cr(III) sorption by Fh organominerals

The latest studies show that the sorption of Cr(III) species by Fh organominerals via adsorption and co-precipitation is significantly reduced at high C loadings in the system (Yang et al., 2020). The presence of OC can inhibit the precipitation of both Cr(III) and Fe(III) (Wang et al., 2018; Yang et al., 2020), and simultaneously, OC can block the binding sites for Cr(III) adsorption (Xia et al., 2020), which inhibits the immobilization of Cr(III), e.g. on soil particles. Besides, Cr(III) prefers to form inner-sphere complexes with end-member Fh in organominerals, whilst Cr(III) can also form complexes with carboxyl groups in OC at higher C loading (Xia et al., 2020).

2.4 Mineralogical transformation of Fh

2.4.1 Mineralogical transformation of Fh in oxic environment

2.4.1.1 Mechanisms for mineralogical transformation during aging

The first phase to precipitate in Fe(III) hydrolysis is ferrihydrite, which is metastable and can transform to other iron minerals with higher stability and crystallinity: goethite α-FeO(OH) or hematite $\alpha\text{-}Fe_2O_3$. The solubility product of ferrihydrite ($Fe(OH)_{3(s)} \leftrightharpoons Fe^{3+} + 3OH^-$, $K_s=10^{-39}$) is higher than those of goethite ($FeOOH_{(s)} + H_2O \leftrightharpoons Fe^{3+} + 3OH^-$, $K_s=10^{-41}$) and hematite ($0.5Fe_2O_{3(s)} + 1.5H_2O \leftrightharpoons Fe^{3+} + 3OH^-$, $K_s=10^{-43}$) at circumneutral pH (Hansel et al., 2004), which favours the dissolution and recrystallization of iron oxyhydroxide. What's more, hematite can be the final product of the mineralogy transformation of 2-line ferrihydrite, with goethite as an intermediary phase (Das et al., 2011b). Additionally, the transformation of Fh can also occur through the internal atomic arrangement / oriented aggregation process of the solid ferrihydrite (solid-state topotactic transformation) to form hematite at neutral environment because of the extreme low solubility (Cudennec and Lecerf, 2006).

2.4.1.2 Influences on transformation of Fh

The pH condition is a determinant factor influencing transformation products as well as the transformation mechanism (Cudennec and Lecerf, 2006). Ferrihydrite has different solubility as a function of pH conditions. Due to aqueous speciation of hydrolysis reaction products, low or high pH conditions (pH 2-5 and pH 10-14) can increase the thermodynamic solubility of ferrihydrite, which facilitates the dissolution and re-crystallization processes and favours the formation of goethite. In neutral environment however, ferrihydrite has low solubility and it is transformed via the internal atomic arrangement to form hematite.

The temperature is another factor with paramount importance for the transformation of ferrihydrite (Schwertmann et al., 1999). Higher temperature can not only favour the formation of hematite, but also increase the reaction rate of transformation of 2-line ferrihydrite at all pH conditions (Cornell and Schwertmann, 2003; Das et al., 2011b). For example, at pH 10 and temperature 1-2 ℃, 100% conversion of 2-line ferrihydrite to hematite was estimated to take 90 years, while this process is completed in 3 hours at 100 ℃ (Das et al., 2011b).

The presence of organic matter and other anions (like Cl^-, SO_4^{2-}, SiO_4^{2-} and PO_4^{3-}) can also influence the rates, pathways and mineralogy of the transformation of ferrihydrite (Cornell and Schwertmann, 1979a; Jones et al., 2009; Liu et al., 2018; Liu et al., 2008; Schwertmann, 1966; Taylor et al., 1987). The presence of OC can influence the factors that control dissolution-recrystallisation and/or solid-state transformation and thus can effect transformation rate. For example, OC can block surface sites and subsequently prevent the dissolution of iron (oxyhydr)oxide to form goethite or the nucleation of hematite (Kaiser and Guggenberger, 2003); OC can complex with aqueous Fe(III) species to inhibit nucleation (Cornell and Schwertmann, 1979b); and OC can influence Fh aggregation and associate with the surface of neoformed mineral nuclei and crystals to inhibit crystal growth (Amstaetter et al., 2012; Eusterhues et al., 2008). Other anions also have an inhibition effect on transformation of ferrihydrite, and they can also influence the product of the transformation. For example, an Cl^- aqueous medium leads to predominantly lepidocrocite and a few star-like goethite precipitates, while an SO_4^{2-} medium leads to rod-like goethite product (Liu et al., 2008).

2.4.2 Fe(II)-induced transformation of Fh

2.4.2.1 Mineralogical transformation of Fh in anoxic environments

The transformation of Fh occurs via a dissolution and re-precipitation process and an oriented aggregation process, both of which are also important in anoxic environments. The presence of Fe(II) facilitates reductive dissolution of iron (oxyhydr)oxide, which catalyzes the mineralogical transformation of iron (oxyhydr)oxide. There are two mechanisms of reductive dissolution. 1) Reducing ligands like those of metal-reducing bacteria, reduced humic substances and sulfide can act as electron donors to reduce surface Fe(III) to Fe(II), which is has more labile bonds to lattice oxyanion and is therefore more rapidly released into solution. 2) Aqueous Fe(II) species are attached to the mineral surface and electrons are transferred to structural Fe(III), where the attached Fe(II) is oxidized to Fe(III) and precipitated as neoformed Fe (oxyhydr)oxide while structural Fe(III) is reduced to Fe(II) and released into solution (Boland et al., 2014; Han et al., 2020b; Handler et al., 2009; Mikutta et al., 2009; Suter et al., 1991). Therefore, the presence of aqueous Fe(II) species can induce mineralogical transformation of iron (oxyhydr)oxide via increasing rates of dissolution and re-crystallization processes. Additionally, oriented aggregation is reported to be an important transformation pathway from ferrihydrite to magnetite (Bazylinski et al., 2007) and from lepidocrocite to goethite (Yan et al., 2015a), where the internal atomic arrangement in the solid phase occurs to form other more crystalline iron minerals.

2.4.2.2 Influences on transformation of Fh

Different pH conditions can influence the transformation rates of Fh by controlling the adsorption of aqueous Fe(II). The Fe^{2+}, as typical cation, has a sigmoid adsorption edge increasing with pH (Boland et al., 2014). In acidic environments, the amount of Fe(II) adsorbed is lower than that at neutral environment, resulting in the lower atom exchange between structure Fe(III) and aqueous Fe(II) (ThomasArrigo et al., 2017). This is why transformation of Fh induced by Fe(II) species is slower in acidic environments than in neutral or alkaline environments.

The presence of OC can also influence the Fe(II)-induced mineralogical transformation of Fh through various mechanisms. OC can block mineral surface sites or micropore entrances that prevents access to interior surfaces or complex with aqueous Fe(II) to hinder Fe(II) adsorption and then inhibit the reductive transformation of Fh (Chen et al., 2014; ThomasArrigo et al., 2017). Some OC can also act as an electron shuttle to facilitate electron transfer between reductants and structural Fe(III), which can trigger the transformation of Fh (Roden et al., 2010; Shimizu et al., 2013). OC can also hinder the mineralogical transformation from lepidocrocite (Lp) to goethite (Gt) by influencing oriented aggregation in the solid phase (ThomasArrigo et al., 2018; Yan et al., 2015a). OC associated with crystals or nuclei can also poison crystal growth by influencing the cross-linking of Fe (O, OH)$_6$ octahedrons and thus inhibit the transformation (Eusterhues et al., 2008). Additionally, OC coated with mineral particles can also sterically hinder the alignment or aggregation of nano-crystals to form larger crystals through bridging different particles or electrostatic repulsion (Amstaetter et al., 2012; Eusterhues et al., 2008; Shimizu et al., 2013). In these processes, many factors are involved like adsorbed/coprecipitated OC with iron (oxyhydr)oxide, types of OC and iron (oxyhydr)oxide, C:Fe molar ratios and electron shuttle properties of OC (Cismasu et al., 2016; Eusterhues et al., 2014; Jones et al., 2009; Mejia et al., 2018; Poggenburg et al., 2018; Wordofa et al., 2019; Zhou et al., 2018b).

2.5 Redistribution of OC during mineralogical transformation of Fh organominerals

The stabilization of OC can be influenced during the mineralogical transformation of iron (oxyhydr)oxide because of different properties of secondary iron minerals (Cornell and Schwertmann, 2003). Generally, the amount of OC associated with solid minerals decreased with aging time (Hu et al., 2020; Jelavić et al., 2020) because the specific surface area and adsorption site density decrease. In this process, OC can influence properties of secondary iron minerals and reversely influence their stabilization, either by increasing or decreasing the stability. For instance, OC is assumed to inhibit the transformation rates of Fh to decrease the release of OC from minerals. OC can also influence the transformation products, for example favouring more lepidocrocite to be formed in the presence of OC, which has more structure defects to host more OC within solid minerals (Hu et al., 2020). The additives in systems, such as other metal ions, can also influence the stabilization of OC during the aging process. It is reported that the presence of Pb(II) species can significantly decrease the release of OC from solid minerals (Lu et al., 2019b). The influence of Cr(VI / III) on OC stabilization has not been reported to date.

2.6 Mobility and fate of Cr(VI) during mineralogical transformation of iron (oxyhydr)oxide under oxic and anoxic conditions

2.6.1 Redistribution of Cr(VI) during aging process under oxic conditions

Cr(VI) is also re-distributed during the mineralogical transformation of iron (oxyhydr)oxide. Cr(VI) exists as aqueous species, adsorbed species on mineral surfaces and incorporated species inside minerals. These forms are operationally defined as aqueous Cr(VI), desorbable Cr(VI) and non-desorbable Cr(VI), respectively. Generally, for the Cr(VI)-pure Fh system, aqueous Cr(VI) concentrations increase with aging time because of the decreasing SSA of secondary iron minerals, whilst the non-desorbable Cr(VI) increases at the expense of desorbable Cr(VI) (Zhu et al., 2019). Additives in systems also influence the distribution of Cr(VI) between non-desorbable and desorbable pools. The presence of silicate in Fh-Si-Cr coprecipitates significantly decreases non-desorbable Cr(VI) during aging at pH 5.0 (Zhu et al., 2019) while the addition of citrate and an anionic surfactant (sodium dodecylbenzene sulfonate) also decreases non-desorable Cr(VI) during aging but increases aqueous Cr(VI) during aging at pH 7.0 (Sun et al., 2021; Yu et al., 2021). The influence of OC on distribution of Cr during the mineralogical transformation of iron (oxyhydr)oxide organominerals has rarely been studied. There are almost no studies that reveal the microsopic mechanistic interactions between iron (oxyhydr)oxide organominerals and Cr(VI), in which the focus is not on the redox reduction of Cr(VI). The influence of OC on Cr(VI) adsorption behaviour to iron (oxyhydr)oxide organominerals, and the mobility and fate of Cr(VI) during the transformation of these organominerals however, remains largely unknown.

2.6.2 Fate of Cr(VI) during mineralogical transformation of iron (oxyhydr)oxide under anoxic condition

Under anoxic conditions, mobile Cr(VI) is readily reduced to less-mobile Cr(III), but the distribution of Cr(III) associated with iron (oxyhydr)oxide organominerals is still unknown during the mineralogical transformation. To the authors' knowledge however, only one study investigates the influence of OC on the distribution of Cr(VI/III) during the transformation under anoxic condition, where it is observed that the transformation of Fh-humic acid composites increases non-desorbable Cr after aging, probably via a redox reaction which reduces more soluble Cr(VI) to less soluble Cr(III) (Yu et al., 2020). Despite this, the influence of OC on re-distribution of desorbable and non-desorbable Cr pools during the mineralogical transformation of iron (oxyhydr)oxide organominerals is significantly unclear.

Chapter 3 Methods

In the following chapter the experimental and analytical methods used throughout this project are described. All measurement are conducted in duplicated at least, where quality control is conducted by analysing standards and blanks every ten samples. For analysing data, the average values with standard deviation are used. To keep individual chapters self-explanatory, the methods described in chapters 4, 5 and 6 may overlap with methods presented here. The methods described in this chapter are as follows:

3.1 Laboratory based methods 30
  3.1.1 Synthesis of pure Fh and Fh organominerals 30
  3.1.2 OC adsorption onto pure Fh 32
  3.1.3 Cr(VI) adsorption onto pure Fh and Fh organominerals 32
  3.1.4 Mineralogical transformation of pure Fh and Fh organominerals 33
  3.1.5 Fe(II)-induced mineralogical transformation of pure Fh and Fh organominerals 34
  3.1.6 Synthesis reference goethite, lepidocrocite and magnetite 35
3.2 Analytical and spectroscopic tools 36
  3.2.1 Inductively Coupled Plasma-Mass Spectrometry (ICP-MS) 36
  3.2.2 Atomoc Absorption Spectrophotometer (AAS) 36
  3.2.3 LECO SC-144DR Dual Range Sulphur and Carbon Analyzer 36
  3.2.4 Attenuated Total Reflectance Fourier transform infra-red spectroscopy (FTIR) 37
  3.2.5 Brunauer-Emmett-Teller surface area analysis (BET) 38
  3.2.6 Ultraviolet–visible (UV–Vis) spectroscopy 38
  3.2.7 X-ray diffraction 39
  3.2.8 Scanning transmission X-ray microscopy near-edge X-ray absorption fine structure spectroscopy (STXM NEXAFS) 40
3.3 OC and Cr(VI) surface complexation modelling 40

3.1 Laboratory based methods

3.1.1 Synthesis of pure Fh and Fh organominerals

Pure ferrihydrite (Fh) was prepared following the method of Schwertmann and Cornell (2000) for the precipitation of 2-line ferrihydrite via hydrolysis of Fe(III) salt solution. Briefly, Fh was prepared by rapid hydrolysis of 0.1 M $Fe(NO_3)_3{\cdot}9H_2O$ (aq) with 1 M KOH to maintain a final pH of 7. Fh was washed several times over a week with 18.2 MΩ·cm MilliQ water until the conductivity of supernatant is same with DI water, after which Fh was stored as a slurry at 4 ^{o}C, following standard protocols to maintain mineralogical integrity (Schwertmann and Cornell, 2000). Plastic labware and AR grade reagents were used throughout the preparations.

Seventeen Fh-OC organomineral coprecipitates with different wt% C were prepared with three simple carboxylic acids, denoted as acid*n/m*, where acid refers to the first three letters of the acid IUPAC name and *n/m* denotes the number of carboxyl groups (*n*) and the number of total carbon atoms (*m*). The acids used were pentanoic acid (Pen1/5), hexanedioic acid (Hex2/6) and butane 1, 2, 4 tricarboxylic acid (But3/7), which have one, two and three carboxyl functional groups, respectively. Briefly, 0.1 M $Fe(NO_3)_3{\cdot}9H_2O$ (aq) solutions were mixed with different amounts of dissolved organic acids and then the pH values of the solutions were adjusted to ~7 with 1 M KOH, whereupon the acids coprecipitated with the Fh, forming Fh organomineral coprecipitates with different wt% C. Fh organomineral coprecipitates were washed several times over a week in equivalent volumes of 18.2 MΩ·cm MilliQ water, after which coprecipitates were stored as a slurry at 4 ^{o}C, and part of the coprecipitates were freeze-dried for further analysis. The C contents of the solids were determined on solid freeze-dried subsamples using a LECO SC-144DR Dual Range Sulphur and Carbon Analyzer. Seventeen coprecipitates were obtained: Fh-pentanoic acid with 1.2wt%C and C:Fe molar ratio 0.098, 1.9wt%C and C:Fe molar ratio 0.157, and 8.7wt%C and

C:Fe molar ratio 0.816 (Fh_Pen1/5_1.2/1.9/8.7wt%C); Fh-hexanedioic acid with 2.9wt%C and C:Fe molar ratio 0.246, 3.3wt%C and C:Fe molar ratio 0.283, 4.1wt%C and C:Fe molar ratio 0.358, 4.5wt%C and C:Fe molar ratio 0.396, 6.4 wt%C and C:Fe molar ratio 0.588, 7.0wt%C and C:Fe molar ratio 0.652, 8.4wt%C and C:Fe molar ratio 0.810 (Fh_Hex2/6_2.9/3.3/4.1/4.5/6.4/7.0/8.4wt%C); and Fh- butane 1, 2, 4 tricarboxylic acid with 5.1 wt%C and C:Fe molar ratio 0.461, 6.0 wt%C and C:Fe molar ratio 0.555, 6.6 wt%C and C:Fe molar ratio 0.620, 7.3wt%C and C:Fe molar ratio 0.699, 7.8 wt%C and C:Fe molar ratio 0.757, 10.1wt%C and C:Fe molar ratio 1.047, and 10.2 wt%C and C:Fe molar ratio 1.060 (Fh_But3/7_5.1/6.0/6.6/7.3/7.8/10.2wt%C). Plastic labware and AR grade reagents were used throughout all the preparations.

Table 3.1 Information of Fh organominerals synthesized

Name	Number of carboxyl groups in organic acids	C:Fe molar ratio	Wt%C
Fh_Pen1/5_1.2wt%C	1	0.098	1.2
Fh_Pen1/5_1.9wt%C	1	0.157	1.9
Fh_Pen1/5_8.7wt%C	1	0.816	8.7
Fh_Hex2/6_2.9wt%C	2	0.246	2.9
Fh_Hex2/6_3.3wt%C	2	0.283	3.3
Fh_Hex2/6_4.1wt%C	2	0.358	4.1
Fh_Hex2/6_4.5wt%C	2	0.396	4.5
Fh_Hex2/6_6.4wt%C	2	0.588	6.4
Fh_Hex2/6_7.0wt%C	2	0.652	7.0
Fh_Hex2/6_8.4wt%C	2	0.810	8.4
Fh_But3/7_5.1wt%C	3	0.461	5.1
Fh_But3/7_6.0wt%C	3	0.555	6.0
Fh_But3/7_6.6wt%C	3	0.620	6.6
Fh_But3/7_7.3wt%C	3	0.699	7.3
Fh_But3/7_7.8wt%C	3	0.757	7.8
Fh_But3/7_10.1wt%C	3	1.047	10.1
Fh_But3/7_10.2wt%C	3	1.060	10.2

3.1.2 OC adsorption onto pure Fh

The OC adsorption experiment onto pure Fh were conducted under oxic condition. The adsorption experiments involved three simple carboxylic acids, namely pentanoic acid (Pen1/5), hexanedioic acid (Hex2/6) and butane 1, 2, 4 tricarboxylic acid (But3/7), which have one, two and three carboxyl functional groups, respectively. Adsorption pH edges of the acids on pure Fh were prepared from pH 3.5 to 10.0. Pure Fh mineral slurry was added into MilliQ water and either Pen1/5, Hex2/6 and But3/7 stock solutions were added to give a total volume of 45 mL, a solid solution ration of 2 g dry sorbent L^{-1} and OC concentrations of 0.4 mM in 0.01 $NaNO_3$ background electrolyte. After addition of stock solution, pH of the resulting suspensions was adjusted by dropwise addition of either dilute HNO_3 or NaOH. After shaking continuously for 48h, the suspensions were filtered with 0.22 μm cellulose nitrate filters using a vacuum filtration apparatus and the solids were collected and rinsed with 5 mL DI water to remove aqueous OC. The solids were then freeze-dried. The total C contents of the solids were determined using a LECO SC-144DR Dual Range Sulphur and Carbon Analyzer. The amount of OC sorbed was calculated by subtracting the amount of C for pure Fh (the control). The C present in pure Fh was derived from some aqueous CO_3^{2-} / HCO_3^- adsorbed onto or coprecipitated with Fh during synthesis process. The calculated OC sorbed (wt%C) and the dry sorbent concentration (2g/L) were then used to calculate the molar concentration of OC adsorbed. All adsorption experiments were conducted in duplicate.

3.1.3 Cr(VI) adsorption onto pure Fh and Fh organominerals

The Cr adsorption experiments onto Fh and Fh organomineral coprecipitates were conducted under oxic condition following the method of Moon and Peacock (2012, 2013). Adsorption pH edges of Cr on Fh or Fh organomineral coprecipitates were prepared from pH 3.5 to pH 10.0. A Cr(VI) stock solution of 100 ppm Cr was prepared with K_2CrO_4. Fh or Fh organomineral slurry was added into MilliQ water and Cr(VI) stock solution was added to give a total volume of 30 mL, a solid solution ratio of 1 g dry sorbent L^{-1} and total Cr(VI) concentrations of 1.92×10^{-6}, 1.92×10^{-5}, 1.92×10^{-4} M (0.01 wt%, 0.1 wt% and 1.0 wt% Cr at 100% adsorption, respectively) for Fh and 1.92×10^{-5} M (0.1wt% Cr at 100% adsorption) for Fh organomineral coprecipitates, in 0.1M $NaNO_3$ background electrolyte. After addition of stock solution, the pH of the resulting suspensions was adjusted by dropwise addition of either dilute HNO_3 or NaOH to give a known final solution volume. After shaking continuously for 48 h to ensure adsorption equilibrium (Saito et al., 2005; Zhu et al., 2010), the suspensions were centrifuged at 2750 rpm for 15 min to obtain a clear supernatant for determination of Cr concentration. Supernatants were filtered using 0.02 μm polycarbonate membrane filters and acidified with 2% HNO_3 for aqueous Cr analysis by inductively coupled plasma mass spectrometry (ICP-MS). All the adsorption experiments were performed in duplicate. Experimental solution speciation of Cr(VI) was calculated as a function of pH using PHREEQC (Parkhurst and Appelo, 1999) and the MINTEQ.V4 database (Charlton and Parkhurst, 2002).

3.1.4 Mineralogical transformation of pure Fh and Fh organominerals

Pure Fh and Fh coprecipitate slurries were added into 0.01 M $NaNO_3$ background electrolyte to produce 2g/L suspensions, and then adjusted to target pH values with dilute HNO_3 or NaOH. The pH values were buffered at 5 and 6.5 by adding 30 mmol L^{-1} organic buffer 2-(N-Morpholino)ethane-sulphonic acid (MES) and 3-(N-Morpholino)propanesulphonic acid (MOPS), respectively. These buffer solutions have been shown to have negligible impact on the transformation of Fh (Bradbury and Baeyens, 1999; Ford et al., 1999). The resultant solutions were then transferred to an electric oven kept at a temperature of 75℃ for 19 days to promote transformation to stable phases. A 19-days reaction time was used after test experiments to determine the time necessary to achieve complete mineralogical transformation in most of reaction systems. During the reactions, the vessels were gently shaken to keep the suspensions homogenized. In order to allow a time-resolved investigation of Fh recrystallisation rate and OC redistribution, aliquots of the solid precipitates and solutions were collected and analyzed at pre-designed time intervals during the transformation process. At each sampling period, the suspensions were cooled to room temperature to stop the transformation and the pH was measured.

3.1.5 Fe(II)-induced mineralogical transformation of pure Fh and Fh organominerals

An aliquot of the non-freeze-dried pure Fh and Fh-organomineral slurries were added to 0.01 M $NaNO_3$ background electrolyte to give a total volume of 50 mL with a solid solution ration of 2 g L^{-1} in the presence or absence of 20 ppm Cr(VI). The suspensions were then adjusted to environmentally relevant pH values of 5.75 and 7 using dilute NaOH or HNO_3 and buffered using 30 mmol L^{-1} organic buffer 2-(N-Morpholino)ethane-sulphonic acid (MES) and 3-(N-Morpholino)propanesulphonic acid (MOPS), respectively. These buffer solutions have been shown to have negligible impact on the transformation of Fh (Bradbury and Baeyens, 1999; Chen et al., 2020; Ford et al., 1999; Wang et al., 2020a). After shaking continuously for 24h to reach equilibrium, the resultant solutions were transferred to an anoxic chamber (95% N_2 and 5% H_2 circulated over heated palladium catalyst to remove traces of $O_2(g)$). All the solutions were purged with high purity N_2 for at least 0.5h before transferred into the glove box and then exposed to the atmosphere of glove box for 24h to remove the trace dissolved oxygen. A stock Fe(II) solution ($FeCl_2$) was then added into the suspension to induce the mineralogical transformation of iron minerals. For experiments with Cr(VI) added, 105 ppm Fe(II) were added to react with Cr(VI) and with the final Fe(II) concentration around 40.5 ppm (0.726 mM). To observe influences of Cr on the transformation, Fe(II) added in experiments without Cr(VI) were also controlled at around 40.5 ppm. During the reactions, the experiments were agitated three times per day. In order to allow a time-resolved investigation of mineralogical transformation, Cr re-distribution and OC re-distribution, aliquots of the suspensions were collected at time intervals of: 0.5 h, 1 d, 2 d, 4 d, 6 d, 8 d, 12 d and 18 d and the pH recorded.

3.1.6 Synthesis of goethite, lepidocrocite and magnetite

Goethite and lepidocrocite were synthesized according to the methods reported by Jones et al. (2009) and Cornell and Schwertmann (2003), respectively. Briefly, Gt was prepared by adding 180 mL of 5 M NaOH to 100 mL of 1 M $Fe(NO_3)_3•9H_2O$, followed by diluting the solution to 2 L with Milli-Q water. The resulting suspension was shaken vigorously in a screw capped polypropylene bottle and then heated at 70 ℃ for 60 h. Lepidocrocite was prepared by oxidizing 600 mL of 0.2 M $FeCl_2$ solution under a flow of compressed air at a flow rate of 100 mL/min. CO_2 in the compressed air was removed before use by bubbling the air flow through 2 M NaOH solution. During the oxidation of the $FeCl_2$ solution, the solution pH was maintained at ~6.5 by dropwise addition of 1 M NaOH until completing precipitation. The resulting particles were washed at least three times using Milli-Q water and then stored at 4 ℃ in fridge.

Magnetite particles were synthesized using a modified coprecipitation method (Sheng et al., 2020a). Briefly, a mixture (100 mL) of 0.1 M $FeCl_2{\cdot}4H_2O$ and 0.2 M $FeCl_3{\cdot}6H_2O$ with $[Fe^{2+}]/[Fe^{3+}]$ ratio of 1:2 was prepared in an anaerobic glovebox (95% N_2 and 5% H_2 over a Pd catalyst). Then, 0.1 M NaOH was dropwise added to the solution under vigorous stirring at ~60 °C, until complete coprecipitation at pH = 9-11. After incubation at ~60 °C for another 30 min, the particles were washed three times with degassed Milli-Q water in the glovebox and stored inside the glovebox in the dark.

3.2 Analytical and spectroscopic tools

3.2.1 Inductively coupled plasma-mass spectrometry (ICP-MS)

Inductively coupled plasma-mass spectrometry is a popular analytical technique used to perform trace/ultra-trace metal analysis. The aqueous samples are aspirated by a nebuliser and a spray chamber/desolvator and then reach the plasma as aerosol. Most elements can be almost completely atomized and ionized at the high temperature in the plasma source. The ions generated are accelerated and extracted through a series of cones and lenses to the mass spectrometer, where the elements of interest are detected based on their mass/charge ratio.

All ICP-MS measurements in this study were conducted by Stephen Reid in the laboratory of the Cohen Group in the School of Earth and Environment at the University of Leeds, using a Thermo iCAP Qc ICP-MS. All samples were diluted with 1% HNO_3 and were measured in duplicate. All standards and calibration blanks were matrix matched.

3.2.2 Atomoc absorption spectrophotometer (AAS)

Flame AAS atomises a sample via an air-acetylene flame. Absorption of the light is observed at a discreet wavelength corresponding to the element. In my experiment, AAS Thermo Scientific Ice 3000 series using SOLAAR software was applied to measure Fe concentration. The calibration line was built using standards diluted with the Fe standard (1000 ppm). All samples were measured in duplicated.

3.2.3 LECO SC-144DR dual range sulfur and carbon analyzer

The LECO analyzer is designed to determine the carbon and sulphur content of materials. The sample is placed in a tube furnace kept at a constant 1350 °C with a flow of pure oxygen atmosphere. At this high temperature the sample combusts releasing CO_2 and SO_2. After flowing through two anhydrone tubes to remove water and a separate halogen trap, the gases go through the IR detection cell to measure the concentration of CO_2 and SO_2. The instrument converts the measurement into percentage (or ppm) values taking into account the sample mass and calibration using standards with known C and S concentrations.

In the current study, the LECO measurement was performed on finely crushed powdered samples with average mass of 0.030 g. The calibration line was built using the Standard (0.924 ± 0.025 %C and 0.017 ± 0.004 %S), which are made with soil samples with known C and S concentrations. The measurement was duplicated for all samples.

3.2.4 Attenuated total reflectance Fourier transform infra-red spectroscopy (FTIR)

Fourier transform infra-red spectrometery measures the intensity of absorption or transmission of infrared radiation through a sample as a function of wavelength/number. Absorbance/transmittance of the sample depends on its composition as different chemical bonds adsorb the infrared radiation with specific energies, resulting in spectra which are used as individual fingerprints for qualitative and quantitative analysis of specific chemical structures or compounds.

In the current study, an Agilent 4500a FTIR with attenuated total reflectance ATR was applied to observe changes in iron mineralogy and the respective proportion of each during the Fe(II)-induced transformation. FTIR spectroscopy was performed on the mineral film formed by air-drying suspensions on the mounting plate. All measurements were conducted with replication at least in duplicate. FTIR spectra were obtained by accumulating 64 scans over an energy range of 650 to 4000 cm^{-1} with a spectral resolution of 4 cm^{-1}. The quantities of goethite (Gt) and lepidocrocite (Lp) in each reaction product were determined from comparison of signature peak heights (lepidocrocite 1020 cm^{-1} and goethite 890 cm^{-1}) to those of synthetic reference materials from a calibration mixture prepared using 0%, 25%, 75% and 100% of a range of Fe(III) oxide mineral mixtures. All spectra were analyzed using the SpectraGryph – an optical spectroscopy software and Origin software program.

3.2.5 Brunauer-Emmett-Teller surface area analysis (BET)

The BET method measures the specific surface area of a sample and estimates the internal pore volume and pore size distribution. The volume of gas adsorbed to the surface of the mineral particles is measured at the boiling point of nitrogen (-196 ℃).The amount of adsorbed gas is correlated to the total surface area of the mineral particles including surface pores. The calculation is based on the BET theory (Brunauer et al., 1938).

In the current study, the specific surface area (SSA) of the Fh was determined by analyzing $N_{2(g)}$ adsorption data using the multi-point BET (Brunauer, Emmett and Teller) isotherm. Measurements were obtained using a Micromeritics Gemini VII Surface Area Analyser, with samples dried and degassed at room temperature for 24 h using N_2 (g) (<1 ppm CO_2 (g)) prior to analysis. The total pore volume was calculated from the volume of adsorbed N_2 at partial pressure $P/P_0 \sim 0.95$. The average pore radius was calculated as $r_p=2V_{lip}/SSA$, where V_{liq} is the volume of liquid N_2 contained in the pores. All SSA analyses were performed in duplicate at least.

3.2.6 Ultraviolet–visible (UV–Vis) spectroscopy

Ultraviolet-visable spectroscopy uses light to determine the absorbance or transmission at specific energy wavelengths when interacting with a chemical species in either solid or aqueous state. In my experiment, UV-vis was applied to measuring aqueous Fe(II) concentrations at 562 nm wavelength by the Ferrozine assay (Stookey, 1970) and measuing Cr(VI) at 540 nm wavelength by 1,5-diphenylcarbazide method (Chakraborty and Mishra, 1992). Disposable polystyrene cuvettes with fixed path length for light transmission were used in this experiment. All samples were measured in duplicate.

3.2.7 X-ray diffraction (XRD)

X-ray diffraction can provide many information such as phase identification, structural properties and quantify different minerals, and thus is routinely used for the structural characterization of polycrystalline samples. When a focused beam of X-rays of known wavelength are generated and passed through a crystalline sample, X-rays are diffracted at a specific angles, which is mathematically related to structural arrangement by the Bragg equation:

$$n\lambda = 2d\sin\theta$$

where n is an integer representing the order of reflection; λ is the wavelength of the x-ray beam; d is the distance between adjacent planes of atoms and θ is the angle of the incident x-rays.

Because the d-spacings are unique to a specific sample, d calculated from the Bragg equation are thus used to identify minerals through being compared to a set of standard reference patterns.

The XRD instrumentation used in this work was a Bruker D8 Diffractometer with Cu-Kα radiation ($\lambda \approx 0.154$ nm). Diffractograms were recorded from 2–90° 2θ with 0.02° 2θ step size and 930 ms acquisition time. Silicon dioxide was used as an analytical standard.

3.2.8 Scanning transmission X-ray microscopy near-edge X-ray absorption fine structure spectroscopy (STXM NEXAFS)

X-ray absorption spectroscopy (XAS) can provide unique structural and compositional information on a sample, such as oxidation state, structural order, and details of the surface complexes. The STXM NEXAFS was used to investigate the binding strength of OC in Fh-OC coprecipitates in Chapter 4, where all measurements were conducted by Lisa Curti. The C 1s STXM NEXAFS for the Fh coprecipitates was recorded on Beamline I08, Diamond Light Source Ltd, Oxfordshire, UK, following the method of Curti et al. (2021).

3.3 OC and Cr(VI) surface complexation modelling

The adsorption data for the carboxylic acids and/or Cr(VI) on Fh was used to fit parameter values (reaction stoichiometry and formation constants) for a thermodynamic surface complexation model using the program EQLFOR (Sherman et al., 2008). The Basic Stern model (BSM) (Westall and Hohl, 1980) was used to account for the effect of surface electrostatic properties in the Fh and Fh organomineral systems (Moon and Peacock, 2013; Otero-Farina, 2017; Zhao et al., 2022) with a 3-site 1 p*K* formalism for protonation of the Fh surface, involving two types of singly-coordinated surface oxygens (edge-sharing $\equiv FeOH_e^{-0.5}$ and corner-sharing $\equiv FeOH_c^{-0.5}$) and the triply-coordinated oxygens ($\equiv Fe_3O^{-0.5}$) (Hiemstra and Van Riemsdijk, 2009; Hiemstra et al., 1989; Hiemstra et al., 1996). The model input parameters for the binding constants for protonation of the surface functional groups, binding constants for electrolyte ions associating with these groups, site densities of the groups and capacitance of the Stern layer were fixed at those used in previous work on Fh and Fh organominerals (Moon and Peacock, 2013; Otero-Farina, 2017). The SSA of the Fh were fixed to the values determined in this study with BET measurements. The surface site concentrations (mole/g) of end-member Fh in Fh organomineral coprecipitates were calculated using the surface site concentration of the pure Fh weighted to the mineral:OC mass ratio of each coprecipitate.

Chapter 4 The role and fate of organic carbon during aging of ferrihydrite

ABSTRACT

The persistence of organic carbon (OC) in natural environments is widely attributed to mineral protection, especially by iron (Fe) (oxyhydr)oxides. The effect of OC binding strength on the aging of Fe (oxyhydr)oxides and the mobility and fate of OC during aging however, is unknown. Here I investigate how OC binding strength controls the aging of ferrihydrite (Fh) and subsequent retention or release of the associated OC. I focus on carboxyl-rich OC coprecipitated with Fh and track the physiochemical properties and OC distribution between solid and solution phases as a function of carboxyl-richness over time. In agreement with previous work I find that during carboxyl-rich OC coprecipitation with Fh, OC is adsorbed to the Fh particle surfaces and that increasing carboxyl-richness results in increasing OC binding strength. I show that OC substantially retards the aging of Fe (oxyhydr)oxide from Fh to more crystalline Fe minerals and that this retardation increases with increasing OC binding strength. I also show that the total amount of OC decreases during aging but that the proportion of the remaining OC that is non-desorbable with 0.1 M NaOH increases with increasing OC binding strength. My results therefore indicate that OC with higher binding strength coprecipitated with Fh becomes proportionally more stable with the solid phase and thus less mobile during aging in natural environments. I suggest that my work might offer a deeper mechanistic insight into the processes responsible for OC persistence with minerals and thus the long-term preservation of OC in natural environments.

4.1 Introduction

Soils are the largest terrestrial reservoir and third largest global reservoir for organic carbon (OC) and are thus a significant component of the global carbon cycle (Jobbágy and Jackson, 2000; Ruddiman, 2001). Soil organic carbon (SOC) also improves soil structure and function, and thus contributes to a wealth of soil ecosystem services (Sparks, 2003). The composition of SOC is a subject of significant research but the OC stored in soils typically comprises a variety of plant- and microbially-derived organic components, and thus includes soil biomass and organic exudates and residues, and humic substances (humin, humic acid and fulvic acid) and non-humic substances (e.g. amino acids, carbohydrates), which although often at low abundance are highly reactive and can pronouncedly influence soil chemistry (Sparks, 2003). Together with organic nitrogen (N), phosphorus (P) and other organic building blocks, SOC forms part of soil organic matter (SOM), which is often conceived as a continuum of progressively decomposing organic compounds that are initially derived from biomolecules (Lehmann and Kleber, 2015). Given the lability of most biomolecules, SOM should readily turn over (Lehmann and Kleber, 2015), however some SOM persists for months to millennia, which is difficult to explain from a thermodynamic perspective (Schmidt et al., 2011).

There are several hypotheses that try to explain how plant- and microbially-derived OC is stored in soils and sediments, that range from storage being due to an inherent recalcitrance of specific types of OC, which leads to their selective preservation (like lignin and cellulose) (Burdige, 2007; Hatcher et al., 1983; Hedges et al., 1985; Kellerman et al., 2015), to the protection of a range of different OC moieties from microbial degradation through their association with mineral particles (Burdige, 2007; Rothman and Forney, 2007; Six et al., 2002; Torn et al., 1997; Vogel et al., 2014). Long residence times of SOC are frequently attributed to the association of organic species with minerals, especially iron (Fe) (oxyhydr)oxides, which can stabilise SOC against microbial degradation under both oxic and anoxic conditions (Hemingway et al., 2019; Kaiser and Guggenberger, 2007; Li et al., 2020; Mikutta et al., 2006; Newcomb et al., 2017; Torn et al., 1997; Zhao et al., 2016). The association of OC with minerals typically occurs through a variety of sequestration processes that remove OC from solution to the solid mineral particles (Sposito, 2008). Sequestration processes can include the surface sorption, or adsorption, of OC to preformed mineral particles and also the coprecipitation of OC with neoformed mineral phases, where OC is removed from solution as a consequence of mineral precipitation (Eusterhues et al., 2011). During coprecipitation OC can become adsorbed at mineral particle surfaces and incorporated into particle interiors, for example by being occluded into mineral pore spaces (Eusterhues et al., 2011). An important proportion (up to 40%) of total SOM in various soils is reportedly bound with reactive Fe minerals, most likely during coprecipitation (Wagai and Mayer, 2007; Zhao et al., 2016). Recent research highlights however, that the relationship between OC and Fe minerals, and thus the protection of OC from microbial degradation, is complex and influenced by soil redox and microbial activity. Reducing conditions can lead to the reductive dissolution of Fe minerals and drive carbon solubilisation, depolymerisation and loss as CO_2 (Chen et al., 2020). Microbial activity can also play a finely balanced role in OC remineralisation, which influences the functional role of Fe in OC cycling (Li et al., 2020). If microbial activity is high, the role of Fe can change from that of a sorbent to an electron acceptor, thus increasing the accessibility of OC to microorganisms (Li et al., 2020). Overall it is clear that the interactions between SOC and Fe minerals in all soil conditions can influence the long-term storage of OC in soils and regulate the global biogeochemical cycling of carbon (Adhikari et al., 2017).

Of the naturally occurring Fe minerals the (oxyhydr)oxide ferrihydrite (Fh) is common in soils and has high surface area with high surface reactivity (Hiemstra, 2013; Larsen and Postma, 2001; Michel et al., 2007b). It therefore possesses extremely high capacity to sequester OC compared to more crystalline Fe minerals (Adhikari et al., 2017; Chen et al., 2014; Kaiser and Guggenberger, 2007). Authigenic Fh is metastable under oxic conditions however, and ages to more crystalline Fe minerals, like goethite (Gt) and hematite (Hm), over time (Das et al., 2011b). Because aging involves dissolution, precipitation, aggregation, sorption and desorption (Sakakibara et al., 2019) and the more crystalline Fe minerals also have different physical and chemical properties compared to Fh (Cornell and Schwertmann, 2003), the aging of Fe (oxyhydr)oxide can either enhance the mobility and migration, and hence the degradation, of OC in soils (Adhikari et al., 2017; Canfield, 1993; Chen et al., 2020; Han et al., 2019), or strengthen OC sequestration and fixation and thus lengthen the residence time of OC in these environments (Hu et al., 2020; Lu et al., 2019b).

Due to the potential importance of Fe (oxyhydr)oxide aging on the mobility and fate of associated OC, there are several studies that investigate the aging of Fh in the presence of associated OC, and the behaviour of the associated OC as aging progresses. Regarding aging, the presence of OC can significantly influence the aging rate of Fh. Previous works shows that OC can suppress the recrystallisation of Fh to more crystalline Fe minerals in both oxic (Hu et al., 2018) and anoxic environments (Chen et al., 2015; Eusterhues et al., 2014; Henneberry et al., 2012), but also facilitate the recrystallisation of Fh by electron shuttling under anoxic conditions (Amstaetter et al., 2012; Bhattacharyya et al., 2019; Jiang and Kappler, 2008; Lovley et al., 1996; Poggenburg et al., 2016). The presence of OC can also influence the physiochemical properties of the aging products formed, resulting in Fe minerals with more defects and greater porosity than those formed from pure Fh (Hu et al., 2020; Lu et al., 2019b), which may provide an effective mechanism to sequester OC. Regarding the mobility and fate of the OC, work shows that during aging of Fh to more crystalline Fe minerals, OC may be sequestered (Hu et al., 2020; Lu et al., 2019b) or partially released from Fe (oxyhydr)oxides (Adhikari et al., 2017; Jelavić et al., 2020). Whether OC is retained or released during aging depends on several factors, including C/Fe ratio (Adhikari et al., 2017; Chen et al., 2015), whether OC is adsorbed or coprecipitated (Han et al., 2019), the structure and electron-shuttling properties of the OC (Amstaetter et al., 2012) and the crystalline structures of the mineral products (Hu et al., 2020; Lu et al., 2019b). Despite these studies however, the effects of different types and binding strengths of OC on the aging of Fh to more crystalline Fe minerals and the mobility and fate of OC are still unknown.

One of the most important types of OC for Fe mineral-OC associations is carboxyl-rich OC. Carboxyl functional groups are prevalent in natural OC (Rothe et al., 2000) and are highly reactive towards different metal ions and mineral surfaces (Rowley et al., 2017). Because of this they play a dominant role in OC sequestration mechanisms and thus in long-term accumulation of OC in soil (Kramer et al., 2012). Spectroscopic studies using Fourier-transform infrared spectroscopy (FTIR) and near edge X-ray absorption fine structure spectroscopy (NEXAFS) provide direct evidence for inner-sphere ligand exchange reactions between carboxyl functional groups and Fe minerals (Chen et al., 2014; Hall et al., 2020; Lv et al., 2016; Solomon et al., 2005). Recent NEXFAS spectroscopy however, also shows that as the number of carboxyl functional groups present in simple carboxylic OC compounds increases, the binding strength, stability and persistence of the OC associated with Fh also increases, due to the formation of an increasing number of inner-sphere ligand exchange complexes between the carboxyl functional groups and the Fh particles (Curti et al., 2021).

Here I investigate how OC binding strength controls the aging of Fh and subsequent retention or release of the associated OC. I focus on carboxyl-rich OC and I use simple mono-, di- and tri-carboxylic acids with either one, two or three carboxyl functional groups and thus increasing carboxyl-richness as model carboxyl-rich compounds. I synthesise Fh organomineral coprecipitates and use X-ray diffraction (XRD) to confirm the mineralogy of the coprecipitates, and scanning transmission X-ray microscopy (STXM) coupled with NEXAFS, together with thermodynamic surface complexation modelling, to determine the binding strength and distribution of OC with the coprecipitates. I then subject my Fh coprecipitates to aging experiments at 75℃ to observe how the presence of the OC influences the chemical reactivity of Fe (oxyhydr)oxide during acid extraction as an operationally defined measure of crystallinity, and how the total amount of OC and the non-desorbable amount of OC changes as a function of carboxyl-richness. My primary objectives were to (1) investigate the influence of carboxyl-rich OC with different binding strengths on the aging of Fh organominerals; (2) investigate the influence of carboxyl-rich OC with different binding strengths on the mobility and fate of OC during aging of Fh organominerals; and (3) use my results to suggest whether OC binding strength to Fh might significantly affect the stabilisation and preservation of OC in natural environments.

4.2 Materials and methods

4.2.1 Preparation of Fh organomineral coprecipitates

Eight Fh organomineral coprecipitates with different wt%C were prepared with three simple carboxylic acids following the method of Curti et al. (2021). The acids were denoted as acid*n/m*, where acid refers to the first three letters of the acid IUPAC name and *n*/*m* denotes the number of carboxyl groups (*n*) and the number of total carbon atoms (*m*). The acids used were pentanoic acid (Pen1/5), hexanedioic acid (Hex2/6) and butane 1, 2, 4 tricarboxylic acid (But3/7), which have one, two and three carboxyl functional groups, respectively. Briefly, 0.1 M $Fe(NO_3)_3 \cdot 9H_2O$ (aq) solutions were mixed with varied amounts of organic acids and then the pH values of the solutions are adjusted to ~7 with 1 M KOH, whereupon the acids coprecipitated with the Fh, forming Fh organomineral coprecipitates with different wt%C sorbed. Fh organomineral coprecipitates were washed several times over a week in equivalent volumes of 18.2 MΩ·cm MilliQ water, after which coprecipitates were stored as a slurry at 4 ^{o}C, and part of the coprecipitates were freeze-dried for further analysis. The amounts of organic acids were varied taking into account the solubility of the acids in solution and their affinity for Fh during coprecipitation. For Pen1/5 solubility and affinity are low and constrain the maximum carbon sequestration to ~1wt%C, while for Hex2/6 and But3/7 affinity is higher and allows a maximum sequestration of at least ~7wt%C (Curti et al., 2021). Pure ferrihydrite (Fh) as 2-line Fh was prepared via hydrolysis of a Fe(III) salt solution following the method of Schwertmann and Cornell (2000). Briefly, Fh was prepared by rapid hydrolysis of 0.1 M $Fe(NO_3)_3 \cdot 9H_2O$ (aq) with 1 M KOH at pH 7. Fh was washed several times over a week in equivalent volumes of 18.2 MΩ·cm MilliQ water, after which Fh was stored as a slurry at 4 ^{o}C (Schwertmann and Cornell, 2000). Plastic labware and AR grade reagents were used throughout the preparations.

The C contents of the solids were determined on solid freeze-dried subsamples using LECO SC-144DR Dual Range Sulphur and Carbon Analyzer. The Fe contents of the solids were determined after total digestion using 6 mol L^{-1} HCl on an Atomic Absorption Spectrophotometer (iCE 3300 AAS). Eight coprecipitates were obtained: Fh-pentanoic acid with 1.2 wt%C and C:Fe molar ratio 0.098 (Fh_Pen1/5_1.2wt%C); Fh-hexanedioic acid with 2.9 wt%C and C:Fe molar ratio 0.246 (Fh_Hex2/6_2.9wt%C), 4.1 wt%C and C:Fe molar ratio 0.358 (Fh_Hex2/6_4.1wt%C), 4.5 wt%C and C:Fe molar ratio 0.396 (Fh_Hex2/6_4.5wt%C), and 7.0 wt%C and C:Fe molar ratio 0.652 (Fh_Hex2/6_7.0wt%C); and Fh-butane 1, 2, 4 tricarboxylic acid with 6.0 wt%C and C:Fe molar ratio 0.555 (Fh Fh_But3/7_6.0wt%C), 7.3 wt%C and C:Fe molar ratio 0.699 (Fh_But3/7_7.3wt%C), and 7.8 wt%C and C:Fe molar ratio 0.757 (Fh Fh_But3/7_7.8wt%C).

4.2.2 Characterisation of Fh organomineral coprecipitates

4.2.2.1 X-ray diffraction and scanning transmission X-ray microscopy near-edge X-ray absorption fine structure spectroscopy

The mineralogy of the Fh coprecipitates and pure Fh prior to aging was confirmed on freeze-dried subsamples via X-ray diffraction (XRD) using a Bruker D8 Diffractometer with Cu-Kα radiation ($\lambda \approx 0.154$ nm). Diffractograms were recorded from 2–90° 2θ with 0.02° 2θ step size and 930 ms acquisition time. Silicon dioxide was used as an analytical standard.

The binding strength of the OC to Fh in the Fh coprecipitates and the distribution of OC with the Fh coprecipitate particles prior to aging was investigated directly using

STXM NEXAFS. The C 1s STXM NEXAFS for the Fh coprecipitates was recorded on Beamline I08, Diamond Light Source Ltd, Oxfordshire, UK, following the method of Curti et al. (2021). Briefly, for analysis ~5 mg of freeze-dried subsample was suspended in ~500 μL of 18.2 MΩ·cm MilliQ water and then an aliquot of ~5 μL of suspension was pipetted onto a glow-discharged Si_3-N_4 membrane window (Silson Ltd) and left to air dry. Stacked data sets for C were collected from 275 to 310 eV, using varied energy resolution across different spectral regions of 0.5, 0.1 and 0.2 eV step size for pre-edge, running up to and over the edge, and post-edge, respectively. To minimise beam damage on the sample, dwell times were set to 10 ms per energy step based on beam damage tests conducted by repeatedly measuring the same area of sacrificial samples. The unreacted acids were analysed as unmodified acid solids or liquids as applicable. X-ray absorption stacks were aligned using the Axis2000 software. The NEXAFS spectra were extracted from individual coprecipitate particles and the dark signal was subtracted from the raw data using the Mantis software. The NEXAFS spectra were then exported for baseline correction, alignment, calibration and normalisation using the Athena software (Ravel and Newville, 2005). Baseline correction and normalisation avoid spectral dependence on the total C content, and spectral features and peak shifts are thus indicative of C molecular structure and chemistry and not C concentration effects occurring during NEXAFS measurement. Peak identification was done with reference to literature assignations. The STXM images were used to show the spatial correlation between C and Fe, again following the method of Curti et al. (2021). Briefly, C and Fe elemental distribution maps were created by aligning and then converting C and Fe images to optical density (OD) using the transmitted flux through the sample (I) and the incident flux measured in an empty region adjacent to the analysed particles (I0) where OD = ln(I0/I). Distribution maps for C and Fe were taken on the same region and with the same number of pixels and were then aligned to common reference features and overlapped. To determine the C-Fe correlation coefficients, elemental thickness values on a pixel-by-pixel basis were compared by extracting the OD values using the Axis 2000 software, saved as an ascii file, and then the OD values for both C and Fe stacks were plotted against one another. The energies for obtaining the C and Fe distribution maps were C 1s 282.0 – 289.0 eV and Fe 2p 705.0 – 712.0 eV.

4.2.2.2 Thermodynamic surface complexation modelling

The binding strength of the OC to Fh in the Fh coprecipitates prior to aging was also investigated indirectly by measuring the adsorption of Pen1/5, Hex2/6 and But3/7 to pure Fh in batch adsorption pH edge experiments and then using a thermodynamic surface complexation model to constrain the binding affinity of these acids. Batch adsorption experiments of the acids on pure Fh were prepared from pH 3.5 to 10.0. Pure Fh mineral slurry was added into 18.2 MΩ·cm MilliQ water and either Pen1/5, Hex2/6 and But3/7 stock solutions were added to give a total volume of 45 mL, a solid solution ration of 2 g dry sorbent L^{-1} and OC concentrations of 0.4 mM in 0.01 $NaNO_3$ background electrolyte. After addition of stock solution, pH of the resulting suspensions was adjusted by dropwise addition of either dilute HNO_3 or NaOH. After shaking continuously for 48 h, the suspensions were filtered with 0.22 μm cellulose nitrate filters using a vacuum filtration apparatus and the solids were collected and rinsed with 5 mL DI water to remove aqueous OC. The solids were then freeze-dried. The total C contents of the solids were determined using a LECO SC-144DR Dual Range Sulphur and Carbon Analyzer. The amount of OC sorbed was calculated by subtracting the amount of C present for pure Fh (the control). The calculated OC sorbed (wt%C) and the dry sorbent concentration (2 g/L) were then used to calculate the molar concentration of OC adsorbed. All adsorption experiments were conducted in duplicate.

Following the successful application of the diffuse double layer model and triple layer model to simulate the adsorption of simple organic acids on Gt (Evanko and Dzombak, 1999; Mesuere and Fish, 1992a, b), the adsorption behaviour of the carboxylic acids on Fh was fit to a thermodynamic surface complexation model using the program EQLFOR (Sherman et al., 2008). The basic Stern model (BSM) (Westall and Hohl, 1980) was used to account for the surface electrostatics in the Fh system with a 3-site

1 p*K* formalism for protonation of the Fh surface, involving two types of singly-coordinated surface oxygens (edge-sharing $\equiv FeOH_e^{-0.5}$ and corner-sharing $\equiv FeOH_c^{-0.5}$) and the triply-coordinated oxygens ($\equiv Fe_3O^{-0.5}$) (Hiemstra and Van Riemsdijk, 2009; Hiemstra et al., 1989; Hiemstra et al., 1996). The model input parameters for the binding constants for protonation of the surface functional groups, binding constants for electrolyte ions associating with these groups, site densities of the groups and capacitance of the Stern layer have been constrained for Fh in previous work (Moon and Peacock, 2013). The binding constants for protonation of the carboxylic acid groups have also been constrained in previous work (Dean, 1987) or were calculated for this study using the ACD/I-Lab 2.0 software (ACD/I-Lab, version 2.0, Advanced Chemistry Development, Inc). The specific surface area (SSA) of the Fh was determined by the multi-point BET (Brunauer, Emmett and Teller) technique using a Micromeritics Gemini VII 2390a Surface Area Analyser, with samples dried and degassed at room temperature for 24 h using N_2 (g) (<1 ppm CO_2 (g)) prior to analysis. All SSA analyses were performed in triplicate.

4.2.3 Aging of Fh organomineral coprecipitates

After preparation and characterisation of the Fh coprecipitates, Fh coprecipitate slurries and pure Fh were added into 0.01 M $NaNO_3$ background electrolyte to produce 2 g/L suspensions, and then adjusted to target pH values with dilute HNO_3 or NaOH. The pH values were buffered at pH 5 and 6.5 by adding 30 mmol/L organic buffer 2-(N-Morpholino)ethane-sulphonic acid (MES) and 3-(N-Morpholino)propanesulphonic acid (MOPS), respectively. These buffer solutions are negligibly sequestered to Fh (see Supplementary Information) and have been shown to have negligible impact on the recrystallisation of Fh to more crystalline Fe minerals during aging (Bradbury and Baeyens, 1999; Ford et al., 1999). The resultant solutions were then transferred to an electric oven kept at a temperature of 75 ℃ for 19 days. During aging, the vessels were gently shaken to keep the suspensions homogenised. Aliquots of the solid precipitates and solutions were collected and analysed at pre-designed time intervals to track changes in the physiochemical characteristics of the Fh coprecipitates as described below. At each sampling, the suspensions were cooled to room temperature and the pH was measured. A temperature of 75 ℃ was used in the aging experiments as it has been shown to accelerate the recrystallisation of Fh to more crystalline Fe minerals during aging without substantially altering the aging process from that observed at 25 ℃ (Das et al., 2011) or causing the decomposition of Pen1/5 (McCollom and Seewald, 2003), Hex2/6 (safety data sheet (Sigma-A26357)) and But3/7 (safety data sheet (Sigma-514101)). A 19 days reaction time was used in the aging experiments based on test experiments that determined the time necessary for no further changes in the physiochemical characteristics of the Fh coprecipitates in most reaction systems.

4.2.4 Measured physiochemical characteristics of Fh organomineral coprecipitates during aging

To investigate the recrystallisation of Fh to more crystalline Fe minerals during aging, an acid extraction method was used that quantified the proportion of the total Fe in the solid phase that was digested by 6 mol L^{-1} HCl ($[Fe(T)_{6\ M\ HCl}]$) compared to the proportion of Fe in the solid phase that was digested by 0.4 mol L^{-1} HCl ($[Fe(T)_{0.4\ M\ HCl}]$ (Wang et al., 2020a). In this approach, the 6 mol L^{-1} HCl step has been shown to cause the total digestion of all solid Fe phases and thus represented the total concentration of all solid phase Fe minerals (Wang et al., 2020a). The 0.4 mol L^{-1} HCl step has been shown to not cause the digestion of the more crystalline Fe minerals formed during the oxic aging of Fh, like Gt (Reddy et al., 2015) and Hm (see Appendixes Section 2). As soluble Fe(III) in the aqueous phase was below detection limits before adding acids (Reddy et al., 2015), the concentration of Fe in the supernatant after the 0.4 mol L^{-1} HCl step thus represented the total concentration of acid reactive solid phase Fe minerals, nominally Fh (Wang et al., 2020a). Test experiments performed to determine the efficiency of extracting Fh from mixtures of Fh and Hm at 0 %, 25 %, 50 %, 75 % and 100 % Fh showed that the extraction efficiency for Fh was over 95 % (see Supplementary Information). To perform the acid extraction subsamples were collected from each batch reactor suspension for analyses of Fe concentrations. Two 1 mL aliquots from each suspension were pipetted into 2 mL centrifuge tubes. Then 1 mL 12 mol L^{-1} HCl was added into one aliquot to get 6 mol L^{-1} HCl in suspension for the determination of total Fe in the solid phase ($[Fe(T)_{6\ M\ HCl}]$), and 1 mL 0.8 mol L^{-1} HCl was added into the other aliquot to get 0.4 mol L^{-1} HCl, reacted for 10 mins, then centrifuged, and filtered for the determination of acid reactive Fe in the solid phase ($[Fe(T)_{0.4\ M\ HCl}]$. The concentration of Fe was determined on an Atomic Absorption Spectrophotometer (iCE 3300 AAS). Then the fraction of remaining Fh was quantitatively calculated through the equation: $[Fe(T)_{0.4\ M\ HCl}]/ [Fe(T)_{6\ M\ HCl}]$. All operations above were conducted at least in duplicate.

To investigate the redistribution of OC during the recrystallisation of Fh to more crystalline Fe minerals during aging, two 15 mL aliquots were subsampled from the reactor and filtered with 0.22 μm cellulose nitrate filters using a vacuum filtration apparatus. The mineral particles were collected and rinsed using 15 mL DI water. One of the mineral particle subsamples was freeze-dried and kept at 4 °C for total solid C measurement ($[C_{total}]$). The other mineral particle subsample was re-suspended in 15 mL 0.1 M NaOH and shaken for 24 h to extract OC from the solid (Kaiser and Guggenberger, 2000), which was operationally defined as desorbable OC ($[C_{desorbable}]$). After the 0.1 M NaOH wash the mineral particles were filtered with 0.22 μm PES filters, washed, collected, freeze-dried and kept for C measurement, which was operationally defined as non-desorbable OC ($[C_{non\text{-}desorbable}]$). The C contents of solids were determined using LECO SC-144DR Dual Range Sulphur and Carbon Analyzer. All operations above were conducted at least in duplicate.

To further investigate the physiochemical characteristics of the Fh coprecipitates as a result of aging, SSA and total pore volume (TPV) of the Fh coprecipitates and pure Fh after aging were measured. Briefly, around 100 mL suspensions after 19 days aging at pH 6.5 were centrifuged at 2750 rpm for 20 mins, and the solid minerals were treated with 0.1 M NaOH to desorb OC. After shaking for 24 h, the suspensions were centrifuged, washed and then freeze-dried for SSA measurement determined from duplicate N_2 gas adsorption-desorption isotherms recorded using a Micromeritics Gemini VII 2390a Surface Area Analyzer, with samples dried and degassed at room temperature for 24 h using N_2 (g) (<1 ppm CO_2 (g)) prior to analysis. The total pore volume was calculated from the volume of adsorbed N_2 at partial pressure $P/P_0 \sim 0.95$. The average pore radius was calculated as $r_p=2V_{lip}/SSA$, where V_{liq} is the volume of liquid N_2 contained in the pores. All measurements were performed in duplicate.

4.3 Results

4.3.1 Characterisation of Fh organomineral coprecipitates prior to aging

The XRD pattern of selected Fh coprecipitates prior to aging are plotted in Figure S3 and confirm that the mineralogy of the initial Fh coprecipitates is Fh, without detectable amounts of more crystalline Fe minerals.

The NEXAFS spectra for selected Fh coprecipitates prior to aging, together with their respective unreacted acid standards, are shown in Figure 4.1. In agreement with previous work for the sequestration of these acids by Fh during coprecipitation (Curti et al., 2021), the Fh coprecipitate spectra exhibit one major peak at ~288.6 eV corresponding to carboxyl C (π*C=O, 287.7 – 289 eV (Curti et al., 2021)), which is reduced in amplitude and broadened, compared to the respective standard (Figure 4.1). This carboxyl peak position is also shifted to lower energy, compared to the respective standard, with the shift becoming increasingly pronounced with an increasing number of carboxyl groups (shift from respective standard for Pen1/5_1.2wt%C: -0.1 ± 0.05 eV; for Fh_Hex2/6 coprecipitates: -0.2 ± 0.05 eV; for Fh_But3/7 coprecipitates: -0.4 ± 0.05 eV) (Figure 4.1). A representative STXM image of the Fh coprecipitates prior to aging is shown in Figure S4. The STXM elemental distribution map shows that C and Fe are highly spatially correlated ($R2 = 0.71$) with C apparently more concentrated at the particle edges (Figure S4).

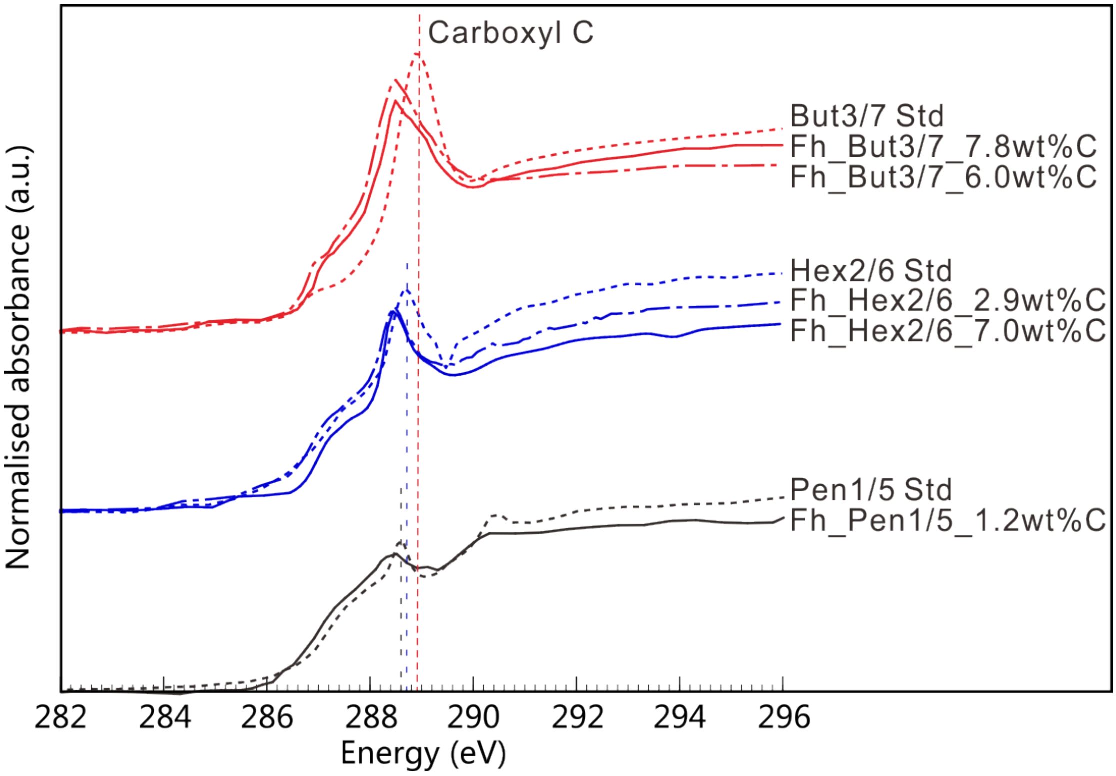

Figure 4.1. Carbon 1s NEXAFS spectra for Fh_Pen1/5_1.2wt%C and both Fh_Hex2/6 and Fh_But3/7 coprecipitates at the lower and upper end of wt%C sequestered (solid and dashed-dotted lines), together with Pen1/5, Hex2/6 and But3/7 unreacted acid standards (dotted lines). Black, blue and red colours represent Pen1/5, Hex2/6 and But3/7 data, respectively. Carboxyl C peak position for the unreacted Pen1/5, Hex2/6 and But3/7 standards are shown with vertical dashed black, blue and red lines, respectively. Spectra are stacked with an arbitrary offset for clarity. Pen1/5, Hex2/6 and But3/7 represent simple carboxyl-rich OC with one, two and three carboxyl groups, respectively.

4.3.2 Adsorption of carboxylic acids to ferrihydrite

The adsorption of Pen1/5, Hex2/6 and But3/7 to pure Fh as a function of pH is plotted in Figure 4.2. In agreement with previous studies for organic acids adsorbed on Fe (oxyhydr)oxides (Lindegren et al., 2009), all carboxylic acids show a reverse sigmoid adsorption edge with higher adsorption in the low-mid (~3.5 to ~6) pH range. Compared to Pen1/5, Hex2/6 and But3/7 show significantly higher maximum adsorption percentages and the adsorption edges, especially for But3/7, shift to higher pH.

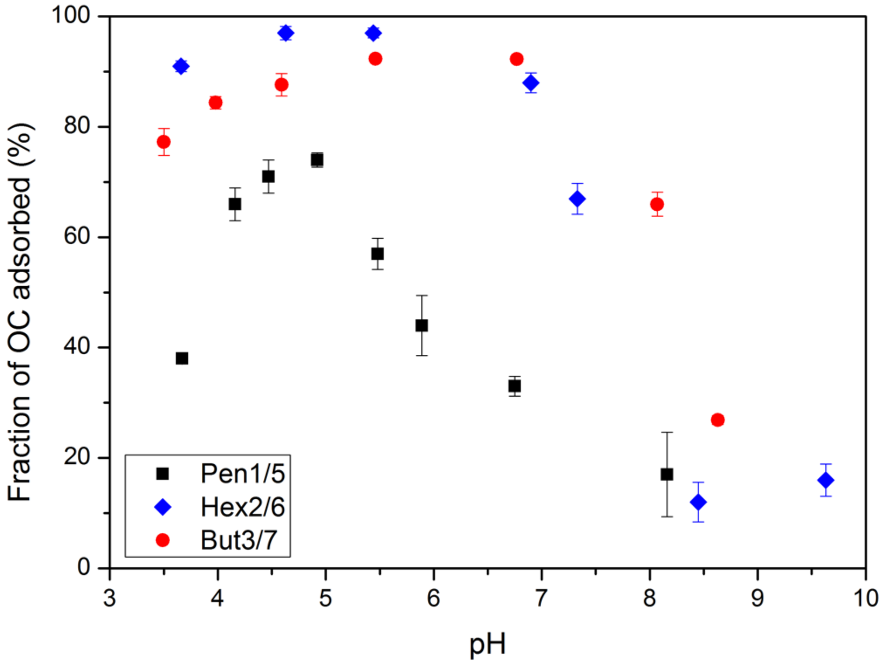

Figure 4.2. OC adsorption on pure Fh as a function of pH (3.5-10). Experiments were performed with about 4 ×10^{-4} M OC (Pen1/5: 4.16 ×10^{-4} M; Hex2/6: 4.29×10^{-4} M and But3/7: 4.17×10^{-4} M) in 0.01 M $NaNO_3$ background electrolyte and a solid-solution ratio of 2 g dry sorbent L^{-1}. Black, blue and red symbols represent Pen1/5, Hex2/6 and But3/7 data, respectively. Pen1/5, Hex2/6 and But3/7 represent simple carboxyl-rich OC with one, two and three carboxyl groups, respectively. Error bars represent standard deviations of duplicate samples.

4.3.3 Aging of ferrihydrite coprecipitates

4.3.3.1 Acid extraction of ferrihydrite coprecipitates as a function of aging time

The acid extraction data for Fh coprecipitates at pH 5 and 6.5 as the fraction of Fh remaining after extraction as a function of aging time is plotted in Figure 4.3. The presence of the carboxylic acids in the coprecipitate systems results in a higher fraction of Fh remaining with reaction time compared to the pure Fh system, and thus the carboxylic acids appear to retard the aging of Fh to more crystalline Fe minerals. This retardation appears to be a function of the number of carboxyl groups in the sequestered acid molecules and thus generally increases in the order Pen1/5 < Hex2/6 < But3/7 (at pH 5) and Pen1/5 < Hex2/6 ~ But3/7 (at pH 6.5), but this trend is complicated by the commensurate increase in the C loading of the coprecipitates with the number of carboxyl groups, so that with increased C loading retardation also generally increases. Specifically at pH 5 retardation as a function of carboxyl richness and C loading follows the order Fh_Pen1/5_1.2wt%C < Fh_Hex2/6_2.9%C ~ Fh_Hex2/6_4.1%C ~ Fh_But3/7_6.0%C < Fh_But3/7_7.3%C ~ Fh_But3/7_7.8%C. While at pH 6 retardation as a function of carboxyl richness and C loading is less pronounced and follows the order Fh_Pen1/5_1.2wt%C < Fh_Hex2/6_2.9%C ~ Fh_Hex2/6_4.1%C ~ Fh_But3/7_6.0%C ~ Fh_But3/7_7.3%C ~ Fh_But3/7_7.8%C.

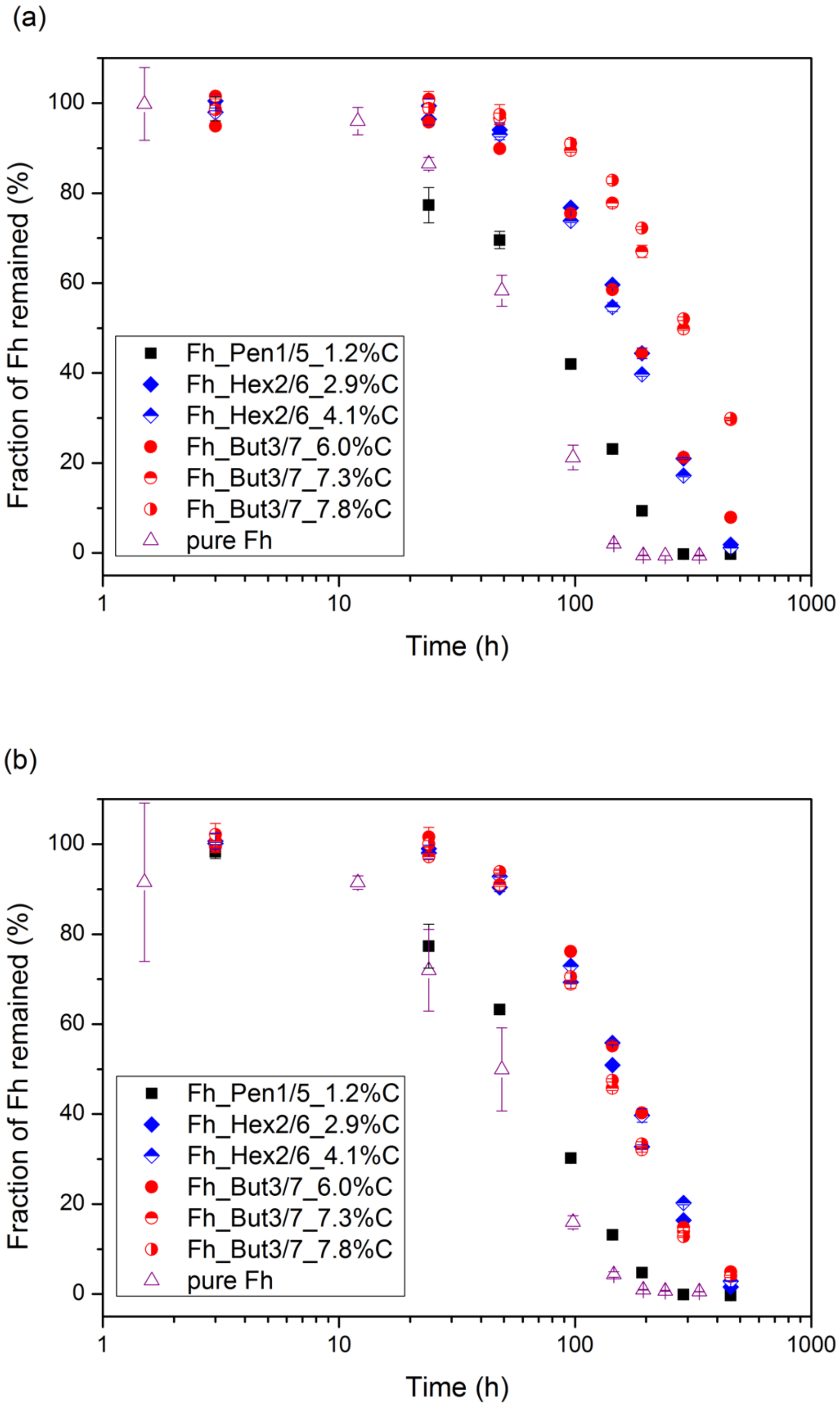

Figure 4.3. Fraction of Fh remaining after acid extraction for Fh coprecipitates and pure Fh at pH 5 (a) and 6.5 (b). Experiments were performed with Fh coprecipitates in 0.01 M $NaNO_3$ background electrolyte and a solid-solution ratio of 2 g dry sorbent L^{-1} at 75 ℃. Black, blue and red symbols represent Pen1/5, Hex2/6 and But3/7 data,

respectively. Pen1/5, Hex2/6 and But3/7 represent simple carboxyl-rich OC with one, two and three carboxyl groups, respectively. Error bars represent standard deviations of at least duplicate samples.

4.3.3.2 Specific surface area and total pore volume of ferrihydrite coprecipitates after aging

The specific surface area (SSA) and total pore volume (TPV) parameters for Fh coprecipitates and pure Fh after 19 days aging at pH 6.5 are listed in Table 4.1. The SSA follows the order pure Fh < Fh_Pen1/5_1.2wt%C < Fh_Hex2/6_7.0wt%C < Fh_But3/7_7.3wt%C, while the TPV follows the order pure Fh < Fh_Pen1/5_1.2wt%C < Fh_But3/7_7.3wt%C < Fh_Hex2/6_7.0wt%C.

Table 4.1. SSA and TPV for pure Fh, Fh_Pen1/5_1.2wt%C, Fh_Hex2/6_7.0wt%C and Fh_But3/7_7.3wt%C after 19 days aging at pH 6.5

	SSA for Fe minerals after 19 days aging (m^2/g)[a]	TPV for Fe minerals after 19 days aging (cm^3/g)[a]
Pure Fh	33 ± 0.1	0.11 ± 0.02
Fh_Pen1/5_1.2wt%C	46 ± 0.1	0.13 ± 0.02
Fh_Hex2/6_7.0wt%C	64 ± 0.6	0.22 ± 0.04
Fh_But3/7_7.3wt%C	103 ± 0.9	0.16 ± 0.02

[a] Fe minerals were treated with 0.1 M NaOH for 24 h to desorb OC

4.3.4 Carbon distribution during aging of ferrihydrite coprecipitates

4.3.4.1 Temporal changes of total C in the solid phase

The changes in the distribution of total solid C ($[C_{total}]$) as a function of aging time at pH 5 and 6.5 are shown in Figure 4.4 and summarised in Table 4.2a. For Fh_Pen1/5 the $C_{[total]}$ at pH 5 and 6.5 is invariant with aging time. For Fh_Hex2/6 and Fh_But3/7 however, the $[C_{total}]$ at pH 5 and 6.5 generally decreases with increasing aging time. Comparing coprecipitates made with the same OC type, the $[C_{total}]$ at pH 5 is higher than that at pH 6.5 at both the beginning and end of the aging. Comparing coprecipitates made with different OC types but with similar C loadings, Fh_Hex2/6_7.0wt%C retains less [C_{total}] compared to Fh_But3/7_6.0wt%C, 7.3wt%C and 7.8 wt%C during the aging process.

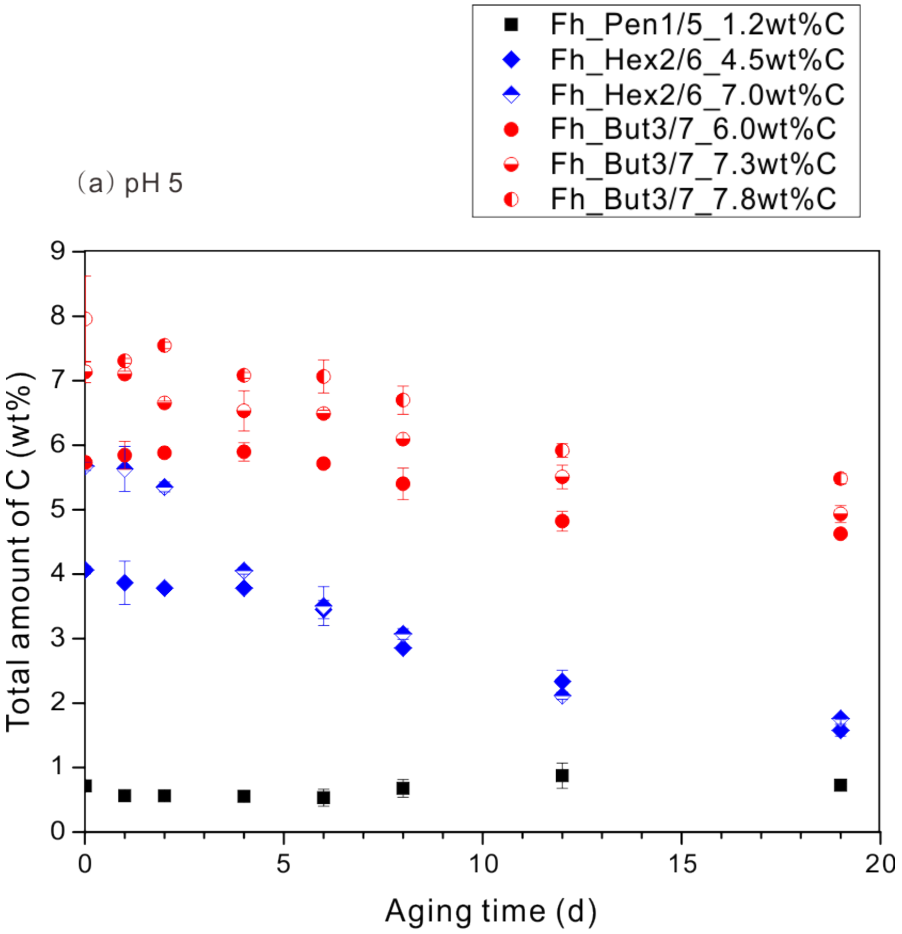

(b) pH 6.5

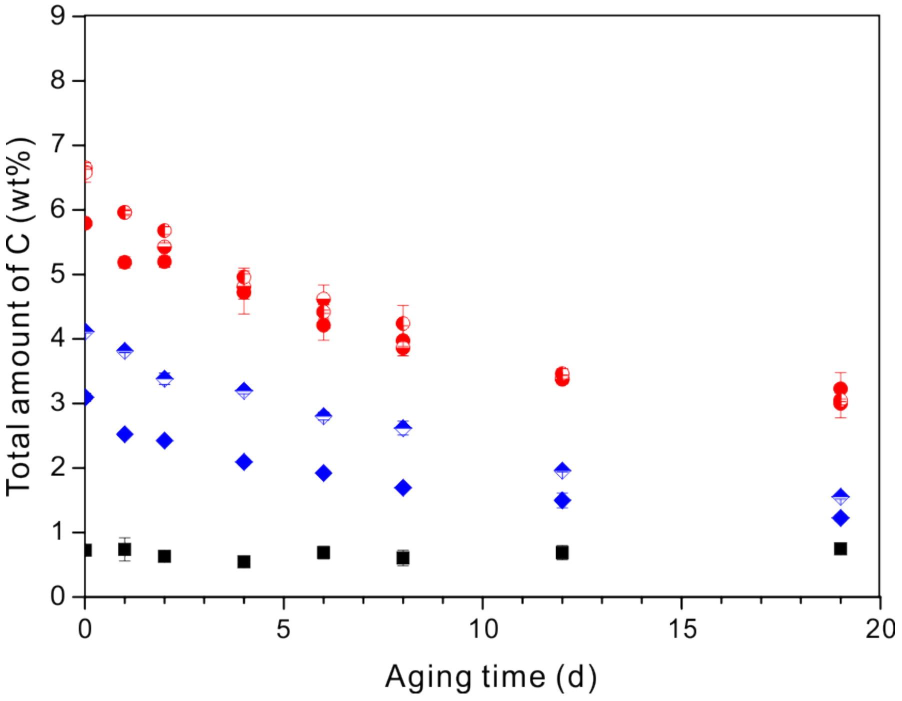

Figure 4.4. Temporal changes in the total amount of C in the Fh coprecipitate solid phase during 19 days aging at a) pH 5.0 and b) pH 6.5. Experiments were performed

with Fh coprecipitates in 0.01 M $NaNO_3$ background electrolyte and a solid-solution ratio of 2 g dry sorbent L^{-1} at 75 ℃. Black, blue and red symbols represent Pen1/5, Hex2/6 and But3/7 data, respectively. Pen1/5, Hex2/6 and But3/7 represent simple carboxyl-rich OC with one, two and three carboxyl groups, respectively. Error bars represent standard deviations of at least duplicate samples.

4.3.4.2 Temporal changes of non-desorbable C in the solid phase

The changes in the distribution of non-desorbable C ($[C_{non\text{-}desorbable}]$) as a function of aging time at pH 5 and 6.5 are shown in Figure 4.5 and summarised in Table 4.2b. For Fh_Pen1/5 and Fh_Hex2/6 the $[C_{non\text{-}desorbable}]$ at pH 5 and 6.5 generally decreases with increasing aging time. For Fh_But3/7 the $[C_{non\text{-}desorbable}]$ at pH 5 and 6.5 is relatively stable over 12 days aging, with a small decrease at 19 days aging. Comparing coprecipitates made with the same OC type, the $[C_{non\text{-}desorbable}]$ at pH 5 is similar to that at pH 6.5. Comparing coprecipitates made with different OC types but with similar C loadings, Fh_Hex2/6_7.0wt%C retains less $[C_{non\text{-}desorbable}]$ compared to Fh_But3/7_ 6.0 wt%C, 7.3wt%C and 7.8wt%C during the aging process.

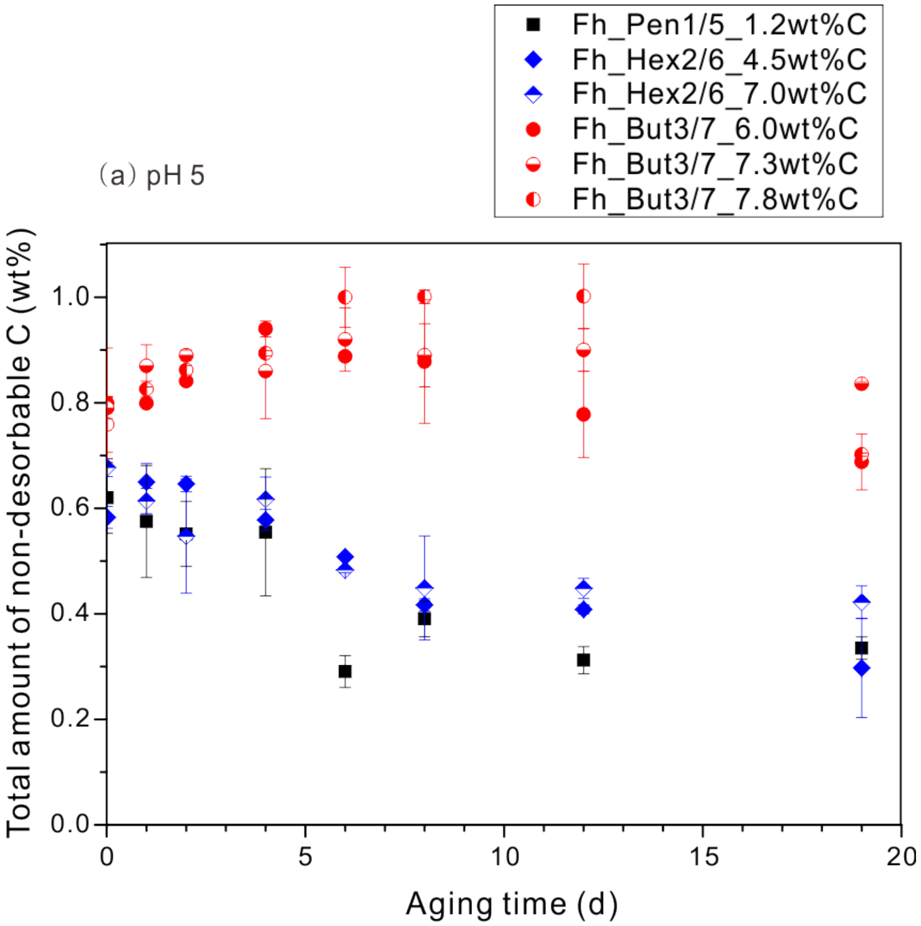
(a) pH 5

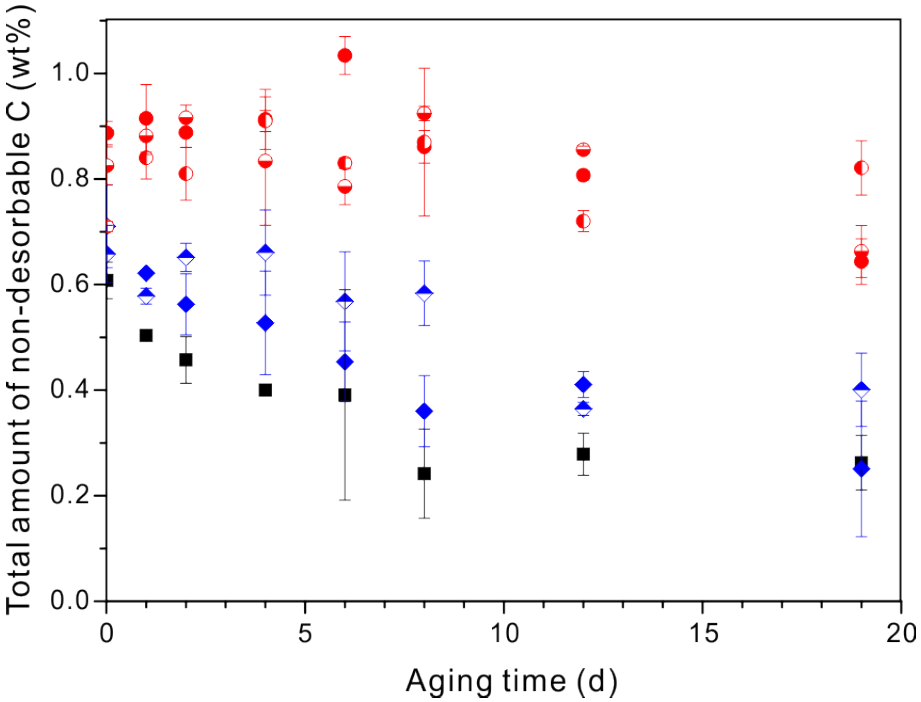
(b) pH 6.5

Figure 4.5. Temporal changes in the total amount of non-desorbable C in the Fh coprecipitates solid phase during 19 days aging at a) pH 5.0 and b) pH 6.5. Experiments

were performed with Fh coprecipitates in 0.01 M $NaNO_3$ background electrolyte and a solid-solution ratio of 2 g dry sorbent L^{-1} at 75 ℃. Black, blue and red symbols represent Pen1/5, Hex2/6 and But3/7 data, respectively. The solid minerals were treated with 0.1 M NaOH for 24 h to extract OC. Pen1/5, Hex2/6 and But3/7 represent simple carboxyl-rich OC with one, two and three carboxyl groups, respectively. Error bars represent standard deviations of at least duplicate samples.

Table 4.2a. Total amount of C in the Fh coprecipitates before and after 19 days aging.

Fh coprecipitates	total amount of C (wt%C) at pH 5.00		total amount of C (wt%C) at pH 6.5	
	Before aging	After aging	Before aging	After aging
Fh_Pen1/5_1.2wt%C	0.72 ± 0.00	0.72 ± 0.03	0.72 ± 0.08	0.75 ± 0.02
Fh_Hex2/6_4.5wt%C	4.06 ± 0.06	1.58 ± 0.09	3.09 ± 0.06	1.23 ± 0.05
Fh_Hex2/6_7.0wt%C	5.67 ± 0.06	1.76 ± 0.01	4.12 ± 0.02	1.55 ± 0.04
Fh_But3/7_6.0wt%C	5.73 ± 0.06	4.62 ± 0.03	5.79 ± 0.01	3.23 ± 0.25
Fh_But3/7_7.3wt%C	7.14 ± 0.17	4.93 ± 0.13	6.65 ± 0.02	3.00 ±0.22
Fh_But3/7_7.8wt%C	7.96 ± 0.67	5.48 ± 0.08	6.58 ± 0.15	3.05 ± 0.02

Table 4.2b. Total amount of non-desorbable C in the Fh coprecipitates before and after 19 days aging.

Fh coprecipitates	amount of non-desorbable C (wt%C) at pH 5.00		amount of non-desorbable C (wt%C) at pH 6.5	
	Before aging	After aging	Before aging	After aging
Fh_Pen1/5_1.2wt%C	0.62 ± 0.07	0.34 ± 0.02	0.61 ± 0.03	0.26 ± 0.05
Fh_Hex2/6_4.5wt%C	0.58 ± 0.02	0.30 ± 0.09	0.71 ± 0.08	0.25 ± 0.13
Fh_Hex2/6_7.0wt%C	0.68 ± 0.02	0.42 ± 0.03	0.66 ± 0.05	0.40 ± 0.07
Fh_But3/7_6.0wt%C	0.80 ± 0.10	0.69 ± 0.05	0.89 ± 0.02	0.64 ± 0.04
Fh_But3/7_7.3wt%C	0.79 ± 0.02	0.84 ± 0.00	0.83 ± 0.04	0.66 ± 0.05
Fh_But3/7_7.8wt%C	0.76 ± 0.05	0.70 ± 0.00	0.71 ± 0.01	0.82 ± 0.05

4.4 Discussion

4.4.1 Sequestration of carboxyl-rich OC with ferrihydrite prior to aging

4.4.1.1 Binding strength and distribution of carboxyl-rich OC with ferrihydrite coprecipitates

In agreement with previous work for the sequestration of carboxyl-rich OC with Fh during coprecipitation (Chen et al., 2014; Curti et al., 2021), a reduction in the amplitude and a broadening of the carboxyl peak for my Fh coprecipitates compared to their respective standards (Figure 4.1) indicates that these acids are sequestered to Fh via inner-sphere carboxyl ligand exchange, occurring between the OH of a carboxyl group and the OH of a mineral hydroxyl. Previous work also observes a shift of the carboxyl peak position to lower energy compared to the respective standards and an increasing magnitude of this shift (Figure 4.1), both in Fh coprecipitate systems with constant carboxyl-richness but decreasing OC sequestered (Chen et al., 2014), and in Fh coprecipitate systems with increasing carboxyl-richness and varying OC sequestered (Curti et al., 2021). In the former case the shift is attributed to an increasing number of carboxyl ligand exchange bonds per sequestered molecule with decreasing OC sequestered (Chen et al., 2014), while in the latter case, and thus in my work here, the shift is attributed to an increasing number of carboxyl ligand exchange bonds per sequestered molecule, that is independent of the amount of OC sequestered and is rather a function of the carboxyl-richness of the OC (Curti et al., 2021). As expected, my NEXAFS therefore confirm that the average number of carboxyl ligand exchange bonds between my carboxyl-rich OC and Fh during coprecipitation increases with increasing carboxyl-richness of the sequestered OC, and thus that the average binding strength of my carboxyl-rich OC increases in the order Pen1/5 < Hex2/6 < But3/7.

During coprecipitation of OC with Fh, OC can be sequestered via adsorption at particle surfaces and also incorporation into mineral particle interiors, for example by being occluded into mineral pore spaces (Eusterhues et al., 2011). In reality there is likely to be a continuum between OC that is adsorbed and OC that is incorporated, in which particle surfaces become saturated and multilayers of OC, macromolecular OC-Fe complexes and OC-Fe (oxyhydr)oxide nanoparticles form with OC occluded into the openings of and inside pores and aggregates (Chen et al., 2014; Lalonde et al., 2012; Lu et al., 2019b; Wagai and Mayer, 2007). My representative STXM image shows that C is apparently more concentrated at the particle edges (Figure S4). Because the particles are of varying thickness, the particle edges are likely to be thinner than the particle interiors. As such the STXM signal at these areas reflects C located mainly at the particle surfaces while the signal over the central area reflects C also incorporated throughout the bulk interior. A concentration of carbon at the edges, rather than a more uniform distribution over the whole particle thus indicates that C is mainly adsorbed at the particle surfaces, without substantial incorporation into the particle interiors (Curti et al., 2021) (see Supplementary Information for further discussion).

In addition to my STXM images, to provide a first order evaluation of the distribution of OC between particle surfaces and interiors, I estimate the surface coverage of my Fh coprecipitates nominally assuming all OC is adsorbed at particle surfaces in a monolayer, without multilayer OC-OC interactions at particle surfaces or incorporation into particle interiors (Table 4.3). I assume OC is adsorbed via either one (for Pen1/5, Hex2/6 and But3/7), two (for Hex2/6 and But3/7) or three carboxyl groups (for But3/7) per adsorbing molecule and that these adsorption complexes can form between OC and every FeOH site (i.e., there is no steric hindrance). I also adopt the SSA of pure Fh with an uncertainty of ±10% as representative of the SSA of Fh coprecipitated in the presence of OC (Eusterhues et al., 2008; Curti et al., 2021).

My estimations show that for my Fh_Pen1/5 (6.82±0.68%) and Fh_Hex2/6 coprecipitates (between 22.98±2.30% at the lowest C loading adopting entirely one-carboxyl adsorption and 75.72±7.57% at the highest C loading adopting entirely two-carboxyl adsorption) the amount of OC is significantly less than 100% surface coverage (Table 4.3). As such this OC could theoretically be adsorbed at Fh particle surfaces in a monolayer, without the need to invoke any extra sequestration capacity that might be provided by adsorption in multilayers and/or incorporation into particle interiors. For my Fh_But3/7 coprecipitates (between 27.62±2.76% at the lowest C loading adopting entirely one-carboxyl adsorption and 113.01±11.30% at the highest C loading adopting entirely three-carboxyl adsorption) the amount of OC is less than or approximately equal to 100% surface coverage (Table 4.3). As such the majority of this OC could theoretically be adsorbed at Fh particle surfaces in a monolayer, but a minor amount might need to be adsorbed in multilayers at particle surfaces and/or incorporated into particle interiors to account for the total C loading. Previous work on the coprecipitation of Pen1/5, Hex2/6 and But3/7 with Fh (Curti et al., 2021) and the coprecipitation of natural organic matter (NOM) with Fh also indicates that at C:Fe molar ratios below ~1, such as those in this study, most OC is adsorbed at the particle surfaces in a monolayer (or patchy 'monolayer equivalent' (Mayer, 1999)), without substantial adsorption in multilayers and/or incorporation into particle interiors (Chen et al., 2014; Curti et al., 2021; Eusterhues et al., 2005; Eusterhues et al., 2008). Taken together my representative STXM image and theoretical estimations indicate that OC in my Fh coprecipitates prior to aging is distributed as an adsorbed monolayer (or 'monolayer equivalent') at particle surfaces.

Table 4.3. Surface coverage of Fh coprecipitates by adsorbed C

	Dry weight (g)	SSA (m^2/g)[a]	Site density ($sites/nm^2$)[b]	Number of surface sites (mmol sites)
Pure ferrihydrite	0.10	300		
$\equiv FeOH^{-0.5(e)}$ sites			2.5	0.125
$\equiv FeOH^{-0.5(c)}$ sites			3.7	0.174
Total amount				0.299

Fh coprecipitates	Organic wt%	Mineral wt%	Total surface sites of Fh (mmol)[c]	Total amount of C (mmol)	Coverage of Fh with one carboxyl adsorbed	Coverage of Fh with two carboxyl adsorbed	Coverage of Fh with three carboxyl adsorbed
Fh_Pen1/5 _1.2wt%C	2.04	97.96	0.2929 ± 0.0293	0.0200	6.82 ± 0.68		
Fh_Hex2/6_4.5wt%C	9.12	90.88	0.2717 ± 0.0272	0.0624	22.98 ± 2.30	45.96 ± 4.60	
Fh_Hex2/6_7.0wt%C	14.18	85.82	0.2566 ± 0.0257	0.0971	37.86 ± 3.79	75.72 ± 7.57	
Fh_But3/7_6.0wt%C	13.58	86.44	0.2585 ± 0.0259	0.0714	27.62 ± 2.76	55.23 ± 5.52	82.84 ± 8.28
Fh_But3/7_7.3wt%C	16.50	83.50	0.2497 ± 0.0250	0.0868	34.76 ± 3.47	69.56 ± 6.96	104.34 ± 10.43
Fh_But3/7_7.8wt%C	17.63	82.37	0.2463 ± 0.0246	0.0928	37.68 ± 3.77	75.34 ± 7.53	113.01 ± 11.3

[a] SSA of pure Fh measured after synthesis

[b] fixed at those calculated by Moon and Peacock (2013).

[c] estimated using the surface site density of pure ferrihydrite and the weight mass ratio of the mineral end-member in each coprecipitate; an uncertainty of ±10% on the SSA of pure Fh is assumed in order to take account of the differences in SSA of pure Fh compared to Fh coprecipitates (Eusterhues et al., 2008).

4.4.1.2 Binding affinity of carboxyl-rich OC with ferrihydrite

Based on my STXM NEXAFS showing that OC is sequestered to Fh coprecipitates via inner-sphere carboxyl ligand exchange complexes and that these are adsorbed at the particle surfaces, I can quantify the binding affinity of these complexes by conducting adsorption experiments and fitting these to a thermodynamic surface complexation model. Based on my STXM NEXAFS for Pen1/5 I invoke the formation of inner-sphere carboxyl ligand exchange complexes that adsorb via one-carboxyl adsorption (Figure 4.6a) in either a single-bonded (to one FeOH site) (reaction 1) or twice-bonded (to two FeOH sites) (reaction 2) configuration. Inner-sphere one-carboxyl adsorption is consistent with previous NEXAFS for adsorption of Pen1/5 to Fh (Curti et al., 2021) and attenuated total reflectance (ATR) spectroscopy for adsorption of other mono-carboxylic acids to metal oxides (Dobson and McQuillan, 1999):

$$\equiv \mathrm{FeOH}^{-0.5}_{(c/e)} + \mathrm{R\text{-}COO}^{-} + \mathrm{H}^{+} = \equiv(\mathrm{FeOOC})\text{-}\mathrm{R}^{-0.5} + \mathrm{H_2O} \qquad (1)$$

$$2\equiv \mathrm{FeOH}^{-0.5}_{(c/e)} + \mathrm{R\text{-}COO}^{-} + 2\mathrm{H}^{+} = \equiv(\mathrm{FeO})_2\mathrm{C\text{-}R} + 2\mathrm{H_2O} \qquad (2)$$

Based on my STXM NEXAFS for Hex2/6 I invoke the formation of inner-sphere carboxyl ligand exchange complexes that adsorb via two-carboxyl adsorption (Figure 4.6b), using two FeOH sites in a bidentate mononuclear or bidentate binuclear configuration, respectively (Curti et al., 2021) (both represented by reaction 3). Inner-sphere two-carboxyl adsorption is consistent with previous NEXAFS for adsorption of Hex2/6 and other di-carboxylic acids to Fh (Curti et al., 2021) and previous ATR spectroscopy for adsorption of Hex2/6 and other di-carboxylic acids to metal oxides (Dobson and McQuillan, 1999). Previous ATR spectroscopy for Hex2/6 adsorption to Hm (Duckworth and Martin, 2001) however, suggests that Hex2/6 might adsorb to Fe (oxyhydr)oxides via inner-sphere one-carboxyl adsorption using one FeOH site in a monodentate mononuclear configuration (Figure 4.6a), possibly because of the steric constraint on the formation of a bidentate structure (reaction 4):

$$2\equiv FeOH^{-0.5}{}_{(c/e)} + R\text{-}2COO^{-2} + 2H^{+} = \equiv (FeOOC)_2\text{-}R^{-1} + 2H_2O \quad (3)$$

$$\equiv FeOH^{-0.5}{}_{(c/e)} + R\text{-}2COO^{-2} + H^{+} = \equiv(FeOOC)\text{-}R\text{-}COO^{-1.5} + H_2O \quad (4)$$

Based on my STXM NEXAFS for But3/7 I invoke the formation of inner-sphere carboxyl ligand exchange complexes that adsorb via three-carboxyl adsorption, in a tridentate trinuclear configuration (Figure 4.6c) (reaction 5). Inner-sphere three-carboxyl adsorption is consistent with previous NEXFAS work for adsorption of But3/7, propanetricarboxylic and ethanetricarboxylic acid to Fh (Curti et al., 2021) and infrared spectroscopy for adsorption of other tricarboxylic acids to Fh and Gt (Cornell and Schindler, 1980). Previous Fourier transform infra-red (FTIR) spectroscopy for propanetricarboxylic acid adsorption to Gt (Lindegren et al., 2009) however, suggests that But3/7 might adsorb to Fe (oxyhydr)oxides via inner-sphere two-carboxyl adsorption, possibly in a bidentate mononuclear chelate configuration (Figure 4.6b) (reaction 6, which also represents a bidentate binuclear configuration):

$$3\equiv FeOH^{-0.5}{}_{(c/e)} + R\text{-}3COO^{-3} + 3H^{+} = \equiv (FeOOC)_3\text{-}R^{-1.5} + 3H_2O \quad (5)$$

$$2\equiv FeOH^{-0.5}{}_{(c/e)} + R\text{-}3COO^{-3} + 2H^{+} = \equiv (FeOOC)_2\text{-}R\text{-}COO^{-2} + 2H_2O \quad (6)$$

For surface reaction, it is important to describe how electrostatic potential at the mineral-water interface changes as a function of surface loading and pH. As such it is key to distribute the charge of a sorbed species between 0-plane and 1-plane in Basic Stern Model. In BSM, 0–plane is the surface plane where H ions are adsorbed and 1-plane is a hypothetic electrostatic plane where the inner-sphere adsorbed complex are located within the Stern layer region. The surface charge difference of 0-plane and 1-plane after forming complexes are represented as Δz_0 and Δz_1. Before the reaction, charge distribution of ferrihydrite surface are: z_0=-0.5, z_1=0 for species $\equiv FeOH^{-0.5}$. For one carboxyl single bonded and assuming the symmetric distribution of over the two C-O bonds, Pauling bond valence of C-O bond υ=z/CN = 3/2 = 1.5, and Pauling bond valence of Fe-O bond υ=z/CN = 3/6 = 0.5 (Rietra et al., 1999). As thus for reaction 1, the net charge of 0-plane (z_0') is +0.5(Fe-O) - 2(O) +1.5(C-O) = 0, while the net charge of 1-plane (z_1') is -2(O) + 1.5 (C-O) = -0.5. Therefore the charge difference of each carboxyl bonded at the 0-plane and 1-plane are $\Delta z_0 = z_0' - z_0 = +0.5$ and $\Delta z_1 = z_1' - z_1 = -0.5$, which are applied to get best fit for Pen1/5 and Hex2/6 adsorption (Table 4.4 and Figure 4.7). While the best fit for But3/7 acid is achieved with adjustment of the surface charge distribution (Δz_0 =+0.65 and Δz_1 =-0.15 for each carboxyl bonded) to take into account its larger molecular weight and more diffuse charge distribution.

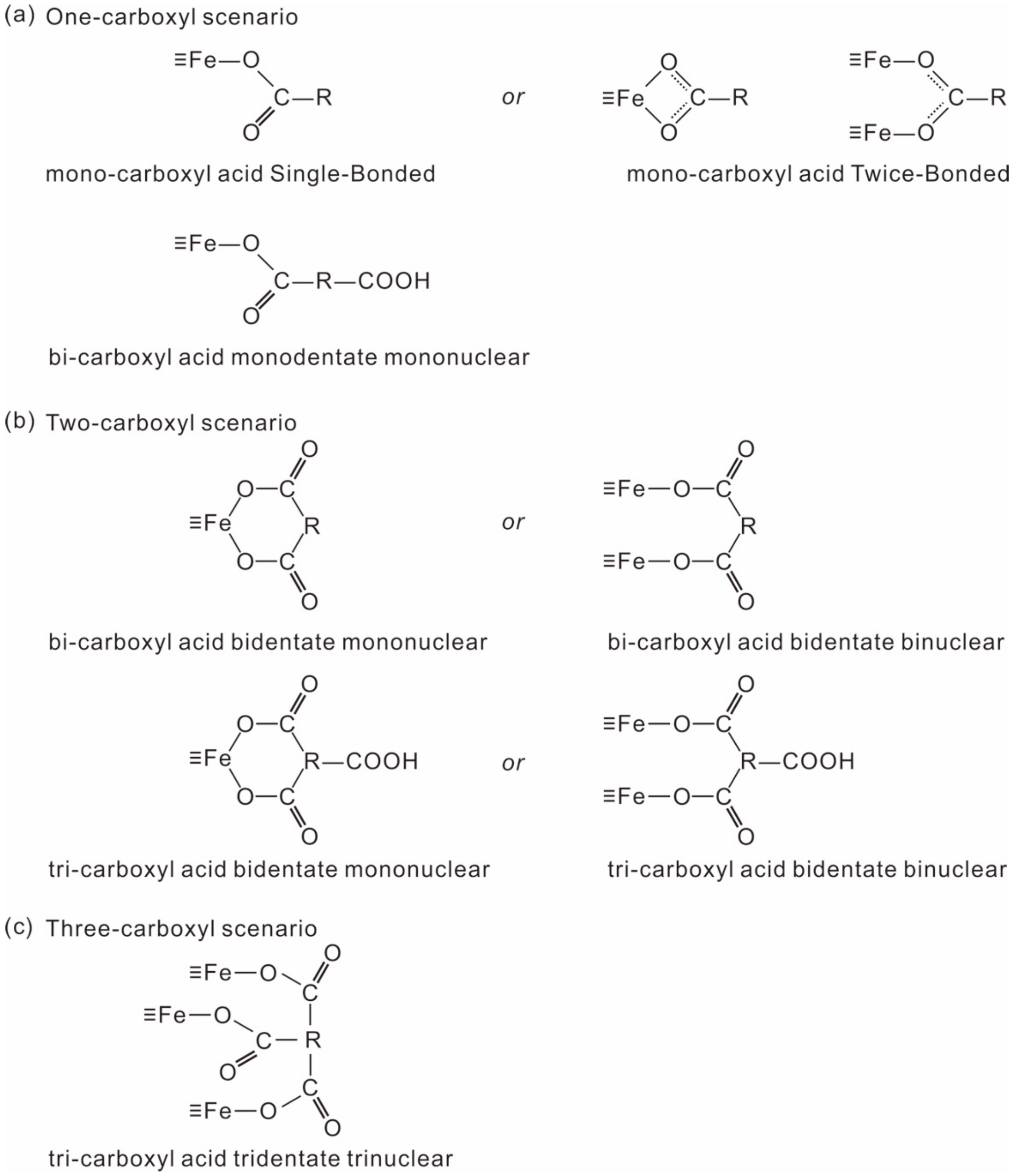

Figure 4.6. Possible adsorption configurations of carboxylic acids adsorbed to Fe (oxyhydr)oxides from spectroscopic evidence: a) One-carboxyl adsorption in which mono-carboxylic acids adsorb via their one carboxyl group in either a single-bonded or twice-bonded configuration, and di-carboxylic acids adsorb via one carboxyl group which binds to one FeOH site in a monodentate mononuclear configuration; b) Two-carboxyl adsorption in which di- and tri-carboxylic acids adsorb using two carboxyl groups which bind to either one FeOH site in a bidentate mononuclear configuration or two FeOH sites in a bidentate binuclear configuration; and c) Three-carboxyl adsorption in which tri-carboxylic acids adsorb using three carboxyl groups in a tridentate trinuclear configuration.

My model is consistent with the bonding environment and distribution of OC as indicated by my STXM NEXAFS results. Previous spectroscopic work on the sequestration of carboxylic acids and carboxylic-rich OC to Fe (oxyhydr)oxides invokes both inner-sphere and outer-sphere complexation, in which inner-sphere complexation can be favoured at low pH and outer-sphere complexation can be favoured at basic pH (Han et al., 2020a). Dampening, broadening and shifts in a spectroscopically identified carboxyl peak however, are the result of inner-sphere coordination between the carboxyl group and a sequestered moiety which alters the absorbance signature of the carboxyl peak (Chen et al., 2014; Duckworth and Martin, 2001), and since these features are common to all my spectra, I attribute my OC sequestration to inner-sphere complexation. I cannot rule out the minor presence of outer-sphere complexes, which would cause only minor or unresolvable changes to the peak features.

For Pen1/5, Hex2/6 and But3/7 I fit each possible surface complexation reaction to the adsorption data individually and in combination with other possible reactions for that carboxylic acid, and consider each reaction with protonated and deprotonated non-bonded carboxyl group(s). The best fitting combination of surface complexation reactions for each carboxylic acid are listed in Table 4.4 and shown on the adsorption data in Figure 4.7.

Table 4.4. Input parameters for the surface complexation model for adsorption of carboxylic acids on pure Fh

		Pure Fh				
Specific surface area (m^2/g)		300[a]				
Site density $\equiv FeOH_e^{-0.5}$ (mol sites/g $\times 10^{-3}$)		1.25[b]				
Site density $\equiv FeOH_c^{-0.5}$ (mol sites/g $\times 10^{-3}$)		1.74[b]				
Site density $\equiv Fe_3O^{-0.5}$ (mol sites/g $\times 10^{-3}$)		0.598[b]				
C_{stern} (F/m^2)		1.10[b]				
Log $K_{FeOH(c)}$	$\equiv FeOH^{-0.5}{}_{(c)} + H^+ = \equiv FeOH_2^{+0.5}{}_{(c)}$	7.99[b]				
Log $K_{FeOH(c)\_Na}$	$\equiv FeOH^{-0.5}{}_{(c)} + Na^+ = \equiv FeOH^{-0.5}{}_{(c)}\text{-}Na^+$	-1.00[b]				
Log $K_{FeOH2(c)\_NO3}$	$\equiv FeOH_2^{+0.5}{}_{(c)} + NO_3^- = \equiv FeOH_2^{+0.5}{}_{(c)}\text{-}NO_3^-$	-1.00[b]				
(where equations above are repeated for ($\equiv FeOH^{-0.5}{}_{(e)}$))						
Log K_{Fe3O}	$\equiv Fe_3O^{-0.5} + H^+ = \equiv Fe_3OH^{+0.5}$	7.99[b]				
Log K_{Fe3O_Na}	$\equiv Fe_3O^{-0.5} + Na^+ = \equiv Fe_3O^{-0.5}\text{-}Na^+$	-1.00[b]				
Log K_{Fe3OH_NO3}	$\equiv Fe_3OH^{+0.5} + NO_3^- = \equiv Fe_3OH^{+0.5}\text{-}NO_3^-$	-1.00[b]				
				pKa_1	pKa_2	pKa_3
Pentanoic acid (Pen1/5)				4.84[c]		
Hexanedioic acid (Hex2/6)				4.42[c]	5.41[c]	
Butane 1, 2, 4 tricarboxylic acid (But3/7)				4.31[d]	4.82[d]	5.21[d]
		Δz_0	Δz_1	Pen1/5	Hex2/6	But3/7
1. Log $K_{FeOH(c/e)\_OOC\text{-}R}$	$\equiv FeOH^{-0.5}{}_{(c/e)} + R\text{-}COO^- + H^+ = \equiv(FeOOC)\text{-}R^{-0.5} + H_2O$	+0.5[e]	-0.5[e]	9.2[e]		
3. Log $K_{FeOH(c/e)\_OOC\text{-}R}$	$2\equiv FeOH^{-0.5}{}_{(c/e)} + R\text{-}2COO^{-2} + 2H^+ = \equiv (FeOOC)_2\text{-}R^{-1} + 2H_2O$	+1.0[e]	-1.0[e]		16.8[e]	
4a. Log $K_{FeOH(c/e)\_OOC\text{-}R}$	$\equiv FeOH^{-0.5}{}_{(c/e)} + R\text{-}2COO^{-2} + H^+ = \equiv(FeOOC)\text{-}R\text{-}COO^{-1.5} + H_2O$	+0.5[e]	-0.5[e]		10.5[e]	
4b. Log $K_{FeOH(c/e)\_OOC\text{-}R}$	$\equiv FeOH^{-0.5}{}_{(c/e)} + R\text{-}2COO^{-2} + 2H^+ = \equiv(FeOOC)\text{-}R\text{-}COOH^{-0.5} + 2H_2O$	+0.5[e]	-0.5[e]		15.4[e]	
5. Log $K_{FeOH(c/e)\_OOC\text{-}R}$	$3\equiv FeOH^{-0.5}{}_{(c/e)} + R\text{-}3COO^{-3} + 3H^+ = \equiv (FeOOC)_3\text{-}R^{-1.5} + 3H_2O$	+1.3[e]	-0.3[e]			26.3[e]
6a. Log $K_{FeOH(c/e)\_OOC\text{-}R}$	$2\equiv FeOH^{-0.5}{}_{(c/e)} + R\text{-}3COO^{-3} + 2H^+ = \equiv (FeOOC)_2\text{-}R\text{-}COO^{-2} + 2H_2O$	+1.3[e]	-0.3[e]			19.0[e]
6b. Log $K_{FeOH(c/e)\_OOC\text{-}R}$	$2\equiv FeOH^{-0.5}{}_{(c/e)} + R\text{-}3COO^{-3} + 3H^+ = \equiv (FeOOC)_2\text{-}R\text{-}COOH^{-1} + 2H_2O$	+1.95[e]	-0.45[e]			23.3[e]

[a] measured in this study;

[b] from Moon and Peacock (2013);

[c] from Dean (1987);

[d] calculated using ACD/I-Lab 2.0 (ACD/I-Lab, version 2.0, Advanced Chemistry Development, Inc);

[e] fit in this study.

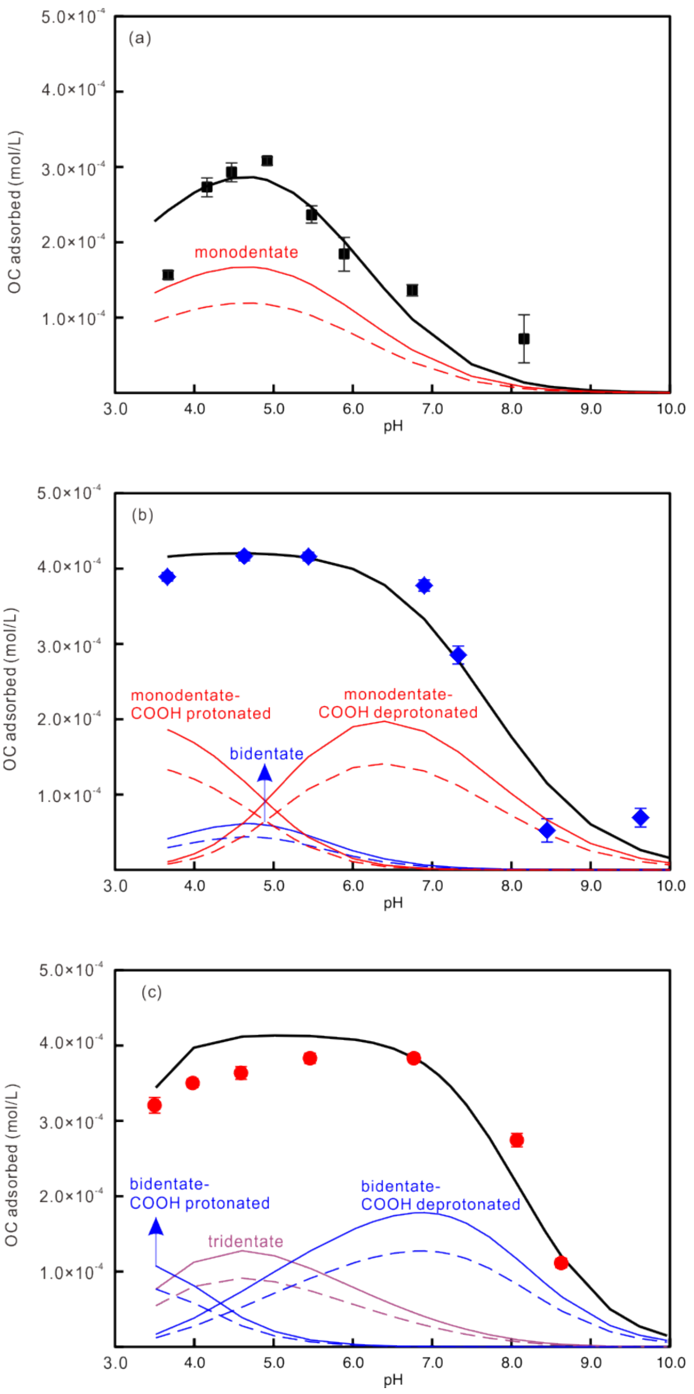

Figure 4.7. Surface species for: a) Pen1/5, b) Hex2/6 and c) But3/7 as function of pH based on complexation model fits (lines) to adsorption data (symbols). Black, blue and red symbols represent Pen1/5, Hex2/6 and But3/7 data, respectively. Monodentate (red lines), bidentate (blue lines) and tridentate (purple lines) represent one, two and three carboxyl binding, respectively, via corner sharing complexation (solid red, blue, purple lines) and edge-sharing complexation (dashed red, blue, purple lines). The black solid lines are the sum of the modelled species, representing the total amount of OC adsorbed.

Pen1/5, Hex2/6 and But3/7 represent simple carboxyl-rich OC with one, two and three carboxyl groups, respectively. Error bars represent standard deviations of at least duplicate samples.

For Pen1/5 the model fits suggest one-carboxyl adsorption occurring on both FeOH edge and corner sites (Figure 4.7a) in a single-bonded monodentate configuration (reaction 1; Figure 4.6a) with a binding constant of Log K 9.2 (Table 4.4). For Hex2/6 the model fits suggest a combination of both two-carboxyl and one-carboxyl adsorption occurring on both FeOH edge and corner sites (Figure 4.7b). The two-carboxyl adsorption occurs in a bidentate mononuclear or bidentate binuclear configuration (reaction 3; Figure 4.6b) with a binding constant of Log K 16.8 (Table 4.4). The one-carboxyl adsorption occurs in a monodentate mononuclear configuration (reaction 4; Figure 4.6a), in which the non-bonding carboxyl group is protonated at low pH (< pH~5.0) with a binding constant of Log K 10.5 (Table 4.4) and deprotonated at higher pH (> pH~5.0) with a binding constant of Log K 15.4 (Table 4.4). Finally for But3/7 the model fits suggest a combination of both three-carboxyl and two-carboxyl adsorption occurring on both FeOH edge and corner sites (Figure 4.7c). The three-carboxyl adsorption occurs in a tridentate trinuclear configuration (reaction 5, Figure 4.6c) with a binding constant of Log K 26.3 (Table 4.4). The two-carboxyl adsorption occurs in a bidentate mononuclear or bidentate binuclear configuration (reaction 6; Figure 4.6b), in which the non-bonding carboxyl group is protonated at low pH (< pH~4.5) with a binding constant of Log K 19.0 (Table 4.4) and deprotonated at higher pH (> pH~4.5) with a binding constant of Log K 23.3 (Table 4.4). Differences in the binding constants for complexes in which the non-bonded carboxyl group is either deprotonated or protonated (one-carboxyl adsorption for Hex2/6 Log K 10.5/15.4 and two-carboxyl adsorption for But3/7 Log K 19.0/23.3) arise because the complexation reaction for the protonated complex (reaction 4b for Hex2/6 and reaction 6b for But3/7, Table 4.4) combines the complexation reaction (one or two carboxyls reacting with FeOH) with the protonation reaction of the non-bonded carboxyl group.

My modelling thus predicts an overall increase in the average number of bonds per sequestered acid molecule and an overall increase in the binding affinity of the sequestered acid molecules in the order Pen1/5 < Hex2/6 < But3/7. The increasing binding affinity of my carboxylic acids explains the macroscopic adsorption behaviour of these acids with Fh, in which adsorption affinity increases in the order Pen1/5 < Hex2/6 ~ But3/7 (Figure 4.2). Overall my STXM NEXAFS and model fitting results indicate that the average number of bonds per sequestered acid molecule and thus the binding strength of carboxylic acids to Fe (oxyhydr)oxides increases with increasing carboxyl-richness (Curti et al., 2021).

4.4.2 Influence of carboxyl-rich OC on the aging of ferrihydrite

4.4.2.1 Kinetics of Fh aging influenced by carboxyl-rich OC

My experiments show that the presence of OC retards the aging of Fh to more crystalline Fe minerals (Figure 4.3a and 4.3b), which is consistent with previous reports that additives of carboxylic acids, humic acids and other kinds of OC can retard the aging of Fh to crystalline iron minerals (Cornell and Schwertmann, 1979b; Cornell, 1985; Hu et al., 2018; Lu et al., 2019b). In oxic environments, two different mechanisms may occur during aging of Fh to more crystalline iron minerals, where one is via dissolution-recrystallisation processes and the other is via solid-state aggregation: aggregation of Fh followed by nucleation and crystal growth within the aggregate (Cornell and Schwertmann, 1979b; Cudennec and Lecerf, 2006; Schwertmann and Fischer, 1966). The presence of OC can influence the factors that control dissolution-recrystallisation and/or solid-state aggregation and thus can effect aging rate, for example, OC can block surface sites and subsequently prevent the dissolution of iron (oxyhydr)oxide to form goethite or the nucleation of hematite (Kaiser and Guggenberger, 2003); OC can complex with aqueous Fe(III) to inhibit nucleation (Cornell and Schwertmann, 1979b); and OC can influence Fh aggregation and associate with the surface of neoformed mineral nuclei and crystals to inhibit crystal growth (Amstaetter et al., 2012; Eusterhues et al., 2008).

For the aging of my Fh coprecipitates compared to pure Fh, it is clear that the retardation effect of OC generally increases in the order Pen1/5 < Hex2/6 < But3/7 (at pH 5) and Pen1/5 < Hex2/6 ~ But3/7 (at pH 6.5) and thus with increasing carboxylic acid binding strength (Figure 4.3a and 4.3b). Previous work reports the influence of aqueous (hydroxyl)-carboxylic acids on the aging of Fh to other more crystalline Fe minerals, where the retardation of aging is also related to the relative adsorption affinity of the acids to Fh (Cornell and Schwertmann, 1979). For Fh coprecipitates made with different OC types but with similar C loadings, my surface complexation modelling indicates that the number of chemical bonds formed between the OC and Fh particles is equal to the number of –FeOH sites used, and both the number of bonds formed and the sites used increase with the carboxyl-richness, where the former controls the binding strength (Friddle et al., 2012) and the later influences the surface coverage. Therefore both the binding strength and surface coverage for a similar adsorbed amount of my different carboxylic acids follow the order Pen1/5 < Hex2/6 < But3/7. As such there is a greater blocking of Fh surface sites and thus a greater retardation of dissolution and recrystallisation in the order Pen1/5 < Hex2/6 < But3/7 (Kaiser and Guggenberger, 2003).

It is also clear that the retardation effect of OC is related to increasing C loading and pH. In general as C loading increases at pH 5 the retardation of aging increases from Fh-Pen1/5_1.2wt%C to Fh_But3/7_7.8wt%C, but individual coprecipitates Fh_Hex2/6_2.9wt%C, Fh_Hex2/6_4.1wt%C and Fh_But3/7_6.0wt%C show similar behaviour (Figure 4.3a). As C loading increases at pH 6.5 however, the retardation of aging increases from Fh-Pen1/5_1.2wt%C to Fh_But3/7_7.8wt%C, but individual Fh_Hex2/6 and Fh_But3/7 coprecipitates all show similar behaviour (Figure 4.3b). Furthermore at pH 6.5, whilst the retardation of aging for the Fh_Pen1/5 and Fh_Hex2/6 coprecipitates is similar to that at pH 5, the retardation of aging for the Fh_But3/7 coprecipitates is reduced (comparing Figures 4.5a and 4.5b). The effect of C loading on retardation of aging may be explained by considering the fact that, because my acids are mostly adsorbed at particle surfaces (Curti et al., 2021), increased C loading results in higher surface coverage and thus a greater retardation of dissolution and recrystallisation (Kaiser and Guggenberger, 2003). Increased C loading can also lead to a greater retardation of aging through the complexation of OC with aqueous Fe(III) to inhibit nucleation (Cornell and Schwertmann, 1979b) and the association of OC with the surface of newly formed mineral nuclei and crystals to inhibit crystal growth (Amstaetter et al., 2012; Eusterhues et al., 2008). For individual coprecipitates Fh_Hex2/6_2.9wt%C and Fh_Hex2/6_4.1wt%C, made with the same OC type but increasing C loading, it appears that the C loading effect cannot indefinitely increase retardation. I suppose that there is maximum retardation effect for simple carboxyl-rich OC, but this requires further investigation.

The OC retardation of aging are weakened at higher pH, where the higher C loading and the higher carboxyl richness in OC moieties (for Fh_Hex2/6 and _But3/7 system) seem not to have indefinitely retardation effect on aging of Fh. This weakening influence of pH on OC retardation of aging may be explained by the fact that under acidic conditions (pH < 7) Fh ages via dissolution-recrystallisation, whereas under neutral conditions (pH ~ 7) Fh ages mainly via solid-state aggregation: aggregation of Fh followed by nucleation and crystal growth within the aggregate (Cornell and Schwertmann, 1979b; Cudennec and Lecerf, 2006; Schwertmann and Fischer, 1966). During dissolution-recrystallisation processes, OC can block surface sites to directly retard the aging process, but during solid-state aggregation this retardation mechanism may be less effective and instead OC might associate with mineral nuclei and newly formed crystals to inhibit oriented aggregation of pure mineral clusters and crystal growth of more crystalline minerals (Amstaetter et al., 2012; Eusterhues et al., 2008). In addition OC may act as a bridging molecule between mineral particles and then stabilise them as low-density aggregates (Amstaetter et al., 2012; Illés and Tombácz, 2006). These more indirect mechanisms for retardation of aging may account for the similarity in the retardation of individual Fh_Hex2/6 and Fh_But3/7 coprecipitates at pH 6.5, and the reduction in retardation of Fh_But3/7 coprecipitates at pH 6.5 compared to pH 5. Furthermore, whilst adsorption of negatively charged OC onto positively charged Fe minerals creates negatively charged OC-coated particles that repel one another and hinder aggregation (Illés and Tombácz, 2006), recent work shows that OC with MW<3 kDa is unable to completely stabilise mineral particles via steric repulsion (Li et al., 2020). This may also contribute to the reduction in retardation of Fh_But3/7 coprecipitates at pH 6.5 compared to pH 5, and again suggests that increasing C loading of simple organic molecules may not result in increased retardation of aging, although this requires further investigation.

4.4.2.2 Properties of Fh coprecipitates after aging influenced by carboxyl-rich OC

My results show that the SSA of the Fe minerals after aging of pure Fh (33±0.1 m^2/g) are significantly less that the SSA of un-aged pure Fh (300 m^2/g), and that the Fe minerals after aging of Fh coprecipitates (46±0.1 – 103±0.9 m^2/g) are also significantly less than the SSA of un-aged Fh coprecipitates (taken as 300 m^2/g with an uncertainty of ±10%) (Table 4.1). In agreement with previous work, it is clear that in both the pure Fh and Fh coprecipitate systems, the Fe minerals present after aging have significantly reduced SSA and thus larger particle size and/or higher crystallinity (Das et al., 2011b; Hu et al., 2018), but it is also apparent that the influence of OC in the Fh coprecipitate systems somewhat mitigates against the decline in SSA. This is likely because OC retards the aging of Fh to more crystalline minerals and inhibits mineral crystal growth (Cornell and Schwertmann, 1979b; Kaiser and Guggenberger, 2003). Thus compared to pure Fh systems, this results in Fe minerals with smaller particle size and/or lower crystallinity, larger lattice spacings and a more porous surface structure and thus a less compact bulk mineral (Eusterhues et al., 2008), as confirmed by scanning transmission electron microscopy (STEM) observations (Lu et al., 2019b).

My results also show that the SSA and TPV of my Fe minerals after aging of Fh coprecipitates increase with increasing carboxylic acid binding strength (Table 4.1), and thus follow the order Fh < Fh_Pen1/5_1.2wt%C < Fh_Hex2/6_7.0wt%C < Fh_But3/7_7.3wt%C. In particular, comparing composites with similar C loading but increased binding strength, namely Fh_Hex2/6_7.0wt%C and Fh_But3/7_7.3wt%C, the latter has significantly higher SSA. Thus whilst the retardation of aging for Fh_Hex2/6_7.0wt%C and Fh_But3/7_7.3wt%C is similar, the more strongly bound But3/7 appears to be able to further inhibit the growth of more crystalline Fe minerals, leading to smaller particle size and/or lower crystallinity and a more porous structure.

4.4.3 Distribution of carboxyl-rich OC during aging of ferrihydrite

4.4.3.1 Mechanisms for temporal changes in the total amount of C

My experiments show that the total amount of C with my Fh_Pen1/5_1.2wt%C coprecipitate is essentially invariant with aging time at pH 5 and 6.5, whilst the total amount of C with my Fh_Hex2/6 and Fh_But3/7 coprecipitates decreases with aging time at pH 5 and 6.5 (Figure 4.4a and 4.4b). These trends may be understood by considering the binding strength of the OC and the properties of Fe minerals after aging of Fh.

Given the SSA of Fe minerals formed after aging of Fh coprecipitates (Table 4.1) I can estimate their surface coverage at the end of aging (after 19 days) following the same approach used to estimate the surface coverage of the initial Fh coprecipitates above (section 4.1.1). My estimations show that the aged Fh_Pen1/5_1.2wt%C still appears to have sufficient SSA (Table 4.5) to theoretically accommodate all the initial OC in an adsorbed monolayer at the particle surfaces (surface coverage 37.37%, Table 4.5a) and a total theoretical adsorption capacity (3.04 wt%C, Table 4.5b) that is well in excess of both the total initial amount of C (1.2 wt%C) and the total remaining amount of C (0.72 – 0.75wt%, Table 4.5b). This might explain why the total remaining amount of C for Fh_Pen1/5_1.2wt%C is essentially invariant with aging time (Figure 4.4a and 4.4b), and implies that both the total initial amount of C and the total remaining amount of C could be adsorbed at the particle surfaces.

The aged Fh_Hex2/6_7.0wt%C appears to have insufficient SSA (Table 4.5) to theoretically accommodate all the initial OC in an adsorbed monolayer at the particle surfaces (surface coverage between 130.58% adopting entirely monodentate adsorption and 261.15% adopting entirely bidentate adsorption, Table 4.5a) and a total theoretical adsorption capacity (between 2.54 wt%C adopting entirely bidentate adsorption and 4.84 wt%C adopting entirely monodentate adsorption, Table 4.5b) that is well below the total initial amount of C (7.0 wt%C) but still in excess of the total remaining amount of C (1.55 – 1.76 wt%C, Table 4.5b). This might explain why the total remaining amount of C for the Fh_Hex2/6 coprecipitates decreases with aging time (Figure 4.4a and 4.4b), but akin to Fh_Pen1/5_1.2wt%C, implies that both the total initial amount of C and the total remaining amount of C are adsorbed at the particle surfaces.

In contrast the aged Fh_But3/7_7.3wt%C appears to have insufficient SSA (Table 4.5) to theoretically accommodate all the initial OC in an adsorbed monolayer at the particle surfaces (surface coverage between 145.05% adopting entirely bidentate adsorption and 217.57% adopting entirely tridentate adsorption, Table 4.5a) and a total theoretical adsorption capacity (between 3.12 wt%C adopting entirely tridentate adsorption and 4.52 wt%C adopting entirely bidentate adsorption, Table 4.5b) that is well below the total initial amount of C (7.3 wt%C) but not in excess of the total remaining amount of C (3.00 – 4.90 wt%C, Table 4.5b). This might explain why the total remaining amount of C for the Fh_But3/7 coprecipitates decreases with aging time (Figure 4.4a and 4.4b), but unlike Fh_Pen1/5_1.2wt%C and the Fh_Hex2/6 coprecipitates, implies that, whilst the total initial amount of C is adsorbed at the particle surfaces, some part of the total remaining amount of C might be incorporated into the particle interiors.

These estimations therefore indicate that the amount of OC retained by Fh coprecipitates during the aging process is strongly coupled to the binding strength of the OC molecules and the initial C loading of the coprecipitates. For Fh coprecipitated with relatively carboxyl-poor OC and with low initial C loading such as Fh_Pen1/5_1.2wt%C, I suggest that net OC release is essentially minimal during aging because the Fe minerals formed after aging have sufficient adsorption capacity to accommodate all the initial OC at the particle surfaces. For Fh coprecipitated with relatively carboxyl-rich OC and with higher but essentially equivalent initial C loading such as Fh_Hex2/6_7.0wt%C and Fh_But3/7_7.3wt%C, I suggest that net OC release is significant during aging because the Fe minerals formed after aging have insufficient adsorption capacity to accommodate all the initial OC at the particle surfaces. For these relatively carboxyl-rich coprecipitates my results suggest that the distribution of the remaining OC between the mineral surfaces vs. incorporation into particle interiors is strongly influenced by the binding strength of the OC because this controls both the initial C loading of the coprecipitates and the physiochemical properties of the Fe minerals after aging.

Table 4.5a. Surface coverage of Fe minerals for Fh_Pen1/5_1.2wt%C, Fh_Hex2/6_7.0wt%C and Fh_But3/7_7.3wt%C after 19 days aging at pH 6.5

	Total initial C with Fh (wt%C)	SSA of Fe minerals after 19 days aging (m^2/g)[a]	Site density of Fe minerals after 19 days aging (sites/nm^2)[b]	Coverage of Fe minerals after 19 days aging with one carboxyl adsorbed	Coverage of Fe minerals after 19 days aging with two carboxyl adsorbed	Coverage of Fe minerals after 19 days aging with three carboxyl adsorbed
Fh_Pen1/5 _1.2wt%C	1.2 wt%C	46	7	37.37		
Fh_Hex2/6_7.0wt%C	7.0 wt%C	64	7	130.58	261.15	
Fh_But3/7_7.3wt%C	7.3 wt%C	103	7		145.05	217.57

Table 4.5b. Adsorption capacity of Fe minerals for Fh_Pen1/5_1.2wt%C, Fh_Hex2/6_7.0wt%C and Fh_But3/7_7.3wt%C after 19 days aging

	SSA of Fe minerals after 19 days aging (m^2/g)[a]	Site density of Fe minerals after 19 days aging (sites/nm^2)[b]	Adsorption capacity of Fe minerals after 19 days aging (one carboxyl binding)	Adsorption capacity of Fe minerals after 19 days aging (two carboxyl binding)	Adsorption capacity of Fe minerals after 19 days aging (three carboxyl binding)	Total remaining C with Fe minera measured after 19 days aging	
						pH 5.0	pH 6.5
Fh_Pen1/5 _1.2wt%C	46	7	3.04wt%C			0.72 wt%C	0.75 wt%C
Fh_Hex2/6_7.0wt%C	64	7	4.84wt%C	2.54wt%C		1.76 wt%C	1.55 wt%C
Fh_But3/7_7.3wt%C	103	7		4.52wt%C	3.12wt%C	4.90 wt%C	3.00 wt%C

[a] SSA of Fe minerals treated with 0.1 M NaOH for 24 h to desorb OC after aging for 19 days at pH 6.5

[b] Site density for Fe minerals calculated from average site density of Gt and Hm (Peacock and Sherman, 2004)

4.4.3.2 Mechanisms for temporal changes in non-desorbable C

We can shed further light on the distribution of the OC during aging as a function of the binding strength of the OC molecules and C loading of the coprecipitates by considering my results for non-desorbable C. In my work I operationally define non-desorbable C as C that cannot be removed from the solid particles with 0.1 M NaOH (Kaiser and Guggenberger, 2007). Previous work on the coprecipitation of Pen1/5, Hex2/6 and But3/7 with Fh using the same experimental coprecipitation conditions as used here (Curti et al., 2021) shows that at C:Fe molar ratios ~0.1 – 0.8, equivalent to those used in this study, between ~10 – 30% of OC adsorbed in a monolayer at the Fh particle surfaces remains adsorbed after washing with 0.1 M NaOH and is thus very strongly adsorbed at particle surfaces or is incorporated into particle interiors, for example by being occluded into mineral pore spaces (Kaiser and Guggenberger, 2007; Lu et al., 2019b).

My experiments show that the total amount of non-desorbable C with my Fh_Pen1/5_1.2wt%C and Fh_Hex2/6 coprecipitates decreases with aging time, while the total amount of non-desorbable C with my Fh_But3/7 coprecipitates is relatively stable over the first 12 days of aging then decreases after 19 days aging time (Figure 4.5a and 4.5b). Given that my surface coverage estimations for the Fh coprecipitates after 19 days aging suggest that the adsorption capacity of the Fe minerals formed after aging of Fh_Pen1/5_1.2wt%C (3.04 wt%C, Table 4.5b) and Fh_Hex2/6_7.0wt%C (2.54 – 4.84 wt%C, Table 4.5b) are well in excess of the total remaining amount of C (0.72 – 0.75wt% for Fh_Pen1/5_1.2wt%C, and 1.55 – 1.76 wt%C for Fh_Hex2/6_7.0wt%C, Table 4.5b), it is therefore possible that both the desorbable and the non-desorbable part of this total remaining C is adsorbed at the particle surfaces. In turn this suggests that the total remaining C after aging is comprised of two pools with differing mobilities; a relatively loosely bound desorbable pool that is released after washing with 0.1 M NaOH and a relatively strongly bound non-desorbable pool that is retained after washing with 0.1 M NaOH. The presence of a loosely bound desorbable pool and more strongly bound non-desorbable pool after repeated washing with 0.1 M NaOH is also observed for un-aged Fh_Pen1/5 and Fh_Hex2/6 coprecipitates and attributed to the presence of binding strength heterogeneities in the local adsorption environment, such as steric hindrance and/or electrostatic repulsion in a patchy 'monolayer equivalent' (Wershaw, 1994), that render some molecules less strongly bound and more susceptible to desorption (Kaiser and Guggenberger, 2007; Curti et al., 2021). In the case of the Hex2/6 acid molecules, these are adsorbed via either a bidentate or monodentate carboxyl adsorption mechanism (Figure 4.7b) and as such, those that experience binding strength heterogeneities as above and also those that are monodentate are similarly likely to be more susceptible to desorption (Kaiser and Guggenberger, 2007; Curti et al., 2021).

In contrast given that my surface coverage calculations for the Fh coprecipitates after 19 days aging indicate that the adsorption capacity of Fe minerals after aging of Fh_But3/7_7.3wt%C (3.12 – 4.52 wt%C, Table 4.5b) are not in excess of the total remaining amount of C (3.05 – 4.90 wt%C, Table 4.5b), it is therefore likely that some part of the total remaining C is incorporated into the particle interiors where it is more difficult to remove with 0.1 M NaOH (Kaiser and Guggenberger, 2007; Lu et al., 2019b). At first glance, the presence of C incorporated into the particle interiors, for example by being occluded into mineral pore spaces (Eusterhues et al., 2011), might be expected to decreased the TPV of aged Fh_But3/7_7.3wt%C compared to aged pure Fh, however, the TPV results show that the TPV of aged Fh_But3/7_7.3wt%C (0.16±0.02 cm^3/g, Table 4.1) is somewhat higher than aged pure Fh (0.11±0.02 cm^3/g, Table 4.1) and Fh_Pen1/5_1.2wt% (0.13±0.02 cm^3/g, Table 4.1). This suggests that the adsorption of desorbable C at shallow pores and pore openings, which is removed by washing with 0.1 M NaOH, creates a more open and porous structure in the aged Fe minerals (Eusterhues et al., 2008), that is then reflected in the higher TPV measurements. These results support my suggestion that the distribution of the remaining OC between the mineral surfaces vs. incorporation into mineral particle interiors after aging depends primarily on the binding strength of the OC because this controls both the initial C loading of the coprecipitates and the physiochemical properties of Fe minerals after aging.

It is also important to note that the ratio of non-desorbable C to total C changes with the aging process (Figure 4.8). For Fh_Pen1/5_1.2wt%C it is likely that a substantial amount of C is desorbed from the Fh coprecipitates during the washing process, that is necessarily performed after synthesis to remove excess salts. This initial loss of C is relatively large for Fh_Pen1/5_1.2wt% compared to the Fh_Hex2/6 and Fh_But3/7 coprecipitates, because the Pen1/5 acid molecules are the least strongly adsorbed. At the start of the aging the total C associated with the particles is thus relatively non-desorbable and the absolute value for the percentage of C that is non-desorbable is ~100% (Figure 4.8). It is then clear that during aging, while the total amount of C is relatively constant, the total amount of non-desorbable C decreases, from an amount nearly equivalent to the total amount of C to an amount significantly less than the total amount of C (Figure 4.4 and 4.5). The percentage of total C that is non-desorbable therefore decreases over time from near 100% to ~40% (Figure 4.8). This suggests that the fraction of OC that is very strongly adsorbed decreases during aging. For the Fh_Hex2/6 coprecipitates, the total amount of C decreases and the total amount of non-desorbable C decreases but at a lesser rate compared to the total amount of C, and from an amount significantly less than the total amount of C (Figure 4.4 and 4.5). The percentage of total C that is non-desorbable is therefore approximately constant over time at ~15 – 20% at pH 5 and 20 – 25% at pH 6.5 (Figure 4.8). This suggests that the fraction of OC that is very strongly adsorbed and/or incorporated is approximately constant during aging. For the Fh_But3/7 coprecipitates, the total amount of C decreases and the total amount of non-desorbable C is relatively constant, but again is significantly less than the total amount of C (Figure 4.4 and 4.5). The percentage of total C that is non-desorbable therefore increases over time from ~10 – 15% to ~12 –

25% at pH 5 and 6.5 (Figure 4.8). This suggests that the fraction of OC that is very strongly adsorbed and/or incorporated increases during aging.

The overarching trend in the percentage of C that is non-desorbable during aging of the Fh_Pen1/5, Fh_Hex2/6 and Fh_But3/7 coprecipitates, where non-desorbable C for Fh_Pen1/5_1.2wt%C decreases, for the Fh_Hex2/6 coprecipitates remains relatively constant and for the Fh_But3/7 coprecipitates increases, follows the increasing binding strength of these acid molecules in the order Pen1/5 < Hex2/6 < But3/7. The absolute values for the percentage of C that is non-desorbable before aging for the Fh_Hex2/6 and Fh_But3/7 coprecipitates are also comparable with previous work in which Hex2/6 and But3/7 are coprecipitated with Fh using the same experimental coprecipitation conditions as used here (Curti et al., 2021). In this previous study un-aged Fh_Hex2/6 and Fh_But3/7 coprecipitates with approximately equivalent C:Fe molar ratios to my coprecipitates, have ~15 – 20% C and ~20 – 30% C, respectively, that is non-desorbable with 0.1 M NaOH (Curti et al., 2021). Thus for the un-aged Fh_Hex2/6 and Fh_But3/7 coprecipitates I see that a small percentage of the total C is non-desorbable at the start of the aging and that this percentage is approximately constant or increases during the aging as the weakly adsorbed desorbable C is released relative to the strongly adsorbed and/or incorporated non-desorbable C. My results therefore indicate that relatively carboxyl-rich OC coprecipitated with Fh becomes proportionally more stable with the solid phase and thus less mobile during aging. My results therefore also indicate that relatively carboxyl-rich OC coprecipitated with Fh is more persistent than relatively carboxyl-poor OC in soils and sediments, which might help to provide a mechanistic explanation for the recently reported relationship between OC-mineral binding strength and OC-mineral persistence over time (Hemingway et al., 2019).

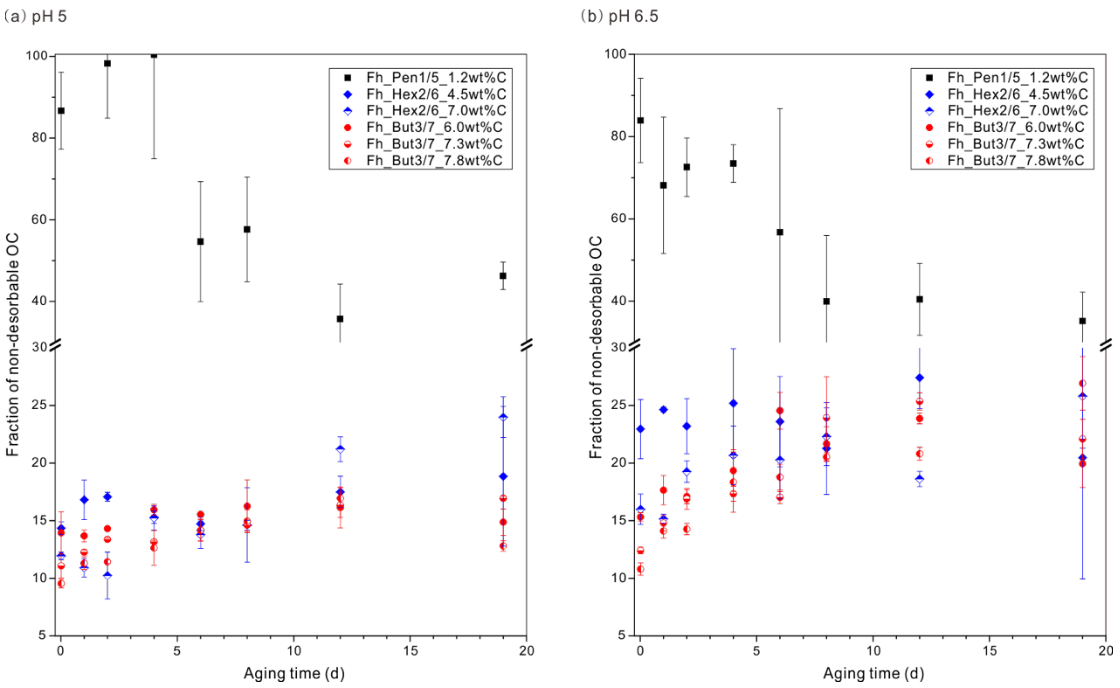

Figure 4.8. Percentage of C that is non-desorbable with aging. The percentage of non-desorbable C is calculated by $[C_{\text{non-desorbable}}]/[C_{\text{total}}]$. Black, blue and red symbols represent Pen1/5, Hex2/6 and But3/7 data, respectively. Pen1/5, Hex2/6 and But3/7 represent simple carboxyl-rich OC with one, two and three carboxyl groups, respectively. Error bars represent standard deviations of at least duplicate samples.

4.5 Conclusions

My STXM NEXAFS and adsorption experiment plus surface complexation model results show that the binding strength of my carboxylic acids sequestered to Fh increases with an increasing number of carboxyl functional groups (Pen1/5 < Hex2/6 < But3/7). Regarding the role of OC in the aging of Fh, I show that OC substantially retards the aging of Fe (oxyhydr)oxide to more crystalline Fe minerals and that this retardation increases with increasing binding strength of the OC, following the order Pen1/5 < Hex2/6 < But3/7 at similar C loading, and with increasing C loading and decreasing pH. The SSA and TPV of Fe minerals formed from aging of my Fh coprecipitates also appear to increase with increasing binding strength of the OC suggesting that OC with higher binding strength is able to further inhibit the growth of more crystalline Fe minerals. Regarding the fate of OC during aging of Fh, I find that the total amount of C retained with the solid during aging is strongly coupled to the binding strength of the OC and the initial C loading of the coprecipitates, where OC with higher binding strength is retained more with the solid by influencing the physiochemical properties of Fe minerals after aging, and partial OC is released if the initial C loading is higher than the adsorption capacity of Fe minerals after aging. I also find that the total amount of non-desorbable C after 19 days aging similarly shows a positive correlation with the binding strength of the OC, where the proportion of non-desorbable C increases with higher binding strength. My results suggest that the distribution of this OC between the mineral surfaces vs. incorporation into particle interiors during aging is strongly influenced by the binding strength of the OC, because this controls both the initial C loading of the coprecipitates and the physiochemical properties of the Fe minerals after aging. Overall I find that carboxyl-rich OC coprecipitated with Fh becomes proportionally more stable with the solid phase because carboxyl-poor OC that has lower binding strength is more readily released during aging. My work might therefore offer a deeper mechanistic insight into the mechanisms responsible for the persistence and long-term preservation of OC in natural environments.

Chapter 5 The mobility and fate of Cr(VI) during aging of ferrihydrite and ferrihydrite organominerals

ABSTRACT

The fixation of environmentally hazardous Cr(VI) is largely attributed to the retention by iron (oxyhydr)oxide in the soil environment, which is prevailingly associated with organic carbon (OC). The effect of OC with different binding strengths on Cr(VI) adsorption and the mobility and fate of Cr(VI) during transformation of iron (oxyhydr)oxide however, are unknown. Here I investigate how OC binding strength influences Cr(VI) adsorption to ferrihydrite (Fh) organominerals, and the subsequent retention or release of OC and Cr(VI) during the mineralogical transformation of Fh organominerals. I conduct Cr(VI) adsorption experiment onto ferrihydrite organominerals, apply surface complexation model to study the relative binding strength between OC and Cr(VI), and then conduct the aging experiment to track re-distribution of Cr(VI). I show that based on the relative binding strength between OC and Cr(VI), the weakly-bound OC at different C loadings has almost no discernable influence on Cr(VI) adsorption, while the strongly-bound OC significantly suppress Cr(VI) adsorption via surface masking and/or electrostatic repulsion. The presence of Cr(VI) retards the aging of Fh at various pH conditions, whilst Cr(VI) also cause discernable retardation on the transformation of Fh organominerals even at a lower concentration. The redistribution of Cr(VI) for Fh organominerals is strongly influenced by the presence of OC. The weakly-bound OC (especially mono-carboxylic Pen1/5) not only almost double the rate of the capture of Cr(VI) in neo-formed minerals at pH 5.0 but also increase the final proportion of Cr(VI) captured, which are attributed to the loose and porous property of Fe minerals and easier replacement of weakly-

bound OC by Cr(VI). This facilitation effect on capture of Cr(VI) are weaken with increasing carboxyl richness in OC moieties and pH conditions. The rate of the capture of Cr(VI) for Fh_But3/7 systems are similar or much lower than than for pure Fh system, which is because the tricarboxylic But3/7 has higher binding strength than Cr(VI) and make it harder for Cr(VI) to replace But3/7 to get surface sites or surface pores to be captured in neo-formed Fe minerals. I speculate that OC with higher carboxyl richness will further suppress the proportion and the rate of the capture of Cr(VI) in Fe minerals, and thus the mobility and fate of Cr(VI) in soils and sediments is therefore likely strongly controlled by the carboxyl-richness of OC in the organominerals.

5.1 Introduction

Chromium, especially hexavalent chromium, can be released into the environment from a variety of industrial sources, like leather processing and finishing, steel processing, ceramic processing, electroplating, catalytic manufacture and drilling muds (Barnhart, 1997; Darrie, 2001; Jacobs and Testa, 2005). Hexavalent chromium Cr(VI) is the most common Cr species, is highly toxic and also more soluble and bioavailable than trivalent chromium Cr(III), and thus presents a mobile biohazard in aquatic and soil ecosystems (Chandra and Kulshreshtha, 2004; Costa, 1997; Shanker et al., 2005). The potential environmental harm posed by Cr(VI) means that it is important to understand how this species interacts with soil constituents in order to predict Cr mobility and fate, and to develop soil remediation methods.

Compared to other soil minerals, iron (oxyhydr)oxides, especially ferrihydrite (Fh), have widespread occurrence, high specific surface area and various binding sites for adsorption of solution species (Hiemstra, 2013; Larsen and Postma, 2001; Michel et al., 2007b). As such they act as efficient adsorbents of organics (Cornell and Schwertmann, 2003) and heavy metal contaminants including Cr(VI) in soils (Gu et al., 2017; Mikutta et al., 2014). In an attempt to gain insight into the mechanisms of Cr(VI) fixation in natural soil environments, Cr(VI) adsorption behaviour to Fh is extensively investigated (Ding et al., 2018; Hajji et al., 2019; Johnston and Chrysochoou, 2012, 2016; Veselská et al., 2016). At the macroscopic level, Cr(VI) adsorption onto Fh exhibits a typical anion adsorption edge, with adsorption decreasing with increasing pH (Veselská et al., 2016). Adsorption edges show no significant difference with changes in Cr(VI) concentration and adsorbate/adsorbent ratio (Cr(VI) concentions of 10^{-6}, 10^{-5}, 10^{-4} M) or ionic strength (0.001, 0.01, 0.1 M KNO_3) (Veselská et al., 2016). At the microscopic level, Cr(VI) tends to form inner-sphere bidentate complexes at high surface coverage and monodentate complexes at lower surface coverage on iron minerals including Fh, goethite (Gt) and hematite (Hm), confirmed by spectroscopic techniques coupled with surface complexation modelling (Fendorf et al., 1997; Johnston and Chrysochoou, 2012, 2014; Veselská et al., 2016; Xie et al., 2015). Monodentate complexes may be the precursor of bidentate complexes (Grossl et al., 1997) and are particularly susceptible to ionic strength effects (Johnston and Chrysochoou, 2012, 2014; Xie et al., 2015). It is also reported that Al substitution in Fh disproportionately suppresses bidentate complexes over monondentate complexes (Johnston and Chrysochoou, 2016).

Authigenic Fh is metastable under oxic conditions however, and undergoes thermodynamically spontaneous transformation to other more stable iron (oxyhydr)oxides, like Gt and Hm (Das et al., 2011b). Because the transformation involves many processes like dissolution, precipitation, aggregation, adsorption and desorption (Sakakibara et al., 2019) and the secondary iron minerals also have different physical and chemical properties (Cornell and Schwertmann, 2003), the mineralogical transformation can influence the mobility of adsorbed heavy metals (Francisco et al., 2018; Hu et al., 2020; Hu et al., 2018; Sakakibara et al., 2019). In addition Fh formed in natural environments is typically associated with organic carbon (OC) to form organominerals. The association of OC and minerals in these organomineral phases typically occurs through a variety of sequestration processes that remove OC from solution to the solid mineral particles (Sposito, 2008). Sequestration processes can include the surface sorption, or adsorption, of OC to preformed mineral particles and also the coprecipitation of OC with neoformed mineral phases, where OC is removed from solution as a consequence of mineral precipitation (Eusterhues et al., 2011). During coprecipitation OC can become adsorbed at mineral particle surfaces and incorporated into particle interiors, for example by being occluded into mineral pore spaces (Eusterhues et al., 2011). Recent studies show that up to 40% of total OC in various soils is bound to reactive iron phases, likely during coprecipitation (Wagai and Mayer, 2007; Zhao et al., 2016). In these organomineral coprecipitates both experimental studies of OC iron (oxyhydr)oxide coprecipitates and investigations of natural OC-iron (oxyhydr)oxide associations show that OC is mostly adsorbed at mineral particle surfaces with a lesser amount incorporated into OC-Fe macromolecules and particle interiors (Eusterhues et al., 2011; Chen et al., 2014; Lehmann et al., 2008; Curti et al., 2021). The presence of OC can significantly influence Fh transformation in terms of transformation rate, pathway and properties of secondary iron minerals (Amstaetter et al., 2012; Fredrickson et al., 1998; Hansel et al., 2003; Hu et al., 2020; Lovley et al., 1996), and also the adsorption properties of Fh and secondary iron minerals, such as adsorption site availability (Chen et al., 2014; Shimizu et al., 2013) and crystallographic defects (Eusterhues et al., 2014) or surface pores (Mikutta et al., 2014). As such the transformation of Fh and Fh organominerals plays an important role in controlling the adsorption and capture of Cr in soils.

A limited number of studies focus on the mobility of Cr(VI) during the mineralogical transformation of iron (oxyhydr)oxides. The transformation of pure Fh to secondary iron minerals can increase the proportion of Cr(VI) (Yu et al., 2020; Yu et al., 2021; Zhu et al., 2019), decreasing the mobility of Cr(VI). On the other hand, aging of pure Fh also increases aqueous Cr(VI) at pH 7.5 (Zhu et al., 2019), increasing the mobility of Cr(VI). Different additives in the adsorption systems also have different influence on the distribution of Cr(VI) between non-desorbable and desorbable pools. The presence of silicate in Fh-Si-Cr coprecipitates significantly decreases the proportion of

Cr(VI) which is non-desorbable with 1.0 M Na_2HPO_4 during aging at pH 5.0 (Zhu et al., 2019) while the addition of citrate also decreases non-desorbable Cr(VI) during aging at pH 5.0 but increases aqueous Cr(VI) during aging at pH 7.0 (Yu et al., 2021). To the authors' knowledge however, only one study investigates the influence of OC on the distribution of Cr during the mineralogical transformation of iron (oxyhydr)oxide organominerals, where it is observed that the transformation of Fh-humic acid composites increases non-desorbable Cr after aging, probably via a redox reaction which reduces more soluble Cr(VI) to less soluble Cr(III) (Yu et al., 2020). Similarly rare are studies that reveal the microsopic mechanistic interactions between iron (oxyhydr)oxide organominerals and Cr(VI), in which the focus is not on the redox reduction of Cr(VI). Early work reveals a competitive adsorption between oxalate and Cr(VI), and emphasises the importance of the relative adsorption affinity of Cr(VI) and OC to iron (oxyhydr)oxides (Measuere and Fish, 1992). The influence of OC on Cr(VI) adsorption behaviour to iron (oxyhydr)oxide organominerals, and the mobility and fate of Cr(VI) during the transformation of these organominerals however, is still largely unknown.

One of the most important types of OC for iron (oxyhydr)oxide-OC associations is carboxyl-rich OC. Carboxyl functional groups are prevalent in natural OC (Rothe et al., 2000) and are highly reactive towards different mineral surfaces and metal ions (Rowley et al., 2017). Carboxyl-rich OC has a high adsorption affinity with iron (oxyhydr)oxides during both its adsorption to preformed iron (oxyhydr)oxides and during its coprecipitation with iron (oxyhydr)oxides (Gu et al., 1995; Curti et al., 2021; Zhao et al., 2022) and thus it is a potential competitor with Cr(VI) for adsorption sites, and also shows a strong influence on the transformation of iron (oxyhydr)oxides in terms of transformation rates and pathway (Cornell and Schwertmann, 1979b). Spectroscopic studies using Fourier-transform infrared (FTIR) spectroscopy and near edge X-ray absorption fine structure (NEXAFS) spectroscopy provide direct evidence for inner-sphere adsorption complexation between carboxyl functional groups and iron (oxyhydr)oxides, and for carboxylic-C and O-alkyl-C functional groups as the dominant forms of OC in soils (Chen et al., 2014; Lv et al., 2016; Solomon et al., 2005). Recent NEXFAS spectroscopy and surface complexation modelling also show that as the number of carboxyl functional groups present in simple carboxylic OC compounds increases, the binding strength and stability of the OC adsorbed to Fh in Fh organomineral coprecipitates also increases, due to the formation of an increasing number of inner-sphere adsorption complexes between the carboxyl functional groups and the Fh particles (Curti et al., 2021; Zhao et al., 2022).

Here I investigate how OC binding strength influences Cr(VI) adsorption to Fh organomineral coprecipitates, the mineralogical transformation of Fh in these Fh organomineral coprecipitates and the subsequent retention or release of OC and Cr(VI) as the transformation proceeds. I focus on carboxyl-rich OC and use simple mono-, bi- and tri-carboxylic acids with either one, two or three carboxyl functional groups as model carboxyl-rich compounds, possessing increasing carboxyl-richness and thus increasing binding strengths to the Fh organomineral coprecipitate particles. I perform Cr(VI) adsorption experiments with pure Fh and Fh-OC organomineral coprecipitates to observe the influence of OC binding strength on Cr adsorption. I then conduct mineralogical transformation experiments at 75 ℃ in Fh-OC-Cr ternary systems to observe the transformation of iron (oxyhydr)oxides, and the distribution of OC and Cr. My primary objectives are to (1) investigate the influence of carboxyl-rich OC with different binding strengths on Cr adsorption to Fh-OC organominerals; (2) investigate the influence of Cr on the transformation of Fh-OC organominerals and the mobility and fate of OC; (3) investigate the influence of carboxyl-rich OC with different binding strengths on the mobility and fate of Cr during the mineralogical transformation of Fh organominerals; and (4) provide novel information for the remediation of Cr(VI) contaminated soils.

5.2 Materials and methods

5.2.1 Preparation of Fh and Fh organomineral coprecipitates

Pure ferrihydrite (Fh) was prepared following the method of Schwertmann and Cornell (2000) for the precipitation of 2-line ferrihydrite via hydrolysis of Fe(III) salt solution. Briefly, Fh was prepared by rapid hydrolysis of 0.1 M $Fe(NO_3)_3 \cdot 9H_2O$ (aq) with 1 M KOH to maintain a final pH of 7. Fh was washed several times over a week with 18.2 MΩ·cm MilliQ water until the conductivity of supernatant is same with DI water, after which Fh was stored as a slurry at 4 ^{o}C, following standard protocols to maintain mineralogical integrity (Schwertmann and Cornell, 2000). The specific surface area (SSA) of the pure Fh was determined by the multi-point BET (Brunauer, Emmett and Teller) technique using a Micromeritics Gemini VII Surface Area Analyser, with samples dried and degassed at room temperature for 24 h using N_2 (g) (<1 ppm CO_2 (g)) prior to analysis. All SSA analyses were performed in triplicate.

Fourteen Fh-OC organomineral coprecipitates with different wt% C were prepared with three simple carboxylic acids, denoted as acid*n/m*, where acid refers to the first three letters of the acid IUPAC name and *n/m* denotes the number of carboxyl groups (*n*) and the number of total carbon atoms (*m*). The acids used were pentanoic acid (Pen1/5), hexanedioic acid (Hex2/6) and butane 1, 2, 4 tricarboxylic acid (But3/7), which have one, two and three carboxyl functional groups, respectively. Briefly, 0.1 M $Fe(NO_3)_3 \cdot 9H_2O$ (aq) solutions were mixed with different amounts of organic acids and then the pH values of the solutions were adjusted to ~7 with 1 M KOH, whereupon the acids coprecipitated with the Fh, forming Fh organomineral coprecipitates with different wt% C. Fh organomineral coprecipitates were washed several times over a week in equivalent volumes of 18.2 MΩ·cm MilliQ water, after which coprecipitates were stored as a slurry at 4 ^{o}C, and part of the coprecipitates were freeze dried for further analysis. The C contents of the solids were determined on solid freeze-dried subsamples using LECO SC-144DR Dual Range Sulphur and Carbon Analyzer.

Fourteen coprecipitates were obtained: Fh-pentanoic acid with 1.2wt%C and C:Fe molar ratio 0.098, and 1.9wt%C and C:Fe molar ratio 0.157 (Fh_Pen1/5_1.2/1.9wt%C); Fh-hexanedioic acid with 2.9wt%C and C:Fe molar ratio 0.246, 3.3wt%C and C:Fe molar ratio 0.283, 4.1wt%C and C:Fe molar ratio 0.358, 4.5wt%C and C:Fe molar ratio 0.396, 6.4 wt%C and C:Fe molar ratio 0.588, and 7.0wt%C and C:Fe molar ratio 0.652 (Fh_Hex2/6_2.9/3.3/4.1/4.5/6.4/7.0wt%C); and Fh- butane 1, 2, 4 tricarboxylic acid with 5.1 wt%C and C:Fe molar ratio 0.461, 6.0 wt%C and C:Fe molar ratio 0.555, 6.6 wt%C and C:Fe molar ratio 0.620, 7.3wt%C and C:Fe molar ratio 0.699, 7.8 wt%C and C:Fe molar ratio 0.757, and 10.2 wt%C and C:Fe molar ratio 1.060 (Fh_But3/7_5.1/6.0/6.6/7.3/7.8/10.2wt%C). Plastic labware and AR grade reagents were used throughout all the preparations.

Table 5.1 Information of Fh organominerals synthesized

Name	Number of carboxyl groups in organic acids	C:Fe molar ratio	Wt%C
Fh_Pen1/5_1.2wt%C	1	0.098	1.2
Fh_Pen1/5_1.9wt%C	1	0.157	1.9
Fh_Hex2/6_2.9wt%C	2	0.246	2.9
Fh_Hex2/6_3.3wt%C	2	0.283	3.3
Fh_Hex2/6_4.1wt%C	2	0.358	4.1
Fh_Hex2/6_4.5wt%C	2	0.396	4.5
Fh_Hex2/6_6.4wt%C	2	0.588	6.4
Fh_Hex2/6_7.0wt%C	2	0.652	7.0
Fh_But3/7_5.1wt%C	3	0.461	5.1
Fh_But3/7_6.0wt%C	3	0.555	6.0
Fh_But3/7_6.6wt%C	3	0.620	6.6
Fh_But3/7_7.3wt%C	3	0.699	7.3
Fh_But3/7_7.8wt%C	3	0.757	7.8
Fh_But3/7_10.2wt%C	3	1.060	10.2

5.2.2 Cr(VI) adsorption on Fh and Fh organomineral coprecipitates and surface complexation modelling

The Cr adsorption experiments onto Fh and Fh organomineral coprecipitates were conducted following the method by Moon and Peacock (2012, 2013). Adsorption pH edges of Cr on Fh or Fh organomineral coprecipitates were prepared from pH 3.5 to pH 10.0. A Cr(VI) stock solution at 100 ppm Cr was prepared with K_2CrO_4. Fh or Fh organomineral slurry was added into MilliQ water and Cr(VI) stock solution was added to give a total volume of 30 mL, a solid solution ration of 1 g dry sorbent L^{-1} and total Cr(VI) concentrations of 1.92×10^{-6}, 1.92×10^{-5}, 1.92×10^{-4} M (0.01 wt%, 0.1 wt% and 1.0 wt% Cr at 100% adsorption, respectively) for Fh and 1.92×10^{-5} M (0.1 wt% Cr at 100% adsorption) for Fh organomineral coprecipitates, in 0.1 M $NaNO_3$ background electrolyte. After addition of stock solution, pH of the resulting suspensions was adjusted by dropwise addition of either dilute HNO_3 or NaOH. After shaking continuously for 48 h to ensure adsorption equilibrium (Saito et al., 2005; Zhu et al., 2010), the suspensions were centrifuged at 2750 rpm for 15 min to obtain a clear supernatant for determination of Cr concentration. Supernatants were filtered using 0.02 μm polycarbonate membrane filters and acidified with 2% HNO_3 for aqueous Cr analysis by inductively coupled plasma mass spectrometry (ICP-MS). All the adsorption experiments were performed in duplicate. Experimental solution speciation of Cr(VI) was calculated as a function of pH using PHREEQC (Parkhurst and Appelo, 1999) and the MINTEQ.V4 database (Charlton and Parkhurst, 2002).

In previous work a surface complexation modelling approach is successfully used to simulate the adsorption of simple organic acids on preformed Gt (Evanko and Dzombak, 1999; Mesuere and Fish, 1992a, b) and the adsorption of Pen1/5, Hex2/6 and But3/7 to Fh during the formation of Fh organomineral coprecipitates (Zhao et al., 2022). A surface complexation modelling approach is also successfully used to simulate the adsorption of Cr(VI) onto iron (oxyhydr)oxides (Bompoti et al., 2019; Veselská et al., 2016; Xie et al., 2015). Following these approaches, Cr(VI) adsorption onto Fh and both OC and Cr(VI) adsorption onto Fh organomineral coprecipitates was fit to a thermodynamic surface complexation model using the program EQLFOR (Sherman et al., 2008). For the Fh system, the adsorption experiment data for the adsorption of Cr(VI) to Fh was fit considering a range of inner-sphere adsorption complexes consistent with spectroscopy (Johnston and Chrysochoou, 2014). For the Fh organomineral coprecipitate system, OC and Cr(VI) adsorption was envisaged as a competition between Cr(VI) and OC for available adsorption sites on Fh. In this approach the binding constants for the adsorption of Pen1/5, Hex2/6 and But3/7 were initially fixed at those determined in the previous work for the adsorption of Pen1/5, Hex2/6 and But3/7 onto pure Fh (Zhao et al., 2022), while the binding constants for the adsorption of Cr(VI) were initially fixed to those determined for the Fh system. After reviewing the initial fits for the Cr(VI) adsorption onto the Fh organomineral coprecipitates generated using the fixed end-member binding constants for OC adsorption onto pure Fh and the fixed end-member binding constants for Cr(VI) adsorption in the Fh system, the final fits were improved with minor iteration of the end-member binding constants for OC adsorption, during which these binding constants changed by < 0.9 log units compared to the end-member binding constants (Zhao et al., 2022).

The basic Stern model (BSM) (Westall and Hohl, 1980) was used to account for the surface electrostatics in the Fh and Fh organomineral coprecipitate systems (Moon and Peacock, 2013; Otero-Farina, 2017; Zhao et al., 2022) with a 3-site 1 p*K* formalism for protonation of the Fh surface, involving two types of singly-coordinated surface oxygens (edge-sharing $\equiv FeOH_e^{-0.5}$ and corner-sharing $\equiv FeOH_c^{-0.5}$) and the triply-coordinated oxygens ($\equiv Fe_3O^{-0.5}$) (Hiemstra and Van Riemsdijk, 2009; Hiemstra et al., 1989; Hiemstra et al., 1996). The model input parameters for the binding constants for protonation of the surface functional groups, binding constants for electrolyte ions associating with these groups and capacitance of the Stern layer were fixed at those used in previous work with Fh and Fh organomineral coprecipitates (Moon and Peacock, 2013; Otero-Farina, 2017). The SSA of the Fh was fixed to the BET measurement while the SSA of the Fh organominerals was calculated using the SSA of the Fh weighted to the mineral:OC mass ratio of each organomineral. The surface site densities of the Fh were fixed to those measured in previous work (Moon and Peacock, 2013; Otero-Farina, 2017) while the surface site densities of the Fh organominerals were calculated using the surface site densities of Fh weighted to the mineral:OC mass ratio of each organomineral.

5.2.3 Mineralogical transformation of Cr(VI)-adsorbed Fh and Fh organomineral coprecipitates

Mineralogical transformation experiments of Cr(VI)-adsorbed Fh and Fh organomineral coprecipitates were prepared by adding Fh or Fh organomineral coprecipitate slurry into MilliQ water and Cr(VI) stock solution was added to produce 2g dry sorbent L^{-1} with 0.1 wt%Cr (Cr/Fe=0.002), 1.1 wt%Cr (Cr/Fe=0.02) and 5.4 wt%Cr (Cr/Fe=0.10) at 100% adsorption for Fh, and 0.1 wt%Cr (Cr/Fe=0.002) at 100% adsorption for Fh organomineral coprecipitates, in 0.01 M $NaNO_3$ background electrolyte. Then these suspensions were adjusted to target pH values with dilute HNO_3 or NaOH. The pH values were buffered at pH 5 by adding 30 mmol L^{-1} organic buffer 2-(N-Morpholino)ethane-sulphonic acid (MES) or pH 6.5 and 8 by adding 3-(N-Morpholino)propanesulphonic acid (MOPS). These buffer solutions have been demonstrated to have negligible impact on the transformation of Fh (Bradbury and Baeyens, 1999; Ford et al., 1999). After shaking for 48 hours to achieve adsorption equilibrium (Saito et al., 2005; Zhu et al., 2010), the resultant solutions were transferred to an electric oven kept at a temperature of 75℃ for up to 19 days to promote transformation to stable phases. During the reactions, the vessels were gently shaken to make the suspensions homogenised. In order to allow a time-resolved investigation of Fh recrystallisation rate and OC and Cr(VI) redistribution, aliquots of the solid precipitates and solutions were collected and analysed at pre-designed time intervals during the transformation process. At each sampling, pH measurement for pure Fh systems were calibrated with buffer solutions heated at 75℃, while pH measurement for Fh organomineral coprecipitate systems was conducted by cooling suspensions to room temperature and calibrating with buffer solutions at same temperature.

For the observation of Fh recrystallisation rate, subsamples were collected from each batch reactor suspension for analyses of Fe concentrations. Two 1 mL aliquots from each suspension were pipetted into 2 mL centrifuge tubes. 1 mL 12 mol L^{-1} HCl was added into one aliquot to get 6 mol L^{-1} HCl in suspension for the determination of total Fe in the solid phase by total digestion of all solid Fe phases ($[Fe(T)_{6\ M\ HCl}]$) (Wang et al., 2020a). These total Fe measurements thus represented the total concentration of Fe (hydr)oxides. 1 mL 0.8 mol L^{-1} HCl was added into the other aliquot to get 0.4 mol L^{-1} HCl, reacted for 10 mins, then centrifuged, and filtered. As soluble Fe(III) in the aqueous phase was below detection limits before adding acids (Reddy et al., 2015) and 0.4 mol L^{-1} HCl could not dissolve goethite (Reddy et al., 2015) and hematite (see Appendixes Section 3), the concentration of Fe in the supernatant after the 0.4 mol L^{-1} HCl addition ($[Fe(T)_{0.4\ M\ HCl}]$ represented the total concentration of untransformed Fh (Wang et al., 2020a). The concentration of Fe was determined on an Atomic Absorption Spectrophotometer (iCE 3300 AAS). Then the fraction of remaining Fh can be quantitatively calculated through the equation: $[Fe(T)_{0.4\ M\ HCl}]/\ [Fe(T)_{6\ M\ HCl}]$. The efficiency of extracting Fh from mixtures of Fh and hematite at 0%, 25%, 50%, 75% and 100% is over 95% (see Appendixes Section 3).

For the observation of OC redistribution, two 15 mL aliquots were subsampled from the reactor and filtered with 0.22 μm cellulose nitrate filters using a vacuum filtration apparatus. The mineral particles were collected and rinsed using 15 mL DI water. One of the mineral particle subsamples was freeze-dried for total solid C measurement (C_{total}) by LECO SC-144DR Dual Range Sulphur and Carbon Analyzer. All measurements were conducted at least in duplicate.

For the observation of Cr(VI) redistribution, two 15-mL aliquots were subsampled from the reactor and either centrifuged (Fh system) or vacuum filtered (Fh organomineral coprecipitates) to separate solid minerals and supernatant or filtrate. The supernatant or filtrate were collected for measurement of aqueous Cr(VI) ($Cr_{aqueous}$). The remaining mineral particles were rinsed with 15 mL DI water, and re-suspended in 15 mL 0.1 M NaOH and shaken for 24 h to extract Cr(VI) following the method to extract As(V) from iron (oxyhydr)oxides (Hu et al., 2020; Hu et al., 2018) (see Appendixes Section 7). Then resulting suspensions were filtered with 0.22 μm PES filters and the filtrate was collected for measurement of Cr(VI), which was operationally defined as desorbable Cr(VI) ($Cr_{desorbable}$). Proportions of Cr(VI) remaining in the solid, operationally defined as non-desorbable Cr(VI) ($Cr_{non\text{-}desorbalbe}$), were calculated based on mass balance. The Cr(VI) concentrations in all solutions generated above were measured by inductively coupled plasma mass spectrometry (ICP-MS). All measurements were conducted at least in duplicate.

5.3 Results

5.3.1 Cr(VI) adsorption on pure ferrihydrite and ferrihydrite organominerals

5.3.1.1 Cr(VI) adsorption experiment

Experimental solution speciation at 1.92×10^{-6}, 1.92×10^{-5}, 1.92×10^{-4} M [$Cr(VI)_{total}$] in 0.1 M $NaNO_3$ background electrolyte was calculated as a function of pH using PHREEQC (Parkhurst and Appelo, 1999) and the MINTEQ.V4 database (Charlton and Parkhurst, 2002), shown in Figure 5.1. Significant concentrations of H_2CrO_4 only occur under the extreme condition of pH 1. Above pH 6.5, CrO_4^{2-} generally dominates, while below pH 6.5, $HCrO_4^-$ dominates. It can be seen that $Cr_2O_7^{2-}$ increases when Cr concentrations increase, but is still less than 1.5 % for 1.92×10^{-4} M $[Cr(VI)]_{total}$. In my adsorption experiments Cr(VI) therefore principally adsorbs as $HCrO_4^-$ and CrO_4^{2-}.

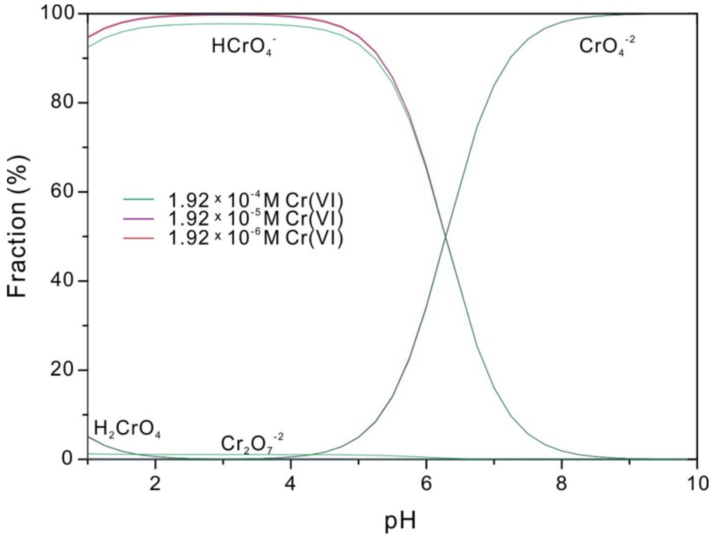

Figure 5.1. Calculation of chromium speciation at 1.92 ×10^{-6}, 1.92 ×10^{-5}, 1.92 ×10^{-4} M [Cr(VI)]$_{total}$ in 0.1 M NaNO$_3$ background electrolyte.

The adsorption of Cr to pure Fh and Fh organominerals is plotted in Figure 5.2 as a function of pH. In all cases Cr(VI) adsorption follows a reverse sigmoid adsorption edge, in which the amount of Cr(VI) adsorbed decreases as pH increases. For Fh_Pen1/5 and Fh_Hex2/6 organominerals, the presence of the organic acids at different loadings has almost no discernable influence on Cr(VI) adsorption. For Fh_But3/7 organominerals however, although Fh_But3/7_5.1wt%C and Fh_But3/7_6.6wt%C have lower or similar OC with respect to Fh_Hex2/6_6.4wt%C, the adsorption edges are shifted to lower pH, which are increasingly shifted with increasing OC loading. The Fh_But3/7_10.2%C organomineral with the highest wt%C significantly suppresses the adsorption of Cr(VI), especially in the low pH regime.

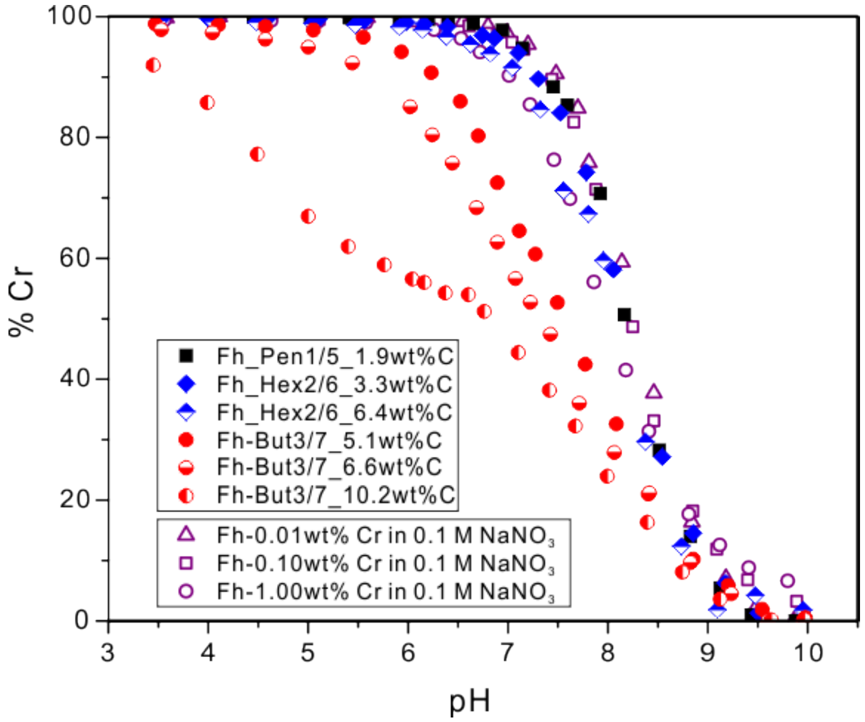

Figure 5.2. Cr(VI) adsorption on pure Fh and Fh organominerals as a function of pH (3.5-10). Experiment conditions are 1.92 $\times 10^{-6}$, 1.92 $\times 10^{-5}$, 1.92 $\times 10^{-4}$ M [Cr(VI) $_{\text{total}}$] for Fh (0.01 wt%, 0.1 wt% and 1.0 wt% Cr at 100% adsorption, respectively) and 1.92 $\times 10^{-5}$ M [Cr(VI) $_{\text{total}}$] for Fh organominerals (0.1 wt% Cr at 100% adsorption), in 1 g sorbent L^{-1} in 0.1 M $NaNO_3$ background electrolyte. Pen1/5, Hex2/6 and But3/7 represent simple carboxyl-rich OC with one-, two- and three-carboxyl groups, respectively. The average error bar for duplicate experiments is smaller than the data points.

5.3.1.2 Surface complexation modelling

The adsorption of Cr(VI) onto pure iron (oxyhydr)oxides is reported to occur via inner-sphere complexation involving ligand exchange between the $HCrO_4^-$ / CrO_4^{2-} oxyanion and iron (oxyhydr)oxide -FeOH surface adsorption sites (Fendorf et al., 1997; Johnston and Chrysochoou, 2012, 2014). Recent spectroscopic work further finds that Cr(VI) adsorbs onto corner-sharing iron (oxyhydr)oxide -FeOH sites as non-protonated monodentate and bidentate complexes and successfully models this adsorption with a surface complexation model that considers the formation of these species at the mineral surfaces (Johnston and Chrysochoou, 2014). As such I represent Cr(VI) adsorption on pure Fh using CrO_4^{2-} as the primary reactive chromate species, which adsorbs to corner-sharing -FeOH sites ($\equiv FeOH_c^{-0.5}$) via monodentate (reaction 1) and bidentate (reaction 2) surface complexes:

$$\equiv FeOH^{-0.5}_{(c)} + CrO_4^{-2} + H^+ = \equiv (FeO)CrO_3^{-1.5} + H_2O \quad (1)$$

$$2\equiv FeOH^{-0.5}_{(c)} + CrO_4^{-2} + 2H^+ = \equiv (FeO)_2CrOO^- + 2H_2O \quad (2)$$

For surface reaction, it is important to describe how electrostatic potential at the mineral-water interface changes as a function of surface loading and pH. As such it is key to distribute the charge of a sorbed species between 0-plane and 1-plane in Basic Stern Model. In BSM, 0–plane is the surface plane where H ions are adsorbed and 1-plane is a hypothetic electrostatic plane where the inner-sphere adsorbed complex are located within the Stern layer region. The surface charge difference of 0-plane and 1-plane after forming complexes are represented as Δz_0 and Δz_1. Before the reaction, charge distribution of ferrihydrite surface are: z_0=-0.5, z_1=0 for species $\equiv FeOH^{-0.5}$. For Cr(VI) complex and assuming the symmetric distribution of over the four Cr-O bonds, Pauling bond valence of Cr-O bond v=z/CN = 6/4 = 1.5, and Pauling bond valence of Fe-O bond v=z/CN = 3/6 = 0.5 (Rietra et al., 1999). As thus for reaction 1, the net charge of 0-plane (z_0’) is +0.5(Fe-O) - 2(O) +1.5(Cr-O) = 0, while the net charge of 1-plane (z_1’) is 3×(-2(O) + 1.5 (Cr-O)) = -1.5. Therefore the charge difference of each carboxyl bonded at the 0-plane and 1-plane are $\Delta z_0 = z_0' - z_0 = +0.5$ and $\Delta z_1 = z_1' - z_1 = -1.5$, which are applied to get best fit for monodentate Cr(VI) complex. For reaction 2, the net charge of 0-plane (z_0’) is 2 × (+0.5(Fe-O) - 2(O) +1.5(Cr-O)) = 0, while the net charge of 1-plane (z_1’) is 2×(-2(O) + 1.5 (Cr-O)) = -1. Therefore the charge difference of each carboxyl bonded at the 0-plane and 1-plane are $\Delta z_0 = z_0' - 2\times z_0 = +1$ and $\Delta z_1 = z_1' - z_1 = -1$, which are applied to get best fit for bidentate Cr(VI) complex.

Previous work reports that OC adsorbed on iron (oxyhydr)oxide organominerals can act as a competitor with heavy metal species for -FeOH surface adsorption sites (Mesuere and Fish, 1992b; Verbeeck et al., 2019; Weng et al., 2009; Yu et al., 2021). In Chapter4 I show that for the same Fh_Pen1/5, Fh_Hex2/6 and Fh_But3/7 organominerals as used here, with equivalent C loadings (up to ~10 wt%C), OC is mainly adsorbed at the Fh particle surfaces via inner-sphere complexation involving ligand exchange between -COOH functional groups and -FeOH sites (Curti et al., 2021; Zhao et al., 2022). As such I represent Cr(VI) adsorption on Fh organominerals as a competition between Cr(VI) and OC for available adsorption sites on Fh. As above for the Fh system, I represent Cr(VI) adsorption on Fh organominerals using CrO_4^{2-} as the primary reactive chromate species, which adsorbs to corner-sharing -FeOH sites ($\equiv FeOH_c^{-0.5}$) via monodentate (reaction 1) and bidentate (reaction 2) surface complexes. I represent OC adsorption according to my previous work in which I constrain the surface complexation reactions for the adsorption of OC on Fh_Pen1/5, Fh_Hex2/6 and Fh_But3/7 (Zhao et al., 2022). For Pen1/5 I find OC adsorption via one carboxyl group in a single-bonded monodentate configuration occurring on both -FeOH edge and corner surface sites, represented by reaction 3 (Zhao et al., 2022). For Hex2/6 I find OC adsorption via one carboxyl group in a monodentate mononuclear configuration occurring on both -FeOH edge and corner surface sites, in which the non-bonding carboxyl group is deprotonated at higher pH (> pH~5) and protonated at lower pH (< pH~5), represented by reactions 4a and b, respectively. I also find OC adsorption via two carboxyl groups in a bidentate mononuclear or bidentate binuclear configuration occurring on both the -FeOH edge and corner surface sites, represented by reaction 5 (Zhao et al., 2022). Finally for But3/7 I find adsorption via two carboxyl groups in a bidentate mononuclear or bidentate binuclear configuration occurring on both the -FeOH edge and corner surface sites, in which the non-bonding carboxyl group is deprotonated at higher pH (> pH~4.5) and protonated at lower pH (< pH~4.5), represented by reactions 6a and b, respectively. I also find OC adsorption via three carboxyl groups in a tridentate trinuclear configuration occurring on both the -FeOH edge and corner surface sites, represented by reaction 7 (Zhao et al., 2022). The description of charge distribution for OC complexes in BSM are following the Chapter 4.

$$\equiv FeOH^{-0.5}_{(c/e)} + R\text{-}COO^{-} + H^{+} = \equiv(FeOOC)\text{-}R^{-0.5} + H_2O \quad (3)$$

$$\equiv FeOH^{-0.5}_{(c/e)} + R\text{-}2COO^{-2} + H^{+} = \equiv(FeOOC)\text{-}R\text{-}COO^{-1.5} + H_2O \quad (4a)$$

$$\equiv FeOH^{-0.5}_{(c/e)} + R\text{-}2COO^{-2} + 2H^{+} = \equiv(FeOOC)\text{-}R\text{-}COOH^{-0.5} + 2H_2O \quad (4b)$$

$$2\equiv FeOH^{-0.5}_{(c/e)} + R\text{-}2COO^{-2} + 2H^{+} = \equiv (FeOOC)_2\text{-}R^{-1} + 2H_2O \quad (5)$$

$$2\equiv FeOH^{-0.5}_{(c/e)} + R\text{-}3COO^{-3} + 2H^{+} = \equiv (FeOOC)_2\text{-}R\text{-}COO^{-2} + 2H_2O \quad (6a)$$

$$2\equiv FeOH^{-0.5}_{(c/e)} + R\text{-}3COO^{-3} + 3H^{+} = \equiv (FeOOC)_2\text{-}R\text{-}COOH^{-1} + 2H_2O \quad (6b)$$

$$3\equiv FeOH^{-0.5}_{(c/e)} + R\text{-}3COO^{-3} + 3H^{+} = \equiv (FeOOC)_3\text{-}R^{-1.5} + 3H_2O \quad (7)$$

All model parameters are collected in Table 5.2, and the model fitting results for Cr(VI) adsorption on pure Fh and Fh organominerals are shown in Figure 5.2. For both the pure Fh and Fh organomineral systems, the bidentate Cr(VI) complex is the primary surface complex at acidic pH while the monodentate Cr(VI) complex dominates at alkaline pH. The presence of But3/7 significantly influences the fractions of bidentate and monodentate Cr(VI) complexes (Figure 5.3). In particular, Fh_But3/7_10.2wt%C with the highest wt%C suppresses the formation of the bidentate Cr(VI) complex and favours the formation of the monodentate complex in the low pH regime, such that the equivalence point for the bidentate and monodentate complexes shifts to a lower pH value (from pH 5.5 in Fh_But3/7_5.1wt%C system to pH 4.4 in Fh_But3/7_10.2wt%C system) (Figure 5.3g, h and l).

Table 5.2. Parameters for the surface complexation model for adsorption of Cr(VI) and carboxylic acids on pure Fh and Fh organominerals

					Pure Fh	Fh organomineral					
						Pen1/5	Hex2/6	Hex2/6	But3/7	But3/7	But3/7
wt% C						1.9[c]	3.3[c]	6.4[c]	5.1[c]	6.6[c]	10.2[c]
Specific surface area (m^2/g)					300[a]	290[d]	280[d]	261[d]	265[d]	255[d]	230[d]
$\equiv FeOH_e^{-0.5}$ (mmol/g)					1.25[b]	1.21[e]	1.17[e]	1.09[e]	1.11[e]	1.06[e]	0.96[e]
$\equiv FeOH_c^{-0.5}$ (mmol/g)					1.74[b]	1.68[e]	1.62[e]	1.51[e]	1.54[e]	1.48[e]	1.34[e]
$\equiv Fe_3O^{-0.5}$ (mmol/g)					0.598[b]	0.579[e]	0.558[e]	0.520[e]	0.529[e]	0.509[e]	0.460[e]
C_{stern} (F/m^2)					1.10[b]	1.10[b]	1.10[b]	1.10[b]	1.10[b]	1.10[b]	1.10[b]
Log $K_{FeOH(c)}$	$\equiv FeOH^{-0.5}{}_{(c)} + H^+ = \equiv FeOH_2{}^{+0.5}{}_{(c)}$				7.99[b]	7.99[b]	7.99[b]	7.99[b]	7.99[b]	7.99[b]	7.99[b]
Log $K_{FeOH(c)\_Na}$	$\equiv FeOH^{-0.5}{}_{(c)} + Na^+ = \equiv FeOH^{-0.5}{}_{(c)}\text{-}Na^+$				-1.00[b]	-1.00[b]	-1.00[b]	-1.00[b]	-1.00[b]	-1.00[b]	-1.00[b]
Log $K_{FeOH2(c)\_NO3}$	$\equiv FeOH_2{}^{+0.5}{}_{(c)} + NO_3^- = \equiv FeOH_2{}^{+0.5}{}_{(c)}\text{-}NO_3^-$				-1.00[b]	-1.00[b]	-1.00[b]	-1.00[b]	-1.00[b]	-1.00[b]	-1.00[b]
(where equations above are repeated for ($\equiv FeOH^{-0.5}{}_{(e)}$))											
Log K_{Fe3O}	$\equiv Fe_3O^{-0.5} + H^+ = \equiv Fe_3OH^{+0.5}$				7.99[b]	7.99[b]	7.99[b]	7.99[b]	7.99[b]	7.99[b]	7.99[b]
Log K_{Fe3O_Na}	$\equiv Fe_3O^{-0.5} + Na^+ = \equiv Fe_3O^{-0.5}\text{-}Na^+$				-1.00[b]	-1.00[b]	-1.00[b]	-1.00[b]	-1.00[b]	-1.00[b]	-1.00[b]
Log K_{Fe3OH_NO3}	$\equiv Fe_3OH^{+0.5} + NO_3^- = \equiv Fe_3OH^{+0.5}\text{-}NO_3^-$				-1.00[b]	-1.00[b]	-1.00[b]	-1.00[b]	-1.00[b]	-1.00[b]	-1.00[b]
		Log K_1	Log K_2	Log K_3							
Pentanoic acid (Pen1/5)		4.84[f]									
Hexanedioic acid (Hex2/6)		4.42[f]	5.41[f]								
Butane 1, 2, 4 tricarboxylic acid (But3/7)		4.31[g]	4.82[g]	5.21[g]							
		Δz_0	Δz_1								
1. Log $K_{FeOH(c)\_Cr}$	$\equiv FeOH^{-0.5}{}_{(c)} + CrO_4^{-2} + H^+ = \equiv (FeO)CrO_3^{-1.5} + H_2O$	+0.5[h]	-1.5[h]		11.58[h]	11.58[h]	11.58[h]	11.58[h]	11.58[h]	11.58[h]	11.58[h]

2. Log $K_{FeOH(c)\_Cr}$	$2{\equiv}FeOH^{-0.5}{}_{(c)} + CrO_4{}^{-2} + 2H^+ = {\equiv}(FeO)_2CrOO^{-1} + 2H_2O$	+1.0[h]	-1[h]	19.25[h]	19.25[h]	19.25[h]	19.25[h]	19.25[h]	19.25[h]	19.25[h]
3. Log $K_{FeOH(c/e)\_OOC\text{-}R}$	${\equiv}FeOH^{-0.5}{}_{(c/e)} + R\text{-}COO^- + H^+ = {\equiv}(FeOOC)\text{-}R^{-0.5} + H_2O$	+0.5[h]	-0.5[h]		9.2[h]					
4a. Log $K_{FeOH(c/e)\_OOC\text{-}R}$	${\equiv}FeOH^{-0.5}{}_{(c/e)} + R\text{-}2COO^{-2} + H^+ = {\equiv}(FeOOC)\text{-}R\text{-}COO^{-1.5} + H_2O$	+0.5[h]	-0.5[h]			10.0[h]	10.0[h]			
4b. Log $K_{FeOH(c/e)\_OOC\text{-}R}$	${\equiv}FeOH^{-0.5}{}_{(c/e)} + R\text{-}2COO^{-2} + 2H^+ = {\equiv}(FeOOC)\text{-}R\text{-}COOH^{-0.5} + 2H_2O$	+0.5[h]	-0.5[h]			15.0[h]	15.0[h]			
5. Log $K_{FeOH(c/e)\_OOC\text{-}R}$	$2{\equiv}FeOH^{-0.5}{}_{(c/e)} + R\text{-}2COO^{-2} + 2H^+ = {\equiv}\ (FeOOC)_2\text{-}R^{-1} + 2H_2O$	+1.0[h]	-1.0[h]			16.0[h]	16.0[h]			
6a. Log $K_{FeOH(c/e)\_OOC\text{-}R}$	$2{\equiv}FeOH^{-0.5}{}_{(c/e)} + R\text{-}3COO^{-3} + 2H^+ = {\equiv}\ (FeOOC)_2\text{-}R\text{-}COO^{-2} + 2H_2O$	+0.65[h]	-0.15[h]					19.70[h]	19.70[h]	19.70[h]
6b. Log $K_{FeOH(c)\_OOC\text{-}R}$	$2{\equiv}FeOH^{-0.5}{}_{(c/e)} + R\text{-}3COO^{-3} + 3H^+ = {\equiv}\ (FeOOC)_2\text{-}R\text{-}COOH^{-1} + 2H_2O$	+1.3[h]	-0.3[h]					24.00[h]	24.00[h]	24.00[h]
7. Log $K_{FeOH(c)\_OOC\text{-}R}$	$3{\equiv}FeOH^{-0.5}{}_{(c/e)} + R\text{-}3COO^{-3} + 3H^+ = {\equiv}\ (FeOOC)_3\text{-}R^{-1.5} + 3H_2O$	+1.95[h]	-0.45[h]					27.20[h]	27.20[h]	27.20[h]

[a] measured in this study;

[b] from Moon and Peacock (2013) and Otero-Farina (2017);

[c] measured by LECO;

[d] calculated using the specific surface area of the pure Fh weighted to the mineral:OC mass ratio of each organomineral;

[e] calculated using the surface site densities of the pure Fh weighted to the mineral:OC mass ratio of each organomineral;

[f] from Dean (1987);

[g] calculated using ACD/I-Lab 2.0 (ACD/I-Lab, version 2.0, Advanced Chemistry Development, Inc);

[h] fitted in my model.

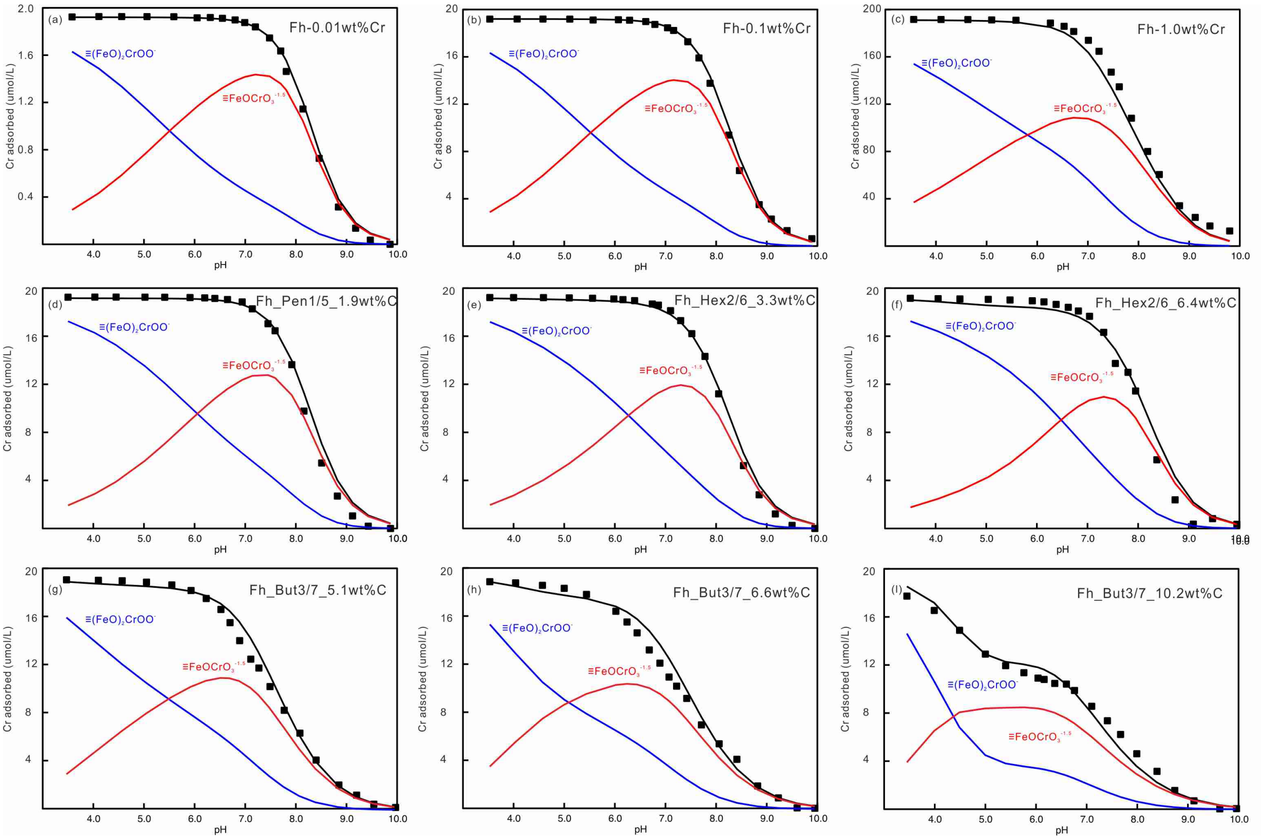

Figure 5.3. Model fits for Cr(VI) adsorption on pure Fh and Fh organominerals. (a)-(c) for pure Fh with Cr(VI) concentrations at 0.01 wt%Cr, 0.1 wt%Cr and 1.0 wt%Cr at 100% adsorption. (d)-(l) for Fh organominerals with Cr(VI) concentration at 0.1 wt%Cr at 100% adsorption. Black solid squares are the Cr(VI) adsorption experimental data; black lines are the predicted total Cr(VI) adsorption; blue lines are the predicted bidentate Cr(VI) complexes (≡(FeO)$_2$CrOO$^-$); red lines are the predicted monodentate Cr(VI) complexes (≡(FeO)CrO$_3^{-1.5}$). Pen1/5, Hex2/6 and But3/7 represent simple carboxyl-rich OC with one-, two- and three-carboxyl groups, respectively.

5.3.2 Transformation rates of pure ferrihydrite and ferrihydrite organominerals under the influence of Cr(VI)

For pure Fh the transformation rates are shown in Figure 5.4. The presence of Cr(VI) suppresses the transformation of pure Fh over the whole pH range (pH 5.0, 6.5 and 8.0) (Figure 5.4c). Increasing concentrations of Cr(VI) result in enhanced supression of transformation up to 1.1 wt%Cr (Cr/Fe=0.02) at 100% adsorption, after which increasing the concentration of Cr(VI) to 5.4 wt%Cr (Cr/Fe=0.1) at 100% adsorption does not result in further supression of transformation (Figure 5.4a). For Fh organominerals the transformation rates are shown in Figure 5.5. In agreement with previous work, the presence of carboxylic acids retards the transformation of Fh in comparison to pure Fh, and retardation increases with both the increasing carboxyl-richness of the sequestered acid molecules (Pen1/5 < Hex2/6 ⩽ But3/7 at pH 5 and pH 6.5) and the increasing C loading of the organominerals (Zhao et al., 2022) (Figure 5.5a and b, open symbols). The presence of Cr(VI) in all Fh organomineral systems further inhibits the transformation of Fh (Figure 5.5c and d), where the magnitude of this retardation effect caused by Cr(VI) at 0.1 wt%Cr (Cr/Fe = 0.002) at 100% adsorption is not pronounced but is similar to that observed in the pure Fh system (Figure 5.4a and b).

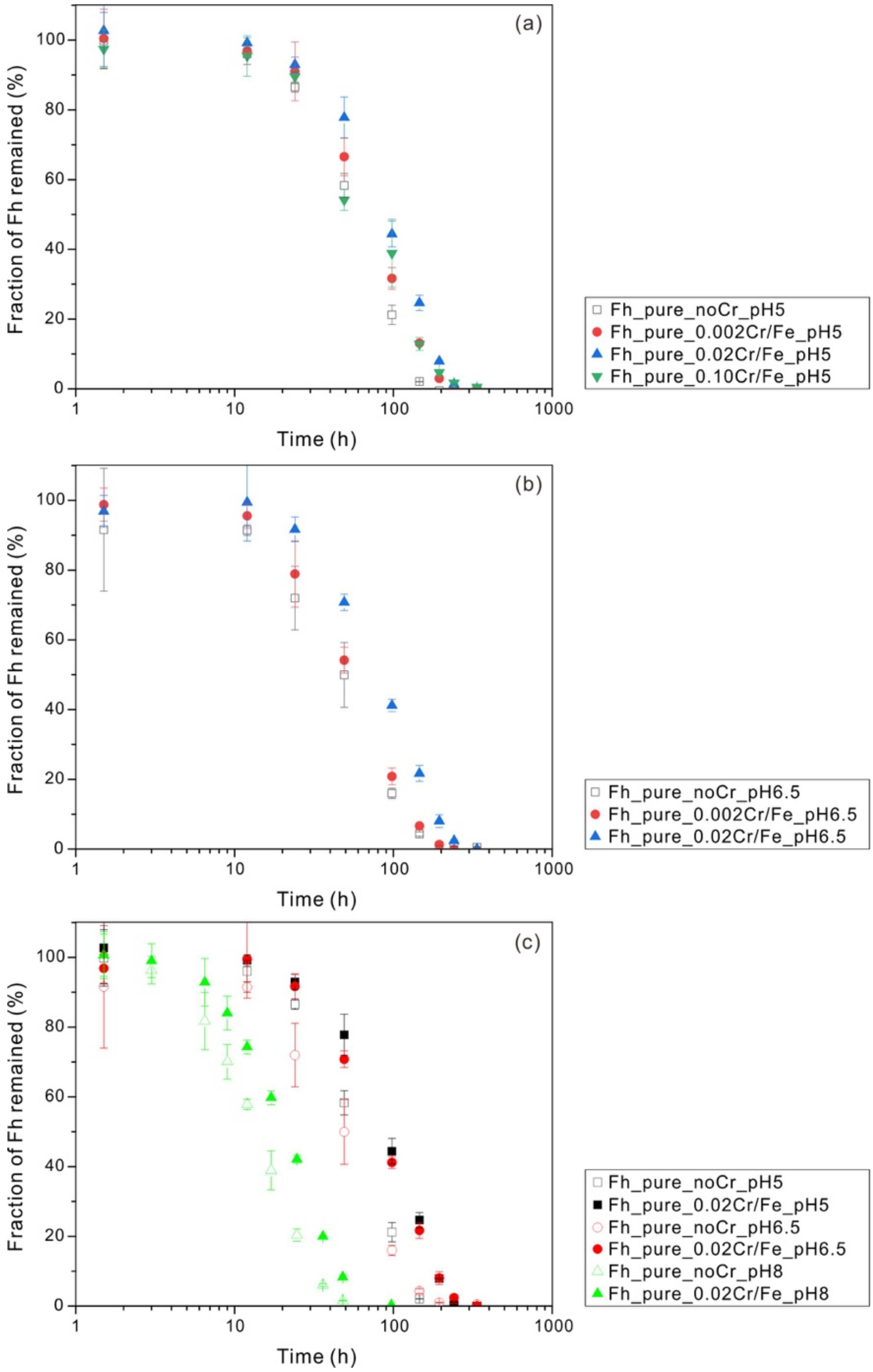

Figure 5.4. Transformation rate of pure Fh with different Cr(VI) adsorbed at (a) pH 5 with 0.1 wt%Cr (Cr/Fe=0.002), 1.1 wt%Cr (Cr/Fe=0.02) and 5.4 wt%Cr (Cr/Fe=0.10) at 100% adsorption; (b) pH 6.5 with 0.1 wt%Cr (Cr/Fe=0.002) and 1.1 wt%Cr (Cr/Fe=0.02) at 100% adsorption; and (c) at different pH conditions (pH 5, pH 6.5 and pH 8) with 1.1 wt%Cr (Cr/Fe=0.02) at 100% adsorption. Error bars represent standard

deviations of at least duplicate samples.

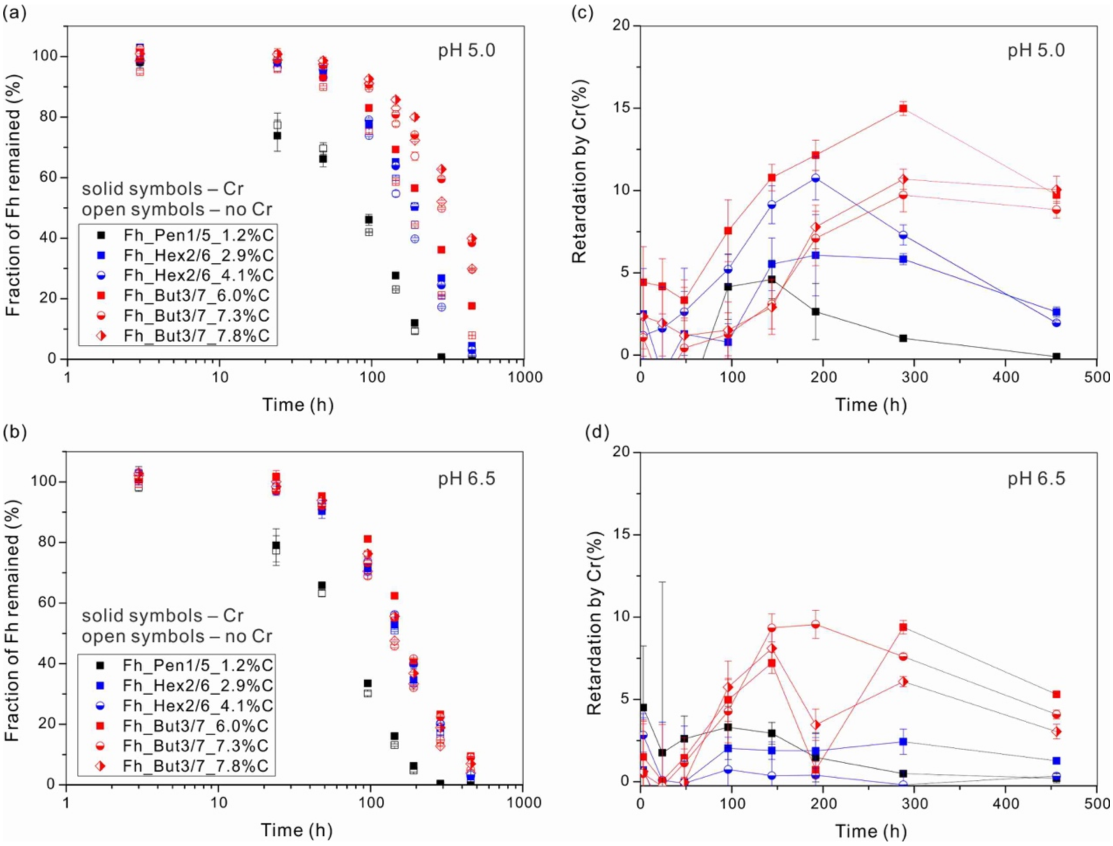

Figure 5.5. Transformation rate of Fh organominerals in the absence and presence of Cr(VI). a) and b) transformation rate of Fh organominerals without Cr(VI) (open symbols) and with Cr(VI) (solid symbols) at 0.1 wt%Cr (Cr/Fe=0.002) at 100% adsorption at pH 5 and pH 6.5, respectively. c) and d) enhanced retardation caused by Cr(VI) at 0.1 wt%Cr (Cr/Fe=0.002) at 100% adsorption at pH 5 and pH 6.5, respectively, derived from transformation rates with Cr(VI) adsorbed minus those without Cr(VI) adsorbed from a) and d), respectively. Pen1/5, Hex2/6 and But3/7 represent simple carboxyl-rich OC with one-, two- and three-carboxyl groups, respectively. Error bars represent standard deviations of at least duplicate samples.

5.3.3 Distribution of OC during the mineralogical transformation

The total C associated with the solid minerals for Fh organominerals without Cr(VI) and with Cr(VI) adsorbed are shown in Figure 5.6. For all systems, the presence of

Cr(VI) at 0.1 wt%Cr (Cr/Fe = 0.002) at 100% adsorption results in no discernable influence on the stabilisation and migration of OC during transformation. For Fh_Pen1/5 coprecipitate the C_{total} at pH 5 and 6.5 is invariant with transformation time. For Fh_Hex2/6 and Fh_But3/7 coprecipitates however, the C_{total} at pH 5 and 6.5 generally decreases with increasing transformation time. Comparing organominerals made with different OC types but with similar C loadings, Fh_Hex2/6_7.0wt%C retains significantly less C_{total} compared to Fh_But3/7_6.0wt% and 7.3wt% during the transformation process.

(a) pH 5

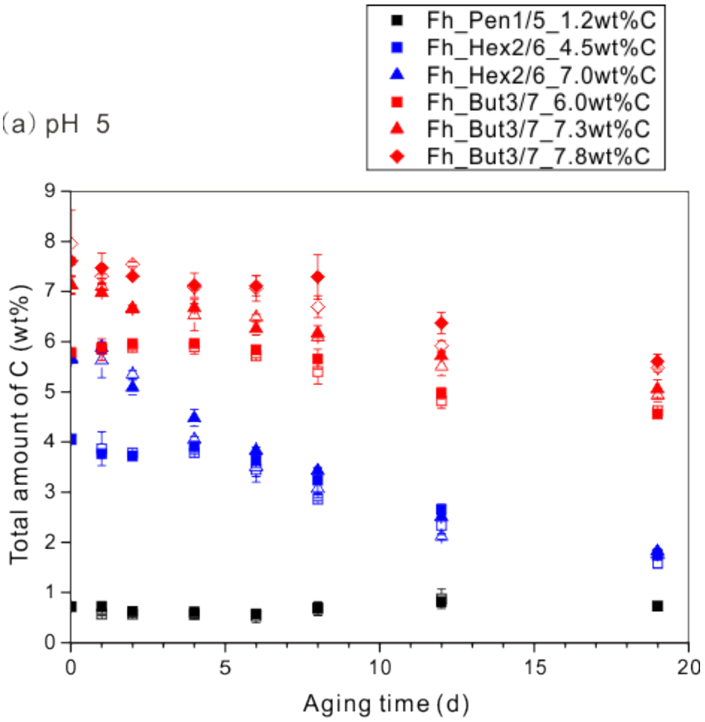

(b) pH 6.5

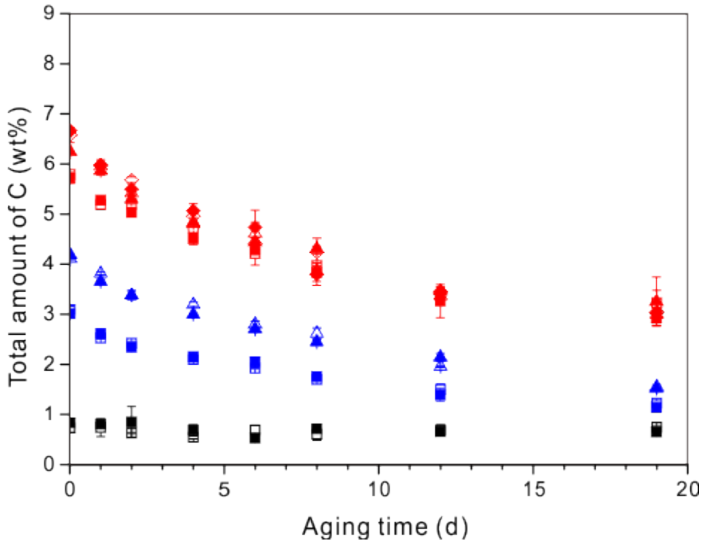

Figure 5.6. Temporal changes of total C% with solid phase in the absence (open symbols) and presence (solid symbols) of Cr(VI) at 0.1 wt%Cr (Cr/Fe=0.002) at 100% adsorption during 19-days transformation at a) pH 5.0 and b) pH 6.5. Experiments were performed with Fh organominerals in 0.01 M $NaNO_3$ background electrolyte and a solid-solution ratio of 2 g dry sorbent L^{-1} at 75℃. Pen1/5, Hex2/6 and But3/7 represent simple carboxyl-rich OC with one- two- and three- carboxyl groups, respectively. Error bars represent standard deviations of at least duplicate samples.

5.3.4 Distribution of Cr(VI) during the mineralogical transformation

For pure Fh the concentration of aqueous Cr(VI) increases with transformation time, and this increase is more pronounced with increasing Cr(VI) concentrations and pH (Figure 5.7). The Cr(VI) associated with the solid minerals exists as non-desorbable ($Cr(VI)_{non\text{-}desorbable}$) and desorbable ($Cr(VI)_{desorbable}$) species. The non-desorbable Cr(VI) increases with transformation time at the expense of the desorbable Cr(VI) at pH 5.0 and pH 6.5. The final proportion of non-desorbable Cr(VI) decreases with increasing Cr(VI) concentration and pH (Figure 5.7).

For Fh organominerals the concentration of aqueous Cr(VI) is negligible for Fh_Pen1/5 and Fh_Hex2/6 coprecipitates during the whole transformation time, but for Fh_But3/7 coprecipitates aqueous Cr(VI) initially increases and then decreases as transformation proceeds, and the total Cr(VI) aqueous at any given time also increases with the C loading of the coprecipitates (Figure 5.8). Similar to the pure Fh system, the Cr(VI) associated with the solid minerals exists as non-desorbable and desorbable species. The final amount of non-desorbable Cr(VI) after 19-days at pH 5 shows no significant difference for all Fh organominerals with around 95% non-desorbable Cr(VI), while at pH 6.5 follows the order Fh_Pen1/5 coprecipitate ~ Fh_Hex2/6 coprecipitates > Fh_But3/7 coprecipitates.

To better evaluate the influence of OC on the capture of Cr(VI), the increasing proportions of non-desorbable Cr(VI) (from 0 to around 80%) with transformation time are fitted with the rate equation:

$$[A]_t = a + b \times t$$

where $[A]_t$ is the fraction of non-desorbable Cr(VI) at time t, a is intercept of the linear fit, b is the slop of the linear fit, represting the increasing rate of the capture of Cr(VI).

The fitted rate graphs are shown in Figure S5 and the rate data Table 5.3 shows that generally the presence of OC increases the rate of non-desorbable Cr(VI) which is captured in neo-formed Fe minerals. This effect appears to decrease with the carboxyl-richness of OC in the sequestered acid molecules and generally follows the order Fh_Pen1/5 coprecipitate > Fh_Hex2/6 coprecipitates > Fh_But3/7 coprecipitates ~ pure Fh at pH 5.0. This trend is complicated by the commensurate increase in the C loading of the coprecipitates with increasing carboxyl-richness, but the Fh_Hex2/6_7.0%C and Fh_But3/7_7.3wt%C have similar C loading, yet the later has lower rates of capture of non-desorbable Cr(VI). The increasing pH condition further weakens the effect of OC, with rates of capture of non-desorbable Cr(VI) following the order Fh_Pen1/5 coprecipitate > Fh_Hex2/6 coprecipitates ~ pure Fh > Fh_But3/7 coprecipitates at pH 6.5.

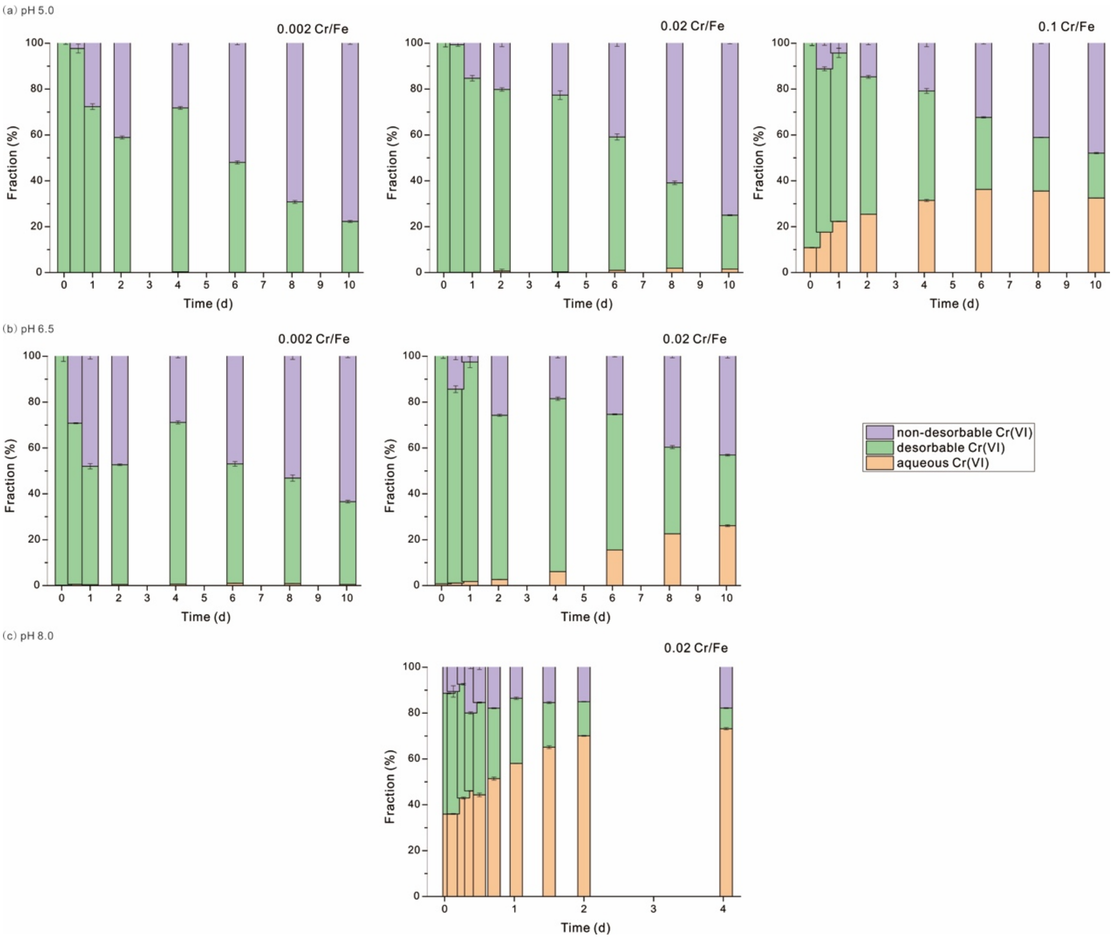

Figure 5.7. Distribution of Cr(VI) with different Cr(VI) adsorbed (0.1 wt%Cr (Cr/Fe=0.002), 1.1 wt%Cr (Cr/Fe=0.02) and 5.4 wt%Cr (Cr/Fe=0.10) at 100% adsorption) during the transformation of pure Fh at pH 5, pH 6.5 and pH 8. Error bars represent standard deviations of at least duplicate samples.

(a) pH 5.0

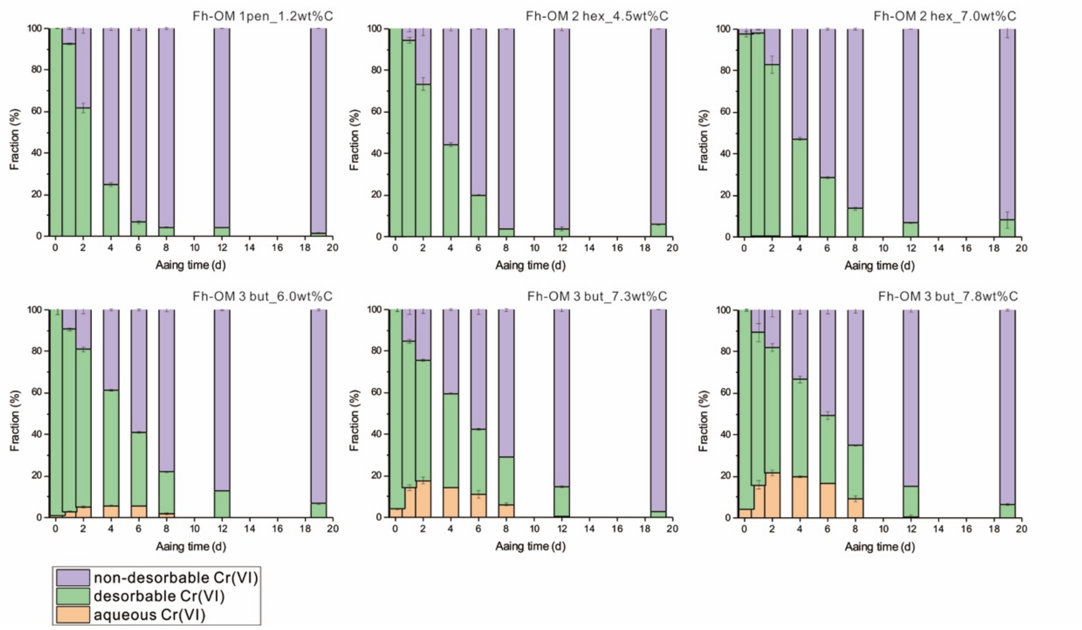

(b) pH 6.5

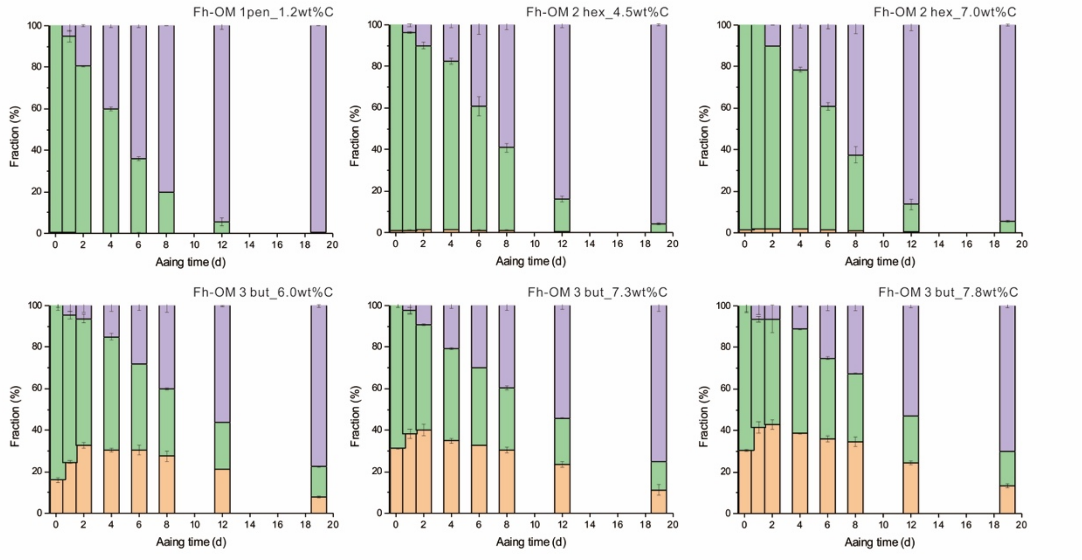

Figure 5.8. Distribution of Cr(VI) with 0.1 wt%Cr (Cr/Fe = 0.002) at 100% adsorption during the transformation of Fh organominerals at a) pH 5 and b) 6.5. Error bars represent standard deviations of at least duplicate samples.

Table 5.3. Rates of capture of non-desorbable Cr(VI) from 0% to ~80% during transformation of pure Fh and Fh organominerals.

	a	*b* (h^{-1})	R^2
	pH 5.0		
pure Fh, Cr/Fe= 0.002[a]	0	0.337 ±0.023	0.96
Fh_Pen1/5_1.2wt%C, Cr/Fe= 0.002	0	0.634 ±0.077	0.93
Fh_Hex2/6_4.5wt%C, Cr/Fe= 0.002	0	0.555 ±0.004	1.00
Fh_Hex2/6_7.0wt%C, Cr/Fe= 0.002	0	0.461 ±0.041	0.96
Fh_But3/7_6.0wt%C, Cr/Fe= 0.002	0	0.406±0.001	1.00
Fh_But3/7_7.3wt%C, Cr/Fe= 0.002	0	0.352 ±0.022	0.97
Fh_But3/7_7.8wt%C, Cr/Fe= 0.002	0	0.305 ±0.009	0.99
	pH 6.5		
pure Fh, Cr/Fe= 0.002 [a]	0	0.351 ±0.113	0.52
Fh_Pen1/5_1.2wt%C, Cr/Fe= 0.002	0	0.418 ±0.001	1.00
Fh_Hex2/6_4.5wt%C, Cr/Fe= 0.002	0	0.279 ±0.015	0.98
Fh_Hex2/6_7.0wt%C, Cr/Fe= 0.002	-4.5	0.308 ±0.016	0.98
Fh_But3/7_6.0wt%C, Cr/Fe= 0.002	0	0.191 ±0.004	1.00
Fh_But3/7_7.3wt%C, Cr/Fe= 0.002	2.59	0.189 ±0.012	0.97
Fh_But3/7_7.8wt%C, Cr/Fe= 0.002	0	0.148 ±0.009	0.97

[a] last four experiment data were used for the fit.

5.4 Discussion

5.4.1 Influence of carboxyl-rich OC with different binding strengths on Cr(VI) adsorption to ferrihydrite organominerals

In agreement with spectroscopic work (Johnston and Chrysochoou, 2012, 2014), my surface complexation model for Fh and Fh organominerals shows that Cr(VI) adsorbs to pure Fh and Fh organominerals predominantly via a bidentate surface complex at pH <5.5 and a monodentate surface complex at pH > 6.0 (Figure 5.3). Therefore the overarching speciation of Cr(VI) is unaffected by the presence of OC. My model fits for Fh and Fh organominerals also predict that the binding strength of the Cr(VI) complexes are the same in both systems, and the bidentate surface complex (Log K 19.25) is stronger than that of the monodentate surface complex (Log K 11.58), due to the formation of two chemical bonds, rather than a single chemical bond, between the Cr(VI) species and the mineral surface (Grossl et al., 1997; Johnston and Chrysochoou, 2014). My stability constants for the formation of the bidentate and monodentate surface complexes are consistent with the Cr(VI) stability constants reported in previous modelling studies for Cr(VI) adsorption on pure Fh (Bompoti et al., 2019; Veselská et al., 2016; Xie et al., 2015). Therefore the binding strengths of Cr(VI) complexes are also unaffected by the presence of OC. Overall my modeling shows that the binding strengths of my carboxylic OC and Cr(VI) complexes follow the order one-carboxyl binding (Log K's 9.2, 10.0/15.0) ~ monodentate Cr(VI) binding (Log K 11.58) < two-carboxyl binding (Log K 16.0, 19.70/24.0) ~ bidentate Cr(VI) binding (Log K 19.25) < three-carboxyl binding (Log K 27.2).

Despite the overarching speciation and binding strength of Cr(VI) complexes to Fh remaining unchanged by the presence of OC, the carboxyl-richness of the OC does have an effect on the adsorption behaviour of Cr(VI). For Fh_Pen1/5 and Fh_Hex2/6 organominerals, the presence of OC at different C loadings has almost no discernable influence on Cr(VI) adsorption (Figure 5.2). For Fh_But3/7 organominerals however, although Fh_But3/7_5.1wt%C and Fh_But3/7_6.6wt%C have lower or similar OC compared to Fh_Hex2/6_6.4wt%C, the adsorption edges and the equivalence point for bidentate and monodentate complexes are shifted to lower pH, which are increasingly shifted with increasing C loading (Figure 5.2.). The suppression of Cr(VI) adsorption for the Fh_But3/7 organominerals can be explained by several mechanisms. The first is the masking of surface adsorption sites on the mineral fraction of the organominerals by the adsorbed organic acids, such that the mineral adsorption capacity is reduced. Surface site masking effects will vary, depending on the concentrations of the organic acids and Cr(VI), on their relative affinities competing for the mineral surface sites and on surface site concentration (Rai, 1986). Surface coverages of the mineral fraction of the different organominerals by organic acids and Cr(VI) are shown in Table 5.4. For But3/7 adsorbed via 2 or 3 of its available carboxyl groups, the surface coverage of the mineral exceeds 100% at the maximum C loadings, demonstrating that surface site masking is potentially a factor in the suppression of Cr(VI) adsorption for the Fh_But3/7 composites. Interestingly the C loading for Fh_Hex2/6_6.4wt%C is very similar to Fh_But3/7_6.6wt%C, but no discernible inhibition of Cr(VI) adsorption is observed (Figure 5.2). This suggests that Hex2/6 adsorbs predominantly via one-carboxyl adsorption in which the surface coverage is significantly lower than But3/7 adsorbing via two- or three- carboxyl adsorption (Table 5.4). This is in agreement with previous spectroscopic and modelling work suggesting that Hex2/6 adsorbs to Fh via one or two of its available carboxyl groups (Curti et al., 2021; Zhao et al., 2022).

Alternatively the monodentate Hex2/6 complex has a lower binding strength (Log K 10.0/15.0; Table 5.2) with Fh than the Cr(VI) bidentate complex (Log K 19.25; Table 5.2). The Cr(VI) may thus be able to better displace (out compete) Hex2/6 from the mineral surface. I suggest that higher concentrations of Hex2/6 are required to suppress Cr(VI) adsorption. My hypothesis is supported by the report that much higher concentrations of weakly binding anions (in my case Hex2/6) are required to reduce adsorption of strongly binding anions (in my case Cr(VI)) (Mesuere and Fish, 1992b). The different surface coverages and binding strengths of OC also explain why But3/7 suppresses the formation of bidentate Cr(VI) but favours the formation of monodentate Cr(VI). The higher surface coverage by But3/7 likely results in a decreasing amount of surface sites available for the formation of bidentate Cr(VI) complexes, which require two surface sites, whilst the higher binding strength of But3/7 makes it more difficult for Cr(VI) to replace OC and make sites available for the formation of bidentate Cr(VI) complexes. In addition, Fh coprecipitated with OC results in Fh with larger lattice spacings, fewer crystal planes, smaller particle diameters and crystallographic defects

(Eusterhues et al., 2014; Eusterhues et al., 2008), which possibly disproportionally decreases adjacent corner-sharing surface sites that are required for the formation of Cr(VI) bidentate complexes. By contrast, the formation of monodentate Cr(VI) complexes is relatively less influenced by the masking of surface site or changes in surface site types, and as a result, monodentate Cr(VI) complexes are possibly favoured for the But3/7 organominerals.

Another mechanism that might explain the suppression of Cr(VI) adsorption for the Fh_But3/7 organominerals may be related to their spatial location on the surface of iron (oxyhydr)oxide minerals. Previous work suggests that Pen1/5 and Hex2/6 adsorbed via monodentate complexes may adsorb perpendicular to the Fh surface, whilst But3/7 adsorbed by bidentate and/or tridentate complexes necessarily requires the acid molecules to align parallel with the Fh surface (Curti et al., 2021). Previous work also shows that competitive adsorption between FA and As(V) on goethite is much stronger than between HA and As(V) because the distribution of FA is closer to the goethite surface, leading to stronger electrostatic repulsion between adsorbed FA and adsorbing As(V) (Weng et al., 2009). As such if the parallel But3/7 is closer to the mineral surface than the perpendicular Pen1/5 and Hex2/6, then electrostatic repulsion between But3/7 and Cr(VI) will be stronger than that between Pen1/5 / Hex2/6 and Cr(VI), and thus the suppression of Cr(VI) adsorption is likely enhanced.

Table 5.4. Surface coverage of surface sites on Fh end-member by organic acids and Cr(VI)

	Dry weight (g)	Site density (mmol sites/g) [a]	Number of surface sites (mmol sites)
Pure ferrihydrite	0.03		
$\equiv FeOH^{-0.5(e)}$ sites		1.25	0.0375
$\equiv FeOH^{-0.5(c)}$ sites		1.74	0.0522
Total amount			0.0897

Organominerals	Organic matter wt%	Mineral wt%	Total surface sites of Fh (mmol)[b]	Cr(VI) at 100% sorption (mmol)	Coverage of Fh by Cr(VI) bidentate complex (%)	Total carboxyl groups (mmol)	Coverage of Fh with one carboxyl adsorbed (%)	Coverage of Fh with two carboxyl adsorbed (%)	Coverage of three adsorbed (%
Fh_Pen1/5_1.9wt%C	4.03	95.97	0.08608	0.00058	1.34	0.01187	13.78		
Fh_Hex2/6_3.3wt%C	6.69	93.31	0.08370	0.00058	1.38	0.02748	16.42	32.84	
Fh_Hex2/6_6.4wt%C	12.97	87.03	0.07807	0.00058	1.48	0.05329	34.13	68.26	
Fh_But3/7_5.1wt%C	11.53	88.47	0.07936	0.00058	1.45	0.05460		45.87	68.8
Fh_But3/7_6.6wt%C	14.92	85.08	0.07632	0.00058	1.51	0.07066		61.72	92.58
Fh_But3/7_10.2wt%C	23.05	76.95	0.06902	0.00058	1.67	0.10919		105.47	158.20

[a] fixed at those calculated by Moon and Peacock (2013).

[b] calculated using the surface site densities of pure Fh weighted to the mineral:OC mass ratio of each organomineral

5.4.2 Influence of Cr(VI) adsorption on the kinetics of ferrihydrite and ferrihydrite organomineral transformation

The presence of Cr(VI) retards the transformation of Fh in acidic, subneutral and alkaline conditions (Figure 5.4), which corresponds with the inhibition effects caused by other metals like As(V) adsorbed to iron (oxyhydr)oxides (Das et al., 2011a; Hu et al., 2020; Hu et al., 2018). The inhibition mechanisms that I observe with Cr(VI) are likely to be similar to those reported previously with As(V) (Manceau, 1995). The formation of inner-sphere Cr(VI) bidentate and monodentate complexes with -FeOH sites (Johnston and Chrysochoou, 2012; Veselská et al., 2016) likely inhibits Fe-O-Fe polymerisation through inducing distortions in the Fe bonding environment, influencing the cross-linking of chains of edge-sharing Fe octahedra via double corners and then retarding the crystal nucleation and growth of secondary iron minerals (Manceau, 1995). As with other adsorbates, the Cr(VI) adsorbed likely also blocks surface sites to prevent the dissolution of iron (Kaiser and Guggenberger, 2003), and/or changes the electrostatic charge of the mineral surface to influence the aggregation of mineral particles. The extent of the retardation of transformation positively correlates with Cr(VI) concentration, increasing from 0.1 wt%Cr (Cr/Fe = 0.002) to 1.1 wt%Cr (Cr/Fe = 0.02) at 100% adsorption. The reason why 5.4 wt%Cr (Cr/Fe = 0.1) at 100% adsorption induces no further suppressive effect on the transformation of Fh is unclear.

The presence of Cr(VI) in all Fh organomineral systems also retards the transformation of Fh (Figure 5.5). The observations are complicated however, by C loading and binding strength. In the first instance, previous work shows that the presence of the carboxylic acids in the organomineral systems retards the transformation of Fh compared to the pure Fh system (Zhao et al., 2022). This retardation appears to be a function of the number of carboxyl groups in the sequesterd acid molecules and thus generally increases in the order Pen1/5 < Hex2/6 < But3/7 (at pH 5) and Pen1/5 < Hex2/6 ~ But 3/7 (at pH 6.5), whilst the retardation also generally increases with increased C loading (Zhao et al., 2022). Compared with the retardation caused by OC, the magnitude of the retardation observed in the presence of Cr(VI) is significantly less pronounced (Figure 5.5c and d) probably because a much lower concentration of Cr(VI) (1.92×10^{-5} M) is added to the system compared with OC (from 3.96×10^{-4} M for Fh_Pen1/5_1.9wt%C to 1.21×10^{-3} M for Fh_But3/7_10.2wt%C). Even at a lower concentration however, the presence of Cr(VI) still causes a discernable retardation effect (Figure 5.5c and d), especially when an increasing binding strength and concentration of OC do not cause further retardation in the Fh_Hex2/6 and Fh_But3/7 systems at pH 6.5 (Zhao et al., 2022). It is therefore possible that Cr(VI) is able to play a more specific role in retarding the transformation of Fh compared to OC. Both Cr(VI) and OC can influence the factors that control dissolution-recrystallisation and/or solid state transformation and thus effect transformation rate, for example, they can block surface sites and subsequently prevent the dissolution of iron (oxyhydr)oxide to form goethite or the nucleation of hematite (Kaiser and Guggenberger, 2003), and they can associate with the surface of neoformed mineral nuclei and crystals to inhibit crystal growth (Amstaetter et al., 2012; Eusterhues et al., 2008). In addition to these mechanisms however, Cr(VI) is a much smaller molecule (aqueous $HCrO_4^-$ or CrO_4^{2-} species) compared to OC (Pen1/5: $C_5H_{10}O_2$; Hex2/6: $C_6H_{10}O_4$; But3/7: $C_7H_{10}O_6$). This may be important because my temporal data for total C associated with the transforming organomineral surfaces shows that total C decreases in both the absence and presence of Cr(VI) as the transformation proceeds (Figure 5.6). In previous work a similar loss of C during the transformation of Fh organominerals is attributed to the fact that the iron (oxyhydr)oxide becomes more compact with lower specific surface area (Zhao et al., 2022). As a result some OC is lost from the shrinking mineral surface because the initial amount of OC associated with the minerals exceeds the adsorption capacity of the secondary iron minerals, whilst steric hindrance and/or electrostatic repulsion between different OC molecules is also enhanced, which renders some molecules more susceptible to desorption (Zhao et al., 2022). As such, in my Cr(VI)-organomineral system, as the transformation proceeds, the influence of OC on transformation likely declines, whilst smaller Cr(VI) species are still able to access the shrinking mineral surface, and thus further induce distortions in the Fe bonding environment and inhibit crystal nucleation and growth. Furthermore my modelling shows that the binding strength of Cr(VI) bidentate complexes (Log K 19.25) is greater than the binding strength of one-carboxyl complexes (Log K’s 9.2, 10.0/15.0), which may lead to greater distortion of the Fe bonding environment, which then more effectively retards the transformation of Fh.

5.4.3 Distribution of Cr(VI) during the mineralogical transformation

5.4.3.1 Distribution of Cr(VI) in pure ferrihydrite systems

Aqueous Cr(VI) increases during the transformation of Fh (Figure 5.7), likely because the iron (oxyhydr)oxide becomes more compact with lower specific surface area (Zhao et al., 2022) and thus the adsorption capacity for Cr(VI) decreases as the transformation proceeds. As expected aqueous Cr(VI) concentrations are therefore higher for Fh systems that have higher Cr(VI) adsorbed (Figure 5.7). Aqueous Cr(VI) concentrations are also higher for Fh transformed under higher pH conditions (Figure 5.7), likely because there are a greater proportion of deprotonated and thus negatively charged -FeOH sites at higher pH, which electrostatically repel anionic Cr(VI) species.

As the transformation proceeds however, in addition to the loss of Cr(VI) to solution, the Cr(VI) that remains associated with the solid minerals also appears to be re-distributed such that the fraction of Cr(VI) that is desorbable with 0.1 M NaOH decreases whilst the fraction of Cr(VI) that is non-desorbable with 0.1 M NaOH increases (Figure 5.7). A change in the proportion of initially desorbable Cr(VI) to non-desorbable Cr(VI) is also observed during the transformation of Cr(VI) coprecipitated with Fh and suggests that the affinity, and thus the bonding environment, of Cr(VI) changes during the transformation process (Sun et al., 2021; Zhu et al., 2019). Previous studies report that heavy metals like As(V) are converted from desorbable As(V) to non-desorbable As(V) during the transformation of iron (oxyhydr)oxide because As(V) species are incorporated into structural defects or surface pores of iron (oxyhydr)oxides like lepidocrocite, hematite and magnetite, as observed by scanning transmission electron microscopy and extended X-ray absorption fine structure spectroscopy (Hu et al., 2020; Hu et al., 2018; Park et al., 2018; Wang et al., 2011). Like As(V) I therefore attribute my observed decrease in the fraction of desorbable Cr(VI) and concomitant increase in the fraction of non-desorbable Cr(VI) to a migration of desorbable Cr(VI), located on mineral surfaces, into mineral structural defects and/or surface pores of secondary iron minerals. During the transformation of iron (oxyhydr)oxide in natural environments my results therefore indicate that some Cr(VI) adsorbed on mineral surfaces is incorporated into secondary iron minerals and becomes non-desorbable, whilst some Cr(VI) is released into solution as aqueous Cr(VI).

It is noteworthy that in systems with 0.1 wt%Cr (Cr/Fe = 0.002) at 100% adsorption and at pH 5 and 6, all Cr(VI) remains associated with the minerals after 10 days transformation, but the final proportion of non-desorbable Cr(VI) at pH 6.5 is lower than at pH 5.0 (Figure 5.7). This might be attributed to a faster transformation rate at pH 6.5 (Figure 5.4c) and thus a reduced time for Cr(VI) to penetrate into structural defects and/or surface pores of secondary iron minerals. This might also be attributed to the different binding strengths of monodentate and bidentate Cr(VI) complexes. It is reported that Se(IV) that is strongly bound to Fh via inner-sphere complexation is more easily captured into secondary iron minerals during Fh transformation than Se(IV) that is weakly bound via outer-sphere complexation (Börsig et al., 2017). In my experiment, the strongly-bound bidentate Cr(VI) complex dominates at pH 5.0, while the weakly-bound monodentate Cr(VI) complex dominates at pH 6.5. During the transformation process at pH 6.5, it is therefore likely that the lower proportion of bidentate Cr(VI) complexes results in less Cr(VI) incorporated into secondary iron minerals.

5.4.3.2 Distribution of Cr(VI) in ferrihydrite organominerals

The presence of OC can influence the distribution of Cr(VI) during the mineralogical transformation process in a number of different ways, namely via influencing Cr(VI) adsorption, influencing the properties of secondary iron minerals and retarding the transformation itself. Regarding Cr(VI) adsorption, in my Cr(VI) adsorption experiment, the presence of But3/7 inhibits Cr(VI) adsorption onto Fh organominerals by masking the surface adsorption sites and/or inducing an electrostatic repulsion between negatively charged OC and Cr(VI) (Figure 5.2). In the presence of carboxyl-rich and/or high concentrations of mineral-associated OC, a reduced concentration of adsorbed Cr(VI) therefore means that there is a reduced concentration of Cr(VI) that is able to migrate into and be captured in structural defects and/or surface pores as transformation proceeds. Regarding the properties of secondary iron minerals, previous work documents that after desorption of OC, secondary iron minerals formed from Fh organominerals have much higher SSA and total volume of pores (TPV) than those formed from pure Fh (Zhao et al., 2022). Previous work also shows that iron (oxyhydr)oxides like Fh (Eusterhues et al., 2014; Mikutta et al., 2014) and hematite (Lu et al., 2019a; Lu et al., 2019b) formed in the presence of OC have a loose and porous structure. The surface pores in Fh then promote the adsorption of As(V) and inhibit the desorption of As(V) (Mikutta et al., 2014). As such the loose and porous structure of my secondary iron minerals (Zhao et al., 2022) may also facilitate the migration and capture of Cr(VI) during transformation. Regarding transformation rate, previous work investigating the influence of OC on the transformation of Fh (Sun et al., 2021; Zhao et al., 2022) shows that OC retards the transformation of Fh, and thus delays the redistribution of Cr(VI) (Sun et al., 2021) and As(V) (Hu et al., 2018) from mineral surfaces into mineral inside, but the retardation of transformation by OC shows no discernable influence on the final proportions of Cr(VI) and As(V) captured in secondary iron minerals (Hu et al., 2018; Sun et al., 2021).

For Fh_Pen1/5_1.2wt%C with 0.1 wt%Cr (Cr/Fe = 0.002) at 100% adsorption, essentially all Cr(VI) is retained by the solid minerals with negligible aqueous Cr(VI) released during the transformation process. After 19 days transformation ~100% of the solid-associated Cr(VI) is non-desorbable (Figure 5.8), which is significantly higher than that for pure Fh with equivalent Cr(VI) (Figure 5.7). The rate constant for the capture of Cr(VI) ($b = 0.634 \pm 0.077$) is nearly twice that for pure Fh (b=0.337±0.023) at pH 5.0, and also higher than that for pure Fh at pH 6.5 (Table 5.3). The effect of Pen1/5 on the distribution of Cr however, is unlikely to be due to a direct influence on Cr(VI) adsorption. Essentially the presence of Pen1/5 results in no discernable decrease in the adsorption of Cr(VI) (Figure 5.2), and actually, previous work shows that Fh organominerals made with weakly-bound OC like Pen1/5 show a faster adsorption of As(V) and desorption of the weakly-bound OC facilitates As(V) uptake (Mikutta et al., 2014). As such a similar situation may occur with Cr(VI) adsorption onto organominerals of iron (oxyhydr)oxide and Pen1/5, because my modelling shows that Pen1/5 has a much weaker binding strength than Cr(VI) (Table 5.2). Additionally, the more strongly-bound Cr(VI) should readily replace Pen1/5 to access adsorption sites if secondary iron minerals cannot host all of the OC and Cr(VI), as the SSA of iron minerals decreases significantly during the transformation (Zhao et al., 2022). The favourable access of Cr(VI) to adsorption sites then likely facilitates its migration into structural defects and/or surface pores and thus its capture into secondary iron minerals. Similarly, whilst the presence of Pen1/5 retards the transformation of Fh (Zhao et al., 2022), the redistribution of Cr(VI) as measured by its rate of capture of non-desorbable Cr(VI) during transformation is not delayed compared to the pure Fh system (Table 5.3). The effect of Pen1/5 on the distribution of Cr is therefore instead attributed to the way that OC influences secondary iron mineral properties. Previous work documents that secondary iron minerals formed from Fh_Pen1/5 organominerals have larger SSA and TPV than those formed from pure Fh (Zhao et al., 2022). This porous structure of the secondary iron minerals likely favours the migration of Cr(VI) into structural defects and/or surface pores during the transformation, and thus leads to the higher final proportion of non-desorbable Cr(VI) (Figure 5.8) and the higher rate constant for the capture of Cr (Table 5.3) compared to the pure Fh system.

For Fh_Hex2/6 organominerals with 0.1 wt%Cr (Cr/Fe = 0.002) at 100% adsorption, again essentially all Cr(VI) is retained by the solid minerals with negligible aqueous Cr(VI) released during the transformation process, and after 19 days transformation >90% of the solid-associated Cr(VI) is non-desorbable (Figure 5.8), which is significantly higher than during the transformation of pure Fh with equivalent Cr(VI) (Figure 5.7). The rate constants for the capture of Cr(VI) (b =0.555±0.004 / 0.461±0.041) are higher than those for pure Fh (b = 0.337±0.023) at pH 5.0, but are much reduced and similar to those for pure Fh as pH increases to 6.5 (b = 0.418±0.001 / 0.279±0.015 for Fh_Hex2/6 composites vs. b = 0.0.351±0.113 for pure Fh, Table 5.3). As for Pen1/5, the effect of Hex2/6 on the distribution of Cr is unlikely to be due to a direct influence on Cr(VI) adsorption. Whilst the presence of Hex2/6 results in a minor decrease in the adsorption of Cr(VI), this is negligible at or below pH 6.5 (Figure 5.2). Again as for Pen1/5, although the presence of Hex2/6 retards the transformation of Fh (Zhao et al., 2022), the redistribution of Cr(VI) as measured by its rate of capture of non-desorbable Cr(VI) during transformation is not delayed compared to the pure Fh system (Table 5.3). The effect of Hex2/6 on the distribution of Cr is therefore also attributed to the way that OC influences secondary iron mineral properties, where the porous structure of the secondary iron minerals formed from Fh_Hex2/6 organominerals (Zhao et al., 2022) likely favours the migration of Cr(VI) into structural defects and/or surface pores during the transformation, and thus leads to the higher final proportion of non-desorbable Cr(VI) (Figure 5.8) and the higher rate constant for the capture of Cr (Table 5.3) compared to the pure Fh system.

It is notable that Fh_Hex2/6 organominerals have much higher rate constants for the capture of Cr(VI) than pure Fh at pH 5, but similar rate constants for the capture of Cr(VI) to pure Fh at pH 6.5. This is possibly an indirect consequence of the influence of Hex2/6 on Cr(VI) adsorption at different pH conditions. During the transformation, the total C% for Fh_Hex2/6 organominerals decreases during the transformation (Figure 5.6), and although the Fh_Hex2/6 organominerals do not have an oversaturated surface coverage with respect to OC (Table 5.4). This suggests that the secondary iron minerals with lower SSA (Zhao et al., 2022) may have an oversaturated surface coverage with respect to OC, such that they cannot host all the OC. The influences of Hex2/6 on Cr(VI) capture at pH 5 is less significant than at pH 6.5 however, because at pH 5.0, Hex2/6 is adsorbed via two- and one-carboxyl binding, with similar or smaller binding strengths compared to bidentate Cr(VI), which dominates Cr(VI) adsorption at this pH; but at pH 6.5, Hex2/6 is also adsorbed via two- and one-carboxyl binding, but with similar binding strengths compared to monodentate Cr(VI), which dominates Cr(VI) adsorption at this pH (Figure 5.3). Thus at pH 5, bidentate Cr(VI) more easily replaces Hex2/6 and is thus more easily captured into structural defects and/or surface pores, resulting in much higher rate constants for the capture of Cr(VI) at pH 5 compared to pure Fh, while at pH 6.5, monodentate Cr(VI) less easily replaces Hex2/6 and is thus less easily captured into structural defects and/or surface pores, resulting in similar rate constants for the capture of Cr(VI) at pH 6.5 compared to pure Fh.

Differing from Fh_Pen1/5 and Fh_Hex2/6 organominerals, for Fh_But3/7 organominerals with 0.1 wt%Cr (Cr/Fe = 0.002) at 100% adsorption not all Cr(VI) is retained by the solid minerals, such that there is significant aqueous Cr(VI) released during the transformation process, and after 19 days transformation up to ~10% of the total Cr(VI) is aqueous Cr(VI), while ~70 - >90% of the solid-associated Cr(VI) is non-desorbable (Figure 5.8). The fraction of non-desorbable Cr(VI) however, is still significantly higher than during the transformation of pure Fh with equivalent Cr(VI) (Figure 5.7). The rate constants for the capture of Cr(VI) (b =0.406±0.001 / 0.352±0.022 / 0.305±0.009) are higher or equivalent to those for pure Fh (b =0.337±0.023) at pH 5.0, but are much reduced and lower than those for pure Fh (b =0.191±0.0.004 / 0.189±0.012 / 0.148±0.009 for Fh_Hex2/6 composites vs. b = 0.351±0.113 for pure Fh) as pH increases to 6.5 (Table 5.3). Notably there is an increase in aqueous Cr(VI) during the initial stages of transformation, which then decreases as the transformation proceeds, where aqueous Cr(VI) also increases with the C loading of the organominerals (Figure 5.8). I attribute the effect of But3/7 on the distribution of Cr(VI) to a combination of a direct influence on Cr(VI) adsorption, an influence on the properties of secondary iron minerals and an influence on the transformation rate.

Regarding the distribution of aqueous Cr(VI), during the adsorption of Cr(VI) onto Fh organominerals, But3/7 causes a strong suppression of adsorption via masking surface sites and/or electrostatic repulsion (Figure 5.2). During the transformation of Fh organominerals, But3/7 increases the SSA and TPV of secondary iron minerals and substantially retards the transformation rate (Zhao et al., 2022). Taken together, the influence of But3/7 on Cr(VI) adsorption becomes more pronounced as the SSA and thus the adsorption capacity of the minerals decrease with the transformation process in the first several days, leading to higher proportions of aqueous Cr(VI) (Figure 5.8).The inhibition effects on Cr(VI) adsorption are alleviated however, by increasing release of OC from the mineral surface with decreasing SSA as the transformation proceeds because of the enhanced steric hindrance and/or electrostatic repulsion (Figure 5.6), and a substantially slowed transformation rate (Zhao et al., 2022), which together makes available more surface sites, and provides more time, for the smaller sized Cr(VI) to be re-adsorbed. After 19 days aging, the final fraction of aqueous Cr(VI) is even lower than that before the aging of organominerals at pH 6.5, suggesting that the transformation of iron (oxyhydr)oxide eventually decrease the mobility of Cr(VI) although the faction of aqueous Cr(VI) indeed increase during transformation process.

Regarding the distribution of desorbable and non-desorbable Cr(VI), during the transformation, the total C% for Fh_But3/7 organominerals decreases during the transformation (Figure 5.6), and in addition, the Fh_But3/7 organominerals have an oversaturated surface coverage with respect to OC (Table 5.4), such that the secondary iron minerals with lower SSA (Zhao et al., 2022) certainly have an oversaturated surface coverage with respect to OC, and cannot host all the OC. The influence of But3/7 on Cr(VI) capture at pH 5.0 is less significant than at pH 6.5 however, because at pH 5.0, But3/7 is adsorbed via three- or two-carboxyl binding with stronger or similar binding strengths compared to bidentate Cr(VI), which dominates Cr(VI) adsorption at this pH; but at pH 6.5, But3/7 is also adsorbed via three- and two-carboxyl binding, but with much stronger binding strengths compared to monodentate Cr(VI), which dominates Cr(VI) adsorption at this pH (Figure 5.3). Thus at pH 5, whilst bidentate Cr(VI) cannot easily replace But3/7, it can more easily replace But3/7 than monodentate Cr(VI) at pH 6.5; and in addition, the presence of But3/7 creates a more loose and porous mineral structure compared to pure Fh and thus increases the availability of structural defects and surface pores for Cr(VI) capture (Zhao et al., 2022). Taken together these effects result in higher rate constants for the capture of Cr(VI) at pH 5.0 compared to pH 6.5 for Fh_But3/7 organominerals, because at pH 5.0 bidentate Cr(VI) is better able to replace But3/7 than monodentate Cr(VI) at pH 6.5; slightly higher or equivalent rate constants for the capture of Cr(VI) at pH 5.0 compared to pure Fh, because the effects of bidentate Cr(VI) and a more porous mineral structure positively combine; but much lower rate constants for the capture of Cr(VI) at pH 6.5 compared to pure Fh, where the effects of significantly suppressed Cr(VI) adsorption, substantially slower transformation rate and monodentate Cr(VI) negatively combine to result in less overall Cr(VI) capture. On the whole, for Fh_But3/7 organominerals with 0.1 wt%Cr (Cr/Fe = 0.002) at 100% adsorption however, the fraction of non-desorbable Cr(VI) at the end of transformation is still slightly higher at pH 5.0 (~90% vs. ~80% for equivalent pure Fh) and pH 6.5 (~70% vs. ~65% for equivalent pure Fh) compared to pure Fh (Figure 5.6 and 5.7).

Overall the redistribution of Cr(VI) during the mineralogical transformation of Fh in organominerals is strongly controlled by the effects of OC on secondary mineral properties, where the presence of OC results in a loose and porous secondary iron mineral structure, which significantly increases the final proportion of Cr(VI) captured by minerals compared to pure Fh (Figure 5.9). The redistribution of Cr(VI) is also influenced by the effects of OC on Cr(VI) adsorption, and specifically the relative binding strength of OC and Cr(VI). Weakly-bound carboxyl-poor OC has negligible influence on Cr(VI) adsorption because Cr(VI) can easily replace OC to access adsorption sites as mineral SSA and thus surface site densities decrease and structural defects and/or surface pores increase in the presence of OC during transformation, which increases the rate constant for the capture of non-desorbable Cr(VI) and increases the final proportion of non-desorbable Cr(VI) captured in neoformed minerals, compared to pure Fh system (Figure 5.9b). Strongly-bound carboxyl-rich OC however, significantly inhibits Cr(VI) adsorption, which results in lower rate constants for the capture of non-desorbable Cr(VI) compared to carboxyl-poor organominerals, and lower rate constants for the capture of non-desorbable Cr(VI) at higher pH compared to pure Fh. Strongly-bound carboxyl-rich OC also decreases the final proportion of non-desorbable Cr(VI) captured in neoformed minerals compared to carboxyl-poor organominerals, but still slightly increases the final proportion of non-desorbable Cr(VI) captured in neoformed minerals compared to pure Fh (Figure 5.9c). Based on my results however, increasingly strongly-bound carboxyl-rich OC and elevated C loadings with iron (oxyhydr)oxides may result in lower rate constants for the capture of non-desorbable Cr(VI) but also lower proportions of non-desorbable Cr(VI) captured in secondary iron minerals compared to pure Fh. The mobility and fate of Cr(VI) in soils and sediments as iron (oxyhydr)oxide organominerals transform is therefore likely strongly controlled by the carboxyl-richness of OC in the organominerals.

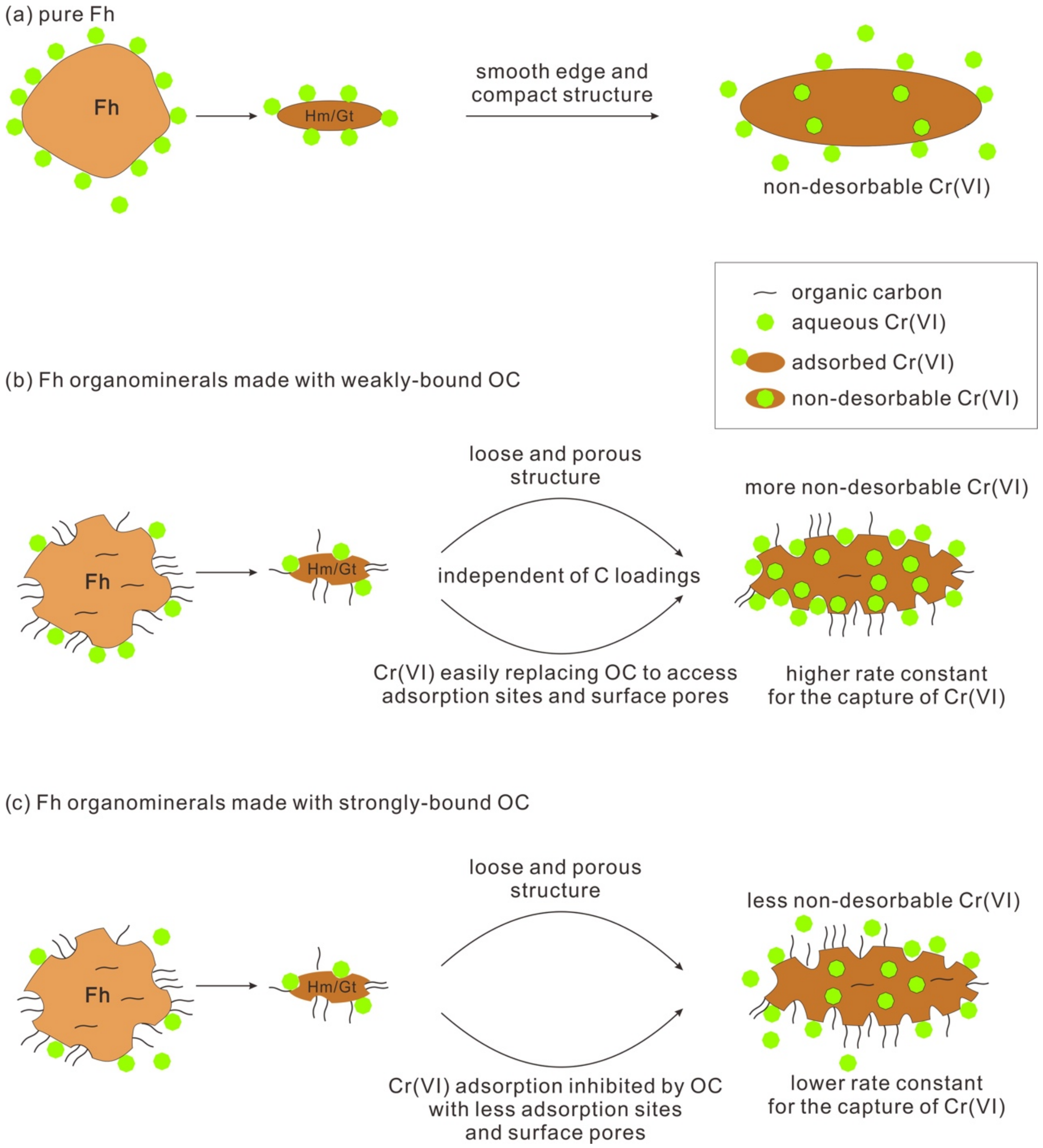

Figure 5.9. Diagram illustrating the influences of OC with different binding strengths on the total amount of Cr(VI) that is non-desorbable with 0.1 M NaOH and the rate constant for the capture of non-desorbable Cr(VI) into structural defects and surface pores during the mineralogical transformation of iron (oxyhydr)oxide organominerals.

5.5 Conclusion

My adsorption experiment and surface complexation model results show that the binding strengths of carboxylic OC and Cr(VI) complexes follow the order one-carboxyl binding ~

monodentate Cr(VI) binding < two carboxyl binding ~ bidentate Cr(VI) binding < three-carboxyl binding. Regarding the influences of OC on Cr(VI) adsorption, for Fh_Pen1/5 and Fh_Hex2/6 organominerals, the presence of weakly-bond OC at different C loadings has almost no discernable influence on Cr(VI) adsorption, while for Fh_But3/7 organominerals, the strongly-bond OC significantly suppress Cr(VI) adsorption via surface masking and/or electrostatic repulsion. Regarding the mineralogical transformation of iron (oxyhydr)oxide, I show that the presence of Cr(VI) retards the transformation rates of Fh in various pH conditions, whilst Cr(VI) also cause discernable retardation on the transformation of Fh organominerals even at a lower concentration, suggesting a more specific role of Cr(VI) in retarding the transformation of Fh compared to OC. Regarding the distribution of Cr(VI) during the transformation process, for pure Fh system the fraction of aqueous Cr(VI) increases with the reaction time, which are enhanced with increasing Cr(VI) concentrations and pH conditions, whilst the fraction of Cr(VI) which are non-desorbable with 0.1 M NaOH increases with transformation process, suggesting the bonding environment of Cr(VI) changes during the transformation. For Fh organominerals, the redistribution of Cr(VI) is strongly controlled by the effects of OC on secondary mineral properties, the presence of OC results in a loose and porous secondary iron mineral structure, which significantly increases the final proportion of Cr(VI) captured by minerals compared to pure Fh. The redistribution of Cr(VI) is also influenced by the effects of OC on Cr(VI) adsorption, and specifically the relative binding strength of OC and Cr(VI): weakly-bound carboxyl-poor OC has negligible influence on Cr(VI) adsorption because Cr(VI) can easily replace OC access adsorption sites, together with the loose and porous structure in secondary iron minerals, which increases the rate constant for the capture of non-desorbable Cr(VI) and increases the final proportion of non-desorbable Cr(VI) captured in neoformed minerals; strongly-bound carboxyl-rich OC however, significantly inhibits Cr(VI) adsorption, which results in lower rate constants for the capture of non-desorbable Cr(VI) and decreases the final proportion of non-desorbable Cr(VI) captured in neoformed minerals compared to carboxyl-poor organominerals. I expect that increasingly strongly-bound carboxyl-rich OC and elevated C loadings with iron (oxyhydr)oxides may result in lower rate constants for the capture of non-desorbable Cr(VI) and also lower proportions of non-desorbable Cr(VI) captured in secondary iron minerals compared to pure Fh. The mobility and fate of Cr(VI) in soils and sediments as iron (oxyhydr)oxide organominerals transform is therefore likely strongly controlled by the carboxyl-richness of OC in the organominerals.

Chapter 6 Behaviours and fate of chromium and carbon during Fe(II)-induced transformation of ferrihydrite organominerals

ABSTRACT

Chromium is one of the most common metal contaminants at high concentration but also one of the most import nutrients at low concentration in soils, whose mobility is controlled by soil minerals, especially iron (oxyhydr)oxide. The influence of organic carbon (OC) with different binding strengths on the mobility and fate of Cr(VI) during Fe(II)-induced transformation of iron (oxyhydr)oxide however, is still unclear. Here I investigate how OC binding strength influences the Fe(II)-induced transformation of Fh and subsequently controls the mobility of Cr, and how Cr influences the retention or release of the associated OC at the same time. I focus on carboxyl-rich OC coprecipitated with ferrihydrite (Fh), track the mineralogical properties of the secondary iron minerals and monitor the re-distribution of Cr(VI/III) and OC. My results show that the presence of OC retards the transformation from Fh to goethite and lepidocrocite at pH 5.75, where the inhibition by OC is enhanced with the carboxyl-richness of the sequestered OC moieties. The carboxyl-rich OC (But3/7 acid) effectively stabilizes Lp for longer time during the Fe(II)-induced transformation process. I also show that the presence of OC appears to rise the rate of capture of non-desorbable Cr, but this facilitation effect is mitigated with the carboxyl-richness of the sequestered acids. Whilst the presence of OC lessens the final proportion of non-desorbable Cr at the end of reaction and the suppression effect is enhanced with the carboxyl richness of the OC moieties. I also show that the presence of Cr(III) causes more structural disorder in the secondary iron minerals, which probably suggests that these secondary iron minerals have lower crystallinity and higher surface OH reactivity. The presence of Cr(III) effectively stabilises lepidocrocite and also aids the stabilisation of OC with the solid phase, where the absolute amount of OC elevated by Cr(III) appears to increase with carboxyl-richness of the sequestered OC moieties. My study sheds new light on the mobility and fate of Cr in redox environments and also deepens my understanding about the potential for remediation of Cr(VI) contaminated soils via a reduction method.

6.1 Introduction

Chromium (Cr) is the 7th most abundant element on Earth (Katz and Salem, 1994) and a bioessential element (Schwarz and Mertz, 1959; Jeejebhoy et al., 1977), yet depending on concentration and valency, Cr is also one of most common metal contaminants (Dhal et al., 2013b). Chromium exists in nine valence states ranging from -2 to +6, being Cr(III) and Cr(VI) are the two most common, with Cr(III) predominating under reducing conditions, and Cr(VI) predominating under oxidising conditions (Emsely, 1989). Cr(III) has a low solubility under natural conditions and readily precipitates as amorphous Cr(III) (hydr)oxide, limiting its mobility, and is essential to fauna in low concentrations (for normal carbohydrate, lipid and protein metabolism, as well as amino- and nucleic acid synthesis) (Schwarz and Mertz, 1959; Jeejebhoy et al., 1977). However, Cr(VI) is highly soluble, bioavailable and highly toxic, presenting a mobile, biohazard in aquatic and soil ecosystems (Chandra and Kulshreshtha, 2004; Costa, 1997; Shanker et al., 2005). Despite these dangers, the interactions between chromium and soil constituents are still poorly understood, which limits my ability to predict its mobility and fate within environmental systems.

Ferrihydrite (Fh) is a common iron (oxyhydr)oxide mineral in soils with near ubiquitous occurrence (Cornell and Schwertmann, 2003; Lu et al., 2020). Fh is highly reactive due to its large adsorption capacity (Hiemstra, 2013; Larsen and Postma, 2001; Michel et al., 2007b), making it the most efficient adsorbent for Cr and organic carbon (OC) in soil systems (Sparks, 2003). The complexation between Fh and OC is widely assumed to facilitate the stability of OC in soils, as iron minerals can adsorb or physically isolate OC and then protect it against microbial degradation (Hemingway et al., 2019; Kaiser and Guggenberger, 2007; Mikutta et al., 2006; Newcomb et al., 2017; Torn et al., 1997). As a result, reactive iron bound OC accounts for up to 40% of the total soil OC pool across a range of soil types (Wagai and Mayer, 2007; Zhao et al., 2016).

The interactions of OC with Fh to form organominerals can alter the reactivity of Fh which may impact its interactions with Cr(VI/III) by: i) increasing crystallographic defects (Eusterhues et al., 2008); ii) increasing Fe reactivity (Eusterhues et al., 2014; Fisher et al., 2020); iii) decreasing sorption capacity by blocking mineral surface sites (Chen et al., 2014; Mikutta et al., 2014) and/or via competitive adsorption (Mesuere and Fish, 1992b). Cr(III) sorption can also be increased by the presence of OC, providing additional sites for Cr(III) to bond with (Gustafsson et al., 2014; Yang et al., 2020; Zhang et al., 2017; Zhang et al., 2018) or increase the mobility of Cr(III) via chelation with dissolved OC moieties such as citric acid (Bartlett, 1991). The presence of OC can also influence the redox reactions of Cr(VI) by acting as an electron donor (Wang et al., 2020b; Zhang et al., 2017; Zhang et al., 2018), electron shuttle (Xu et al., 2019) or improving the reactivity of Cr(VI) toward the reduction reaction by forming complexes between Cr(VI) and OC (Jiang et al., 2019).

Under anoxic conditions transformation of Fh is significantly catalysed by Fe(II). This is likely via electron transfer between bound Fe(II) and Fe(III) within the mineral structure. This electron transfer can facilitate the reductive dissolution of Fh which subsequently re-crystallises in more crystalline forms such as Lp and Gt (Pedersen et al., 2005; Tronc et al., 1992). Despite this classic dissolution and recrystallisation mechanism, oriented aggregation is also very important in the Fe(II)-induced transformation of Lp to Gt (Yan et al., 2015b). The transformation of Fh catalysed by Fe(II) may significantly impact the mobility and fate of Cr(VI) (Hu et al., 2019; Yu et al., 2020). Under reducing conditions, highly mobile and toxic Cr(VI) readily oxidises Fe(II) to Fe(III) and as a result is itself reduced to the low-mobility and less toxic Cr(III) oxidation state (Buerge and Hug, 1997). This Cr(III) can be rapidly and strongly adsorbed by iron (oxyhydr)oxides (Richard and Bourg, 1991b; Xia et al., 2020), increasing the retention of Cr(III) in soils. Additionally, Cr(III) is found to substitute into the crystal structure of various iron minerals like goethite (Gt), hematite (Hm) and magnetite (Mg) (Charlet and Manceau, 1992; Choppala and Burton, 2018; Dai et al., 2016; Hua et al., 2018; Manceau et al., 2000; Maslar et al., 2001; Tang et al., 2010; Trolard et al., 1995) but not lepidocrocite (Lp) (Cornell and Schwertmann, 2003). During this substitution process, some Cr(VI) is also found to be incorporated into the Cr(III)-Fe(III) co-precipitates, lowering the mobility of Cr(VI) (Hu et al., 2019; Yu et al., 2020).

To date, only one study examines the Fe(II)-catalyzed transformation of Fh and Fh organominerals with Cr(VI) adsorbed (Yu et al., 2020), and finds that humic acids in the organominerals immobilise more Cr by reducing Cr(VI) to Cr(III) and providing adsorption sites for Cr(III) to form complexes. Cr(III) preferentially associates with Fh in Fh organominerals observed by extended X-ray absorption fine structure spectroscopy (Xia et al., 2022; Xia et al., 2020), and thus the OC in Fh organominerals may impact Cr(III) capture indirectly through influencing the transformation of iron (oxyhydr)oxide. The capture of Cr(III) may be suppressed by OC via these mechanisms: OC can decrease the transformation rates of

Fh to inhibit the coprecipitation of $(Cr,Fe)(OH)_3$; OC can favour the formation of Lp, which can not host any Cr(III) within the mineral structure (Cornell and Schwertmann, 2003); OC can inhibit the crystal growth of Gt by passivating mineral surface and hindering the oriented aggregation. The capture of Cr(III) may be accelerated because of the different properties of iron (oxyhydr)oxide coprecipitated with OC. It is reported that iron (oxyhydr)oxides like Fh (Eusterhues et al., 2014; Mikutta et al., 2014) and Hm (Lu et al., 2019a; Lu et al., 2019b) coprecipitated with OC have loose and porous structures, and the secondary iron minerals formed from Fh organominerals made with the same OC as this study have much higher specific surface area and total volume of pores than secondary iron minerals formed from pure Fh (Zhao et al., 2022). It is likely that the loose and porous structure in iron (oxyhydr)oxide may also facilitate the capture of Cr during Fe(II)-induced transformation. There is still a large knowledge gap however, about how OC with different binding strengths influences the transformation rates, pathways and properties of iron minerals (Chen et al., 2015; Chen and Sparks, 2018; Hu et al., 2020; Karimian et al., 2019; Sheng et al., 2020b; Zhou et al., 2018b) and then impacts the mobility of Cr in a reductive environment.

In addition to the redistribution of Cr during the transformation of iron (oxyhydr)oxide, the stabilisation of OC is also affected by the Fe(II)-induced transformation of Fh organominerals (Chen et al., 2020; Chen et al., 2015). The reductive dissolution of Fh organominerals releases bound OC, making it more bioavailable for microbes, enhancing degradation of OC in soils (Adhikari et al., 2017; Canfield, 1993; Chen et al., 2020; Han et al., 2019). The transformation of Fh to Gt or Lp however, may also decrease the bioavailability of OC via occlusion within mineral structure defects or nano-pore spaces, strengthening OC fixation and thus increasing the residence time of OC in soils (Hu et al., 2020). The stabilisation of OC may also be influenced by adsorbates on Fh organominerals. Where anions like phosphate and arsenate compete for adsorption sites on the surface of iron minerals, increasing the desorption of OC (Grafe et al., 2002), while polycations like Ca(II) and Mg(II) might increase the OC sequestration by cation-bridging effects, forming iron (oxyhydr)oxide-cation-OC ternary complexes (Rowley et al., 2017; Sowers et al., 2018a; Sowers et al., 2018b). As a result of the complex interactions between ions, OC and Fh described above, little is known about how each component may impact the others mobility and bioavailability in soil systems where they coexist. Specifically, how Cr(VI) species existing as oxyanions influence the migration of OC or how Cr(III) cations influence the stabilisation of OC with solid during Fe(II)-induced transformation of Fh organominerals are unknown.

To address these knowledge gaps this study aims to (1) determining how different OC moieties with different carboxyl richness and Cr(III) influence the rates and pathway of Fh mineralogical transformation; (2) investigating how OC carboxyl-richness impacts the distribution of Cr during the Fe(II)-induced transformation of Fh and Fh organominerals; and (3) investigating how Cr(III) influences the properties of secondary iron minerals and thus influences the stabilisation of OC during the transformation process. To achieve these objectives I use simple mono-, di- and tri-carboxylic acids as analogues for common low molecular weight, carboxyl-rich soil OC, possessing increasing carboxyl-richness and thus increasing binding strength to the Fh organomineral coprecipitate particles (Curti et al., 2021). After reaching equilibrium for Cr(VI) adsorption onto Fh and Fh organominerals, I conduct Fe(II)-induced transformation experiments of Fh and Fh organominerals under anoxic conditions to observe the transformation of iron (oxyhydr)oxides, and the changes in the distribution of Cr and OC.

6.2 Experimental methods

6.2.1 Preparations for mineralogical transformation experiment

Pure ferrihydrite (Fh) was prepared following the method of Schwertmann and Cornell (2000) for the precipitation of 2-line ferrihydrite via hydrolysis of Fe(III) salt solution. Briefly, Fh was prepared by rapid hydrolysis of 0.1 M $Fe(NO_3)_3 \cdot 9H_2O$ (aq) with 1 M KOH to maintain a final pH of 7. Fh was washed several times over a week with 18.2 MΩ·cm MilliQ water until the conductivity of supernatant was the same as DI water, after which Fh was stored as a slurry at 4 ^oC, following standard protocols to maintain mineralogical integrity (Schwertmann and Cornell, 2000). Plastic labware and AR grade reagents are used throughout the preparations.

Three Fh-OC organomineral composites with different wt%C were prepared with three simple carboxylic acids, denoted as acid*n/m*, where acid refers to the first tree letters of the acid IUPAC name; *n* denotes the number of carboxyl groups and *m* denotes the total number of carbon atoms. The acid used were pentanoic acid (Pen1/5), hexanedioic acid (Hex2/6) and butane 1, 2, 4 tricarboxylic acid (But3/7), which have one, two and three carboxyl functional groups, respectively. The 0.1 M $Fe(NO_3)_3 \cdot 9H_2O$ (aq) solutions were mixed with different organic acid solutions prior to hydrolysis up to pH 7 as above for the pure Fh. An aliquot of each composite was then freeze-dried for C analysis with LECO SC-144DR Dual Range

Sulphur and Carbon Analyzer. As a result, three organominerals were obtained: Fh-pentanoic acid with 8.7 wt%C (Fh_Pen1/5_8.7wt%C), Fh-hexanedioic acid with 8.4 wt%C (Fh_Hex2/6_8.4wt%C) and Fh-butane 1, 2, 4 tricarboxylic acid with 10.1 wt%C (Fh_But3/7_10.1wt%C).

An aliquot of the non-freeze-dried pure Fh and Fh organomineral slurries were added to 0.01 M $NaNO_3$ background electrolyte to give a total volume of 50 mL with a solid solution ration of 2 g L^{-1} in the presence or absence of 20 ppm Cr(VI). The suspensions were then adjusted to environmentally relevant pH values of 5.75 and 7 using dilute NaOH or HNO_3 and buffered using 30 mmol L^{-1} organic buffer 2-(N-Morpholino)ethane-sulphonic acid (MES) and 3-(N-Morpholino)propanesulphonic acid (MOPS), respectively. These buffer solutions are negligibly sequestered to Fh (see Supplementary Information) and have been shown to have negligible impact on the recrystallisation of Fh to more crystalline Fe minerals during aging (Bradbury and Baeyens, 1999; Chen et al., 2020; Ford et al., 1999; Wang et al., 2020a). After shaking continuously for 24h to reach equilibrium, the resultant solutions were transferred to an anoxic chamber (95% N_2 and 5% H_2). All the solutions were purged with high purity N_2 for at least 0.5h before they were transferred into the glove box and then exposed to the atmosphere of glove box for 24h to remove the trace dissolved oxygen. A stock Fe(II) solution ($FeCl_2$) was then added to the suspension to induce the mineralogical transformation of the iron minerals. For experiments with Cr(VI) added, 105 ppm Fe(II) (1.88 mM) were added to reduce 20 ppm Cr(VI) (0.385 mM) to Cr(III), where theoretically Fe(II) remained were calculated based on the conversation of electron: $Fe(II)_{remained} = Fe(II)_{total} - 3 \times Cr(VI)_{reduced} = 1.88\ mM - 3 \times 0.385\ mM = 0.725\ mM$ (40.5 ppm). To observe the influence of Cr on the transformation, Fe(II) added in experiments without Cr(VI) were also controlled at around 40.5 ppm corresponding to 0.363 mmol Fe(II)/g Fh. The amount of Fe(II) added in our systems were lower than 10% compared to our total amount of Fe(III) in Ferrihydrite (2g/L). The 18-days reaction time was sufficient to achieve complete mineralogical transformation in most reaction systems, which were monitored by Fourier-transform infrared spectroscopy (FTIR). During the reactions, the experiments were agitated three times per day. In order to allow a time-resolved investigation of mineralogical transformation, Cr redistribution and OC redistribution, aliquots of the suspensions were collected at time intervals of: 0.5 h, 1 d, 2 d, 4 d, 6 d, 8 d, 12 d and 18 d and the pH was recorded at the same time.

For the observation of mineralogical transformation, subsamples were collected from each experiment for Fe(II) analyses and Fourier-transform infrared spectroscopy (FTIR) measurement following the method of (Sheng et al., 2020a; Xiao et al., 2017). Briefly, 1 mL samples of the homogeneous suspension were removed and centrifuged at around 6000 g for 3 minutes. The supernatant was filtered with 0.22 μm PES syringe filters for the measurement of aqueous Fe(II) concentration ([Fe(II)$_{aq}$]). After the removal of the supernatant, 1 mL of 5 mM or 10 mM HCl was then added to remove Fe(II) adsorbed on the minerals. For pure Fh and Fh_Pen1/5 systems, 5 mM could desorb Fe(II) at a high efficiency, while for Fh_Hex2/6 and Fh_But3/7 systems, 10 mM was needed because the adsorbed OC could react with aqueous H^+ and influence the pH of the suspensions. The suspension was mixed homogeneously three times at least by hand then centrifuged after reacting for 10 min. The supernatant was also filtered with 0.22 μm PES syringe filters for Fe(II) measurement, which is operationally defined as desorbable Fe(II) (Fe(II)$_{desorbable}$). The concentration of Fe(II) was measured by ferrozine assay (Sheng et al., 2020a; Stookey, 1970) within 6 h and the recovery efficiency are shown in Appendixes Section 7. The iron oxide solid remaining was then rinsed with 18.2 MΩ·cm Milli-Q water and then made up to 100 μL with 18.2 MΩ·cm Milli-Q water for mineral characterisation by FTIR. Another 1 mL aliquots were centrifuged and washed with 18.2 MΩ·cm Milli-Q water for FTIR measurement to characterise mineral properties, where the 5 mM or 10 mM HCl acids were not applied because HCl acids may change the surface properties of iron minerals.

For the observation of Cr species and distribution, two 1 mL aliquots were collected from each reactor suspension at regular time intervals. After centrifugation at around 6000 g for 3 mins, the supernatant was filtered with 0.22 μm PES syringe filters for the measurement of aqueous Cr(VI) with 1,5-diphenylcarbazide (Bartlett and James, 1979; Borges et al., 2002) and aqueous Cr (VI and III) by inductively coupled plasma mass spectrometry (ICP-MS). After removing all supernatant, the solid minerals were removed from the anoxic chamber. One aliquot was treated with 1 mL 0.1 M NaOH to desorb Cr(VI) like the treatment of As(V) (Hu et al., 2018), which was operationally defined as desorbable Cr(VI) (Cr(VI)$_{desorbable}$). After shaking gently for 24 h, the suspension was centrifuged and filtered with 0.22 μm PES syringe filters for the measurement of desorbable Cr(VI) by 1,5-diphenylcarbazide method, which was also checked by ICP-MS to ensure the absence of Cr(III). The other aliquot was treated with 1mL 200 ppm $KMnO_4$ and 0.1 M NaOH mixture solution to desorb Cr(VI and III) from the mineral surface.

The $KMnO_4$ solution can oxidize Cr(III) to Cr(VI) quickly and effectively (Rogers, 2016), and then the Cr(VI) will be desorbed from minerals. After shaking for 24 h, the suspensions were centrifuged and the supernatant was transferred into new tubes. Then the supernatants were heated at 75℃ for 24 h to decompose $KMnO_4$ because the presence of $KMnO_4$ can influence the measurement of Cr(VI) by 1,5-diphenylcarbazide method (Rogers, 2016). The desorption efficiency in my treatments was over 95% (see Appendixes Section 7). The desorbable Cr(III) was calculated by desorbable Cr(VI and III) minus desorbable Cr(VI), and the non-desorbable Cr was calculated based on the mass balance.

For the observation of OC redistribution, two 15 mL aliquots were subsampled from the reactor and filtered with 0.22 μm cellulose nitrate filters using a vacuum filtration system. The mineral particles were collected and rinsed using 15 mL DI water. One of the mineral particle subsamples was freeze-dried and kept at 4 ^{o}C for total solid C measurement ($C_{\text{solid-total}}$). The other mineral particle subsample was re-suspended in 15 mL 0.1 M NaOH and shaken for 24 h to extract OC from the solid (Kaiser and Guggenberger, 2000). After the mineral particles treated with 0.1 M NaOH were filtered with 0.22 μm PES filters, they were washed, freeze-dried and kept for C measurement, which was operationally defined as non-desorbable OC ($C_{\text{non-desorbable}}$). For Fh-OC organominerals, the C data obtained by LECO were not modified by subtracting the inorganic C content in pure Fh. All operations above were conducted at least in duplicate.

6.2.2 FTIR characterization

FTIR spectra of the solid mineral phase were collected using Attenuated Total Reflectance Fourier transform infrared spectroscopy (ATR-FTIR) (Agilent 4500a FTIR with an ATR) to observe changes in iron mineralogy and the respective proportions of each mineral phase during the transformation process (Namduri and Nasrazadani, 2008; Xiao et al., 2017). To achieve this, a 1.5 μL aliquot of well mixed sample suspension was placed onto the 1 mm diameter ZnSe crystal of a mounting plate and air dried. Complete coverage of the 1 mm diamond crystal was achieved by adding an additional 1.5 μL aliquot, which did not cause any increase in intensity (Xiao et al., 2017). FTIR spectra were obtained by accumulating 64 scans over an energy range of 650 to 4000 cm^{-1} with a spectral resolution of 4 cm^{-1}. The quantities of Gt and Lp in each reaction product were determined from comparison of signature peak heights (Lp 1020 cm^{-1} and Gt 890 cm^{-1}) to those of synthetic reference materials from calibration mixture prepared using 0%, 25%, 75% and 100% of a range of Fe(III) oxide mixtures. After three equivalent runs of each of the sets of the samples, the average values of background subtracted peak intensity results were used for obtaining calibration curve. All spectra were analyzed using the SpectraGryph - optical spectroscopy software and Origin software program.

The OH stretching vibrations observed by FTIR spectroscopy provide robust information about the crystallinity and cation substitution of iron minerals (Cornell and Schwertmann, 2003), which are applied to trace the increase in structural order during the transformation from Fh to Gt (Bazilevskaya et al., 2012) and to study the influence of Cr on changes in structural order and crystallinity of iron (oxyhydr)oxide here. The OH stretching vibrations are characterised by relatively broad bands which overlap, therefore Gaussian deconvolution of the peaks is required to extract information about the contributions of the different OH groups (Bazilevskaya et al., 2012; Boily et al., 2006). The IR OH-stretching vibrations from 2600 to 3800 cm^{-1} for iron minerals are attributed to three major types, namely non-stoichiometric hydroxyls and stoichiometric (or bulk) OH groups (Bazilevskaya et al., 2012) with a shoulder at lower frequencies (Boily et al., 2006). The non-stoichiometric hydroxyl units are related to structural defects and their formation can be explained by one iron ion being replaced by three hydrogen ions (Ruan et al., 2002). Most of the non-stoichiometric hydroxyls is considered to have high reactivity and mobility which indicate a greater degree of disorder (Ruan et al., 2002). Their stretches can form higher energy bands in the range of 3400-3480 cm^{-1} for Gt, where weakly hydro-bonded surface hydroxyl may also exist (Rochester and Topham, 1979). The stoichiometric OH groups are those located in the bulk structure, which are not reactive in adsorption/desorption processes (Morterra et al., 1984). The stretching vibrations of these stoichiometric OH groups tend to form a main infrared band with a shoulder at lower frequencies like Gt with structural hydroxyl stretches in the range of 3050-3240 cm^{-1} with a shoulder at 2760 cm^{-1} (Boily et al., 2006). The frequencies of stoichiometric OH stretching are influenced by crystallinity and crystal size of iron minerals and by the infrared technique used (Bazilevskaya et al., 2012), which explains the differences in the OH stretching bands for my standard minerals and products.

6.3 Results

6.3.1 Mineralogical transformation of iron minerals

6.3.1.1 Temporal variations in Fe(II) pools

The total amount of aqueous Fe(II) and desorbable Fe(II) for all systems are shown in Figure 6.1. As mentioned above, 105 ppm Fe(II) was added to react with Cr(VI), but at the first sampling at 0.5 h the total amount of aqueous and desorbable Fe(II) are similar to that without Cr(VI) present (~40.5 ppm Fe(II) added), suggesting that most Cr(VI) have undergone a redox reaction with Fe(II) within 0.5 h. At pH 5.75, the total amount of aqueous and desorbable Fe(II) are constant for all systems over 18 days (Figure 6.1a and b). By contrast, at pH 7 the total amount of aqueous and desorbable Fe(II) for Fh, Fh_Pen/5_8.7wt%C and Fh_Hex2/6_8.4wt%C show a decreasing trend with reaction time, while Fh_But3/7_10.1wt%C has stable amount of aqueous and desorbable Fe(II) (Figure 6.1c and d).

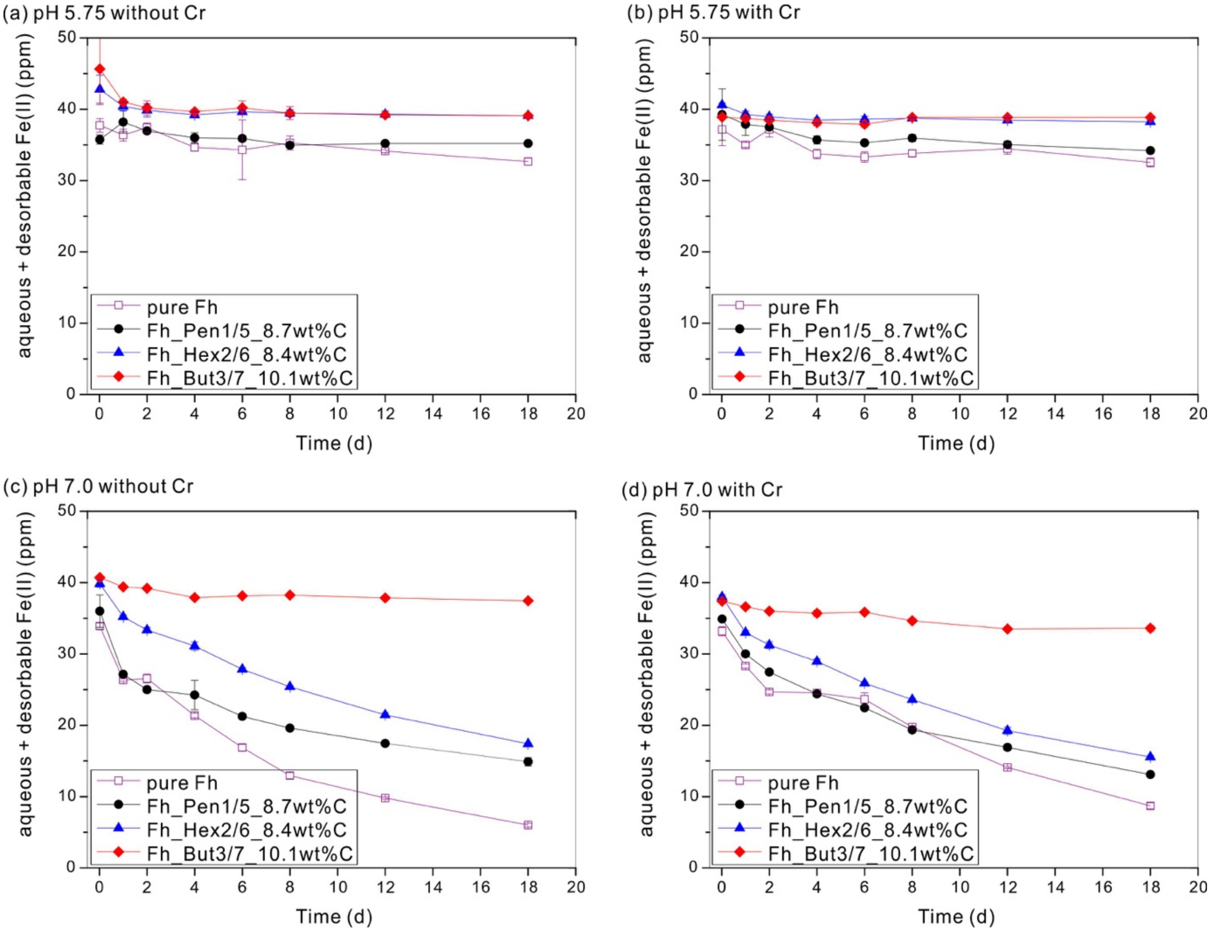

Figure 6.1. Time-dependent changes in total amount of aqueous and desorbable Fe(II) during the transformation of pure Fh and Fh organominerals with and without Cr(VI) adsorbed. Pen1/5,

Hex2/6 and But3/7 represent simple carboxyl-rich OC with one, two and three carboxyl groups, respectively. Error bars represent standard deviations of duplicate samples.

6.3.1.2 Solid characterisation by FTIR

The relative proportions of Gt and Lp during the transformation of pure Fh and Fh organominerals are shown in Figure 6.2. The quantitative analysis were conducted by measuring the absorbance of characteristic bands for Gt (890 cm^{-1}) and Lp (1020 cm^{-1}) (Xiao et al., 2017). For all systems, the proportion of Gt increases with reaction time, whilst the proportion of Lp generally increases firstly and then decreases. The rates for the formation of Gt and Lp are higher at pH 7.00 (Figure 6.2 i-p) than at pH 5.75 (Figure 6.2 a-h). The inhibitive influence of OC on the formation of Gt and Lp at pH 5.75 increases with the carboxyl-richness in the sequestered organic molecules and follow the order pure Fh ~ Pen1/7 < Hex2/6 < But3/7.

In the pure Fh, Fh_Pen1/5_8.7wt%C and Fh_Hex2/6_8.4wt%C experiments, the final total proportion of Gt and Lp are around 100% at pH 5.75 after 18 days, higher than that at pH 7.00. For Fh_But3/7_10.1wt%C however, the final proportions of Gt and Lp are near 100% at pH 7.00 (Figure 6.2o). It is also observed that the presence of the But3/7 acid and Cr inhibits the conversion from Lp to other minerals in pure Fh (Figure 6.2i and j) and Fh_But3/7_8.4 wt%C experiments (Figure 6.2o and p) at pH 7.00.

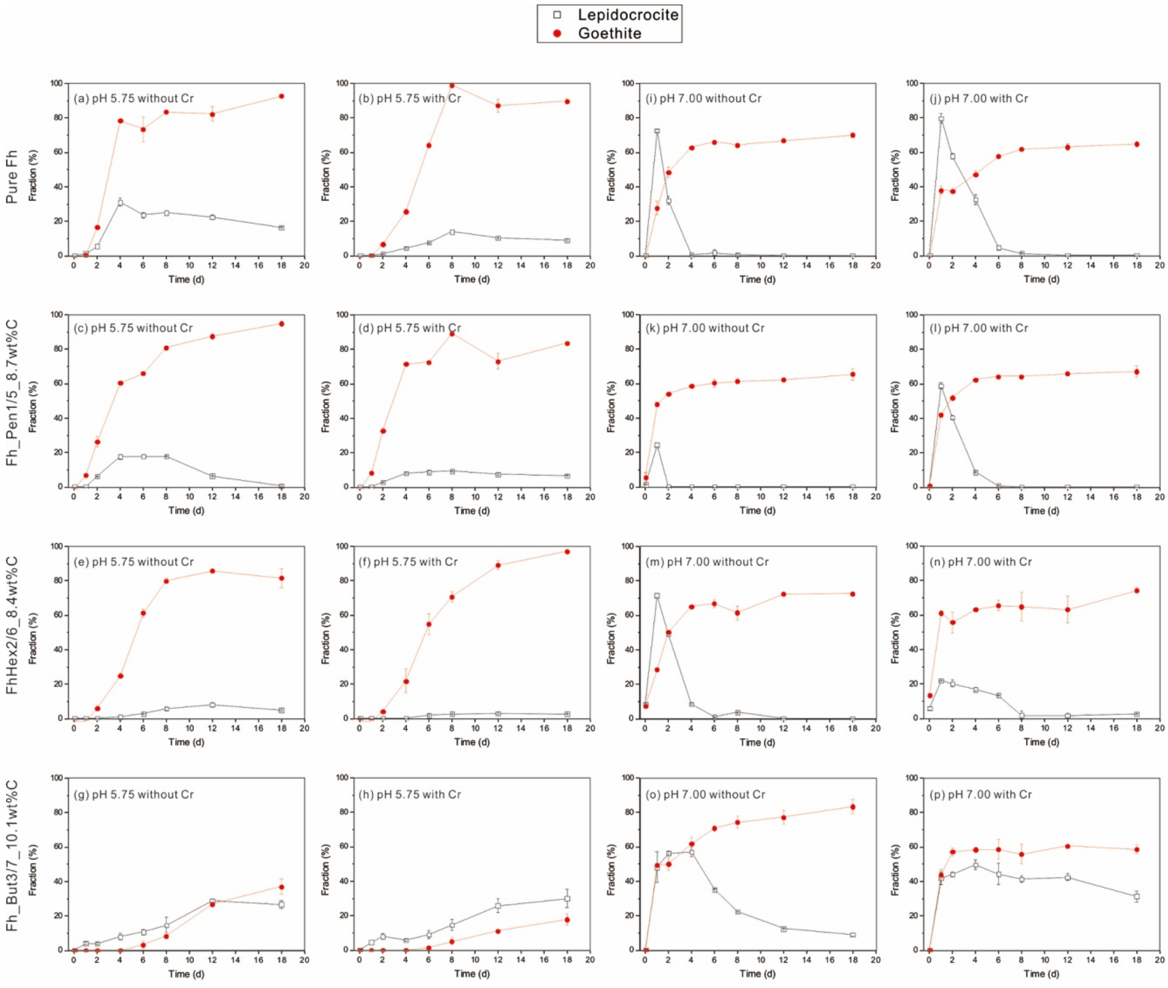

Figure 6.2. Relative proportions of Gt (red solid circles) and Lp (black open squares), respectively, during the Fe(II)-catalysed transformation of pure Fh and Fh organominerals (Fh_Pen1/5_8.7wt%C, Fh_Hex2/6_8.4wt%C and Fh_But3/7_10.1wt%C) with or without Cr(VI) at pH 5.75 and 7.00. Pen1/5, Hex2/6 and But3/7 represent simple carboxyl-rich OC with one, two and three carboxyl groups, respectively. Error bars represent standard deviations of at least duplicate samples.

6.3.2 Distribution of Cr species during Fe(II)-induced transformation of pure Fh and Fh organominerals

Changes in the distribution of Cr species with reaction time are shown in Figure 6.3. For all systems, no aqueous Cr(VI) or Cr(III) are detected throughout the whole transformation process (Figure 6.3). Therefore all Cr is associated with the solid minerals, and is operationally classified as either desorbable Cr(VI) ($\mathrm{Cr(VI)_{desorbable}}$), desorbable Cr(III) ($\mathrm{Cr(III)_{desorbable}}$) or non-desorbable Cr ($\mathrm{Cr_{non\text{-}desorbable}}$). The $\mathrm{Cr(VI)_{desorbable}}$ pool remains constant at ~4% of total Cr in all systems, therefore the observed increase in the $Cr_{non\text{-}desorbable}$ pool with time originates from the $Cr(III)_{desorbable}$ pool.

To better evaluate the capture of Cr, the increasing proportions of non-desorbable Cr with reaction time are fitted with the rate equation:

$$[A]_t = [A]_0 \times (1 - e^{-kt})$$

where $[A]_t$ is the fraction of $Cr_{non\text{-}desorbable}$ at time *t*, $[A]_0$ is final proportion of non-desorbable Cr after the transformation, *k* is the rate constant and *t* is time.

For pure Fh, the rate of exchange from $Cr(III)_{desorbable}$ to $Cr_{non\text{-}desorbable}$ at pH 5.75 is much slower than at pH 7.00 (Table 6.1). As a result, the proportion of $Cr_{non\text{-}desorbable}$ at pH 5.75 is lower after 18 days reaction time but reaches the same equilibrium as pH 7.00 after 90 days reaction time (Figure 6.3).

For Fh-organominerals, the presence of OC appears to increase the rate of exchange from the $Cr(III)_{desorbable}$ to the $Cr_{non\text{-}desorbable}$ pool at pH 5.75 in the order Fh_Pen1/5_8.7wt%C ~ Fh_Hex2/6_8.4wt%C > Fh_But3/7_10.1wt%C > pure Fh (Table 6.3, Figure S6), but this influence is weakened at pH 7.00. After 90 days reaction, the final proportion of $Cr_{non\text{-}desorbable}$ decreases with the carboxyl-richness of the OC in the sequestered acid molecules and generally follows the order: pure Fh ~ Fh_Pen1/5_8.7wt%C > Fh_Hex2/6_8.4wt%C > Fh_But3/7_10.1wt%C at both pH 5.75 and pH 7.0 (Figure 6.3 and Table 6.1). It is worth noting that the final proportion of $Cr_{non\text{-}desorbable}$ for pure Fh is higher than that for Fh-organominerals after 90 days reaction, although the rate of exchange from the $Cr(III)_{desorbable}$ to the $Cr_{non\text{-}desorbable}$ at pH 5.75 is the lowest.

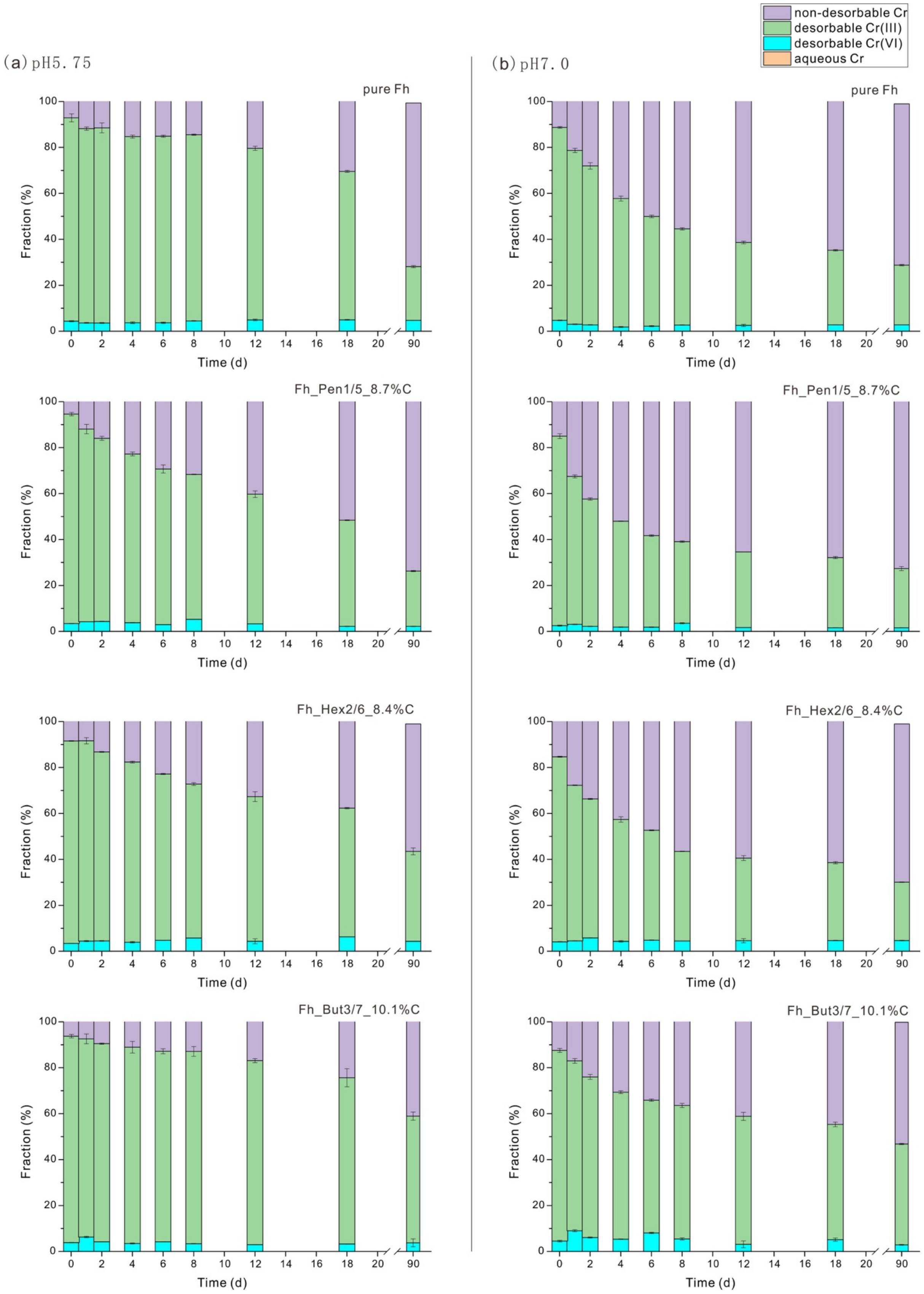

Figure 6.3. Temporal changes of Cr species during the Fe(II)-catalysed transformation of pure Fh and Fh organominerals at a) pH 5.75 and b) pH 7.00. Experiments were performed with Fh-

OC composites in 0.01 M $NaNO_3$ background electrolyte and a solid-solution ration of 2 g dry sorbent L^{-1} in the presence of 40.5 ppm Fe(II) by batch experiment. Pen1/5, Hex2/6 and But3/7 represent simple carboxyl-rich OC with one, two and three carboxyl groups, respectively. Error bars represent standard deviations of at least duplicate samples.

Table 6.1. Rate of exchange from $Cr(III)_{desorbable}$ to $Cr_{non\text{-}desorbable}$ during Fe(II)-induced transformation of pure Fh and Fh organominerals.

	$[A_0]$ (%)	k (d^{-1})	R^2
	pH 5.75		
pure Fh	70	0.0351±0.00529	0.92
Fh_Pen1/5_8.7wt%C	73	0.0755 ±0.00612	0.96
Fh_Hex2/6_8.4wt%C	56	0.0807 ±0.00656	0.95
Fh_But3/7_10.1wt%C	41	0.053 ±0.00673	0.91
	pH 7.00		
pure Fh	70	0.2240 ±0.02395	0.94
Fh_Pen1/5_8.7wt%C	70	0.414 ±0.07108	0.85
Fh_Hex2/6_8.4wt%C	69	0.2492 ±0.0437	0.78
Fh_But3/7_10.1wt%C	54	0.1757 ±0.02965	0.77

$[A]_0$: final proportion of non-desorbable Cr after the transformation;
k: the rate constant;
R^2: the coefficient of determination.

6.3.3 Influence of Cr on properties of secondary iron minerals

The OH stretching vibrations consist of three major components shown by Gaussian deconvolution analyses (Figure 6.4, 6.5 and 6.6): non-stoichiometric hydroxyls and stoichiometric (or bulk) OH groups with a shoulder at lower frequencies.

For Fh, Lp and Gt (Figure 6.4), the wavenumber of non-stoichiometric OH stretching bands follows the order Fh ~Lp > Gt, while the wavenumber of stoichiometric OH stretching bands follows the order Fh > Lp ~ Gt, suggesting increasing crystallinity (Fh < Lp < Gt).

The FTIR spectroscopy for pure Fh in the presence and absence of Cr (mainly Cr(III)) during reacting over 18 days at pH 5.75 and at pH 7.00 are shown in Figure 6.5 and Figure 6.6, respectively. For all experiments, the OH stretch bands shift from broad high energy bands to thin lower energy bands over 18-days reaction. At pH 5.75, the presence of Cr (mainly Cr(III)) results in a higher intensity and a higher wavenumber of non-stoichiometric OH stretching bands after reacting for 18 days (Figure 6.5c and d), whilst at pH 7.00 the difference in non-stoichiometric OH bands is also observed after reacting for 1 day, but disappears after reacting for 6 days (Figure 6.6b and c).

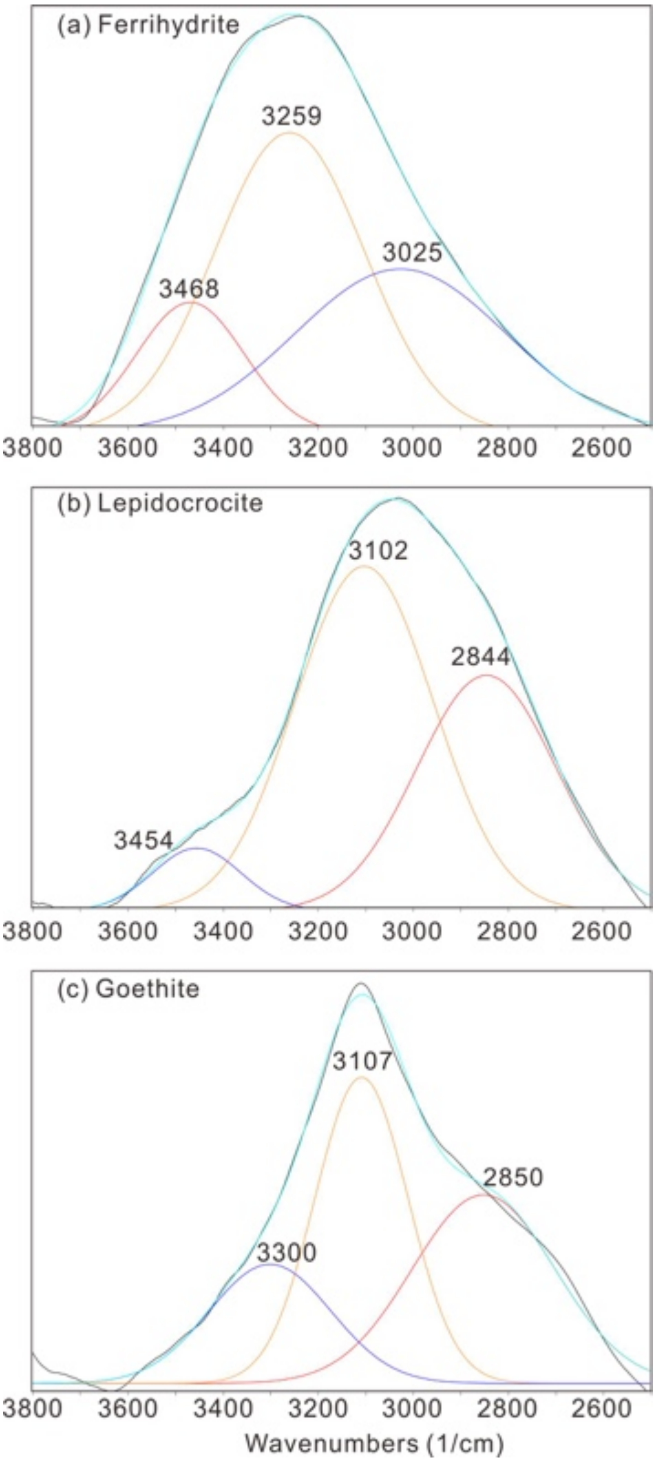

Figure 6.4. Gaussian deconvolution analyses of the OH-stretching region in ATR-FTIR spectra for pure a) ferrihydrite, b) goethite and c) lepidocrocite. From higher to lower frequencies are non-stoichiometric hydroxyls and stoichiometric (or bulk) OH groups with a shoulder.

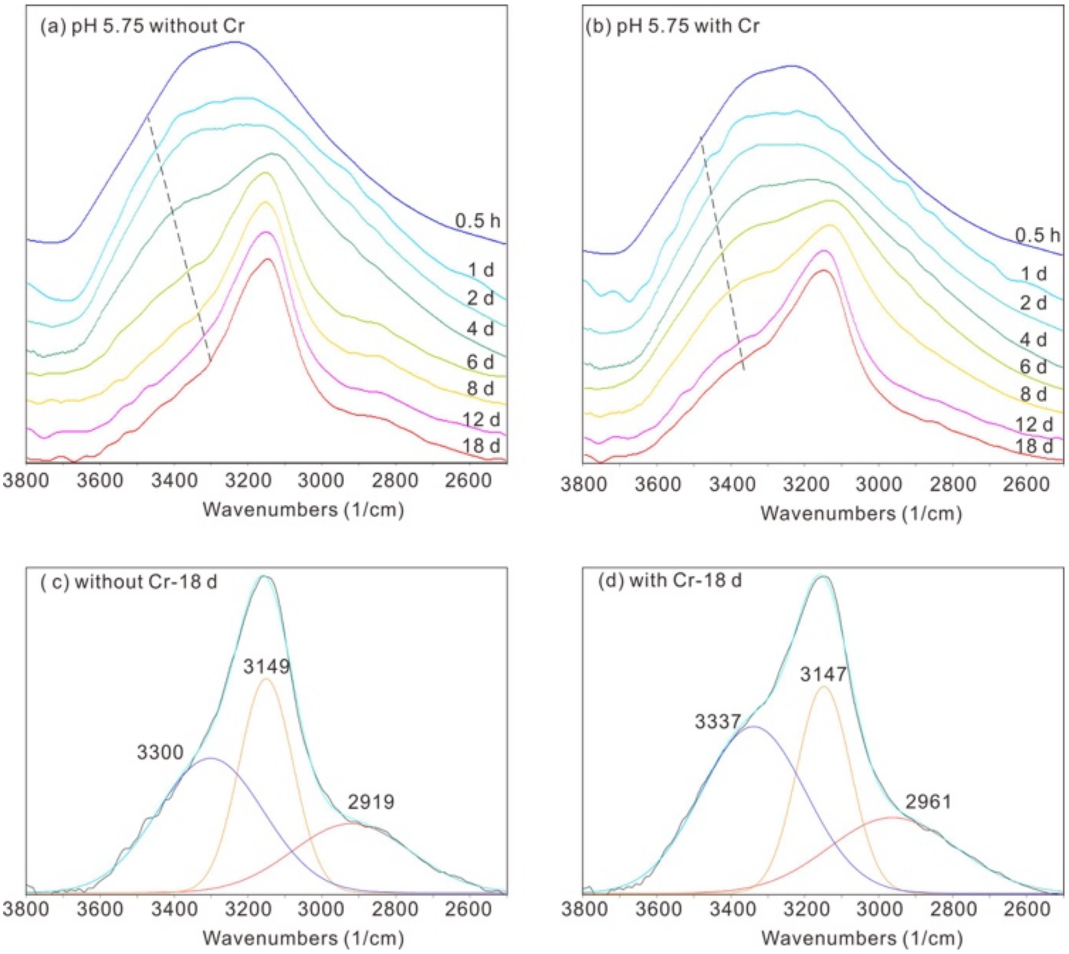

Figure 6.5. ATR-FTIR spectra at pH 5.75 as a function of time for pure Fh a) without Cr and b) with Cr and the corresponding Gaussian deconvolution analyses after reacting for 18 days c) without Cr and d) with Cr. The solid lines in a) and b) are the sum of different OH groups in each sample, where solid lines with different colours indicate the total band migration over the 18 days and the dashed line indicates changes in non-stoichiometric OH stretching bands. From higher to lower frequencies in c) and d) are non-stoichiometric hydroxyls and stoichiometric (or bulk) OH groups with a shoulder.

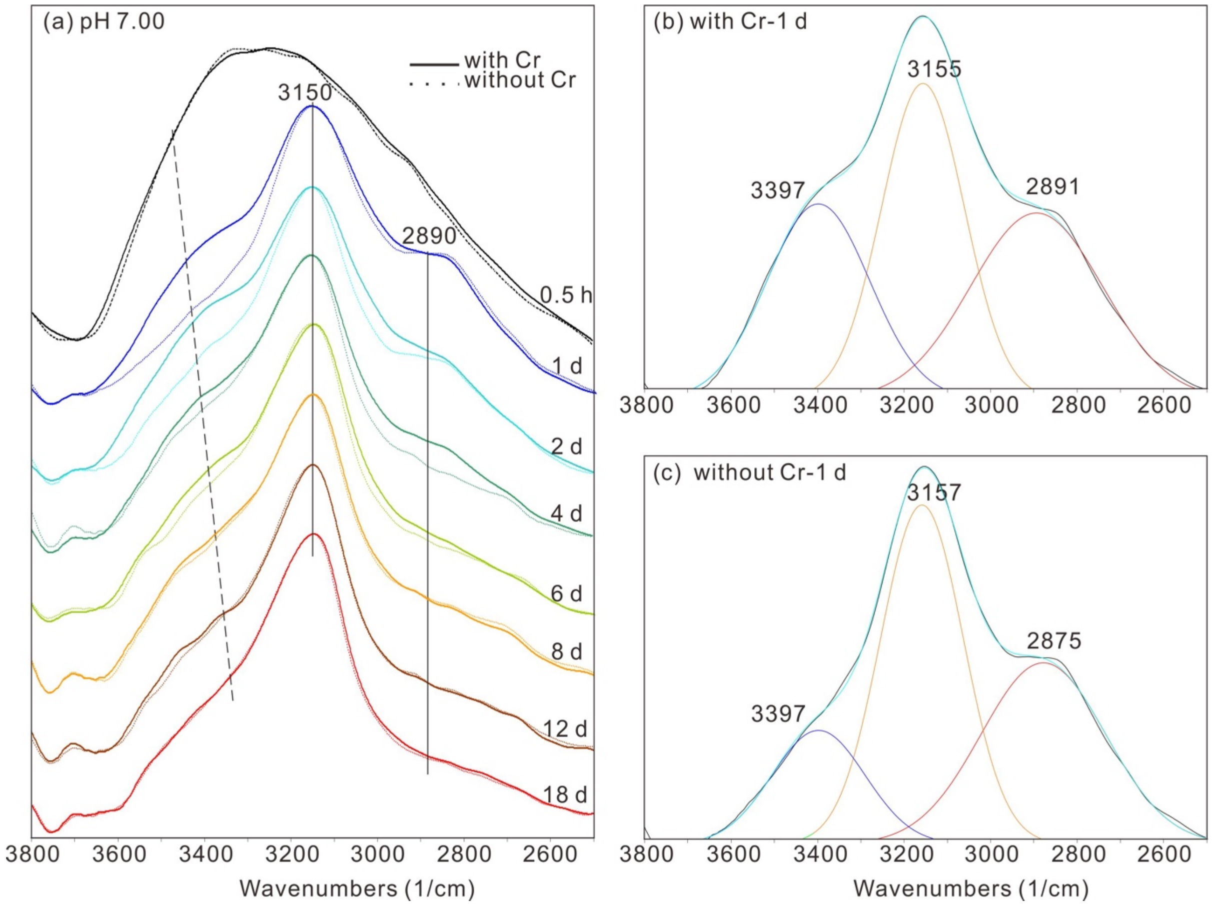

Figure 6.6. ATR-FTIR spectra at pH 7.00 as a function of time for pure Fh a) without and with Cr and Gaussian deconvolution analyses after reacting for 1day b) with Cr and c) without Cr. The dashed line in a) indicates changes in non-stoichiometric OH stretching bands. From higher to lower frequencies in b) and c) are non-stoichiometric hydroxyls and stoichiometric (or bulk) OH groups with a shoulder.

6.3.4 Carbon distribution during Fe(II)-catalysed transformation

6.3.4.1 Temporal changes of total C in the solid phase

The changes in the distribution of total solid C ($C_{total-solid}$) in the presence and absence of Cr at pH 5.75 and pH 7.00 are shown in Figure 6.7. In most experiments, $C_{total-solid}$ generally decreases with increasing reaction time and pH, regardless of whether Cr is present or not. Comparing Fh organominerals made with different OC types but with similar C loadings, the $C_{total-solid}$ at the end of reaction appears to increase with the binding strength (Pen1/5 < Hex2/6 < But3/7) and follow the order Fh_Pen1/5_8.7wt%C < Fh_Hex2/6_8.4wt%C < Fh_But3/7_10.1wt%C. Comparing the same Fh-organomineral with or without Cr, the presence of Cr can stabilise more C$_{\text{total-solid}}$ with the solid at pH 5.75, while, except for Fh_Pen1/5_8.7wt%C, this stabilisation effect at pH 7.00 is obvious during the first/mid-stage of transformation but then decreases with further reaction.

(a) pH 5.75

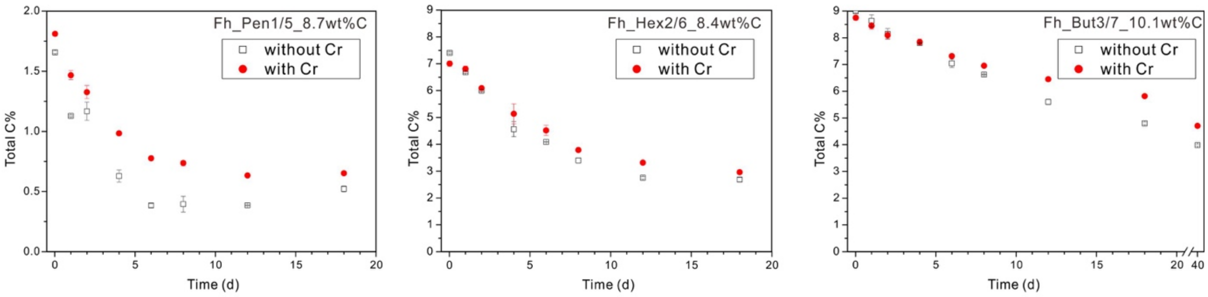

(b) pH 7.00

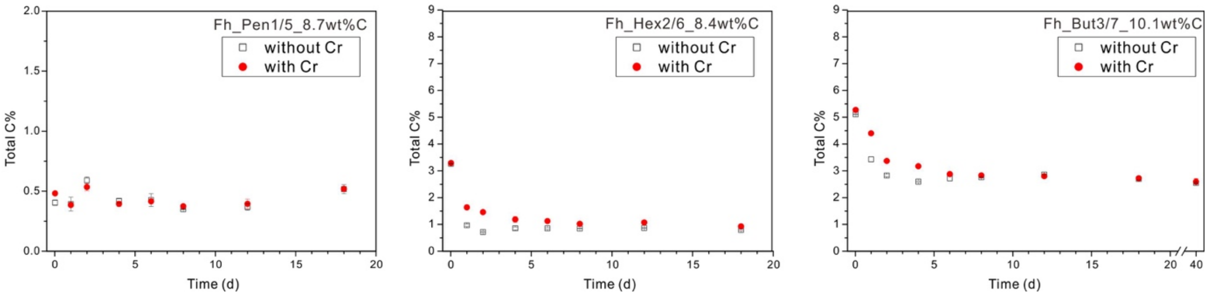

Figure 6.7. Temporal changes in the total amount of C in solid phase during Fe(II)-induced transformation at a) pH 5.75 and b) pH 7.00 in the presence of Cr (red solid circles) and in the absence of Cr (black open squares). Experiments were performed with Fh-OC coprecipitates in 0.01 M $NaNO_3$ background electrolyte and a solid-solution ration of 2 g dry sorbent L^{-1} in the presence of 40.5 ppm Fe(II). Pen1/5, Hex2/6 and But3/7 represent simple carboxyl-rich OC with one, two and three carboxyl groups, respectively. Error bars represent standard deviations of at least duplicate samples. Note differing scale on y-axis for Fh_Pen1/5_8.7wt%C.

6.3.4.2 Temporal changes of non-desorbable C in the solid phase

The changes in the distribution of non-desorbable (C$_{\text{non-desorbable}}$) in the presence and absence of Cr at pH 5.75 and pH 7.00 are shown in Figure 6.8. Comparing Fh organominerals made with different OC types, C$_{\text{non-desorbable}}$ for Fh_Pen1/5_8.7wt%C and Fh_Hex2/6_8.4wt%C shows a stable trend with reaction time, while C$_{\text{non-desorbable}}$ for Fh_But3/7_10.1wt%C increases gradually. Comparing the same Fh organomineral with or without Cr, the presence of Cr (mainly Cr(III)) increases $C_{non\text{-}desorbable}$ for Fh_Hex2/6_8.4 wt%C and for Fh_But3/7_8.7 wt%C at pH 5.75 and pH 7.00.

(a) pH 5.75

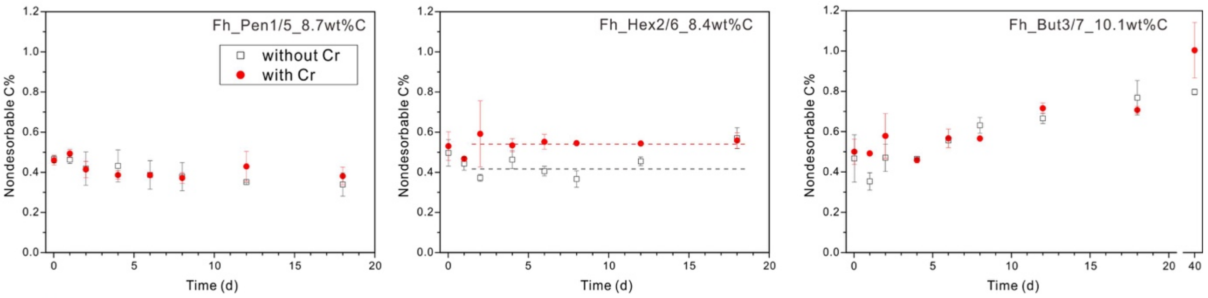

(b) pH 7.00

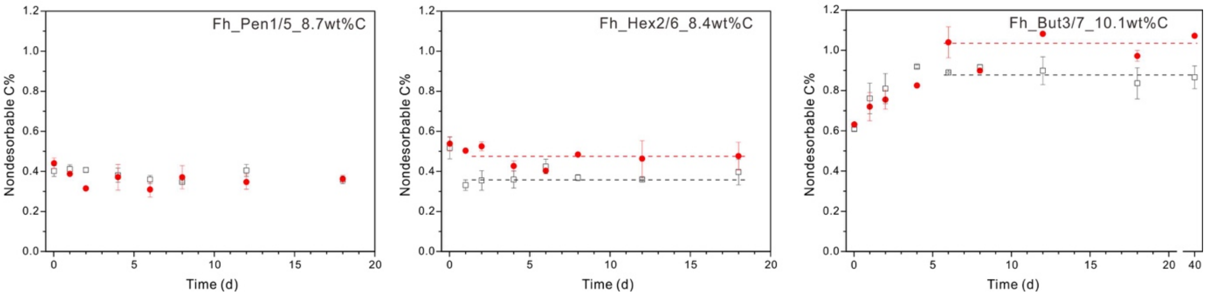

Figure 6.8. Temporal changes in the total amount of non-desorbable C in the Fh-organominerals solid phase during Fe(II)-induced transformation at a) pH 5.75 and b) pH 7.00 in the presence of Cr (red solid circles) and in the absence of Cr (black open squares). The red and black dotted lines are with and without Cr, respectively, indicating influence of Cr(III) on the amount of non-desorbable C. Pen1/5, Hex2/6 and But3/7 represent simple carboxyl rich OC with one, two and three carboxyl groups, respectively. Error bars represent standard deviations of at least duplicate samples.

6.4 Discussion

6.4.1 Fe(II)-induced ferrihydrite and Fh organominerals transformation in the presence of Cr and OC

6.4.1.1 Transformation rates of Fh in the presence of OC

My experiment shows that the presence of tri-carboxylic But3/7 in Fh organominerals significantly retards the formation of Gt and Lp at pH 5.75 (Figure 6.2), which is in agreement with previous studies which find OC suppresses the Fe(II)-induced transformation of Fh to more crystalline minerals (Sheng et al., 2020a; ThomasArrigo et al., 2019; Zhou et al., 2018b). The tri-carboxylic But3/7 acid can inhibit the reaction between Fe(II) and Fe(III) within the mineral structure by blocking mineral surface sites (Jones et al., 2009; ThomasArrigo et al., 2017) or chelating with Fe(II) (Chen et al., 2015); But3/7 can also form a negatively charge coating on mineral particles that then repel one another (Illés and Tombácz, 2006) or act as a bridge between minerals particles (Amstaetter et al., 2012; Illés and Tombácz, 2006) to hinder aggregation, which inhibits the growth of crystalline minerals (ThomasArrigo et al., 2018).

During the Fe(II)-induced transformation of Fh organominerals, the inhibition effect of OC on the formation of Gt and Lp at pH 5.75 increases in the order Pen1/7 < Hex2/6 < But3/7 and thus with increasing carboxyl-richness and hence binding strength. My Fh organominerals namely Fh_Pen1/5_8.7 wt%C, Fh_Hex2/6_8.4wt%C, But3/7_10.1wt%C roughly have similar C loadings, and thus the carboxyl-richness in the sequestered organic moiety controls the number of carboxyl functional groups present to influence the reaction between iron minerals and Fe(II). Alternatively, the increasing binding strength of carboxylic acids helps stabilise more OC associated with minerals (Zhao et al., 2022), which plays an important role in inhibiting the transformation of Fh. Previous studies show that the atomic exchange between aqueous Fe(II) and Fe(III) in bulk iron minerals is not altered substantially by the presence of OC (Sheng et al., 2020a; ThomasArrigo et al., 2019; Zhou et al., 2018b), but the transformation of Fh to crystalline minerals is still inhibited, which is attributed to OC associated with solid minerals hindering the aggregation (ThomasArrigo et al., 2018). In my experiment, the $C_{total-solid}$ follows the order Fh_But3/7_10.1wt%C > Fh_Hex2/6_8.4wt%C > Fh_Pen1/5_8.7wt%C during the Fe(II)-induced transformation of Fh (Figure 6.7). The most strongly-bound But3/7 has the highest amount of OC associated with Fe minerals to influence transformation process. The higher number of carboxyl functional groups in But3/7 acid means it can effectively form a negatively charge coating on iron minerals (Illés and Tombácz, 2006) or bridge different mineral particles (Amstaetter et al., 2012; Cornell and Schwertmann, 1979b; Illés and Tombácz, 2006), which results in a greater hinderance on the aggregation of minerals. As such, OC with higher carboxyl-richness and binding strength causes greater retardation of Fe(II)-induced transformation of Fh organominerals.

The transformation rates of Fh to Lp and Gt at pH 5.75 (Figure 6.2a-h) are much slower than at pH 7.00 (Figure 6.2i-p), suggesting the pH of the experiments significantly influences the transformation rates. This is attributed to the lower amount of Fe(II) adsorbed at lower pH, which results in less Fe atom exchange between aqueous Fe(II) and Fe(III) within mineral structure than that at pH 7.00 (ThomasArrigo et al., 2017). As such, the reductive dissolution and recrystallisation process at pH 5.75 is slower than at pH 7.00, and the formation of Lp and Gt is also slower at pH 5.75.

6.4.1.2 Transformation pathway of Fh in the presence of Cr and OC

In the presence of Fe(II), Fh can be directly transformed to Lp, Gt and Mg (Hansel et al., 2005), whilst Lp can be further transformed to Gt (Cornell and Schwertmann, 2003) and/or Mg (Tamaura et al., 1981; Tamaura et al., 1983). In my experiment, it is observed that the presence of But3/7 acid and Cr inhibits the conversion from Lp to other minerals in pure Fh and Fh_But3/7_8.4wt%C experiments at pH 7.00. The formation of Lp generally peaks after the first few days (Figure 6.2) before altering to other more stable minerals via further dissolution and reprecipitation processes (Hansel et al., 2005). A reason for the inhibition of the conversion from Lp to other minerals is that But3/7 and Cr are adsorbed onto the Lp surface and then hinder the dissolution of Lp to form Gt or Mg.

It is also observed that the final total proportion of Gt and Lp for pure Fh, Fh_Pen1/5_8.7wt%C and Fh_Hex2/6_8.4wt%C at pH 7.00 (Figure 6.2i-p) are much lower than 100% with respect to that at pH 5.75 (Figure 6.2a-h). For Fh_But3/7_10.1wt%C however, the final total proportions of Gt and Lp are near 100% at pH 7.00 (Figure 6.2). Based on the observation that the total amount of aqueous and desorbable Fe(II) decreases with reaction time at pH 7.00 regardless of whether Cr is present or not (Figure 6.1), the lower total proportions of Gt and Lp for pure Fh, Fh_Pen1/5_8.7wt%C and Fh_Hex2/6_8.4wt%C at pH 7.00 are speculatively attributed to the formation of Mg (Fe_3O_4), the formation of which consumes Fe(II). By contrast, for Fh_But3/7_10.1 wt%C, without the formation of Mg is suggested as the total amount of aqueous and desorbable Fe(II) are constant at both pH 5.75 and pH 7.00. I suppose that carboxyl-rich OC more effectively inhibit the formation of magnetite than the carboxyl-poor OC, but this requires further investigation and direct evidence.

6.4.2 Cr speciation and distribution during Fe(II)-catalysed Fh transformation

6.4.2.1 Cr distribution during Fe(II)-catalysed transformation of pure Fh

Under anoxic conditions, Cr(VI) is readily reduced to Cr(III), and thus the reaction between Cr(III) and iron (oxyhydr)oxides determines the fate of Cr during the transformation process. Cr(III) can be associated with solid iron minerals by adsorption, surface precipitation and chemical substitution. The "solid solution" of $Cr(OH)_3$ and Gt is evident in the formation of coprecipitated $(Fe,Cr)(OH)_3$ which can exist in any ratios of Cr and Fe (Amonette and Rai, 1990), and where the solid minerals are not physical mixtures but are chemical substitution products (Charlet and Manceau, 1992; Tang et al., 2010).

In the present work of pure Fh, all detectable Cr exists in the solid phase and transitions from the desorbable to the non-desorbable pool as mineralogical transformation progresses (Figure 6.3), which is likely due to substitution of Cr(III) into iron mineral structure (Charlet and Manceau, 1992; Dai et al., 2016; Fendorf et al., 1996; Sass and Rai, 1987; Singh et al., 2002; Tang et al., 2010). The rate of exchange of $Cr_{desorbable}$ to $Cr_{non\text{-}desorbable}$ for pure Fh at pH 5.75 is much lower than that at pH 7.00. As a result, the proportion of $Cr_{non\text{-}desorbable}$ at pH 5.75 is lower after 18 days reaction time but reaches the same equilibrium as pH 7.00 after 90 days reaction time (Figure 6.3). The lower rate of capture of non-desorbable Cr at pH 5.75 is attributed to the lower transformation rate of Fh as shown in Figure 6.2. The proportion of non-desorbable Cr is at a low level even when all Fh is transformed to Gt or Lp after 18 days reaction, but the non-desorbable Cr keeps increasing with reaction time. Thus the capture of $Cr_{non\text{-}desorbable}$ is postulated to occur in two phases based on the transformation process (Figure 6.9a). The first phase is that during the transformation of Fh to Gt or Lp, some Cr(III) incorporates into Gt structure via chemical substitution while the remaining Cr(III) is enriched at mineral surface through adsorption and surface precipitation (Dai et al., 2016). The second phase is that with Gt coarsening via Oswold ripening (Cornell and Schwertmann, 2003), oriented aggregation (Hockridge et al., 2009) or oxidation of Fe(II) on the mineral surface (Boland et al., 2014), the mineral surface rich in Cr(III) is then covered with Gt formed through recrystallization or rearrangement of primary-formed nanoparticles. Because of the solid solution between $Cr(OH)_3$ and Gt, the process of Gt covering another particle with Cr(III) enriched surfaces occurs readily and the progressively changing structure exists stably, after which Cr(III) transitions from the desorbable pool to the non-desorbable pool.

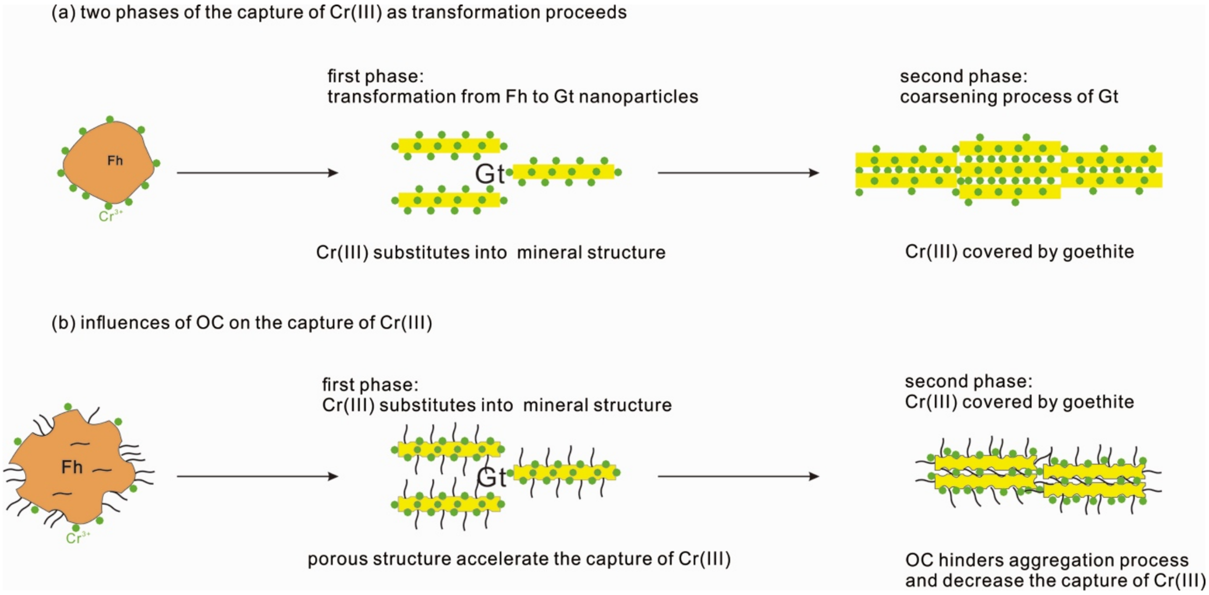

Figure 6.9 The capture of Cr(III) during Fe(II)-induced transformation of Fh and Fh organominerals. a) two phases of capture of Cr(III) based on the transformation processes and b) influences of OC on the capture of Cr(III) during the transformation process.

6.4.2.2 Cr distribution during Fe(II)-catalysed transformation of Fh organominerals

For Fh organominerals, all detectable Cr exists in the solid phase and transitions from the desorbable to the non-desorbable pool as mineralogical transformation progresses (Figure 6.3). The presence of OC appears to increase the rate of exchange from the Cr(III)$_{desorbable}$ to Cr$_{non-desorbable}$ pool at pH 5.75 in the order Fh_Pen1/5_8.7wt%C ~ Fh_Hex2/6_8.4wt%C > Fh_But3/7_10.1wt%C > pure Fh (Table 6.3), but this influence is weakened at pH 7.00. This may be related to the porous structure of my iron (oxyhydr)oxide, where the structural defects and surface nano-pores provide additional ways for Cr(III) to be captured by iron minerals and/or help Cr(III) readily substitute into the iron mineral structure during the oriented aggregation or recrystallisation process. Comparing my OC with different carboxyl-richness and binding strength (Pen1/5 < Hex2/6 < But3/7), Pen1/5 has the lowest binding strength with iron minerals and therefore is readily released from the mineral (Figure 6.7), leaving a porous surface for Cr(III) to be captured in structural defects, surface nano-pores or within lattice structure (Figure 6.9b). As Hex2/6 and But3/7 have a higher binding strength, they are not so readily released from the mineral surface (Figure 6.7) therefore the facilitation of Cr exchange from the Cr(III)$_{desorbable}$ to Cr$_{non-desorbable}$ pool is weakened with increasing binding strength.

After 90 days reaction, the proportion of $Cr_{non\text{-}desorbable}$ decreases with increasing carboxyl-richness of the sequestered OC and generally follows the order pure Fh ~ Fh_Pen1/5_8.7wt%C > Fh_Hex2/6_8.4wt%C > Fh_But3/7_10.1wt%C at pH 5.75 and 7.00 (Figure 6.3 and Table 6.1). It is worth noting that the final proportion of $Cr_{non\text{-}desorbable}$ for pure Fh is higher than that for Fh-organominerals after 90-days reaction, although its rate of exchange from the $Cr(III)_{desorbable}$ to the $Cr_{non\text{-}desorbable}$ pool at pH 5.75 is the lowest. The decrease in the final proportion of $Cr_{non\text{-}desorbable}$ with increasing carboxyl-richness may result from the impact of the OC on the transformation of Fh, but this influence is not obvious for my Fh organominerals because the proportion of $Cr_{non\text{-}desorbable}$ for all Fh organominerals is higher than that for pure Fh over 18 days reaction. Alternatively, the presence of OC inhibits the coarsening of Gt (from 18 days to 90 days), which controls the second phase of the capture of $Cr_{non\text{-}desorbable}$ (Figure 6.9b), where the Cr(III) enriched at mineral surfaces is covered by Gt during the coarsening process. Therefore the encapsulation of Cr in iron minerals is inhibited in the presence of OC (Figure 6.9b). The lower final proportion of $Cr_{non\text{-}desorbable}$ with increasing carboxyl-richness and binding strength is likely due to $C_{solid\text{-}total}$ increasing with increasing binding strength as mentioned above, as a greater C content associated with the mineral can more effectively inhibit the dissolution and reprecipitation process and hinder the aggregation of minerals as shown above (Section 4.1). Another reason for the lowest proportion of non-desorbable Cr for Fh_But3/7_10.1wt%C is that But3/7 acid favours the formation of Lp and stabilises Lp at a high proportion of the total solid product (Figure 6.2). Because Lp cannot host any Cr(III) in its structure (Cornell and Schwertmann, 2003), a large proportion of Lp leads to more Cr(III) enriched on the mineral surface as $Cr_{desorbable}$.

Higher pH weakens the influence of OC in terms of the rate of capture of Cr and the final proportion of $Cr_{non\text{-}desorbable}$ in my experiments (Figure 6.3 and Table 6.1). This is likely because Fe(II) adsorption increases with increasing pH and the reaction between Fe(II) and iron (oxyhydr)oxide is stronger and faster with increasing pH, which results in a faster transformation from Fh toGt and a faster coarsening of Gt, and thus the two stages of capture of $Cr_{non\text{-}desorbable}$ are accelerated at pH 7.00. Additionally, the adsorption of OC also decreases with increasing pH (Figure 6.7). A lower C content associated with the mineral weakens the inhibition effect of OC on the dissolution and re-precipitation process and the aggregation of minerals, which therefore results in less influences of OC on the capture of $Cr_{non\text{-}desorbable}$. Natural soil, however, are commonly acidic, and thus more comparable to the set of experiments conducted at pH 5.75, where the capture of Cr is slower (Table 6.3) and easily influenced by the presence of OC.

6.4.2.3 Existence of Cr(VI) in reducing environments

As shown in Figure 6.3, most Cr(VI) is reduced to Cr(III) in the presence of Fe(II) within 0.5 h, because Cr(VI) and Fe(II) are very strong oxidants and reductants, respectively. Solid-phase Cr(VI) is not completely reduced however, with a small amount persisting at least up to 90 days. It is unlikely the residual Cr(VI) is sorbed directly on the mineral surface because iron (oxyhydr)oxides can act as a "redox conveyor belt" to transfer electrons via the lattice (Handler et al., 2009; Handler et al., 2014; Neumann et al., 2015; Yanina and Rosso, 2008) to react with the Cr(VI) (Tomaszewski et al., 2017). It is therefore more likely the residual Cr(VI) is associated with the Cr(III) or adsorbed onto Cr(III) hydroxide (Hu et al., 2019), which can form a barrier to electron transfer between Fe(II) and Cr(VI) and protect Cr(VI) from reduction by electrons. This would also explain why Cr(VI) remains in the desorbable pool (Figure 6.3), as it is likely less protected if it was strongly bound directly to the iron mineral surface.

6.4.3 Influences of Cr on properties of secondary iron minerals

Comparing OH stretching bands for Fh, Lp and Gt (Figure 6.4), the wavenumber of non-stoichiometric OH stretching bands follows the order Fh ~Lp > Gt, while the wavenumber of stoichiometric OH stretching bands follows theorder Fh > Lp ~ Gt. The highest wavenumber and intensity of non-stoichiometric OH at 3468 cm^{-1} for Fh reflects the fact it has highest reactivity and structure disorder (Cornell and Schwertmann, 2003). Ferrihydrite is followed by Lp at 3454 cm^{-1} and then by Gt at 3300 cm^{-1}, which reflects the increasing structural order of these iron minerals. Comparing the stoichiometric OH stretching bands, the situation is similar with non-stoichiometric OH except that Lp has a broader band at the same wavenumber with Gt, reflecting lower crystallinity. Therefore, OH stretching bands observed by FTIR reflect the increasing crystallinity in the order Fh < Lp < Gt, which is consistent with their stability as well as the transformation pathway (Cornell and Schwertmann, 2003; Hansel et al., 2005).

The FTIR spectroscopy for pure Fh in the presence and absence of Cr after reacting for 18 days at pH 5.75 and at pH 7.00 are shown in Figure 6.5 and Figure 6.6, respectively. For all experiments, the OH stretching bands shift from broad high energy bands to thin lower energy bands over 18 days reaction. At pH 5.75, the presence of Cr results in a higher intensity and a higher wavenumber of non-stoichiometric OH stretching bands after reacting for 18 days (Figure 6.5c and d), whilst at pH 7.00 the difference in non-stoichiometric OH bands is also observed after reacting for 1 day, but disappears after reacting for 6 day (Figure 6.6b and c). The universal transitions of OH stretching bands to thin and lower energy bands are also observed by Bazilevskaya et al. (2012), and reflect increases in the structural order and crystallinity as Fh transforms to Gt or Lp. Considering that all Fh has been transformed to Gt or Lp after 12 days, the difference of non-stoichiometric OH stretching bands in the presence and absence of Cr at pH 5.75 is likely due to the fact that Cr(III) hydroxides provide additional weakly H-bound surface hydroxyls (Amonette and Rai, 1990; Papassiopi et al., 2014) and/or Cr(III) inhibits the crystal growth secondary iron minerals (Amonette and Rai, 1990; Choppala and Burton, 2018), resulting in lower crystallinity and higher OH reactivity.

For experiments of pure Fh at pH 7.00, the difference in non-stoichiometric OH bands after 1 day reaction should also be caused by the presence of Cr (mainly Cr(III)) because Fh can be fully transformed within 1 day (Figure 6.2). Similar to pH 5.75, the much higher band for non-stoichiometric OH at 3397 cm^{-1} in the presence of Cr at pH 7.00 also suggests greater structural disorder, lower crystallinity and higher OH reactivity. The difference in non-stoichiometric bands decreases with reaction time however, which means the influence of Cr on structural disorder or surface OH units decreases with reaction time. This may be due to the incorporation of Cr(III) into the iron minerals, removing Cr(III) from the surface and allowing the continuing crystallization process as the reaction with Fe(II) proceeds.

6.4.4 Carbon distribution during Fe(II)-induced ferrihydrite transformation

6.4.4.1 Decrease in total solid C lessened by Cr

The $C_{total\text{-}solid}$ associated with minerals generally decreases with reaction time, and this effect is enhanced by increasing pH conditions to pH 7.00 (Figure 6.7). Comparing Fh organominerals made with different OC types but with similar C loadings, the $C_{total\text{-}solid}$ at the end of the reaction appears to increase with the binding strength (Pen1/5 < Hex2/6 < But3/7) and follow the order Fh_Pen1/5_8.7 wt%C < Fh_Hex2/6_8.4 wt%C < Fh_But3/7_10.1 wt%C. The decrease in $C_{total\text{-}solid}$ associated with the minerals is consistent with previous studies

(Jelavić et al., 2020; Lu et al., 2019b) and attributed to the decreasing adsorption capacity of iron minerals as the SSA decreases with the transformation of Fh. (Cudennec and Lecerf, 2006; Das et al., 2011b; Johnston and Lewis, 1983; Manceau and Drits, 1993; Schwertmann and Murad, 1983; Schwertmann et al., 2004). The distribution of OC is also controlled by the adsorption affinity to iron minerals, where OC with higher binding strength has higher affinity to iron minerals (Zhao et al., 2022) and tend to persist with soil and sediments minerals for a longer time (Hemingway et al., 2019).

The presence of Cr (predominantly as Cr(III)) aids OC stabilisation with solid phase, especially at pH 5.75 (Figure 6.7), where more OC is stabilised with Cr than that without Cr during the latter transformation process (after 6 days). A potential mechanism for this enhanced stabilisation is the inhibition of mineral transformation from Fh to secondary iron minerals in the presence of Cr, allowing the more reactive Fh to sorb more OC. Alternatively, it is because the presence of Cr leads to more structural defects and lower crystallinity of secondary iron minerals, and results in the increasing surface OH reactivity, or a combination of these. The increase in surface OH reactivity elevated by Cr(III) is enhanced with reaction time at pH 5.75 observed by FTIR (Figure 6.5), which corresponds to the higher $C_{total\text{-}solid}$ elevated by Cr(III) with reaction time. Early in the mineralogical transformation, the solid phase is predominantly Fh where surface OH sites for OC adsorption are in excess. As the proportion of Fh diminishes however, and other crystalline minerals forms, the number of surface OH sites decreases, making the impact of Cr on OH reactivity more pronounced, resulting in more OC stabilized with minerals (Figure 6.10a). Whereas, the elevation of $C_{total-solid}$ by Cr(III) fades with reaction time at pH 7.00, which is also consistent with increase in the structural disorder of secondary minerals elevated by Cr(III) disappearing with reaction time observed by FTIR (Figure 6.6). As more and more Cr is converted from surface species to species incorporated into minerals with reaction time, the continuing decrease in structural disorder coupled with the decrease in surface OH reactivity, leads to the decrease in OC adsorption.

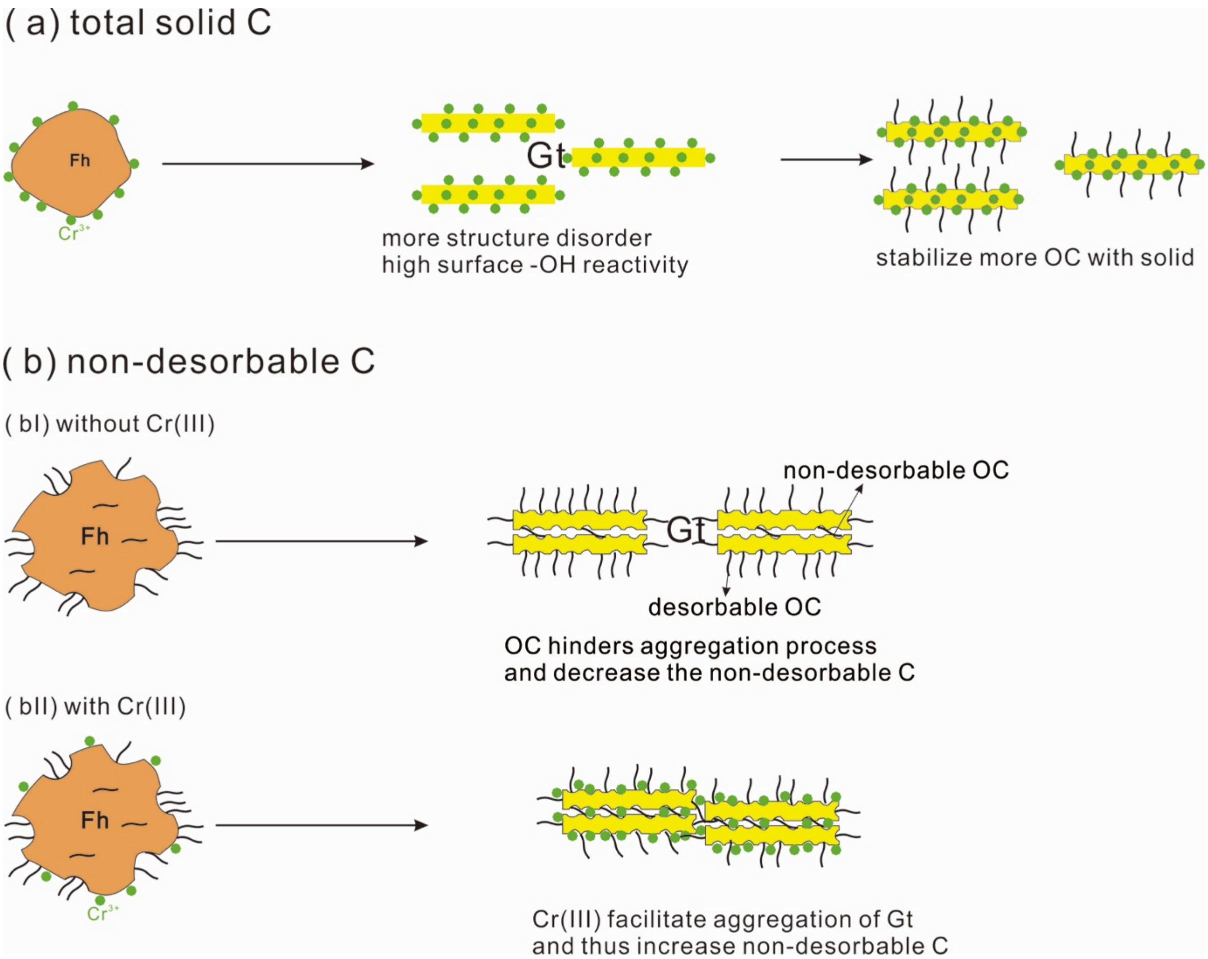

Figure 6.10 Influences of Cr(III) on the stabilization of OC including a) the total solid C and b) the non-desorbable C during Fe(II)-induced transformation.

The increase in $C_{total\text{-}solid}$ elevated by Cr(III) differs for Fh organominerals made with different carboxyl-rich OC. The absolute value of $C_{total\text{-}solid}$ that is elevated by Cr after 18-days reaction at pH 5.75 generally increases in the order Pen1/5 < Hex2/6 < But3/7, but the proportion of $C_{total\text{-}solid}$ elevated by Cr is around 20% for the three Fh organomineral systems (Table 6.2). The higher absolute value of $C_{total\text{-}solid}$ increasing with the carboxyl-richness of the OC moieties is likely due to the fact that OC with higher binding strength has higher affinity for iron minerals (Zhao et al., 2022 and Curti et al., 2021). Because the $C_{total\text{-}solid}$ after 18 days reaction also follow the order Pen1/5 < Hex2/6 < But3/7, the proportion of $C_{total\text{-}solid}$ elevated by Cr(III) is very similar. Overall, the presence of Cr(III) aids OC stabilisation with the solid phase especially in the sub-acidic environment, where around 20% of total $C_{total\text{-}solid}$ were elevated at pH 5.75.

Table 6.2 The elevation of $C_{total\text{-}solid}$ by Cr(III) after 18-days Fe(II)-induced transformation of Fh organominerals at pH 5.75

	$C_{total\text{-}solid}$ without Cr (wt%C)	$C_{total\text{-}solid}$ with Cr (wt%C)	$C_{total\text{-}solid}$ elevated by Cr (wt%C)	Percentage of $C_{total\text{-}solid}$ elevated by Cr
Fh_Pen1/5_8.7wt%C	0.52±0.025	0.65±0.016	0.13	25%
Fh_Hex2/6_8.4wt%C	2.68±0.084	2.96±0.059	0.28	21%
Fh_But3/7_10.1wt%C	4.80±0.046	5.82±0.023	1.02	21%

6.4.4.2 Increase in non-desorbable C elevated by Cr

In this work I operationally define non-desorbable OC as that which cannot be removed from the solid particles with 0.1 M NaOH (Kaiser and Guggenberger, 2007). This non-desorbable OC may be very strongly bound onto the mineral surface (Curti et al., 2021), whilst other studies suggest that this non-desorbable OC may also be incorporated into the interior of aggregates, for example by being occluded into mineral pore spaces (Kaiser and Guggenberger, 2007; Lu et al., 2019b).

During the Fe(II)-induced transformation $C_{non\text{-}desorbable}$ for Fh_Pen1/5_8.7wt%C and Fh_Hex2/6_8.4wt%C shows a stable or decreasing trend with reaction time, while $C_{non\text{-}desorbable}$ for Fh_But3/7_10.1wt%C increases gradually (Figure 6.8). The different changes in $C_{non\text{-}desorbable}$ for OC with different binding strength are also observed in my previous work (Zhao et al., 2022), where $C_{non\text{-}desorbable}$ for weakly-bound OC (Pen1/5 and Hex2/6) decrease while $C_{non\text{-}desorbable}$ for strongly-bound OC (But3/7) stay constant / increase as the transformation of Fh proceeds. It is suggested some part of solid C (But3/7) is incorporated into the particle interiors (Zhao et al., 2022), where it is more difficult to remove with 0.1 M NaOH (Kaiser and Guggenberger, 2007; Lu et al., 2019b).

Comparing the same organomineral with or without Cr, the presence of Cr obviously increases $C_{non\text{-}desorbable}$ for Fh_Hex2/6_8.4wt%C and Fh_But3/7_10.1wt%C (Figure 6.8), suggesting that Cr(III) aids OC sequestration by iron minerals. In the absence of Cr(III), OC is adsorbed onto positively charged iron minerals to form negatively charged OC-coated iron minerals, which would hinder the aggregation of iron mineral particles due to electrostatic repulsion (Illés and Tombácz, 2006), decreasing the effect of occlusion (Figure 6.10a). By contrast, Cr(III) surface polymers/ precipitates act as a good substrate for Fe(III) to precipitate around, or for the already formed iron mineral particles to aggregate around, occluding both Cr(III) as well as OC in aggregate pore spaces (Figure 6.10b). Additionally, the presence of Cr(III) stabilizes Lp for longer time (Figure 6.2), where Lp has more structural defects or nano-pore spaces than goethite observed by transmission electron microscopy (TEM), which help fix OC as non-desorbable C (Hu et al., 2020).

The increase in $C_{\text{non-desorbable}}$ elevated by Cr(III) appears to be weakened with decreasing binding strength of OC. There is no difference in $C_{\text{non-desorbable}}$ for Fh_Pen1/5_8.7wt%C (Figure 6.8), probably because OC with lower binding strength is readily desorbed from the mineral particles during the aggregation process. By contrast, OC with higher binding strength is more stable against desorption and can be sequestered in minerals during aggregation facilitated by Cr(III).

6.5 Conclusion

The results obtained in this work show that the presence of OC retards the transformation from Fh to Gt and Lp at pH 5.75, where the inhibition by OC is enhanced with the carboxyl-richness of the sequestered OC moieties. Similar to Cr(III), the carboxyl-rich OC (But3/7 acid) effectively stabilizes Lp for longer time during the Fe(II)-induced transformation process. Regarding Cr distribution, for pure Fh all detectable Cr exists in the solid phase and almost all exist as Cr(III). The Cr transitions from the desorbable to the non-desorbable pool however, as transformation progresses, whilst the final proportion of non-desorbable Cr after 90 days reaction appears to be independent of pH conditions. For Fh organominerals, the presence of OC appears to rise the rate of capture of non-desorbable Cr, but this elevated capture effect is mitigated with the carboxyl-richness of the sequestered OC. Whilst the presence of OC lessens the final proportion of non-desorbable Cr after 90 days reaction and this inhibition effect are enhanced with the carboxyl-richness of the sequestered OC. Regarding the properties of secondary iron minerals, the presence of Cr causes more structural disorder in the iron minerals, which suggests they have a lower crystallinity and higher surface reactivity. Regarding the distribution of OC, the presence of Cr(III) aids the stabilisation of the OC with the solid phase, where the absolute value of total solid C elevated by Cr(III) increases with carboxyl-richness of the OC moieties and for all systems the percentage of total solid C elevated by Cr(III) accounts around for 20% after 18-days transformation at pH 5.75. The presence of Cr(III) increases in an important way the amount of C that is non-desorbable with 0.1 M NaOH, suggesting a stronger bonding of OC, where this facilitation effect appears to increase with carboxyl-richness of the sequestered OC moieties. Overall results show that the capture of Cr is strongly inhibited by carboxyl-rich OC during Fe(II)-induced transformation of Fe minerals, while Cr(III) aids more OC stabilization with the solid phase because OC influences the properties of Fe minerals. The current work sheds new light on the mobility and fate of Cr in redox environments and also provides important mechanistic information necessary to develop a reduction method for remediating Cr(VI) contaminated soils, thus reducing the environmental hazardous impacts of Cr(VI), stabilising more OC in soils and thus benefitting the recultivation of contaminated soils.

Chapter 7 Summary and suggestions for future research

This investigates how carboxyl-rich OC in iron (oxyhydr)oxide organominerals controls Cr cycling during the mineralogical transformation of iron (oxyhydr)oxide under different redox conditions. To achieve this aim, adsorption experiments and surface complexation modelling are utilized to observe the influence of OC binding strength on the adsorption of OC and Cr, and mineralogical transformation experiments are also conducted under different redox conditions to observe the re-distribution of OC and Cr. The main findings of this work are summarized here, and possible future research directions are also suggested.

7.1 The role and fate of organic carbon during aging of ferrihydrite

By combining OC adsorption experiments, surface complexation modelling and aging experiments under oxic conditions, the influence of OC binding strength on aging of Fh and OC preservation in the soil environment are investigated. This work finds that:

- Organic carbon substantially retards aging of Fh and this retardation increases with increasing binding strength of the OC, following the order Pen1/5 (mono-carboxylic acid) < Hex2/6 (di-carboxylic acid) < But3/7 (tri-carboxylic acid) at similar C loading, and with increasing C loading and decreasing pH;

- The presence of OC alters the physiochemical properties of Fh and Fe minerals formed during aging, in particular the presence of OC lessens the decrease in the SSA and TPV of Fe minerals formed from aging, and this affect is enhanced with increasing binding strength of the OC;

- The total amount of C retained with the solid during aging is strongly coupled to the binding strength of the OC and the initial C loading of the organominerals, where OC with higher binding strength is retained more with the solid, and partial OC is released if the initial C loading is higher than the adsorption capacity of the aged Fe minerals;

• The total amount of non-desorbable C after 19-days aging similarly shows a positive correlation with the binding strength of the OC, where the proportion of non-desorbable C increases with higher binding strength;

• Overall results suggest that carboxyl-rich OC coprecipitated with Fh becomes proportionally more stable with the solid phase because OC with lower binding strength is more readily released during mineralogical transformation.

The experiment results presented here are consistent with previous work in which the binding strength of OC is closely related to its carboxyl richness and OC can influence the physiochemical properties and aging of Fh. The work here newly finds however, that the carboxyl richness and hence the binding strength of the OC play an important role in the aging of iron (oxyhydr)oxide and the mobility and fate of OC associated with these minerals. In this thesis the treatment of Fe minerals with 0.1 M NaOH to desorb OC is developed as a method to remove OC and measure the SSA and TPV of the naked Fe minerals. This method is shown to be practical to quantify the influence of OC on the physiochemical properties of Fe minerals. Furthermore in this thesis the developed desorption method is shown to be practical to estimate the distribution and hence the mobility and fate of OC with Fe minerals, as either non-desorbable vs. desorbable.

As natural OC is carboxyl-rich and a significant proportion of OC is associated with Fe minerals, the behaviour of the carboxylic acids associated with Fe minerals in this work suggests there should be a similar trend for the relationship between carboxyl-richness and stabilization of natural carboxyl-rich OC associated with Fe minerals in natural environments. As such this work predicts that in natural environments, OC with higher carboxyl-richness will be strongly bound with Fe minerals and will become proportionally more stable during the mineral aging process. Similarly the findings concerned with the concentration of carboxylic acids associated with Fe minerals in this work suggests there should be a similar trend for the for the relationship between OC concentration and mobility of natural carboxyl-rich OC associated with Fe minerals in natural environments. As such this work predicts that in natural environments, some OC will be released and decomposed by microorganisms when the initial OC concentrations are higher than the adsorption capacity of the secondary Fe minerals formed during the aging process. Overall the work in this thesis offers a deeper insight into the mechanisms responsible for the persistence and long-term preservation of OC in natural environments.

7.2 The mobility and fate of Cr during aging of ferrihydrite and ferrihydrite organominerals

By combining Cr(VI) adsorption experiments, surface complex modelling and transformation experiments the influence of OC binding strength on Cr(VI) adsorption and distribution during aging of Fh under oxic conditions are investigated. This work finds that:

- The binding strengths of carboxylic OC and Cr(VI) complexes follow the order one-carboxyl binding ~ monodentate Cr(VI) binding < two carboxyl binding ~ bidentate Cr(VI) binding < three- carboxyl binding;

- The weakly-bound OC at different C loadings has almost no discernable influence on Cr(VI) adsorption, while the strongly-bound OC significantly suppress Cr(VI) adsorption via surface masking and/or electrostatic repulsion；

- The presence of Cr(VI) retards the transformation rates of Fh under various pH conditions, whilst Cr(VI) also causes discernable retardation on the transformation of Fh organominerals even at a low concentration;

- The redistribution of Cr(VI) for Fh organominerals is strongly controlled by the properties of the secondary iron minerals: the presence of OC results in a loose and porous secondary iron mineral structure, which significantly increases the final proportion of Cr(VI) captured by minerals compared to pure Fh;

- The redistribution of Cr(VI) is also influenced by the effects of OC on Cr(VI) adsorption, and specifically the relative binding strength of OC and Cr(VI): Cr(VI) can easily replace OC to access adsorption sites, which increases the rate constant for the capture of non-desorbable Cr(VI) and increases the final proportion of non-desorbable Cr(VI) captured in neo-formed minerals; Cr(VI) adsorption is inhibited by strongly-bound carboxyl-rich OC, which results in lower rate constants for the capture of non-desorbable Cr(VI) and decreases the final proportion of non-desorbable Cr(VI) captured in neo-formed minerals, compared to carboxyl-poor organominerals.

- Overall results show that the adsorption and fixation of Cr(VI) under oxic conditions is suppressed by the carboxyl rich OC in Fh organominerals rather than carboxyl-poor OC because Cr(VI) can easily replace the weakly-bond OC.

The work here newly finds that the presence of OC in Fh organominerals can influence the distribution of Cr(VI) during the mineral aging process, where it is first observed that different binding strengths of OC lead to different effects on the capture of Cr(VI). Specifically this study demonstrates the importance of relative binding strength between OC and Cr(VI) in controlling the mobility and fate of Cr(VI), which provides a new insight into the role of different additives, like OC, in controlling the cycling of Cr in geochemical systems. In contaminated soils, the carboxyl-richness of OC might be used as a factor to estimate the environmental risk of Cr(VI), because the work in this thesis predicts that Cr(VI) will have higher mobility in the presence of carboxyl-rich OC and thus that this mobile Cr(VI) may pose more hazardous risk to plants and animals. In addition, the pH condition is another factor that might be used to estimate the environmental risk of Cr(VI) in contaminated soils because the work in this thesis predicts that higher pH conditions will lead to higher mobility of Cr(VI). Most notably, the risk of Cr(VI) even at low concentrations should not be ignored in the presence of carboxyl-rich OC or at high pH conditions in industrial solid waste/sludge and contaminated soils. This is particularly pertinent considering that most remediation methods for Cr(VI) contamination have limited application in remediating Cr(VI) with low concentrations because of economic viability. The experiment results presented here indicate that Fh organominerals made with weakly-bound OC may be a potential material to effectively fix Cr(VI) in contaminated soils, especially for low concentrations of Cr(VI) (1-20 ppm). Overall, this work provides new information about fundamental mechanisms that might be developed for remediating Cr(VI) contaminated soils.

7.3 Behaviour and fate of chromium and carbon during Fe(II)-induced transformation of ferrihydrite organominerals

By conducting Fe(II)-induced transformation of Fh organominerals, the influence of OC on Cr distribution and the influence of Cr on OC distribution during the transformation process are investigated. This work finds that:

- Carboxyl-rich OC (But3/7 acid) and Cr(III) effectively stabilize lepidocrocite for a longer time during the Fe(II)-induced transformation process;

- For pure Fh and Fh organominerals, all detectable Cr exists in the solid phase and almost all Cr exists as Cr(III), which transitions from the desorbable to the non-desorbable pool as transformation progresses;

- The presence of OC appears to increase the rate of capture of non-desorbable Cr in neo-formed minerals, but this facilitation influence is weakened with increasing carboxyl-richness of the sequestered OC, whilst the presence of OC decreases the final proportion of non-desorbable Cr with respect to pure Fh and the decline of the final proportion of non-desorbable Cr is enhanced with increasing carboxyl-richness of the sequestered OC;

- The presence of Cr(III) causes more structural disorder in secondary iron minerals, which suggests that the secondary iron minerals have lower crystallinity and higher surface OH reactivity;

- The presence of Cr(III) aids more OC to be stabilized with solid phase after 19-days transformation at pH 5.75, where the absolute amount of OC elevated by Cr(III) appears to increase with carboxyl-richness of the sequestered OC moieties;

- The presence of Cr(III) appears to increase the amount of C that is non-desorbable with 0.1 M NaOH, especially for the carboxyl-rich OC (But3/7 acid) at pH 7;

- Overall results show that the capture of Cr is strongly inhibited by carboxyl-rich OC during Fe(II)-induced transformation of Fe minerals, while Cr(III) aids more OC stabilization with the solid phase because OC influences the properties of Fe minerals.

The work here newly finds that the carboxyl richness of OC play an important role in controlling the capture of Cr in neo-formed Fe minerals and conversely Cr(III) also influence the stabilization of OC associated with Fe minerals. As such the work here may be used to shed new light on the behaviour of Cr in natural environments with changing redox conditions. In natural environments, the redox conditions can change from oxic to anoxic conditions, for example when flooding occurs or soil depth increases. The work in this thesis predicts that under anoxic conditions, Cr(III) reduced from Cr(VI) will preferentially exist in the solid phase as adsorbates or precipitates, but that these Cr(III) will still have high potential to be re-mobilized or oxidized to Cr(VI). As such the capture of Cr(III) inside Fe minerals is likely a better pathway for the complete fixation of Cr in soils, which is influenced by OC and pH. This work predicts that the presence of OC in soils will suppress Cr(III) captured in Fe minerals, and that this suppression will be enhanced with increasing carboxyl-richness of OC and decreasing pH. A lower pH of soils will likely lead to the slower capture of Cr(III) in Fe minerals, which means Cr(III) species will have high potential to be re-mobilized over longer time periods with respect to neutral or alkaline soils. Conversely Cr(III) reduced from Cr(VI) may aid more OC stabilization in soils and thus benefit the recultivation of contaminated soils. As such the best scenario for Cr(III) capture inside Fe minerals and recultivation of contaminated soils might be achieved in soils with relatively carboxyl-poor OC at relatively high pH, so that the suppression of Cr(III) capture is less significant, and the presence of Cr(III) can aid OC stabilization. It should also be noted that this study provides a good case study for the application of ATR-FTIR to track the influence of trace metals on the properties of Fe minerals. Overall, this thesis deepens our understanding about the mobility and fixation of Cr(VI) in contaminated soils under different redox conditions.

In its entirety the work in this thesis emphasizes the importance of interactions among Fe minerals, OC and trace metals, which influence the properties of Fe minerals and control the mobility of OC and trace metals in natural environments.

7.4 Suggestions for future research

A better understanding of cycling of nutrients like C, N and P, and metal elements like Cr, Cu and Cd in terrestrial environments is essential to sustainable soil development. Previous work shows that elemental mobility and fate are controlled through interactions with sediment and soil minerals and the interplay between mineralogical and microbiological processes. Based on the work in this thesis, some specific suggestions are presented here.

Regarding the preservation of OC in soils, this research highlights the importance of OC binding strength, but it just focuses on the mobility of carboxyl-rich OC in short-term experiments. Thus it will be interesting to investigate the mobility of organic matter with other functional groups and even make a comparison between different types of OM in terms of binding strength and their stabilization during the mineralogical transformation, which can help estimate the contributions of each functional group in the preservation of OM in natural environments. Additionally, long-term culture experiments are also encouraged to test the role of OC binding strength in long-term preservation processes.

Regarding the mobility and fate of Cr(VI) under oxic conditions, this research shows that the mobility of Cr(VI) is controlled by the carboxyl-richness of OC during the transformation of Fh in ferrihydrite organominerals, but it did not investigate the bonding environment of Cr(VI) in neo-formed minerals and did not observe the influences of Cr(VI) on the stabilization of OC, probably because of the low Cr(VI) concentration. The influences of Cr(VI) on the mobility of organic C, N and P, especially low molecular weight organic matter, should be further investigated. More spectroscopic techniques can also be utilized to observe the bonding environment of Cr(VI), which can help estimate the migration of Cr(VI) in the long term. Additionally, Fh organominerals made with carboxyl-poor OC show a good adsorption and/or capture of Cr(VI), which may be applied to remediate Cr(VI) contaminated soils.

Regarding the re-distribution of OC and Cr in anoxic environments, this research shows that the re-distribution of Cr(III) and the transformation pathway of iron (oxyhydr)oxide are controlled by the carboxyl-richness of OC, and mutually Cr(III) also influences the properties of iron (oxyhydr)oxide and subsequently influences the stabilization of OC. Here, it is interesting to further study influences of OC on the formation of magnetite because magnetite can serve an electron sink or electron source contributing to the biogeochemical cycling of Fe. Besides, how different types of OC influence the distribution of Cr(III) should be further investigated, where some functional groups may have stronger affinity than –FeOH sites to Cr(III), which can further influence the migration of Cr. Additionally, how Cr(III) influences the properties of iron (oxyhydr)oxide and how Cr(III) aids OC stabilization with minerals needs more direct evidence to support the detailed mechanisms suggested in my study. It is also suggested to study the influences of microbiological activities on the migration and fixation of Cr(VI), where the systems are more complex due to the presence of various kinds of OM and the reactivity of microorganisms.

Overall, there are still knowledge gaps about the influence of OC and iron (oxyhydr)oxide on the mobility and fate of Cr and more research work is encouraged to advance our understanding, and thus help protect soil health.

Appendixes

Section S1: MOPS and MES buffers

In my experiments MOPS and MES buffers were chosen because they have negligible impact on the transformation of Fh (Bradbury and Baeyens, 1999; Ford et al., 1999). It was unclear however, whether they can be sequestered to Fe minerals. To determine the sequestration of MOPS and MES buffers test experiments were conducted. Fh_Pen1/5, Fh_Hex2/6 and Fh_But3/7 coprecipitate slurries were mixed with MOPS to produce 2 g/L suspensions with 30 mM MOPS in 0.01 M $NaNO_3$ background electrolyte. Control experiments without MOPS buffer were also prepared. After shaking for 24 h, two 15 mL aliquots were subsampled from the container and filtered with 0.22 μm cellulose nitrate filters using a vacuum filtration apparatus. The mineral particles were collected, rinsed using 15 mL DI water and then freeze-dried for total solid C measurement.

The total amount of solid C (wt%) for the Fh coprecipitates mixed with MOPs are the same as those generated in the controls without MOPS added (Figure S1), indicating that MOPS has negligible influence on OC adsorption behaviour. As such we are confident that MOPS sequestration is negligible and has no discernable influence on the distribution of OC during aging. We also consider that MES sequestration is negligible and has no discernable influence on the distribution of OC during aging because MOPS and MES have similar structure and the same functional group that would be responsible for sequestration.

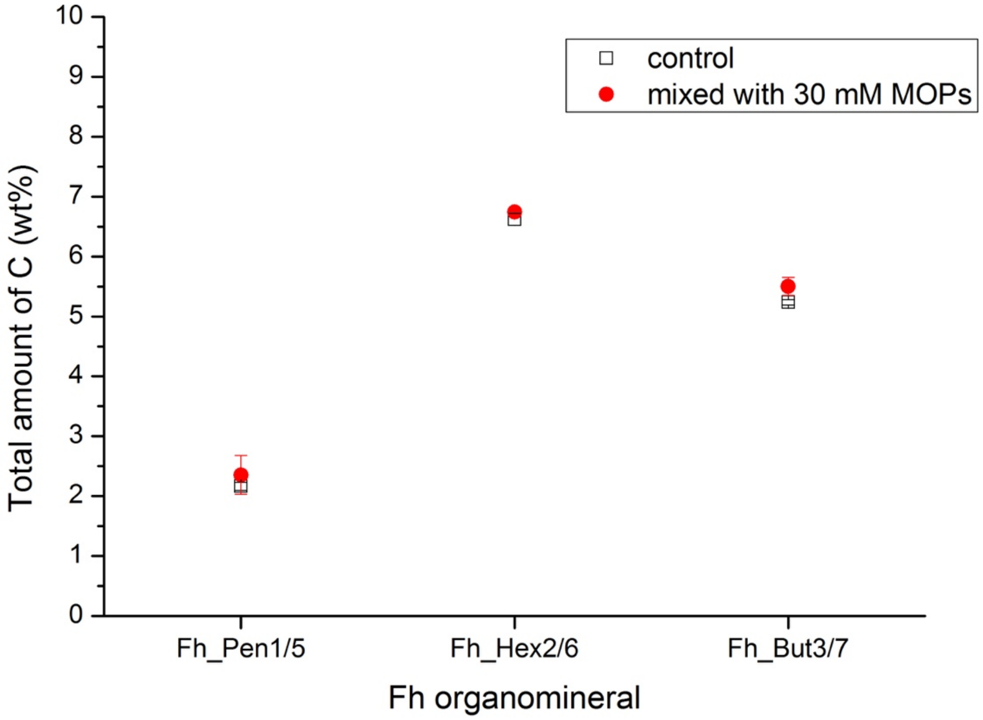

Figure S1. Influence of MOPS on total amount of C for different Fh coprecipitates. The red solid circles are experiments mixed with 30 mM MOPS and the black open squares are the control experiments without MOPS added. Fh_Pen1/5, Fh_Hex2/6 and Fh_But3/7 are Fh coprecipitates made with Pen1/5, Hex2/6 and But3/7, which represent simple carboxyl-rich OC with one, two and three carboxyl groups, respectively. Error bars represent standard deviations of duplicate samples.

Section S2: Observation of Fh aging using acid leaching method

The acid leaching method has been applied to observe the transformation rate of Fh in the study by Wang et al. (2020), where 0.4 M HCl is used to extract untransformed Fh. We conducted a test experiment to study the extraction efficiency of this acid leaching method. Fh and Hm slurries were mixed at 0 %, 25 %, 50 %, 75 % and 100 % Fh based on Fe atomic ratio, where the total Fe atomic ratios were equal to those in the aging experiment. Seven 1 mL aliquots from each suspension were pipetted into 2 mL centrifuge tubes. 1 mL 12 mol L^{-1} HCl was added into one aliquot to produce 6 mol L^{-1} HCl in suspension for the determination of total Fe in the solid phase by total digestion of all solid Fe phases ($[Fe(T)_{6\ M\ HCl}]$) (Wang et al., 2020a). 1 mL 0.8 mol L^{-1} HCl was added into the other aliquot to produce 0.4 mol L^{-1} HCl, reacted for 10 mins, then centrifuged, and filtered. As soluble Fe(III) in the aqueous phase was below detection limits before adding acids (Reddy et al., 2015), the concentration of Fe in the supernatant after the 0.4 mol L^{-1} HCl addition ($[Fe(T)_{0.4\ M\ HCl}]$ represented the total concentration of acid reactive solid phase Fe minerals, nominally Fh (Wang et al., 2020a). The concentration of Fe was determined on an Atomic Absorption Spectrophotometer (iCE 3300 AAS). Then the fraction of remaining Fh was quantitatively calculated through the equation: $[Fe(T)_{0.4\ M\ HCl}]/ [Fe(T)_{6\ M\ HCl}]$. All operations above were conducted at least in duplicate.

As shown in Figure S2, the efficiency of extracting Fh from mixtures of Fh and Hm is over 95%. As such we are confident that Hm dissolution is negligible while Fh dissolution is essentially complete in 0.4 M HCl. It is also reported that 0.4 M HCl cannot dissolve Gt (Reddy et al., 2015), and as such 0.4 M HCl can be used to extract untransformed Fh from mixtures of Fh, Hm and Gt.

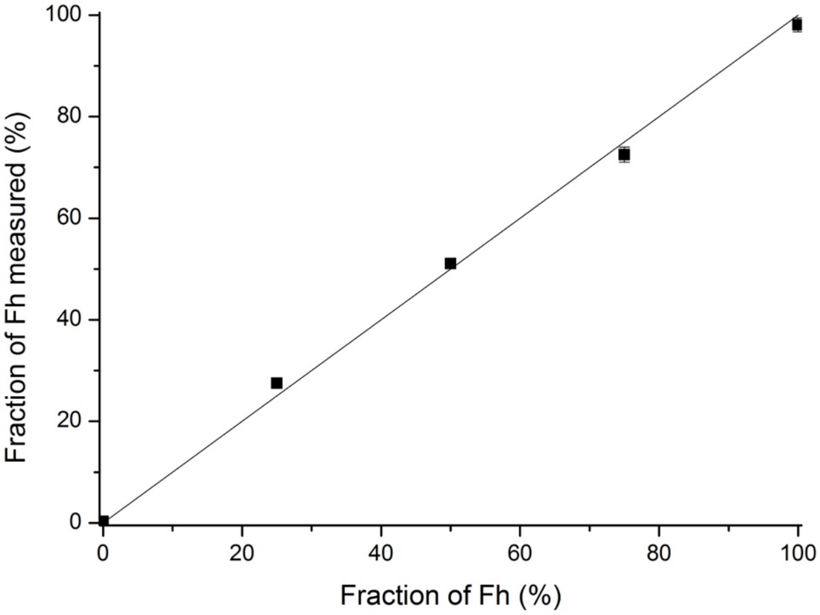

Figure S2. Fraction of Fh extracted from mixtures of Fh and Hm at 0 %, 25 %, 50 %, 75 % and 100 % Fh using acid leaching method. The line shows the 1:1 line, corresponding to the theoretical fraction of Fh in the mixtures.

Section S3: XRD pattern of selected Fh coprecipitates prior to aging

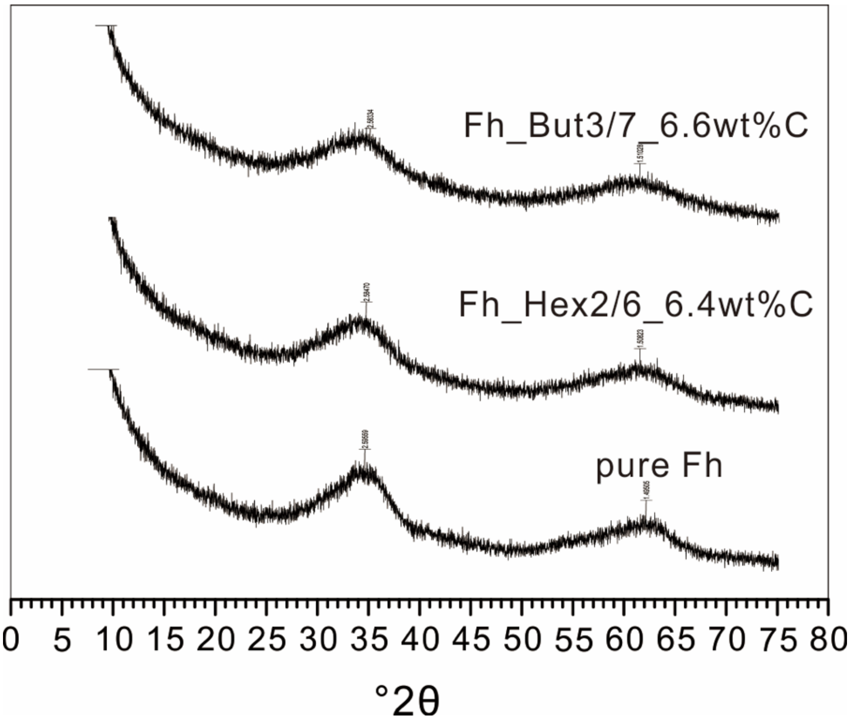

Figure S3. X-ray diffraction patterns of selected Fh coprecipitates prior to aging.

Section4: STXM image for Fh_But3/7_7.8wt%C

My representative STXM elemental distribution map of the Fh coprecipitates prior to aging is shown for Fh_But3/7_7.8wt%C, i.e., my Fh coprecipitate with the highest C loading. The map shows that C (cyan) is apparently more concentrated at the particle edges. Given that the lowest energy used for mapping is for C, and heavier elements (mainly Fe) in the particle absorb X-rays, C is not quantitatively mapped for particles like ours with varying thickness. Areas where the particles are thinner can thus appear more concentrated in C than areas where the particles are thicker. As such relative changes in OD across a particle are not necessarily indicative of C distribution. For particles of varying thickness however, the edges are typically thinner than the central areas, and the STXM signal at the edges therefore reflects C mainly located at the particle surfaces, while the STXM signal in the centre reflects C located at the particle surfaces and in the particle interiors. If C appears to be more concentrated at the edges than the centre, then the distribution of C across the whole particle is approximately equal to that at the particle surfaces and is not substantially augmented in the central area by additional C associated with the greater particle volume. In this case C can be interpreted to be mainly distributed at the particle surfaces, without substantial incorporation into the particle interior (Curti et al., 2021).

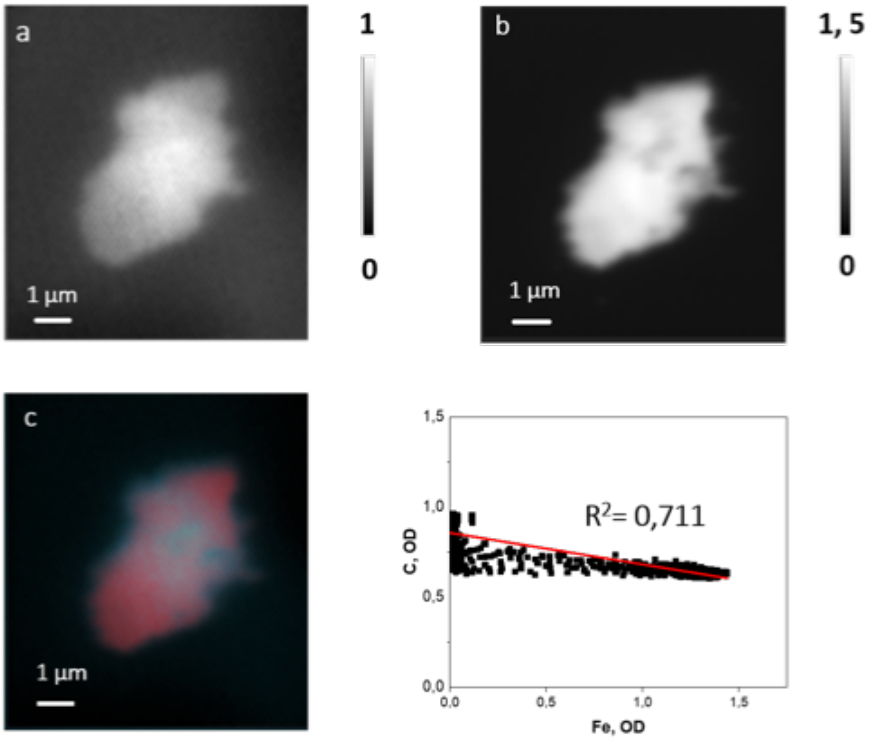

Figure S4. STXM elemental distribution maps of (a) carbon and (b) iron for a selected particle of Fh_But3/7_7.8wt%C. The gray scale indicates thickness in optical density. The scale bar is 1 µm. (c) Colour-coded composite maps of carbon (cyan) and iron (red). (d) Correlation plots of thickness (OD) values of carbon and iron obtained from STXM elemental distribution maps; $R^2 = 0.711$.

Section 5: Fitting to the increasing rates of Cr(VI) captured in neo-formed minerals

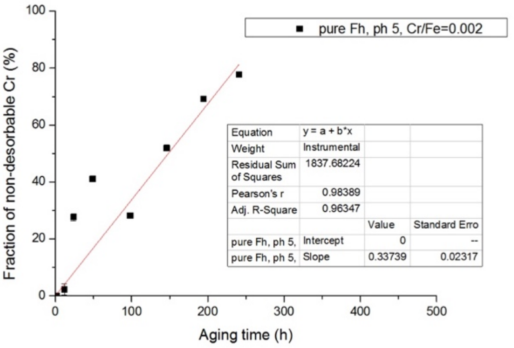

Equation	y = a + b*x		
Weight	Instrumental		
Residual Sum of Squares	1837.68224		
Pearson's r	0.98389		
Adj. R-Square	0.96347		
		Value	Standard Erro
pure Fh, ph 5,	Intercept	0	--
pure Fh, ph 5,	Slope	0.33739	0.02317

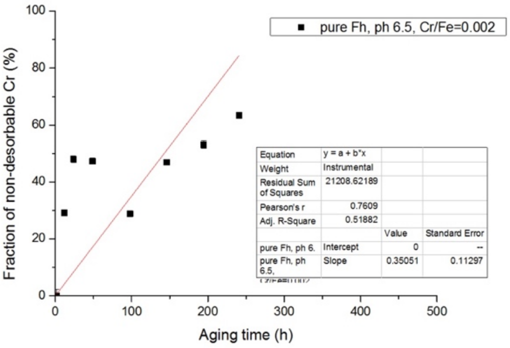

Equation	y = a + b*x		
Weight	Instrumental		
Residual Sum of Squares	21208.62189		
Pearson's r	0.7609		
Adj. R-Square	0.51882		
		Value	Standard Error
pure Fh, ph 6.	Intercept	0	--
pure Fh, ph 6.5,	Slope	0.35051	0.11297

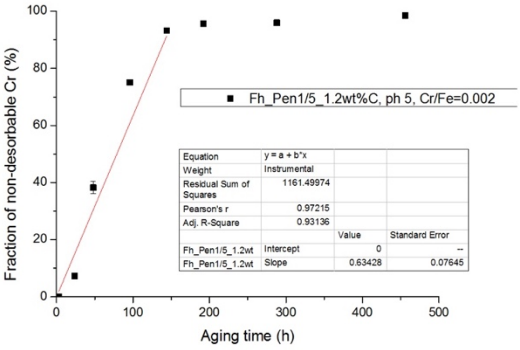

Equation	y = a + b*x		
Weight	Instrumental		
Residual Sum of Squares	1161.49974		
Pearson's r	0.97215		
Adj. R-Square	0.93136		
		Value	Standard Error
Fh_Pen1/5_1.2wt	Intercept	0	--
Fh_Pen1/5_1.2wt	Slope	0.63428	0.07645

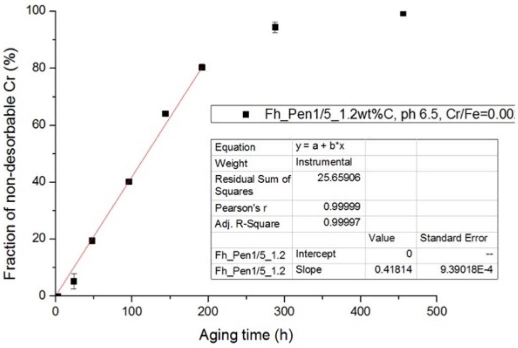

Equation	y = a + b*x		
Weight	Instrumental		
Residual Sum of Squares	25.65906		
Pearson's r	0.99999		
Adj. R-Square	0.99997		
		Value	Standard Error
Fh_Pen1/5_1.2	Intercept	0	--
Fh_Pen1/5_1.2	Slope	0.41814	9.39018E-4

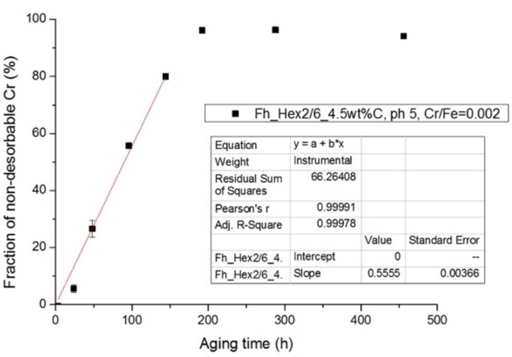

Equation	y = a + b*x		
Weight	Instrumental		
Residual Sum of Squares	66.26408		
Pearson's r	0.99991		
Adj. R-Square	0.99978		
		Value	Standard Error
Fh_Hex2/6_4.	Intercept	0	--
Fh_Hex2/6_4.	Slope	0.5555	0.00366

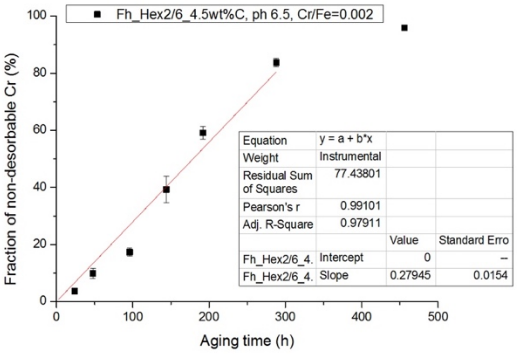

Equation	y = a + b*x		
Weight	Instrumental		
Residual Sum of Squares	77.43801		
Pearson's r	0.99101		
Adj. R-Square	0.97911		
		Value	Standard Erro
Fh_Hex2/6_4.	Intercept	0	--
Fh_Hex2/6_4.	Slope	0.27945	0.0154

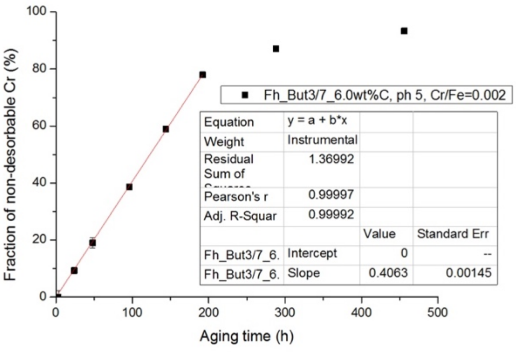

Equation	y = a + b*x		
Weight	Instrumental		
Residual Sum of	1.36992		
Pearson's r	0.99997		
Adj. R-Squar	0.99992		
		Value	Standard Err
Fh_But3/7_6.	Intercept	0	--
Fh_But3/7_6.	Slope	0.4063	0.00145

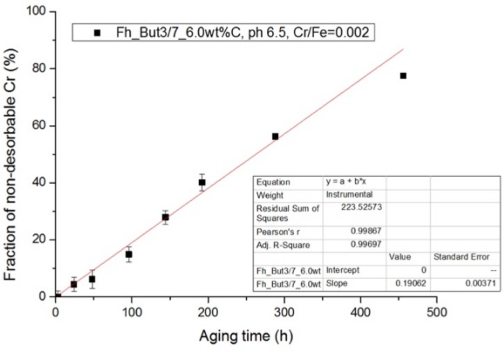

Equation	y = a + b*x		
Weight	Instrumental		
Residual Sum of Squares	223.52573		
Pearson's r	0.99867		
Adj. R-Square	0.99697		
		Value	Standard Error
Fh_But3/7_6.0wt	Intercept	0	--
Fh_But3/7_6.0wt	Slope	0.19062	0.00371

Figure S5. Linear fit to the rates of non-desorbable Cr(VI) during the mineralogical transformation of pure Fh and selected Fh organominerals. The percentate of non-desorbable Cr(VI) from 0% to 80% is fitted with linear equation $[A_0] = a + b \times t$, where $[A_0]$ is the percentate of non-desorbable Cr(VI) at time t, a is the intercept and b is the slop representing the rate of the capture of Cr(VI).

Section 6: Fitting to the rate of Cr captured in neo-formed minerals during Fe(II)-induced transformation of pure Fh and Fh organominerals

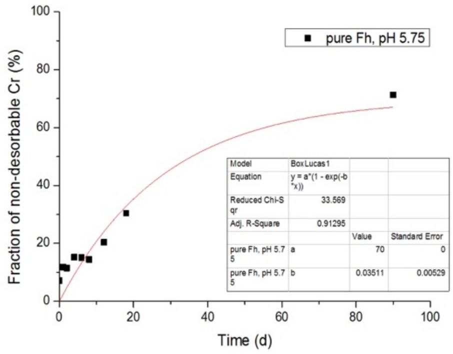

Model	BoxLucas1		
Equation	y = a*(1 - exp(-b*x))		
Reduced Chi-Sqr	33.569		
Adj. R-Square	0.91295		
		Value	Standard Error
pure Fh, pH 5.75	a	70	0
pure Fh, pH 5.75	b	0.03511	0.00529

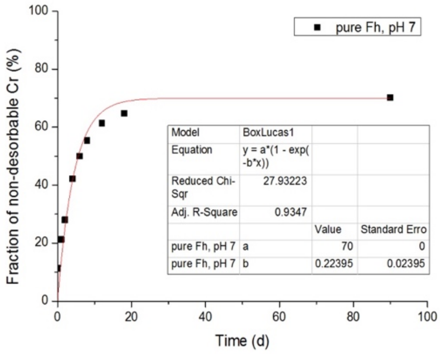

Model	BoxLucas1		
Equation	y = a*(1 - exp(-b*x))		
Reduced Chi-Sqr	27.93223		
Adj. R-Square	0.9347		
		Value	Standard Erro
pure Fh, pH 7	a	70	0
pure Fh, pH 7	b	0.22395	0.02395

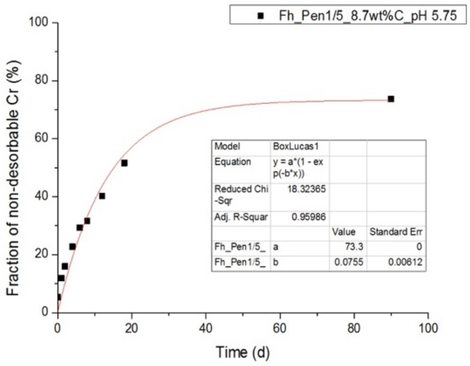

Model	BoxLucas1		
Equation	y = a*(1 - exp(-b*x))		
Reduced Chi-Sqr	18.32365		
Adj. R-Squar	0.95986		
		Value	Standard Err
Fh_Pen1/5_	a	73.3	0
Fh_Pen1/5_	b	0.0755	0.00612

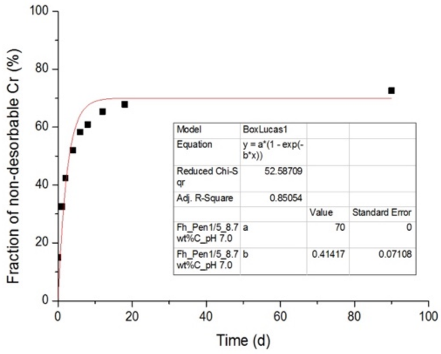

Model	BoxLucas1		
Equation	y = a*(1 - exp(-b*x))		
Reduced Chi-Sqr	52.58709		
Adj. R-Square	0.85054		
		Value	Standard Error
Fh_Pen1/5_8.7wt%C_pH 7.0	a	70	0
Fh_Pen1/5_8.7wt%C_pH 7.0	b	0.41417	0.07108

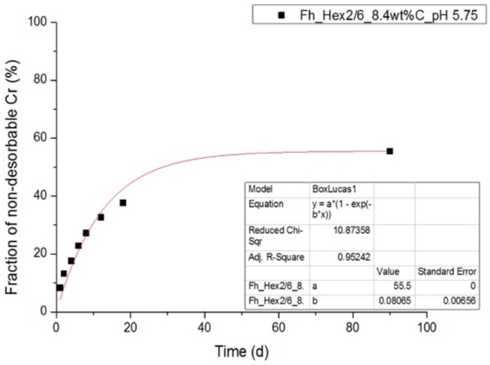

Model	BoxLucas1		
Equation	y = a*(1 - exp(-b*x))		
Reduced Chi-Sqr	10.87358		
Adj. R-Square	0.95242		
		Value	Standard Error
Fh_Hex2/6_8.	a	55.5	0
Fh_Hex2/6_8.	b	0.08065	0.00656

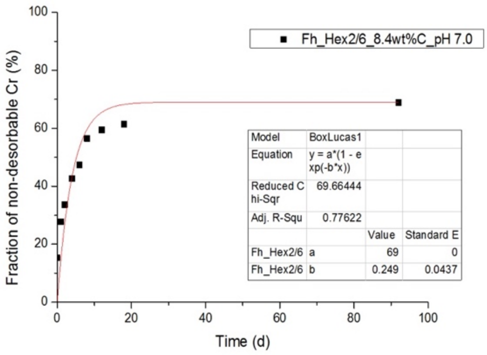

Model	BoxLucas1		
Equation	y = a*(1 - exp(-b*x))		
Reduced Chi-Sqr	69.66444		
Adj. R-Squ	0.77622		
		Value	Standard E
Fh_Hex2/6	a	69	0
Fh_Hex2/6	b	0.249	0.0437

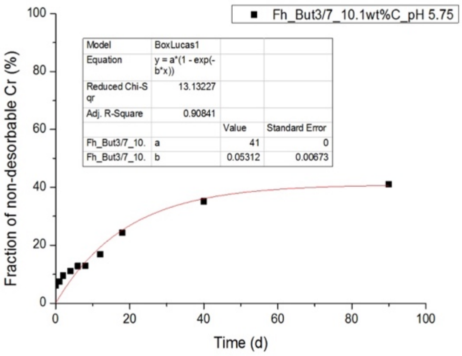

Model	BoxLucas1		
Equation	y = a*(1 - exp(-b*x))		
Reduced Chi-Sqr	13.13227		
Adj. R-Square	0.90841		
		Value	Standard Error
Fh_But3/7_10.	a	41	0
Fh_But3/7_10.	b	0.05312	0.00673

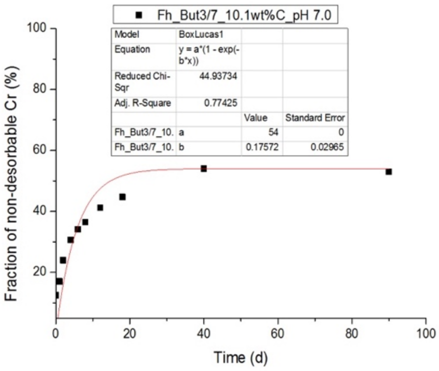

Model	BoxLucas1		
Equation	y = a*(1 - exp(-b*x))		
Reduced Chi-Sqr	44.93734		
Adj. R-Square	0.77425		
		Value	Standard Error
Fh_But3/7_10.	a	54	0
Fh_But3/7_10.	b	0.17572	0.02965

Figure S6. Model fit to the rates of non-desorbable Cr during Fe(II)-induced transformation of pure Fh and Fh organominerals. The percentates of non-desorbable Cr are fitted with the rate equation $[A]_t = a \times (1 - e^{-bt})$ where $[A]_t$ is the fraction of $Cr_{non\text{-}desorbable}$ at time *t*, *a* is final proportion of non-desorbable Cr after the transformation, *b* is the rate constant.

Section 7: Extraction of Cr(VI), Fe(II) and Cr(III) with wet chemical methods

Section 7.1 Extraction of Cr(VI) from iron minerals

The alkaline leaching method has been used to desorb Cr(VI) from iron minerals in the study (Hu et al., 2019), where 0.1 M NaOH is used. We conducted a test experiment to study the extraction efficiency of this alkaline leaching method. Ferrihydrite slurry and Cr(VI) stock solution were added into MilliQ water to give a total volume of 50 mL, a solid solution ration of 2 g dry sorbent L^{-1} with 0.1%Cr at 100% adsrotpion (Cr(VI) 2.17 ppm). Then the pH of suspensions was adjusted to pH 5 and pH 6.5 with dilute HCl and NaOH solutions, after which the reactors were shaken for 24 h to get equllibrium.

Three 2-mL aliquots were subsampled from the reactor and centrifuged to separate solid minerals and supernatant. The supernatant was collected for measurement of aqueous Cr(VI). The remaining mineral particles were rinsed with 2 mL DI water, and re-suspended in 2 mL 0.1 M NaOH and shaken for 24 h to extract Cr(VI). Then resulting suspensions were filtered with 0.22 μm PES filters and the filtrate was collected for measurement of Cr(VI), which was operationally defined as desorbable Cr(VI) ($Cr_{desorbable}$). Proportions of Cr(VI) remaining in the solid, operationally defined as non-desorbable Cr(VI) ($Cr_{non\text{-}desorbalbe}$), were calculated based on mass balance. The Cr(VI) concentrations in all solutions generated above were measured by inductively coupled plasma mass spectrometry (ICP-MS). All measurements were conducted in triplicate.

As shown in Table S1, the extraction efficiency is over 95%. As such, I'm confident that the alkaline leaching method can be applied to observe the distribution of Cr(VI) during mineralogical transformation of pure Fh and Fh organomienrals.

Table S1. Alkaline leaching of Cr(VI) with 0.1 M NaOH from pure Fh

	pH	Aqueous Cr(VI)	Desorbable Cr(VI) with 0.1 M NaOH (ppm)	Total Cr(VI) added (ppm)	Extraction efficiency (%)
Pure Fh	5	0	2.13	2.17	98.18
	5	0	2.11	2.17	97.48
	5	0	2.14	2.17	98.91
	6.5	0	2.12	2.17	97.71
	6.5	0	2.15	2.17	99.28
	6.5	0	2.16	2.17	99.52

Section 7.2 Measurement and extraction of Fe(II)

The ferrozine method has been widely applied to measure Fe(II) (Stookey, 1970), but whether the presence of Pen1/5, Hex2/6 and But3/7 in my study influence the measurement of Fe(II) is unkown. I have conducted the test experiment to study the influence of carboxylic acids. The Fe(II) stock solution ($NH_4Fe(SO_4)_2$), Cr(III) stocks solution and each organic acids stock solution were added into MilliQ water to give a total volume of 50 mL, Fe(II) concention of 50 ppm, Cr(III) concention of 20 ppm, each OC concentration of 0.4 mM in the 30 mM MES buffer solution. Then the mixture solution were shaken 1 h to make it homogeneous. Then the concentration of Fe(II) was measured by ferrozine assay. As shown in Table S2, the aqueous Fe(II) measured was same with the total amount of Fe(II) added in system. Therefore, the presence of my carboxylic acdis, Cr(III) and MES buffer has no discernable influence on Fe(II) measurement under my experiment conditions.

Table S2. Measuremnt of Fe(II) with ferrozine assay in the presence of 0.4 mM OC, 20 ppm Cr(III) and 30 mM MES

			Total Fe(II) added (ppm)	Fe(II) measured (ppm)
Pen1/5_0.4 mM	Cr(III)_20 ppm	MES 30 mM	50	49.81
			50	50.68
Hex2/6_0.4mM	Cr(III)_20 ppm	MES 30 mM	50	50.16
			50	49.93
But3/7_0.4 mM	Cr(III)_20 ppm	MES 30 mM	50	50.02
			50	49.80

The acid leaching method has been used to track changes of Fe(II) adsorbed on iron mienrals during Fe(II)-induced tranformation of Fh (Sheng et al., 2020a; Xiao et al., 2017), where 5 mM HCl is used to desorb Fe(II) from Fe minerals. I also conducted the experiments to test the extraction efficiency of this method.

An aliquot of the non-freeze-dried pure Fh and Fh organomineral slurries were added to 0.01 M $NaNO_3$ background electrolyte to give a total volume of 50 mL with a solid solution ration of 2 g L^{-1}. The suspensions were then adjusted to environmentally relevant pH values of 5.75 and 7 using dilute NaOH or HNO_3 and buffered using 30 mmol L^{-1} organic buffer 2-(N-Morpholino)ethane-sulphonic acid (MES) and 3-(N-Morpholino)propanesulphonic acid (MOPS), respectively. All the solutions were purged with high purity N_2 for at least 0.5h before they were transferred into the glove box and then exposed to the atmosphere of glove box for 24h to remove the trace dissolved oxygen. A stock Fe(II) solution ($FeCl_2$) was then added to the suspension to induce the mineralogical transformation of the iron minerals. After reaction for 0.5 h to get equilibrium, 1 mL samples of the homogeneous suspension were removed and centrifuged at around 6000 g for 3 minutes. The supernatant was filtered with 0.22 μm PES syringe filters for the measurement of aqueous Fe(II) concentration ($[Fe(II)_{aq}]$). After the removal of the supernatant, 1 mL of 5 mM or 10 mM HCl was then added to remove Fe(II) adsorbed on the minerals. The suspension was mixed homogeneously three times at least by hand then centrifuged after reacting for 10 min. The supernatant was also filtered with 0.22 μm PES syringe filters for Fe(II) measurement, which is operationally defined as desorbable Fe(II) ($Fe(II)_{desorbable}$). The concentration of Fe(II) was measured by ferrozine assay (Sheng et al., 2020a; Stookey, 1970). All experiments were conducted in duplicate.

As shown in Table S3, the recovery efficiency of Fe(II) is generally over 90% for all systems except Fh_Pen1/5 system (>80%), which indicates the acid leaching method is a useful method to track changes aqueous and desorbable Fe(II) during the Fe(II)-induced transformation of Fe minerals.

Table S3. Recovery of Fe(II) with acid leaching method during Fe(II)-induced tranformation of Fh and Fh organominerals after reacting for 0.5 h.

	Extraction method	pH	Aqueous Fe(II) (ppm)	Desorbable Fe(II) (ppm)	Total Fe(II) added (ppm)	Recovery efficiency (%)
Pure Fh	5 mM HCl	5.75	103.91	4.93	109.76	99.16
			104.90	4.19	109.76	99.39
	5 mM HCl	7.00	59.68	41.22	109.76	91.93
			61.78	40.97	109.76	93.61
Fh_Pen1/5_ 8.4wt%C	5 mM HCl	5.75	31.9	4.3	43.9	82.46
			31.5	3.8	43.9	80.41
	5 mM HCl	7.00	8.2	29.4	43.9	85.65
			6.8	27.6	43.9	78.36
Fh_Hex2/6 _8.1wt%C	10 mM HCl	5.75	34.8	6.6	43.9	94.31
			36.0	8.2	43.9	100.68
	10 mM HCl	7.00	12.1	27.4	43.9	89.98
			12.4	27.8	43.9	91.57
Fh_But3/7_ 10.1wt%C	10 mM HCl	7.00	8.6	32.0	43.9	92.48
			8.6	32.2	43.9	92.94

Section 7.3. Extraction of Cr(III) from Fe mineral surface

Here I design an extraction method to observe the distribution of Cr during Fe(II)-induced transformation, where 200 ppm $KMnO_4$ and 0.1 M NaOH mixture solution is used to extract Cr(III) from Fe mineral surface. The test experiments were conducted to study the extraction efficiency. Ferrihydrite slurry and Cr(III) stock solution was added into MilliQ water to give a total volume of 50 mL, a solid solution ration of 2 g dry sorbent L^{-1} and Cr(III) concentration of 2.17 ppm (406.3 uM). An 1 mL aluquot was collected from reaction and then centrifuged at around 6000 g for 3 mins. The supernatant was filtered with 0.22 μm PES syringe filters for the measurement of aqueous Cr(III) by inductively coupled plasma mass spectrometry (ICP-MS). After removing all supernatant, the solid minerals were removed from the anoxic chamber and treated with 1mL 200 ppm $KMnO_4$ and 0.1 M NaOH mixture solution to desorb Cr(III) from the mineral surface. The $KMnO_4$ solution can oxidize Cr(III) to Cr(VI) quickly and effectively (Rogers, 2016), and then these Cr(VI) will be desorbed from minerals in the presence of 0.1 M NaOH. After shaking for 24 h, the suspensions were centrifuged and the supernatant was transferred into new tubes. Then the supernatants were heated at 75℃ for 24 h to decompose $KMnO_4$ because the presence of $KMnO_4$ can influence the measurement of Cr(VI) by 1,5-diphenylcarbazide method (Rogers, 2016).

As shown in Table S4, the desorption efficiency in my treatments was over 95%. As such, this method can be effectively applied to observe changes of Cr(III) from desorbable pool to non-desorbable pool during Fe(II)-induced transformation of Fh and Fh organominerals.

Table S4. Extraction of Cr(III) from Fh surface with 200 ppm $KMnO_4$ and 0.1 M NaOH mixture solution

Mineral	Aqueous Cr(III)	Cr(VI) desorbed (uM)	Total Cr(III) added (uM)	Extraction efficiency (%)
Pure Fh	0	384.7	406.3	94.7
	0	395.7	406.3	97.4
	0	385.4	406.3	94.9
	0	387.3	406.3	95.3
	0	399.5	406.3	98.3
	0	400.7	406.3	98.6

Reference:

Adriano, D. C. (1984). In R. S. De Santo (Ed.), Chromium. Heavy metals in natural water. Heidelberg, Germany: Springer-Verlag Pub. Co.

Adriano, D.C. (1986). Chromium. In: Trace elements in the terrestrial environment (pp. 58–76). New York: Springer Pub. Co.

Adhikari, D., Zhao, Q., Das, K., Mejia, J., Huang, R., Wang, X., Poulson, S.R., Tang, Y., Roden, E.E. and Yang, Y. (2017) Dynamics of ferrihydrite-bound organic carbon during microbial Fe reduction. Geochimica et Cosmochimica Acta 212, 221-233.

Alcacio, T.E., Hesterberg, D., Chou, J.W., Martin, J.D., Beauchemin, S. and Sayers, D.E. (2001) Molecular scale characteristics of Cu(II) bonding in goethite–humate complexes. Geochimica et Cosmochimica Acta 65, 1355-1366.

Alexander, J. and Aaseth, J.J.A. (1995) Uptake of chromate in human red blood cells and isolated rat liver cells: the role of the anion carrier. Analyst 120.

Ali, M.A. and Dzombak, D.A. (1996) Effects of simple organic acids on sorption of Cu2+ and Ca2+ on goethite. Geochimica et Cosmochimica Acta 60, 291-304.

Amonette, J.E. and Rai, D. (1990) Identification of Noncrystalline (Fe,Cr)(Oh)3 by Infrared Spectroscopy. Clays and Clay Minerals 38, 129-136.

Amstaetter, K., Borch, T. and Kappler, A. (2012) Influence of humic acid imposed changes of ferrihydrite aggregation on microbial Fe(III) reduction. Geochimica et Cosmochimica Acta 85, 326-341.

Avudainayagam, S., Megharaj, M., Owens, G., Kookana, R.S., Chittleborough, D. and Naidu, R. (2003) Chemistry of chromium in soils with emphasis on tannery waste sites, Reviews of environmental contamination and toxicology. Springer, pp. 53-91.

Babula, P., Adam, V., Opatrilova, R., Zehnalek, J., Havel, L. and Kizek, R. (2009) Uncommon heavy metals, metalloids and their plant toxicity: a review, Organic Farming, Pest Control and Remediation of Soil Pollutants. Springer, pp. 275-317.

Barnhart, J. (1997) Occurrences, Uses, and Properties of Chromium. Regulatory Toxicology and Pharmacology 26, S3-S7.

Barrera-Díaz, C.E., Lugo-Lugo, V. and Bilyeu, B. (2012) A review of chemical, electrochemical and biological methods for aqueous Cr(VI) reduction. Journal of Hazardous Materials 223-224, 1-12.

Bartlett, R. and James, B. (1979) Behavior of Chromium in Soils: III. Oxidation. 8, 31-35.

Bartlett, R.J. (1991) Chromium cycling in soils and water: links, gaps, and methods. Environ Health Perspect 92, 17-24.

Bazilevskaya, E., Archibald, D.D. and Martínez, C.E. (2012) Rate constants and mechanisms for the crystallization of Al nano-goethite under environmentally relevant conditions. Geochimica et Cosmochimica Acta 88, 167-182.

Bazylinski, D.A., Frankel, R.B. and Konhauser, K.O. (2007) Modes of Biomineralization of Magnetite by Microbes. Geomicrobiology Journal 24, 465-475.

Bhattacharyya, A., Schmidt, M.P., Stavitski, E., Azimzadeh, B. and Martínez, C.E. (2019) Ligands representing important functional groups of natural organic matter facilitate Fe redox transformations and resulting binding environments. Geochimica et Cosmochimica Acta 251, 157-175.

Boily, J.-F., Szanyi, J. and Felmy, A.R. (2006) A combined FTIR and TPD study on the bulk and surface dehydroxylation and decarbonation of synthetic goethite. Geochimica et Cosmochimica Acta 70, 3613-3624.

Boland, D.D., Collins, R.N., Miller, C.J., Glover, C.J. and Waite, T.D. (2014) Effect of Solution and Solid-Phase Conditions on the Fe(II)-Accelerated Transformation of Ferrihydrite to Lepidocrocite and Goethite. Environmental Science & Technology 48, 5477-5485.

Bompoti, N.M., Chrysochoou, M. and Machesky, M.L. (2019) A Unified Surface Complexation Modeling Approach for Chromate Adsorption on Iron Oxides. Environmental Science & Technology.

Borges, S.d.S., Korn, M., Costa Lima, J., eacute and Luis Fontes, d. (2002) Chromium(III) Determination with 1,5-Diphenylcarbazide Based on the Oxidative Effect of Chlorine Radicals Generated from CCl₄ Sonolysis in Aqueous Solution. Analytical Sciences 18, 1361-1366.

Börsig, N., Scheinost, A.C., Shaw, S., Schild, D. and Neumann, T. (2017) Uptake mechanisms of selenium oxyanions during the ferrihydrite-hematite recrystallization. Geochimica et Cosmochimica Acta 206, 236-253.

Bradbury, M.H. and Baeyens, B. (1999) Modelling the sorption of Zn and Ni on Ca-montmorillonite. Geochimica et Cosmochimica Acta 63, 325-336.

Brose, D.A. and James, B.R. (2013) Hexavalent Chromium Reduction by Tartaric Acid and Isopropyl Alcohol in Mid-Atlantic Soils and the Role of Mn(III,IV)(hydr)oxides. Environmental Science & Technology 47, 12985-12991.

Brunauer, S., Emmett, P.H. and Teller, E. (1938) Adsorption of Gases in Multimolecular Layers. Journal of the American Chemical Society 60, 309-319.

Buerge, I.J. and Hug, S.J. (1997) Kinetics and pH Dependence of Chromium(VI) Reduction by Iron(II). Environmental Science & Technology 31, 1426-1432.

Burdige, D.J. (2007) Preservation of Organic Matter in Marine Sediments: Controls, Mechanisms, and an Imbalance in Sediment Organic Carbon Budgets? Chemical Reviews 107, 467-485.

Butera, S., Trapp, S., Astrup, T.F. and Christensen, T.H. (2015) Soil retention of hexavalent chromium released from construction and demolition waste in a road-base-application scenario. Journal of Hazardous Materials 298, 361-367.

Canfield, D.E., Jørgensen, B.B., Fossing, H., Glud, R., Gundersen, J., Ramsing, N.B., Thamdrup, B., Hansen, J.W., Nielsen, L.P. and Hall, P.O. (1993) Pathways of organic carbon oxidation in three continental margin sediments. . Marine Geology 113, 27-40.

Cervantes, C., Campos-García, J., Devars, S., Gutiérrez-Corona, F., Loza-Tavera, H., Torres-Guzmán, J.C. and Moreno-Sánchez, R. (2001) Interactions of chromium with microorganisms and plants. FEMS Microbiology Reviews 25, 335-347.

Chakraborty, A.R. and Mishra, R.K. (1992) Speciation and determination of chromium in waters+. Chemical Speciation & Bioavailability 4, 131-134.

Chandra, P. and Kulshreshtha, K. (2004) Chromium accumulation and toxicity in aquatic vascular plants. The Botanical Review 70, 313-327.

Charlet, L. and Manceau, A.A. (1992) X-ray absorption spectroscopic study of the sorption of Cr(III) at the oxide-water interface: II. Adsorption, coprecipitation, and surface precipitation on hydrous ferric oxide. Journal of Colloid and Interface Science 148, 443-458.

Charlton, S.R. and Parkhurst, D.L. (2002) PHREEQCI--A graphical user interface to the geochemical model PHREEQC, Fact Sheet.

Chen, C., Dynes, J.J., Wang, J. and Sparks, D.L. (2014) Properties of Fe-Organic Matter Associations via Coprecipitation versus Adsorption. Environmental Science & Technology 48, 13751-13759.

Chen, C., Hall, S.J., Coward, E. and Thompson, A. (2020) Iron-mediated organic matter decomposition in humid soils can counteract protection. Nature Communications 11.

Chen, C., Kukkadapu, R. and Sparks, D.L. (2015) Influence of Coprecipitated Organic Matter on Fe2+(aq)-Catalyzed Transformation of Ferrihydrite: Implications for Carbon Dynamics. Environ Sci Technol 49, 10927-10936.

Chen, C. and Sparks, D.L. (2018) Fe(II)-Induced Mineral Transformation of Ferrihydrite–Organic Matter Adsorption and Co-precipitation Complexes in the Absence and Presence of As(III). ACS Earth and Space Chemistry 2, 1095-1101.

Chen, K.-Y., Tzou, Y.-M., Chan, Y.-T., Wu, J.-J., Teah, H.-Y. and Liu, Y.-T. (2019) Removal and simultaneous reduction of Cr(VI) by organo-Fe(III) composites produced during coprecipitation and coagulation processes. Journal of Hazardous Materials 376, 12-20.

Chen, T., Chang, Q., Liu, J., Clevers, J.G.P.W. and Kooistra, L. (2016) Identification of soil heavy metal sources and improvement in spatial mapping based on soil spectral information: A case study in northwest China. Science of The Total Environment 565, 155-164.

Choppala, G. and Burton, E.D. (2018) Chromium(III) substitution inhibits the Fe(II)-accelerated transformation of schwertmannite. PLoS One 13, e0208355.

Chorover, J. and Amistadi, M.K. (2001) Reaction of forest floor organic matter at goethite, birnessite and smectite surfaces. Geochimica et Cosmochimica Acta 65, 95-109.

Cismasu, A.C., Michel, F.M., Tcaciuc, A.P., Tyliszczak, T. and Brown, J.G.E. (2011) Composition and structural aspects of naturally occurring ferrihydrite. Comptes Rendus Geoscience 343, 210-218.

Cismasu, A.C., Williams, K.H. and Nico, P.S. (2016) Iron and Carbon Dynamics during Aging and Reductive Transformation of Biogenic Ferrihydrite. Environ Sci Technol 50, 25-35.

Cornell, R. and Schwertmann, U. (1979a) Influence of organic anions on the crystallization of ferrihydrite. Clays and Clay Mineral 27, 402-410.

Cornell, R. and Schwertmann, U. (1979b) Influence of organic anions on the crystallization of ferrihydrite. Clays and Clay Minerals 27, 402-410.

Cornell, R.M. (1985) Effect of Simple Sugars on the Alkaline Transformation of Ferrihydrite into Goethite and Hematite. Clays and Clay Minerals 33, 219-227.

Cornell, R.M. and Schindler, P.W. (1980) Infrared study of the adsorption of hydroxycarboxylic acids onα-FeOOH and amorphous Fe (III)hydroxide. Colloid and Polymer Science 258, 1171-1175.

Cornell, R.M. and Schwertmann, U. (2003) The iron oxides: structure, properties, reactions, occurrences and uses. John Wiley & Sons.

Costa, M. (1997) Toxicity and Carcinogenicity of Cr(VI) in Animal Models and Humans. Critical Reviews in Toxicology 27, 431-442.

Cudennec, Y. and Lecerf, A. (2006) The transformation of ferrihydrite into goethite or hematite, revisited. Journal of Solid State Chemistry 179, 716-722.

Curti, L., Moore, O.W., Babakhani, P., Xiao, K.-Q., Woulds, C., Bray, A.W., Fisher, B.J., Kazemian, M., Kaulich, B. and Peacock, C.L. (2021) Carboxyl-richness controls organic carbon preservation during coprecipitation with iron (oxyhydr)oxide in the natural environment. Communications Earth & Environment 2, 229.

Dai, C., Zuo, X., Cao, B. and Hu, Y. (2016) Homogeneous and Heterogeneous (Fex, Cr1-x)(OH)3 Precipitation: Implications for Cr Sequestration. Environ Sci Technol 50, 1741-1749.

Dai, J., Becquer, T., Rouiller, J.H., Reversat, G., Bernhard-Reversat, F. and Lavelle, P. (2004) Influence of heavy metals on C and N mineralisation and microbial biomass in Zn-, Pb-, Cu-, and Cd-contaminated soils. Applied Soil Ecology 25, 99-109.

Darrie, G. (2001) Commercial Extraction Technology and Process Waste Disposal in the Manufacture of Chromium chemicals From Ore. Environmental Geochemistry and Health 23, 187-193.

Das, S., Hendry, M.J. and Essilfie-Dughan, J. (2011a) Effects of Adsorbed Arsenate on the Rate of Transformation of 2-Line Ferrihydrite at pH 10. Environmental Science & Technology 45, 5557-5563.

Das, S., Hendry, M.J. and Essilfie-Dughan, J. (2011b) Transformation of Two-Line Ferrihydrite to Goethite and Hematite as a Function of pH and Temperature. Environmental Science & Technology 45, 268-275.

Dean, J.A. (1987) Handbook of Organic Chemistry. NY: McGraw-Hill Book Co., New York.

Dhal, B., Thatoi, H.N., Das, N.N. and Pandey, B.D. (2013a) Chemical and microbial remediation of hexavalent chromium from contaminated soil and mining/metallurgical solid waste: A review. Journal of Hazardous Materials 250-251, 272-291.

Dhal, B., Thatoi, H.N., Das, N.N. and Pandey, B.D. (2013b) Chemical and microbial remediation of hexavalent chromium from contaminated soil and mining/metallurgical solid waste: a review. J Hazard Mater 250-251, 272-291.

Ding, C., Li, X., Zhang, T., Ma, Y. and Wang, X. (2014) Phytotoxicity and accumulation of chromium in carrot plants and the derivation of soil thresholds for Chinese soils. Ecotoxicology and Environmental Safety 108, 179-186.

Ding, Z., Fu, F., Dionysiou, D.D. and Tang, B. (2018) Coadsorption and subsequent redox conversion behaviors of As(III) and Cr(VI) on Al-containing ferrihydrite. Environmental Pollution 235, 660-669.

Dobson, K.D. and McQuillan, A.J. (1999) In situ infrared spectroscopic analysis of the adsorption of aliphatic carboxylic acids to TiO2, ZrO2, Al2O3, and Ta2O5 from aqueous solutions. Spectrochimica Acta Part A: Molecular and Biomolecular Spectroscopy 55, 1395-1405.

Dreyfuss, J. (1964) Characterization of a Sulfate- and Thiosulfate-transporting System in Salmonella typhimurium. Journal of Biological Chemistry 239, 2292-2297.

Drits, V.A., Sakharov, B.A., Salyn, A.L. and Manceau, A. (1993) Structural model for ferrihydrite. Clay Minerals 28, 185-207.

Du, H., Peacock, C.L., Chen, W. and Huang, Q. (2018) Binding of Cd by ferrihydrite organo-mineral composites: Implications for Cd mobility and fate in natural and contaminated environments. Chemosphere 207, 404-412.

Duckworth, O.W. and Martin, S.T. (2001) Surface complexation and dissolution of hematite by C1-C6 dicarboxylic acids at pH = 5.0. Geochimica et Cosmochimica Acta 65, 4289-4301.

Ertani, A., Mietto, A., Borin, M. and Nardi, S. (2017) Chromium in Agricultural Soils and Crops: A Review. Water, Air, & Soil Pollution 228.

Eusterhues, K., Hädrich, A., Neidhardt, J., Küsel, K., Keller, T.F., Jandt, K.D. and Totsche, K.U. (2014) Reduction of ferrihydrite with adsorbed and coprecipitated organic matter: microbial reduction by Geobacter bremensis vs. abiotic reduction by Na-dithionite. Biogeosciences 11, 4953-4966.

Eusterhues, K., Rennert, T., Knicker, H., Kögel-Knabner, I., Totsche, K.U. and Schwertmann, U. (2011) Fractionation of Organic Matter Due to Reaction with Ferrihydrite: Coprecipitation versus Adsorption. Environmental Science & Technology 45, 527-533.

Eusterhues, K., Rumpel, C. and Kögel-Knabner, I. (2005) Organo-mineral associations in sandy acid forest soils: importance of specific surface area, iron oxides and micropores. 56, 753-763.

Eusterhues, K., Wagner, F.E., Häusler, W., Hanzlik, M., Knicker, H., Totsche, K.U., Kögel-Knabner, I. and Schwertmann, U. (2008) Characterization of Ferrihydrite-Soil Organic Matter Coprecipitates by X-ray Diffraction and Mössbauer Spectroscopy. Environmental Science & Technology 42, 7891-7897.

Evanko, C.R. and Dzombak, D.A. (1999) Surface Complexation Modeling of Organic Acid Sorption to Goethite. Journal of Colloid and Interface Science 214, 189-206.

Fariña, A.O., Peacock, C.L., Fiol, S., Antelo, J. and Carvin, B. (2018) A universal adsorption behaviour for Cu uptake by iron (hydr)oxide organo-mineral composites. Chemical Geology 479, 22-35.

Fasulo, M., Bassi, M. and Donini, A. (1983) Cytotoxic effects of hexavalent chromium in Euglena gracilis . II. Physiological and ultrastructural studies. Protoplasma 114, 35-43.

Fendorf, S., Eick, M.J., Grossl, P. and Sparks, D.L. (1997) Arsenate and Chromate Retention Mechanisms on Goethite. 1. Surface Structure. Environmental Science & Technology 31, 315-320.

Fendorf, S.E., Li, G. and Gunter, M.E. (1996) Micromorphologies and Stabilities of Chromium (III) Surface Precipitates Elucidated by Scanning Force Microscopy. Soil Science Society of America Journal 60, 99-106.

Fisher, B.J., Moore, O.W., Faust, J.C., Peacock, C.L. and März, C. (2020) Experimental evaluation of the extractability of iron bound organic carbon in sediments as a function of carboxyl content. Chemical Geology 556.

Ford, R.G., Kemner, K.M. and Bertsch, P.M. (1999) Influence of sorbate-sorbent interactions on the crystallization kinetics of nickel- and lead-ferrihydrite coprecipitates. Geochimica et Cosmochimica Acta 63, 39-48.

Fortin, D. and Langley, S. (2005) Formation and occurrence of biogenic iron-rich minerals. Earth-Science Reviews 72, 1-19.

Francisco, P.C.M., Sato, T., Otake, T., Kasama, T., Suzuki, S., Shiwaku, H. and Yaita, T. (2018) Mechanisms of Se(IV) Co-precipitation with Ferrihydrite at Acidic and Alkaline Conditions and Its Behavior during Aging. Environmental Science & Technology 52, 4817-4826.

Fredrickson, J.K., Zachara, J.M., Kennedy, D.W., Dong, H., Onstott, T.C., Hinman, N.W. and Li, S.-m. (1998) Biogenic iron mineralization accompanying the dissimilatory reduction of hydrous ferric oxide by a groundwater bacterium. Geochimica et Cosmochimica Acta 62, 3239-3257.

Friddle, R.W., Noy, A. and De Yoreo, J.J. (2012) Interpreting the widespread nonlinear force spectra of intermolecular bonds. Proc Natl Acad Sci USA 109, 13573-13578.

Goldberg, S., Criscenti, L.J., Turner, D.R., Davis, J.A. and Cantrell, K.J. (2007) Adsorption–Desorption Processes in Subsurface Reactive Transport Modeling. Vadose Zone Journal 6, 407-435.

Grafe, M., Eick, M.J., Grossl, P.R. and Saunders, A.M. (2002) Adsorption of Arsenate and Arsenite on Ferrihydrite in the Presence and Absence of Dissolved Organic Carbon. Journal of Environmental Quality 31, 1115-1123.

Grossl, P.R., Eick, M., Sparks, D.L., Goldberg, S. and Ainsworth, C.C. (1997) Arsenate and Chromate Retention Mechanisms on Goethite. 2. Kinetic Evaluation Using a Pressure-Jump Relaxation Technique. Environmental Science & Technology 31, 321-326.

Gu, X., Xie, J., Wang, X. and Evans, L.J. (2017) A simple model to predict chromate partitioning in selected soils from China. Journal of Hazardous Materials 322, 421-429.

Gustafsson, J.P., Persson, I., Oromieh, A.G., van Schaik, J.W., Sjostedt, C. and Kleja, D.B. (2014) Chromium(III) complexation to natural organic matter: mechanisms and modeling. Environ Sci Technol 48, 1753-1761.

Hajji, S., Montes-Hernandez, G., Sarret, G., Tordo, A., Morin, G., Ona-Nguema, G., Bureau, S., Turki, T. and Mzoughi, N. (2019) Arsenite and chromate sequestration onto ferrihydrite, siderite and goethite nanostructured minerals: Isotherms from flow-through reactor experiments and XAS measurements. Journal of Hazardous Materials 362, 358-367.

Hall, S.J., Ye, C., Weintraub, S.R. and Hockaday, W.C. (2020) Molecular trade-offs in soil organic carbon composition at continental scale. Nature Geoscience 13, 687-692.

Han, J., Kim, M. and Ro, H.-M. (2020a) Factors modifying the structural configuration of oxyanions and organic acids adsorbed on iron (hydr)oxides in soils. A review. Environmental Chemistry Letters 18, 631-662.

Han, L., Sun, K., Keiluweit, M., Yang, Y., Yang, Y., Jin, J., Sun, H., Wu, F. and Xing, B. (2019) Mobilization of ferrihydrite-associated organic carbon during Fe reduction: Adsorption versus coprecipitation. Chemical Geology 503, 61-68.

Han, X., Tomaszewski, E.J., Sorwat, J., Pan, Y., Kappler, A. and Byrne, J.M. (2020b) Effect of Microbial Biomass and Humic Acids on Abiotic and Biotic Magnetite Formation. Environmental Science & Technology 54, 4121-4130.

Handler, R.M., Beard, B.L., Johnson, C.M. and Scherer, M.M. (2009) Atom Exchange between Aqueous Fe(II) and Goethite: An Fe Isotope Tracer Study. Environmental Science & Technology 43, 1102-1107.

Handler, R.M., Frierdich, A.J., Johnson, C.M., Rosso, K.M., Beard, B.L., Wang, C., Latta, D.E., Neumann, A., Pasakarnis, T., Premaratne, W.A.P.J. and Scherer, M.M. (2014) Fe(II)-Catalyzed Recrystallization of Goethite Revisited. Environmental Science & Technology 48, 11302-11311.

Hansel, C.M., Benner, S.G. and Fendorf, S. (2005) Competing Fe(II)-Induced Mineralization Pathways of Ferrihydrite. Environmental Science & Technology 39, 7147-7153.

Hansel, C.M., Benner, S.G., Neiss, J., Dohnalkova, A., Kukkadapu, R.K. and Fendorf, S. (2003) Secondary mineralization pathways induced by dissimilatory iron reduction of ferrihydrite under advective flow. Geochimica et Cosmochimica Acta 67, 2977-2992.

Hansel, C.M., Benner, S.G., Nico, P. and Fendorf, S. (2004) Structural constraints of ferric (hydr)oxides on dissimilatory iron reduction and the fate of Fe(II)3 3Associate editor: J. B. Fein. Geochimica et Cosmochimica Acta 68, 3217-3229.

Harrington, R., Hausner, D.B., Xu, W., Bhandari, N., Michel, F.M., Brown, G.E., Strongin, D.R. and Parise, J.B. (2011) Neutron Pair Distribution Function Study of Two-Line Ferrihydrite. Environmental Science & Technology 45, 9883-9890.

Hatcher, P.G., Spiker, E.C., Szeverenyi, N.M. and Maciel, G.E. (1983) Selective preservation and origin of petroleum-forming aquatic kerogen. Nature 305, 498-501.

Hedges, J.I., Cowie, G.L., Ertel, J.R., James Barbour, R. and Hatcher, P.G. (1985) Degradation of carbohydrates and lignins in buried woods. Geochimica et Cosmochimica Acta 49, 701-711.

Hemingway, J.D., Rothman, D.H., Grant, K.E., Rosengard, S.Z., Eglinton, T.I., Derry, L.A. and Galy, V.V. (2019) Mineral protection regulates long-term global preservation of natural organic carbon. Nature 570, 228-231.

Henneberry, Y.K., Kraus, T.E.C., Nico, P.S. and Horwath, W.R. (2012) Structural stability of coprecipitated natural organic matter and ferric iron under reducing conditions. Organic Geochemistry 48, 81-89.

Hiemstra, T. (2013) Surface and mineral structure of ferrihydrite. Geochimica et Cosmochimica Acta 105, 316-325.

Hiemstra, T. and Van Riemsdijk, W.H. (2009) A surface structural model for ferrihydrite I: Sites related to primary charge, molar mass, and mass density. Geochimica et Cosmochimica Acta 73, 4423-4436.

Hiemstra, T., Van Riemsdijk, W.H. and Bolt, G.H. (1989) Multisite proton adsorption modeling at the solid/solution interface of (hydr)oxides: A new approach: I. Model description and evaluation of intrinsic reaction constants. Journal of Colloid and Interface Science 133, 91-104.

Hiemstra, T., Venema, P. and Riemsdijk, W.H.V. (1996) Intrinsic Proton Affinity of Reactive Surface Groups of Metal (Hydr)oxides: The Bond Valence Principle. Journal of Colloid and Interface Science 184, 680-692.

Hockridge, J.G., Jones, F., Loan, M. and Richmond, W.R. (2009) An electron microscopy study of the crystal growth of schwertmannite needles through oriented aggregation of goethite nanocrystals. Journal of Crystal Growth 311, 3876-3882.

Hu, S., Liang, Y., Liu, T., Li, F., Lu, Y. and Shi, Z. (2020) Kinetics of As(V) and carbon sequestration during Fe(II)-induced transformation of ferrihydrite-As(V)-fulvic acid coprecipitates. Geochimica et Cosmochimica Acta 272, 160-176.

Hu, S., Lu, Y., Peng, L., Wang, P., Zhu, M., Dohnalkova, A.C., Chen, H., Lin, Z., Dang, Z. and Shi, Z. (2018) Coupled Kinetics of Ferrihydrite Transformation and As(V) Sequestration under the Effect of Humic Acids: A Mechanistic and Quantitative Study. Environ Sci Technol.

Hu, Y., Xue, Q., Tang, J., Fan, X. and Chen, H. (2019) New insights on Cr(VI) retention by ferrihydrite in the presence of Fe(II). Chemosphere 222, 511-516.

Hua, J., Chen, M., Liu, C., Li, F., Long, J., Gao, T., Wu, F., Lei, J. and Gu, M. (2018) Cr Release from Cr-Substituted Goethite during Aqueous Fe(II)-Induced Recrystallization. Minerals 8.

Illés, E. and Tombácz, E. (2006) The effect of humic acid adsorption on pH-dependent surface charging and aggregation of magnetite nanoparticles. Journal of Colloid and Interface Science 295, 115-123.

Jacobs, J.A. and Testa, S.M. (2005) Overview of chromium (VI) in the environment: background and history. Chromium handbook, 1-21.

Jansen, E., Kyek, A. and Schwertmann, W.S. (2002) The structure of six-line ferrihydrite. Applied Physics A.

Jeejeebhoy, K.N., Chu, R., Marliss, E., Greenberg, G.R. and Bruce-Robertson, A. (1977) Chromium deficiency, glucose intolerance, and neuropathy reversed by chromium supplementation, in a patient receiving long-term total parenteral nutrition. The American Journal of Clinical Nutrition 30, 531-538.

Jelavić, S., Mitchell, A.C. and Sand, K.K. (2020) Fate of organic compounds during transformation of ferrihydrite in iron formations. Geochemical Perspectives Letters 15, 25-29.

Jiang, B., Gong, Y., Gao, J., Sun, T., Liu, Y., Oturan, N. and Oturan, M.A. (2019) The reduction of Cr(VI) to Cr(III) mediated by environmentally relevant carboxylic acids: State-of-the-art and perspectives. Journal of Hazardous Materials 365, 205-226.

Jiang, B., He, H., Liu, Y., Tang, Y., Luo, S. and Wang, Z. (2018) pH-dependent roles of polycarboxylates in electron transfer between Cr(VI) and weak electron donors. Chemosphere 197, 367-374.

Jiang, J. and Kappler, A.J. (2008) Kinetics of microbial and chemical reduction of humic substances: implications for electron shuttling. Environmental science
technology 42, 3563-3569.

Jobbágy, E.G. and Jackson, R.B. (2000) The vertical distribution of soil organic carbon and its relation to climate and vegetation. Ecological Applications 10, 423-436.

Jobby, R., Jha, P., Yadav, A.K. and Desai, N. (2018) Biosorption and biotransformation of hexavalent chromium [Cr(VI)]: A comprehensive review. Chemosphere 207, 255-266.

Johnston, C.P. and Chrysochoou, M. (2012) Investigation of Chromate Coordination on Ferrihydrite by in Situ ATR-FTIR Spectroscopy and Theoretical Frequency Calculations. Environmental Science & Technology 46, 5851-5858.

Johnston, C.P. and Chrysochoou, M. (2014) Mechanisms of chromate adsorption on hematite. Geochimica et Cosmochimica Acta 138, 146-157.

Johnston, C.P. and Chrysochoou, M. (2016) Mechanisms of Chromate, Selenate, and Sulfate Adsorption on Al-Substituted Ferrihydrite: Implications for Ferrihydrite Surface Structure and Reactivity. Environmental Science & Technology 50, 3589-3596.

Johnston, J.H. and Lewis, D.G. (1983) A detailed study of the transformation of ferrihydrite to hematite in an aqueous medium at 92°C. Geochimica et Cosmochimica Acta 47, 1823-1831.

Jones, A.M., Collins, R.N., Rose, J. and Waite, T.D. (2009) The effect of silica and natural organic matter on the Fe(II)-catalysed transformation and reactivity of Fe(III) minerals. Geochimica et Cosmochimica Acta 73, 4409-4422.

Kabata-Pendias, A. (2000) Trace elements in soils and plants. CRC press.

Kaiser, K. and Guggenberger (2003) Mineral surfaces and soil organic matter. European Journal of Soil Science 54, 219-236.

Kaiser, K. and Guggenberger, G. (2000) The role of DOM sorption to mineral surfaces in the preservation of organic matter in soils. Organic Geochemistry 31, 711-725.

Kaiser, K. and Guggenberger, G. (2007) Sorptive stabilization of organic matter by microporous goethite: sorption into small pores vs. surface complexation. European Journal of Soil Science 58, 45-59.

Karimian, N., Burton, E.D. and Johnston, S.G. (2019) Antimony speciation and mobility during Fe(II)-induced transformation of humic acid-antimony(V)-iron(III) coprecipitates. Environmental Pollution 254.

Katz, S.A. and Salem, H. (1994) The biological and environmental chemistry of chromium. VCH Publishers, pp. 139-156.

Kellerman, A.M., Kothawala, D.N., Dittmar, T. and Tranvik, L.J. (2015) Persistence of dissolved organic matter in lakes related to its molecular characteristics. Nature Geoscience 8, 454-457.

Kimbrough, D.E., Cohen, Y., Winer, A.M., Creelman, L., Mabuni, C.J.C.r.i.e.s. and technology (1999) A critical assessment of chromium in the environment. 29, 1-46.

Kramer, M.G., Sanderman, J., Chadwick, O.A., Chorover, J. and Vitousek, P.M. (2012) Long-term carbon storage through retention of dissolved aromatic acids by reactive particles in soil. Global Change Biology 18, 2594-2605.

Kukkadapu, R.K., Zachara, J.M., Fredrickson, J.K., Smith, S.C., Dohnalkova, A.C. and Russell, C.K. (2003) Transformation of 2-line ferrihydrite to 6-line ferrihydrite under oxic and anoxic conditions. American Mineralogist 88, 1903-1914.

Kulczycki, E., Fowle, D.A., Fortin, D. and Ferris, F.G. (2005) Sorption of Cadmium and Lead by Bacteria–Ferrihydrite Composites. Geomicrobiology Journal 22, 299-310.

Lalonde, K., Mucci, A., Ouellet, A. and Gélinas, Y. (2012) Preservation of organic matter in sediments promoted by iron. Nature 483, 198.

Larsen, O. and Postma, D. (2001) Kinetics of reductive bulk dissolution of lepidocrocite, ferrihydrite, and goethite. Geochimica et Cosmochimica Acta 65, 1367-1379.

Lehmann, J. and Kleber, M. (2015) The contentious nature of soil organic matter. Nature 528, 60-68.

Li, Y., Shahbaz, M., Zhu, Z., Chen, A., Nannipieri, P., Li, B., Deng, Y., Wu, J. and Ge, T. (2020) Contrasting response of organic carbon mineralisation to iron oxide addition under conditions of low and high microbial biomass in anoxic paddy soil. Biology and Fertility of Soils.

Lilli, M.A., Moraetis, D., Nikolaidis, N.P., Karatzas, G.P. and Kalogerakis, N. (2015) Characterization and mobility of geogenic chromium in soils and river bed sediments of Asopos basin. Journal of Hazardous Materials 281, 12-19.

Lindegren, M., Loring, J.S. and Persson, P. (2009) Molecular structures of citrate and tricarballylate adsorbed on alpha-FeOOH particles in aqueous suspensions. Langmuir 25, 10639-10647.

Liu, G., Yu, H., Wang, N., Jin, R., Wang, J. and Zhou, J. (2018) Microbial reduction of Ferrihydrite in the presence of reduced Graphene oxide materials: Alteration of Fe(III) reduction rate, biomineralization product and settling behavior. Chemical Geology 476, 272-279.

Liu, H., Guo, H., Li, P. and Wei, Y. (2008) The transformation of ferrihydrite in the presence of trace Fe(II): The effect of the anionic media. Journal of Solid State Chemistry 181, 2666-2671.

Lovley, D.R., Coates, J.D., Blunt-Harris, E.L., Phillips, E.J. and Woodward, J.C. (1996) Humic substances as electron acceptors for microbial respiration. Nature 382, 445-448.

Lu, Y., Hu, S., Liang, Z., Zhu, M., Wang, Z., Wang, X., Liang, Y., Dang, Z. and Shi, Z. (2020) Incorporation of Pb(ii) into hematite during ferrihydrite transformation. Environmental Science: Nano 7, 829-841.

Lu, Y., Hu, S., Liu, F., Liang, Y. and Shi, Z. (2019a) Effects of humic acid and fulvic acid on the sequestration of copper and carbon during the iron oxide transformation. Chemical Engineering Journal.

Lu, Y., Hu, S., Wang, Z., Ding, Y., Lu, G., Lin, Z., Dang, Z. and Shi, Z. (2019b) Ferrihydrite transformation under the impact of humic acid and Pb: kinetics, nanoscale mechanisms, and implications for C and Pb dynamics. Environmental Science: Nano 6, 747-762.

Lv, J., Zhang, S., Wang, S., Luo, L., Cao, D. and Christie, P. (2016) Molecular-Scale Investigation with ESI-FT-ICR-MS on Fractionation of Dissolved Organic Matter Induced by Adsorption on Iron Oxyhydroxides. Environmental Science & Technology 50, 2328-2336.

Maillot, F., Morin, G., Wang, Y., Bonnin, D., Ildefonse, P., Chaneac, C. and Calas, G. (2011) New insight into the structure of nanocrystalline ferrihydrite: EXAFS evidence for tetrahedrally coordinated iron(III). Geochimica et Cosmochimica Acta 75, 2708-2720.

Manceau, A. (1995) The mechanism of anion adsorption on iron oxides: Evidence for the bonding of arsenate tetrahedra on free Fe(O, OH)6 edges. Geochimica et Cosmochimica Acta 59, 3647-3653.

Manceau, A. and Drits, V. (1993) Local structure of ferrihydrite and feroxyhite by EXAFS spectroscopy. Clay minerals 28, 165-184.

Manceau, A., Schlegel, M.L., Musso, M., Sole, V.A., Gauthier, C., Petit, P.E. and Trolard, F. (2000) Crystal chemistry of trace elements in natural and synthetic goethite. Geochimica et Cosmochimica Acta 64, 3643-3661.

Maslar, J.E., Hurst, W.S., Bowers, W.J., Hendricks, J.H., Aquino, M.I. and Levin, I. (2001) In situ Raman spectroscopic investigation of chromium surfaces under hydrothermal conditions. Applied Surface Science 180, 102-118.

Mayer, L.M. (1999) Extent of coverage of mineral surfaces by organic matter in marine sediments. Geochimica et Cosmochimica Acta 63, 207-215.

McCollom, T.M. and Seewald, J.S. (2003) Experimental study of the hydrothermal reactivity of organic acids and acid anions: II. Acetic acid, acetate, and valeric acid. Geochimica et Cosmochimica Acta 67, 3645-3664.

Mejia, J., He, S., Yang, Y., Ginder-Vogel, M. and Roden, E.E. (2018) Stability of Ferrihydrite-Humic Acid Coprecipitates under Iron-Reducing Conditions. Environmental Science and Technology 52, 13174-13183.

Mesuere, K. and Fish, W. (1992a) Chromate and oxalate adsorption on goethite. 1. Calibration of surface complexation models. Environmental Science & Technology 26, 2357-2364.

Mesuere, K. and Fish, W. (1992b) Chromate and oxalate adsorption on goethite. 2. Surface complexation modeling of competitive adsorption. Environmental Science & Technology 26, 2365-2370.

Michel, F., Barrón, V., Torrent, J., Morales, M.d.P., Serna, C., Boily, J.-F., Liu, Q., Ambrosini, A., Cismasu, A. and Brown, G. (2010) Ordered ferrimagnetic form of ferrihydrite reveals links among structure, composition, and magnetism. Proceedings of the National Academy of Sciences 107, 2787-2792.

Michel, F.M., Ehm, L., Antao, S.M., Lee, P.L., Chupas, P.J., Liu, G., Strongin, D.R., Schoonen, M.A., Phillips, B.L. and Parise, J.B. (2007a) The structure of ferrihydrite, a nanocrystalline material. Science 316, 1726-1729.

Michel, F.M., Ehm, L., Liu, G., Han, W.Q., Antao, S.M., Chupas, P.J., Lee, P.L., Knorr, K., Eulert, H., Kim, J., Grey, C.P., Celestian, A.J., Gillow, J., Schoonen, M.A.A., Strongin, D.R. and Parise, J.B. (2007b) Similarities in 2- and 6-Line Ferrihydrite Based on Pair Distribution Function Analysis of X-ray Total Scattering. Chemistry of Materials 19, 1489-1496.

Mikutta, C. (2011) X-ray absorption spectroscopy study on the effect of hydroxybenzoic acids on the formation and structure of ferrihydrite. Geochimica et Cosmochimica Acta 75, 5122-5139.

Mikutta, C., Wiederhold, J.G., Cirpka, O.A., Hofstetter, T.B., Bourdon, B. and Gunten, U.V. (2009) Iron isotope fractionation and atom exchange during sorption of ferrous iron to mineral surfaces. Geochimica et Cosmochimica Acta 73, 1795-1812.

Mikutta, R., Kleber, M., Torn, M.S. and Jahn, R. (2006) Stabilization of Soil Organic Matter: Association with Minerals or Chemical Recalcitrance? Biogeochemistry 77, 25-56.

Mikutta, R., Lorenz, D., Guggenberger, G., Haumaier, L. and Freund, A. (2014) Properties and reactivity of Fe-organic matter associations formed by coprecipitation versus adsorption: Clues from arsenate batch adsorption. Geochimica et Cosmochimica Acta 144, 258-276.

Moon, E.M. and Peacock, C.L. (2013) Modelling Cu(II) adsorption to ferrihydrite and ferrihydrite–bacteria composites: Deviation from additive adsorption in the composite sorption system. Geochimica et Cosmochimica Acta 104, 148-164.

Morterra, C., Chiorlno, A. and Borello, E. (1984) An IR spectroscopic characterization of α-FeOOH (goethite). Materials Chemistry and Physics 10, 119-138.

Namduri, H. and Nasrazadani, S. (2008) Quantitative analysis of iron oxides using Fourier transform infrared spectrophotometry. Corrosion Science 50, 2493-2497.

Neumann, A., Wu, L., Li, W., Beard, B.L., Johnson, C.M., Rosso, K.M., Frierdich, A.J. and Scherer, M.M. (2015) Atom Exchange between Aqueous Fe(II) and Structural Fe in Clay Minerals. Environmental Science & Technology 49, 2786-2795.

Newcomb, C.J., Qafoku, N.P., Grate, J.W., Bailey, V.L. and De Yoreo, J.J. (2017) Developing a molecular picture of soil organic matter-mineral interactions by quantifying organo-mineral binding. Nat Commun 8, 396.

Palmer, C.D. and Wittbrodt, P.R. (1991) Processes affecting the remediation of chromium-contaminated sites. Environmental health perspectives 92, 25-40.

Park, S., Lee, J.-H., Shin, T.J., Hur, H.-G. and Kim, M.G. (2018) Adsorption and Incorporation of Arsenic to Biogenic Lepidocrocite Formed in the Presence of Ferrous Iron during Denitrification by Paracoccus denitrificans. Environmental Science & Technology 52, 9983-9991.

Parkhurst, D.L. and Appelo, C. (1999) User's guide to PHREEQC (Version 2): A computer program for speciation, batch-reaction, one-dimensional transport, and inverse geochemical calculations. Water-resources investigations report 99, 312.

Peacock, C.L. and Sherman, D.M. (2004) Copper(II) sorption onto goethite, hematite and lepidocrocite: a surface complexation model based on ab initio molecular geometries and EXAFS spectroscopy. Geochimica et Cosmochimica Acta 68, 2623-2637.

Peak, D. and Regier, T. (2012) Direct Observation of Tetrahedrally Coordinated Fe(III) in Ferrihydrite. Environmental Science & Technology 46, 3163-3168.

Pedersen, H.D., Postma, D., Jakobsen, R. and Larsen, O. (2005) Fast transformation of iron oxyhydroxides by the catalytic action of aqueous Fe(II). Geochimica et Cosmochimica Acta 69, 3967-3977.

Pérez, C., Antelo, J., Fiol, S. and Arce, F. (2014) Modeling oxyanion adsorption on ferralic soil, part 2: Chromate, selenate, molybdate, and arsenate adsorption. Environ Toxicol Chem 33, 2217-2224.

Poggenburg, C., Mikutta, R., Sander, M., Schippers, A., Marchanka, A., Dohrmann, R. and Guggenberger, G. (2016) Microbial reduction of ferrihydrite-organic matter coprecipitates by Shewanella putrefaciens and Geobacter metallireducens in comparison to mediated electrochemical reduction. Chemical Geology 447, 133-147.

Poggenburg, C., Mikutta, R., Schippers, A., Dohrmann, R. and Guggenberger, G. (2018) Impact of natural organic matter coatings on the microbial reduction of iron oxides. Geochimica et Cosmochimica Acta 224, 223-248.

Quantin, C., Ettler, V., Garnier, J. and Šebek, O. (2008) Sources and extractibility of chromium and nickel in soil profiles developed on Czech serpentinites. Comptes Rendus Geoscience 340, 872-882.

Rai, D., Sass, B. and Moore, D. (1986) Chromium (III) hydrolysis constants and solubility of chromium (III) hydroxide. Inorg. Chem. 26.

Rai, D., Sass, B.M. and Moore, D.A. (1987) Chromium(III) hydrolysis constants and solubility of chromium(III) hydroxide. Inorganic Chemistry 26, 345-349.

Rai, D. and Zachara, J.M. (1986) Geochemical behavior of chromium species. interim report EPRI EA-4544, E.P.R.I., Palo Alto. Calif.

Rai, D., Zachara, J.M., Eary, L.E., Girvin, D.C., Moore, D.A., Resch, C.T., Sass, B.M. and Schmidt, R.L. (1986) geochemical behaviour of chromium species. interim report EPRI EA-4544, E.P.R.I., Palo Alto. Calif.

Reddy, T.R., Frierdich, A.J., Beard, B.L. and Johnson, C.M. (2015) The effect of pH on stable iron isotope exchange and fractionation between aqueous Fe(II) and goethite. Chemical Geology 397, 118-127.

Richard, F.C. and Bourg, A.C. (1991a) Aqueous geochemistry of chromium: a review. Water research 25, 807-816.

Richard, F.C. and Bourg, A.C.M. (1991b) Aqueous geochemistry of chromium: A review. Water Research 25, 807-816.

Rochester, C.H. and Topham, S.A. (1979) Infrared study of surface hydroxyl groups on goethite. Journal of the Chemical Society, Faraday Transactions 1: Physical Chemistry in Condensed Phases 75, 591-602.

Roden, E.E., Kappler, A., Bauer, I., Jiang, J., Paul, A., Stoesser, R., Konishi, H. and Xu, H. (2010) Extracellular electron transfer through microbial reduction of solid-phase humic substances. Nature Geoscience 3, 417.

Rogers, N.D. (2016) Chromium Oxidation by Disinfectants and Oxidants Used in Drinking Water treatment. All Graduate Theses and Dissertation 5028.

Rothe, J., Denecke, M.A. and Dardenne, K. (2000) Soft X-Ray Spectromicroscopy Investigation of the Interaction of Aquatic Humic Acid and Clay Colloids. Journal of Colloid and Interface Science 231, 91-97.

Rothman, D.H. and Forney, D.C. (2007) Physical Model for the Decay and Preservation of Marine Organic Carbon. Science 316, 1325.

Rowley, M.C., Grand, S. and Verrecchia, É.P. (2017) Calcium-mediated stabilisation of soil organic carbon. Biogeochemistry 137, 27-49.

Ruan, H.D., Frost, R.L., Kloprogge, J.T. and Duong, L. (2002) Infrared spectroscopy of goethite dehydroxylation. II. Effect of aluminium substitution on the behaviour of hydroxyl units. Spectrochimica Acta Part A: Molecular and Biomolecular Spectroscopy 58, 479-491.

Ruddiman, W.F. (2001) Earth's Climate: Past, Present and Future. W.H. Freeman, New York.

Sakakibara, M., Tanaka, M., Takahashi, Y. and Murakami, T. (2019) Redistribution of Zn during transformation of ferrihydrite: Effects of initial Zn concentration. Chemical Geology 522, 121-134.

Sass, B.M. and Rai, D. (1987) Solubility of amorphous chromium(III)-iron(III) hydroxide solid solutions. Inorganic Chemistry 26, 2228-2232.

Scawarz, K. and Mertz, W. (1959) Chromium (III) and the glucose tolerance factor. Archives of Biochemistry 85, 292-295.

Schmidt, M.W., Torn, M.S., Abiven, S., Dittmar, T., Guggenberger, G., Janssens, I.A., Kleber, M., Kogel-Knabner, I., Lehmann, J., Manning, D.A., Nannipieri, P., Rasse, D.P., Weiner, S. and Trumbore, S.E. (2011) Persistence of soil organic matter as an ecosystem property. Nature 478, 49-56.

Schwertmann, U. (1966) Inhibitory Effect of Soil Organic Matter on the Crystallization of Amorphous Ferric Hydroxide. Nature 212, 645-646.

Schwertmann, U. and Cornell, R.M. (2008) Iron oxides in the laboratory: preparation and characterization. John Wiley & Sons.

Schwertmann, U. and Fischer, W. (1966) Zur Bildung von α - FeOOH und α - Fe2O3 aus amorphem Eisen (III) - hydroxid. III. Zeitschrift für anorganische und allgemeine Chemie 346, 137-142.

Schwertmann, U., Friedl, J. and Stanjek, H. (1999) From Fe(III) Ions to Ferrihydrite and then to Hematite. Journal of Colloid and Interface Science 209, 215-223.

Schwertmann, U. and Murad, E. (1983) Effect of pH on the Formation of Goethite and Hematite from Ferrihydrite. Clays and Clay Minerals 31, 277-284.

Schwertmann, U., Stanjek, H. and Becher, H.-H. (2004) Long-term in vitro transformation of 2-line ferrihydrite to goethite/hematite at 4, 10, 15 and 25 C. Clay Minerals 39, 433-438.

Scott, D.T., McKnight, D.M., Blunt-Harris, E.L., Kolesar, S.E. and Lovley, D.R. (1998) Quinone Moieties Act as Electron Acceptors in the Reduction of Humic Substances by Humics-Reducing Microorganisms. Environmental Science & Technology 32, 2984-2989.

Shahid, M., Shamshad, S., Rafiq, M., Khalid, S., Bibi, I., Niazi, N.K., Dumat, C. and Rashid, M.I. (2017) Chromium speciation, bioavailability, uptake, toxicity and detoxification in soil-plant system: A review. Chemosphere 178, 513-533.

Shanker, A.K., Cervantes, C., Loza-Tavera, H. and Avudainayagam, S. (2005) Chromium toxicity in plants. Environment International 31, 739-753.

Sheng, A., Li, X., Arai, Y., Ding, Y., Rosso, K.M. and Liu, J. (2020a) Citrate Controls Fe(II)-Catalyzed Transformation of Ferrihydrite by Complexation of the Labile Fe(III) Intermediate. Environ Sci Technol.

Sheng, A., Liu, J., Li, X., Qafoku, O., Collins, R.N., Jones, A.M., Pearce, C.I., Wang, C., Ni, J., Lu, A. and Rosso, K.M. (2020b) Labile Fe(III) from sorbed Fe(II) oxidation is the key intermediate in Fe(II)-catalyzed ferrihydrite transformation. Geochimica et Cosmochimica Acta.

Sherman, D.M., Peacock, C.L. and Hubbard, C.G. (2008) Surface complexation of U(VI) on goethite (α-FeOOH). Geochimica et Cosmochimica Acta 72, 298-310.

Shimizu, M., Zhou, J., Schröder, C., Obst, M., Kappler, A. and Borch, T. (2013) Dissimilatory Reduction and Transformation of Ferrihydrite-Humic Acid Coprecipitates. Environmental Science & Technology 47, 13375-13384.

Shtiza, A., Swennen, R. and Tashko, A. (2008) Chromium speciation and existing natural attenuation conditions in lagoonal and pond sediments in the former chemical plant of Porto-Romano (Albania). Environmental Geology 53, 1107-1128.

Singh, B., Sherman, D.M., Gilkes, R.J., Wells, M.A. and Mosselmans, J.F.W. (2002) Incorporation of Cr, Mn and Ni into goethite (α-FeOOH): mechanism from extended X-ray absorption fine structure spectroscopy. Clay Minerals 37, 639-649.

Six, J., Conant, R.T., Paul, E.A. and Paustian, K. (2002) Stabilization mechanisms of soil organic matter: Implications for C-saturation of soils. Plant and Soil 241, 155-176.

Sneddon, C. (2012) Chromium and its negative effects on the environment: case study. Missoula, Montana-US: Department of Earth Sciences, Montana State University.

Solomon, D., Lehmann, J., Kinyangi, J., Liang, B. and Schäfer, T. (2005) Carbon K-Edge NEXAFS and FTIR-ATR Spectroscopic Investigation of Organic Carbon Speciation in Soils. Soil Science Society of America Journal 69, 107-119.

Song, Y., Swedlund, P.J., Singhal, N. and Swift, S. (2009) Cadmium(II) Speciation in Complex Aquatic Systems: A Study with Ferrihydrite, Bacteria, and an Organic Ligand. Environmental Science & Technology 43, 7430-7436.

Sowers, T.D., Adhikari, D., Wang, J., Yang, Y. and Sparks, D.L. (2018a) Spatial Associations and Chemical Composition of Organic Carbon Sequestered in Fe, Ca, and Organic Carbon Ternary Systems. Environ Sci Technol 52, 6936-6944.

Sowers, T.D., Stuckey, J.W. and Sparks, D.L. (2018b) The synergistic effect of calcium on organic carbon sequestration to ferrihydrite. Geochemical Transactions 19.

Sparks, D.L. (2003) Environmental soil chemistry. Elsevier.

Sposito, G. (2008) The chemistry of soils. Oxford university press.

Stookey, L.L. (1970) Ferrozine---a new spectrophotometric reagent for iron. Analytical Chemistry 42, 779-781.

Stumm, W. and Morgan, J.J. (1996) Aquatic Chemistry (3rd ed.). John Wiley & Sons, Singapore.

Sun, G., Fu, F., Yu, G., Yu, P. and Tang, B. (2021) Migration behavior of Cr(VI) during the transformation of ferrihydrite-Cr(VI) co-precipitates: The interaction between surfactants and co-precipitates. Sci Total Environ 767, 145429.

Suter, D., Banwart, S. and Stumm, W. (1991) Dissolution of hydrous iron (III) oxides by reductive mechanisms. Langmuir 7, 809-813.

Tamaura, Y., Buduan, P. and Katsura, T. (1981) Studies on the Oxidation of Iron(II) Ion during the Formation of Fe3O4 and α-FeO(OH) by Air Oxidation of Fe[OH]2 Suspensions.

Journal of The Chemical Society-dalton Transactions - J CHEM SOC DALTON TRANS 12.

Tamaura, Y., Ito, K. and Katsura, T. (1983) Transformation of γ-FeO(OH) to Fe3O4 by adsorption of iron(II) ion on γ-FeO(OH). Journal of The Chemical Society-dalton Transactions - J CHEM SOC DALTON TRANS 2.

Tang, Y., Michel, F.M., Zhang, L., Harrington, R., Parise, J.B. and Reeder, R.J. (2010) Structural Properties of the Cr(III)−Fe(III) (Oxy)hydroxide Compositional Series: Insights for a Nanomaterial "Solid Solution". Chemistry of Materials 22, 3589-3598.

Taylor, R.M., Self, P.G. and Fitzpatrick, R.W. (1987) The influence of sucrose and glycerol on the formation and transformation of iron oxides — The implication for soil formation. Applied Clay Science 2, 41-62.

ThomasArrigo, L.K., Byrne, J.M., Kappler, A. and Kretzschmar, R. (2018) Impact of Organic Matter on Iron(II)-Catalyzed Mineral Transformations in Ferrihydrite-Organic Matter Coprecipitates. Environ Sci Technol 52, 12316-12326.

ThomasArrigo, L.K., Kaegi, R. and Kretzschmar, R. (2019) Ferrihydrite Growth and Transformation in the Presence of Ferrous Iron and Model Organic Ligands. Environ Sci Technol.

ThomasArrigo, L.K., Mikutta, C., Byrne, J., Kappler, A. and Kretzschmar, R. (2017) Iron(II)-Catalyzed Iron Atom Exchange and Mineralogical Changes in Iron-rich Organic Freshwater Flocs: An Iron Isotope Tracer Study. Environ Sci Technol 51, 6897-6907.

Tomaszewski, E.J., Lee, S., Rudolph, J., Xu, H. and Ginder-Vogel, M. (2017) The reactivity of Fe(II) associated with goethite formed during short redox cycles toward Cr(VI) reduction under oxic conditions. Chemical Geology 464, 101-109.

Torn, M.S., Trumbore, S.E., Chadwick, O.A., Vitousek, P.M. and Hendricks, D.M. (1997) Mineral control of soil organic carbon storage and turnover. Nature 389, 170-173.

Trolard, F., Bourrie, G., Jeanroy, E., Herbillon, A.J. and Martin, H. (1995) Trace metals in natural iron oxides from laterites: A study using selective kinetic extraction. Geochimica et Cosmochimica Acta 59, 1285-1297.

Tronc, E., Belleville, P., Jolivet, J.P. and Livage, J. (1992) Transformation of ferric hydroxide into spinel by iron(II) adsorption. Langmuir 8, 313-319.

Turpeinen, R., Kairesalo, T. and Häggblom, M.M. (2004) Microbial community structure and activity in arsenic-, chromium- and copper-contaminated soils. FEMS Microbiology Ecology 47, 39-50.

van Beinum, W., Meeussen, J.C.L. and van Riemsdijk, W.H. (2006) Competitive sorption and diffusion of chromate and sulphate in a flow system with goethite in gel beads. Journal of Contaminant Hydrology 86, 262-278.

Verbeeck, M., Warrinnier, R., Gustafsson, J.P., Thiry, Y. and Smolders, E. (2019) Soil organic matter increases antimonate mobility in soil: An Sb(OH)6 sorption and modelling study. Applied Geochemistry 104, 33-41.

Vermeer, A.W.P., McCulloch, J.K., van Riemsdijk, W.H. and Koopal, L.K. (1999) Metal Ion Adsorption to Complexes of Humic Acid and Metal Oxides: Deviations from the Additivity Rule. Environmental Science & Technology 33, 3892-3897.

Veselská, V., Fajgar, R., Číhalová, S., Bolanz, R.M., Göttlicher, J., Steininger, R., Siddique, J.A. and Komárek, M. (2016) Chromate adsorption on selected soil minerals: Surface complexation modeling coupled with spectroscopic investigation. Journal of Hazardous Materials 318, 433-442.

Veselská, V., Šillerová, H., Göttlicher, J., Michálková, Z., Siddique, J.A., Číhalová, S., Chrastný, V., Steininger, R., Mangold, S. and Komárek, M. (2019) The role of soil components in synthetic mixtures during the adsorption and speciation changes of Cr(VI): Conjunction of the modeling approach with spectroscopic and isotopic investigations. Environment International 127, 848-857.

Villalobos, M., Trotz, M.A. and Leckie, J.O. (2001) Surface Complexation Modeling of Carbonate Effects on the Adsorption of Cr(VI), Pb(II), and U(VI) on Goethite. Environmental Science & Technology 35, 3849-3856.

Vogel, C., Mueller, C.W., Höschen, C., Buegger, F., Heister, K., Schulz, S., Schloter, M. and Kögel-Knabner, I. (2014) Submicron structures provide preferential spots for carbon and nitrogen sequestration in soils. Nature Communications 5, 2947.

Wagai, R. and Mayer, L.M. (2007) Sorptive stabilization of organic matter in soils by hydrous iron oxides. Geochimica et Cosmochimica Acta 71, 25-35.

Wang, D., Ye, Y., Liu, H., Ma, H. and Zhang, W. (2018) Effect of alkaline precipitation on Cr species of Cr(III)-bearing complexes typically used in the tannery industry. Chemosphere 193, 42-49.

Wang, S., Lei, L., Zhang, D., Zhang, G., Cao, R., Wang, X., Lin, J. and Jia, Y. (2020a) Stabilization and transformation of selenium during the Fe(II)-induced transformation of Se(IV)-adsorbed ferrihydrite under anaerobic conditions. Journal of Hazardous Materials 384.

Wang, X., Li, L., Yan, X., Meng, X. and Chen, Y. (2020b) Processes of chromium (VI) migration and transformation in chromate production site: A case study from the middle of China. Chemosphere 257, 127282.

Wang, Y., Morin, G., Ona-Nguema, G., Juillot, F., Calas, G. and Brown, G.E. (2011) Distinctive Arsenic(V) Trapping Modes by Magnetite Nanoparticles Induced by Different Sorption Processes. Environmental Science & Technology 45, 7258-7266.

Weerasooriya, R. and Tobschall, H.J. (2000) Mechanistic modeling of chromate adsorption onto goethite. Colloids and Surfaces A: Physicochemical and Engineering Aspects 162, 167-175.

Weng, L., Van Riemsdijk, W.H. and Hiemstra, T. (2009) Effects of Fulvic and Humic Acids on Arsenate Adsorption to Goethite: Experiments and Modeling. Environmental Science & Technology 43, 7198-7204.

Wershaw, R.L. (1994) Membrane-micelle model for humus in soils and sediments and its relation to humification, Water Supply Paper.

Westall, J. and Hohl, H. (1980) A comparison of electrostatic models for the oxide/solution interface. Advances in Colloid and Interface Science 12, 265-294.

Whitaker, A.H., Austin, R.E., Holden, K.L., Jones, J.L., Michel, F.M., Peak, D., Thompson, A. and Duckworth, O.W. (2021) The Structure of Natural Biogenic Iron (Oxyhydr)oxides Formed in Circumneutral pH Environments. Geochim Cosmochim Acta 308, 237-255.

Wiegand, H.J., Ottenwälder, H. and Bolt, H.M.J.a.o.t. (1985) Fast uptake kinetics in vitro of 51 Cr (VI) by red blood cells of man and rat. archives of toxicology 57, 31-34.

Wordofa, D.N., Adhikari, D., Dunham-Cheatham, S.M., Zhao, Q., Poulson, S.R., Tang, Y. and Yang, Y. (2019) Biogeochemical fate of ferrihydrite-model organic compound complexes during anaerobic microbial reduction. Sci Total Environ 668, 216-223.

Xia, X., Wang, J., Hu, Y., Liu, J., Darma, A.I., Jin, L., Han, H., He, C. and Yang, J. (2022) Molecular Insights into Roles of Dissolved Organic Matter in Cr(III) Immobilization by Coprecipitation with Fe(III) Probed by STXM-Ptychography and XANES Spectroscopy. Environ Sci Technol 56, 2432-2442.

Xia, X., Yang, J., Yan, Y., Wang, J., Hu, Y. and Zeng, X. (2020) Molecular Sorption Mechanisms of Cr(III) to Organo-Ferrihydrite Coprecipitates Using Synchrotron-Based EXAFS and STXM Techniques. Environ Sci Technol 54, 12989-12997.

Xiao, W., Jones, A.M., Collins, R.N., Bligh, M.W. and Waite, T.D. (2017) Use of fourier transform infrared spectroscopy to examine the Fe(II)-Catalyzed transformation of ferrihydrite. Talanta 175, 30-37.

Xie, J., Gu, X., Tong, F., Zhao, Y. and Tan, Y. (2015) Surface complexation modeling of Cr(VI) adsorption at the goethite–water interface. Journal of Colloid and Interface Science 455, 55-62.

Xu, Z., Xu, X., Tao, X., Yao, C., Tsang, D.C.W. and Cao, X. (2019) Interaction with low molecular weight organic acids affects the electron shuttling of biochar for Cr(VI) reduction. Journal of Hazardous Materials.

Yan, w., Liu, H., Chen, R., xie, j. and Wei, Y. (2015a) Dissolution and oriented aggregation: transformation from lepidorocite to goethite by the catalysis of aqueous Fe (II). RSC Adv. 5.

Yan, W., Liu, H., Chen, R., Xie, J. and Wei, Y. (2015b) Dissolution and oriented aggregation: transformation from lepidorocite to goethite by the catalysis of aqueous Fe(ii). RSC Advances 5, 106396-106399.

Yang, J., Xia, X., Liu, J., Wang, J. and Hu, Y. (2020) Molecular Mechanisms of Chromium(III) Immobilization by Organo–Ferrihydrite Co-precipitates: The Significant Roles of Ferrihydrite and Carboxyl. Environmental Science & Technology 54, 4820-4828.

Yanina, S.V. and Rosso, K.M. (2008) Linked Reactivity at Mineral-Water Interfaces Through Bulk Crystal Conduction. Science 320, 218.

Yu, G., Fu, F., Ye, C. and Tang, B. (2020) Behaviors and fate of adsorbed Cr(VI) during Fe(II)-induced transformation of ferrihydrite-humic acid co-precipitates. Journal of Hazardous Materials 392.

Yu, P., Fu, F., Sun, G. and Tang, B. (2021) Effects of oxalate and citrate on the behavior and redistribution of Cr(VI) during ferrihydrite-Cr(VI) co-precipitates transformation. Chemosphere 266, 128977.

Zachara, J.M., Resch, C.T. and Smith, S.C. (1994) Influence of humic substances on Co2+ sorption by a subsurface mineral separate and its mineralogic components. Geochimica et Cosmochimica Acta 58, 553-566.

Zeng, F., Ali, S., Zhang, H., Ouyang, Y., Qiu, B., Wu, F. and Zhang, G. (2011) The influence of pH and organic matter content in paddy soil on heavy metal availability and their uptake by rice plants. Environmental Pollution 159, 84-91.

Zhang, J., Chen, L., Yin, H., Jin, S., Liu, F. and Chen, H. (2017) Mechanism study of humic acid functional groups for Cr(VI) retention: Two-dimensional FTIR and 13C CP/MAS NMR correlation spectroscopic analysis. Environmental Pollution 225, 86-92.

Zhang, J., Yin, H., Chen, L., Liu, F. and Chen, H. (2018) The role of different functional groups in a novel adsorption-complexation-reduction multi-step kinetic model for hexavalent chromium retention by undissolved humic acid. Environmental Pollution 237, 740-746.

Zhao, Q., Poulson, S.R., Obrist, D., Sumaila, S., Dynes, J.J., McBeth, J.M. and Yang, Y. (2016) Iron-bound organic carbon in forest soils: quantification and characterization. Biogeosciences 13, 4777-4788.

Zhao, Y., Geng, J., Wang, X., Gu, X. and Gao, S. (2011) Adsorption of tetracycline onto goethite in the presence of metal cations and humic substances. Journal of Colloid and Interface Science 361, 247-251.

Zhou, J., Xia, B., Treves, D., Wu, L.Y., Marsh, T., O'Neill, R., Palumbo, A. and Tiedje, J. (2002) Spatial and Resource Factors Influencing High Microbial Diversity in Soil. Applied and environmental microbiology 68, 326-334.

Zhou, T., Wu, L., Luo, Y. and Christie, P. (2018a) Effects of organic matter fraction and compositional changes on distribution of cadmium and zinc in long-term polluted paddy soils. Environmental Pollution 232, 514-522.

Zhou, Z., Latta, D.E., Noor, N., Thompson, A., Borch, T. and Scherer, M.M. (2018b) Fe(II)-Catalyzed Transformation of Organic Matter-Ferrihydrite Coprecipitates: A Closer Look Using Fe Isotopes. Environ Sci Technol 52, 11142-11150.

Zhu, L., Fu, F. and Tang, B. (2019) Three-dimensional transfer of Cr(VI) co-precipitated with ferrihydrite containing silicate and its redistribution and retention during aging. Science of the Total Environment 696.